Numerical Methods for Unsteady Conjugate Heat Transfer

Yann Drèze
Wadham College
University of Oxford
Supervised by Luca di Mare

A thesis submitted for the degree of
Doctor of Philosophy

Trinity Term 2025

Acknowledgements

This thesis would not have been possible without the guidance, support, and encouragement of many individuals.

First and foremost, I extend my deepest gratitude to my advisor, Luca, for his constant support, feedback, and mentorship throughout this journey.

Then come my colleagues, whom I thank for providing a stimulating and productive work environment. From the porridge breaks to the whiteboard surveys or the constant silence in the office, I have enjoyed every moment spent with you.

To my friends, those I met while doing this thesis and those I have known for years, who have made my time in Oxford unforgettable.

To my family, who have always been there for me, no matter the distance.

Finally, to everyone who has contributed to this beautiful journey in ways big and small:

merci, grazie, thank you.

Abstract

The DPhil thesis enclosed herein addresses key challenges associated with unsteady conjugate heat transfer (CHT) modelling in the context of compressible flows. It establishes a foundation for efficient, high-fidelity simulations of coupled conduction-convection systems and provides insights into transient heat transfer dynamics that are critical to aerospace and energy applications.

First, this work develops a method for generating unsteady inflow conditions in scale-resolving simulations. Most practical CHT applications involve turbulent flows, which require accurate representation of unsteady inflow conditions for capturing complex downstream flow physics. The synthetic inflow generator offers a flexible and efficient solution to this challenge. Validation against experimental data demonstrates superior performance compared to existing methods.

The second contribution focuses on the simulation of unsteady CHT problems. Two primary challenges are addressed: the large disparities in time scales and length scales between solid and fluid domains. To tackle the length scale mismatch, a modal decomposition of the solid temperature field is proposed, which allows for an efficient representation of the unsteady heat conduction problem. The decomposition is coupled with a local, refined solution in the solid domain. To handle the time scale challenge, the decoupled modal equations are accelerated individually based on their respective time constants.

The thesis is concluded with a study of the unsteady effects of CHT in compressible flows. The transient evolution of global flow quantities in a transonic nozzle case is monitored using simulations with different levels of fidelity. Notably, the study reveals that transient thermal drifts are governed by the ratio of thermal capacity to the Stanton number. Results show exponential decay towards steady state, with initial temperature differences dictating drift bounds but not decay rates.

Contents

Appendices

Publications

1. Dreze Y., Hao M. and di Mare L. "Divergence-free turbulent inflow data from realistic covariance tensor" (2023), *Physics of Fluids* 35, 025120. `doi.org/10.1063/5.0136568`[1]

2. Dreze Y. and di Mare L. "Unsteady Conjugate Heat Transfer Effects on Flow Characteristics in Transonic Flow" (2025), *International Journal of Heat and Mass Transfer*, Volume 246, `https://doi.org/10.1016/j.ijheatmasstransfer.2025.127036` [1]

3. Dreze Y. and di Mare L. "Unsteady Conjugate Heat Transfer modelling via modal projection", Draft submitted to *Journal of Computational Physics* in April 2025[1]

4. Lomele M., Dreze Y., Smyth A. and Wildren R. "A mesh moving algorithm for fluid-structure interactions of wind turbine blades ", manuscript currently being written. [2]

---

[1] Included in this thesis

[2] Not included in this thesis

List of Figures

List of Abbreviations

1D, 2D, 3D	One-, two- or three-dimensional, referring in this thesis to spatial dimensions.
CHT	Conjugate heat transfer.
CFD	Computational fluid dynamics.
LES	Large eddy simulation.
DNS	Direct numerical simulation.
RANS	Reynolds-averaged Navier-Stokes.
URANS	Unsteady Reynolds-averaged Navier-Stokes.
FVM	Finite volume method.
TET	Turbine entry temperature.
HPT	High-pressure turbine.
NGV	Nozzle guide vane.
N-S	Navier-Stokes equations.
TPS	Thermal protection system.
H4X	High-fidelity heat transfer and fluid dynamics simulation framework.
FE	Finite element solution.
MFE	Modal finite element solution.

Nomenclature

ρ	Density (kg/m^3)
μ	Dynamic viscosity (Pa $\cdot$ s)
ν	Kinematic viscosity (m^2/s)
T	Temperature (K)
p	Pressure (Pa)
u, v, w	Velocity components (m/s)
$\vec{U}$	Velocity vector (m/s)
Re	Reynolds number
Pr	Prandtl number
Nu	Nusselt number
Bi	Biot number
Fo	Fourier number
St	Stanton number
L	Characteristic length (m)
t	Time (s)
x, y, z	Spatial coordinates (m)
∇	Gradient operator
k	Thermal conductivity (W/m $\cdot$ K)
c_p	Specific heat capacity (J/kg $\cdot$ K)
α	Thermal diffusivity (m^2/s)
h	Heat transfer coefficient (W/m^2 $\cdot$ K)
q	Heat flux (W/m^2)
ω	Angular frequency (rad/s)
f	Frequency (Hz)

λ	Eigenvalue
ϕ	Eigenfunction/mode shape
σ	Growth rate
δ_P	Thermal penetration depth (m)
η	Ideal thermal efficiency
y^+	Dimensionless wall distance
Q	Heat source (W)
Ω	Physical Domain
$\partial\Omega$	Boundary of the physical domain
Γ	Interface between fluid and solid domain
$\vec{n}$	Normal vector to a surface
Δt	Time step (s)
N	Test function
U	Modal amplitude
λ	Eigenvalue
Γ_m	Flow capacity
$\dot{m}$	Mass flow rate (kg/s)
A_x	Cross-sectional area (m^2)
γ	Ratio of specific heats
M	Mach number
c	Speed of sound (m/s)
R	Specific gas constant (J/kg $\cdot$ K)

Chapter 1 Introduction

The evolution of Computational Fluid Dynamics (CFD) over recent decades has transformed the landscape of engineering design and scientific research. Driven by exponential advancements in computational resources, algorithmic innovation, and the rise of high-performance computing, CFD has emerged as the primary design tool across a wide range of engineering systems, from aircraft and automobiles to energy systems and environmental modelling. Where once the analysis of complex fluid-structure interactions, turbulence, or multiphase systems was constrained by prohibitive computational costs or theoretical simplifications, modern CFD now enables high-fidelity simulations that bridge the gap between idealised models and real-world scenarios.

Building on this progress, the focus in CFD has expanded beyond isolated fluid domains to seek a more holistic view of engineering challenges. Recognising that real-world problems often involve interactions across multiple physical domains, researchers and engineers have increasingly turned their attention to the coupling of fluid flow with various physical phenomena, such as thermal effects, structural deformations, electromagnetic fields, and chemical reactions [Dowell and Hall, 2001, Keyes et al., 2013, Lomele et al., 2025]. One prominent example of this multiphysics approach is Conjugate Heat Transfer (CHT), which specifically addresses the interplay between heat transfer within solid structures and the surrounding fluid flow. By simulating these coupling, CHT proves to be an accurate tool for predicting temperature distributions and thermal stresses in systems where fluid-solid thermal interactions are critical, such as in high-temperature turbomachinery and heat exchangers.

Modelling a multiphysics problem is inherently challenging because each domain—whether fluid, thermal, structural, or otherwise—comes with its own specific requirements and characteristics. The physical models and computational methods used in one domain may not be directly applicable to another, and achieving a fully optimised solution across all domains is difficult. This complexity requires the development of sophisticated numerical algorithms capable of handling the specificities of each domain while ensuring accurate and stable coupling between them. As a result, multiphysics simulations in CFD often demand a delicate balance between accuracy, computational cost, and robustness, pushing the boundaries of what traditional CFD methods can achieve.

1.1 Objectives and thesis organisation

The primary motivation behind the present thesis is to develop a method for efficiently simulating unsteady conjugate heat transfer cases, specifically to treat the convergence toward thermal steady-state conditions. Unsteady characterisation of thermal effects is a challenge in engineering design, [Starke et al., 2008, Cui and Bose, 2022, Illingworth et al., 2005]. The temporal dimension in CHT adds complexity to both modelling and analysis, as will be discussed in subsection 2.2.1, yet it is needed for understanding real-world aerospace applications where conditions rarely remain at perfect equilibrium. For example, the coupling of spatiotemporal heat flux fluctuations in fluid-solid systems can often be nonlinear and lead to an effect known as "augmentation" [Zudin, 2012, Mathie et al., 2013, Greiner et al., 2002, Suzuki and Suzuki, 1994], which quantitatively describes how time-averaged heat flux values may differ from those predicted by simplified mean-value calculations Current state-of-the-art methods for unsteady CHT simulations are either too computationally expensive or are based on simplifying assumptions that limit their applicability or accuracy.

To achieve this objective, a computational framework for CHT simulations (section 1.2 and chapter 4) has been developed. This framework has led to two research contributions focused on computational methodologies: a turbulent inflow generator to provide realistic inflow conditions for CHT simulations and a novel multiscale modelling approach for improved efficiency in unsteady CHT analysis.

An additional goal of this thesis is to promote the adoption of conjugate analysis in industry and research. Despite their critical role in accurately assessing thermal performance and achieving design objectives, conjugate simulations remain underutilised. This motivation led to a third research contribution, which explores the application of CHT simulations to studying the effects of heat transfer on the discharge characteristics of transonic flow nozzles.

The thesis is structured as follows:

- Chapter 2 provides the background and motivation for the research, outlining the relevance of unsteady conjugate heat transfer simulations across various engineering disciplines, with a focus on turbomachinery flows.

- Chapter 3 presents the development of an inflow generator for scale-resolving simulations, which will prove essential for the accurate prediction of unsteady CHT in turbulent flows. The chapter, complemented with Appendix A, details the methodology used to generate inflow conditions and the validation of the inflow generator against reference data. This chapter is based on the work published in Dreze et al. [2023].

- Chapter 4 introduces an original multiscale method for unsteady CHT applications. The chapter details the challenges of unsteady CHT modelling and provides insights into their resolution. Followed by the formulation of the multiscale method and its implementation in a CFD solver. The methodology and validation was presented in Dreze et al. [2025]. It is followed by application of unsteady conjugate heat transfer to study its effects on flow characteristics, published in Dreze and di Mare [2025].

- Chapter 5 presents the conclusions of the project, summarising the key findings and contributions of the thesis alongside suggested future works. The chapter also outlines potential future research directions and applications of the developed methods.

1.2 Description of the numerical solver H4X

All numerical simulations in the present thesis were conducted using the in-house CFD code, `H4X`. This work implemented several methodologies within the `H4X` framework, including a turbulent inflow generator, diverse meshing algorithms, conjugate heat transfer capabilities, and a multiscale approach for conjugate heat transfer analysis. All key contributions are discussed throughout the present thesis.

`H4X` is a general-purpose three-dimensional Large Eddy Simulation (LES) solver with a cell-centred, density-based finite-volume arrangement. It has been developed over the past seven years by the Numerical Analysis group at the University of Oxford [Hope-Collins, 2022, Hao et al., 2022, Dreze et al., 2023, Hope-Collins and di Mare, 2023, Herkewitz, 2024]. Details of the baseline numerical schemes used in `H4X` are given in Appendix B.

Scale-resolving unsteady CHT simulations are computationally intensive; to keep simulation runtimes low, massively parallel environments are required. In that regard, `H4X` employs a block-structured topology that enables multiple levels of parallelism.

Node parallelism is exposed by abstractions of the typical functionalities of point-to-point message-passing interfaces. These abstractions support common data management techniques such as interleaving of communication and computation and the use of pre-mapped addresses for message passing. Typical operations such as evaluation of right-hand side vectors for time advancement of the solution take place by starting a round of non-blocking communications, performing operations on the internal cells and then visiting the halos as data become available from the message passing operations. Global operations are then kept to a minimum.

Thread-level parallelism is exposed through the blocks of the multiblock grid, which lend themselves to concurrent processes by teams of threads. Provisions are also available for multithreaded execution of loops operating on halo entities, when these become available. Within each block, operations such as flux and source term evaluation are arranged in such a way to maximise temporal locality of the data. To this effect a core loop is performed that operates on the inner cells by evaluating three fluxes and a volume term for each cell, followed by a suitable number of peel loops to deal with cells near the block boundary.

Instruction-level parallelism is exposed in the loops within each block by two aspects of the code. The first is that functions for operations such as flux evaluation are templated so that vector code can be easily generated. Second, memory mapping classes hide the physical layout of main arrays from the logical access pattern, thereby allowing efficient vectorisation with aligned loads/stores. The memory mapping classes overload common algebraic operators using AVX and AVX2 intrinsics and use similar intrinsics to perform memory loads and stores [Herkewitz, 2024].

`H4X` has been validated on a range of test cases and its scalability has been proven on up to 6000 cores on the ARCHER [Beckett et al., 2024] and ARCUS [Richards, 2015] high performance computing platforms.

Chapter 2 Background and motivation

Contents

This chapter presents a comprehensive review of the available literature on the modelling and applications of conjugate heat transfer. While the methods and approaches developed during the present thesis have broad applicability across various domains involving heat transfer, this review emphasises the specific challenges and developments within the context of turbomachinery.

2.1 Conjugate Heat Transfer

When a solid body is in contact with a moving fluid at a different temperature, heat is exchanged between them through a process known as convective heat transfer. An example is illustrated in Figure 2.1.

Historically, convective heat transfer was characterised in a decoupled manner, using a heat transfer coefficient and treating the solid and fluid domains as separate, uncoupled entities, [He, 2023]. Numerically, this decoupling was largely due to limitations in the available simulation codes, which were not designed for transfer between domains. The solid surfaces were often modelled as non-porous, restricting the simulation domain to the fluid side only. However, unlike the velocity field, for instance, the temperature field being continuous can exhibit large gradients in both the solid and fluid domains, as depicted in Figure 2.1.

Then in the 1960s, Perelman [1961] introduced the term "conjugate" to describe the simultaneous solution of heat conduction equations for both the solid and fluid domains. Since then, conjugate heat transfer methods have been continuously developed and applied to various engineering problems.

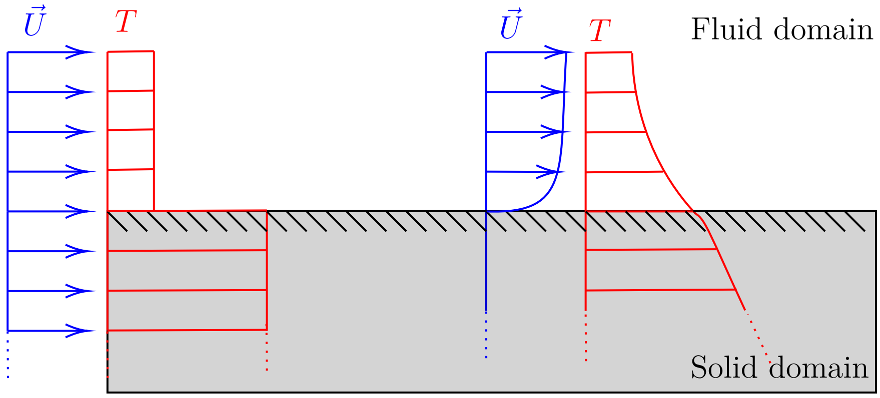

Figure 2.1: Velocity and thermal boundary layers in a conjugate heat transfer problem

Despite these advances, many numerical simulations today still do not fully incorporate CHT, [Dorfman, 2010]. Instead, boundary conditions between solid walls and fluid domains are often simplified using fixed heat flux or temperature values. This is because CHT is not always necessary; simplified models can be sufficiently accurate when temperature gradients are small or when the thermal interaction between the fluid and solid has minimal impact on the overall system performance. However, in the opposite case, such simplifications may lead to inaccurate predictions—misrepresenting thermal loads, temperature distributions, or even the performance and safety of materials.

In CHT analysis, the dimensionless number characterising the heat transfer at the interface is the Biot number (Bi), defined as:

$$\mathrm{Bi} = \frac{hL}{\kappa} \tag{2.1}$$

Where h is the heat transfer coefficient at the interface, κ is the heat conductivity of the solid and L is a characteristic length. This dimensionless parameter quantifies the relative dominance of conductive resistance within the solid versus convective resistance in the fluid. $\mathrm{Bi} \ll 1$ implies that the thermal resistance to heat conduction within the solid is significantly lower than the resistance to heat convection at the surface. This leads negligible temperature gradients within the solid because the high internal thermal conductivity relative to the surface convection ensures that any heat transfer is quickly distributed throughout its volume. Therefore, the solid domain can be treated as isothermal, allowing lumped-capacitance approximations (typically $\mathrm{Bi} < 0.1$), [Lienhard, 1985]. Conversely, $\mathrm{Bi} \gg 1$ indicates significant internal temperature variations. The surface of the solid will tend to rapidly reach the temperature of the surrounding fluid due to the relatively low convective resistance, but the interior of the solid will lag behind, experiencing a slower rate of temperature change due to the high internal conductive resistance. This regime requires detailed spatial resolution of the solid's thermal field, which therefore requires CHT analysis. Finally, $\mathrm{Bi} \approx 1$ signifies a balanced heat transfer regime where both conduction and convection are equally important, also requiring CHT.

In addition to the Biot number, the Fourier number (Fo) characterises the transient response of the solid to fluid temperature fluctuations.

$$\mathrm{Fo} = \frac{\alpha t}{L^2} \tag{2.2}$$

Where α is the thermal diffusivity of the solid domain, t is a time and L is a characteristic length. The Fourier number directly determines the thermal penetration depth (δ_P) in transient conduction problems. The penetration depth is defined as the distance from the coupled interface at which the temperature fluctuations have decayed by a factor $1/e$, [Kaviany, 2011]. For a semi-infinite solid subjected to a step change in surface temperature:

$$\delta_P \propto \sqrt{\alpha t} = L\sqrt{\mathrm{Fo}} \tag{2.3}$$

If $\mathrm{Fo} \ll 1$, the thermal forcing has very limited penetration into the solid, requiring detailed near-surface resolution but the solid may be assumed steady further away. For Fo $\mathcal{O}(1)$, the thermal front penetrates the solid, necessitating full transient analysis. When Fo $\gg$ 1, the solid approaches steady-state conditions, enabling quasi-static approximations, [Kaviany, 2011].

2.2 CHT modelling

The governing equations for a conjugate heat transfer problem are the Navier-Stokes equations for the fluid side (Equations (B.1) to (B.3)) and the heat conduction equation for the solid (Equation (2.4)). For a problem (depicted in Figure 2.2) with two subdomains which will be denoted as Ω_F and Ω_S where Ω_F solves Equations (B.1) to (B.3) and Ω_S solves Equation (2.4). We denote $\delta\Omega$ the outer surface of a specified domain and Γ the interface between the domains Ω_S and Ω_F. The unsteady heat conduction equation is given by:

$$\rho_s c_{p,s} \frac{\partial T_s}{\partial t} = \nabla \cdot (\kappa_s \nabla T_s) + Q_s \quad \text{in } \Omega_S \tag{2.4}$$

Where Q_s is the heat source term.

To solve the CHT problem, the modelling needs to couple Equation 2.4 with the fluid equations using the shared interface $\Gamma = \Omega_S \cap \Omega_F$. Nevertheless, as will be discussed in subsection 2.2.1, achieving this coupling is non-trivial, and various strategies have been developed by researchers to address it, as outlined in Equation 2.2.1.

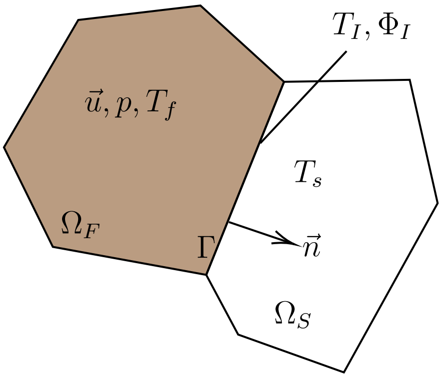

Figure 2.2: Description of the boundaries of the CHT problem.

2.2.1 Challenges in CHT modelling

Coupling domains with distinct governing equations presents significant modelling challenges. These challenges stem from the physical processes present (conduction-dominated in the solid and convection-dominated in most fluids) that operate on different spatial and temporal scales, which complicates achieving accurate and efficient simulations. In addition, the numerical coupling at the fluid–solid interface itself poses challenges—balancing stability and accuracy, choosing between weak (partitioned) and strong (monolithic) strategies, and handling interpolation and time-synchronisation across disparate grids and time steps.

Challenges related to different physical processes

With the exception of a limited number of cases involving purely laminar and steady flows, the majority of engineering flows exhibit unsteady behavior. Unsteady simulations inherently involve a time scale, and a significant disparity exists between the time scales of the slow conduction in the solid and fast convection of the fluid. Section 4.2 develops a dimensional analysis of the time scales in CHT problems. The analysis shows that the time scale ratio τ_S/τ_F between the two domains is given by Equation 2.5 where a is a scaling factor for the boundary layer height with the Reynolds number. For a typical air-steel system, the ratio is about 10,000, similar scaling laws have been found by Hermann [2025], He and Oldfield [2011].

$$\frac{\tau_S}{\tau_F} = \frac{\frac{\kappa_f \rho_f c_{p,f}}{\kappa_s \rho_s c_{p,s}} \mathrm{St}\mathrm{Re}^a}{\left(\frac{\mathrm{Re}^{-1+2a}}{\mathrm{Pr}}\right)} \tag{2.5}$$

The majority of current simulation methods rely on a time-marching approach, which imposes a timestep limitation dictated by the temporal resolution of the scheme. Typically, the fluid flow uses a significantly smaller temporal resolution compared to the solid. Therefore, the small timesteps used combined with a strict grid requirement for the solid side will be resource-intensive when simulating over times of the order of the solid scales.

Several strategies have been employed to address the time-scale mismatch in CHT simulations and improve convergence.

An early strategy was the fully decoupled model, where the solid domain is treated as steady-state during each iterative step of the fluid domain [Li and Kassab, 1994]. This approach, however, is ill-suited for unsteady simulations as it fails to capture critical time-varying characteristics such as first and second moments.

A more flexible alternative is the time desynchronisation, which decouples the time steps of the fluid and solid solvers [Duchaine et al., 2009]. In this method, each unsteady solver operates independently with its own time step, and the two are coupled only after a specified physical time interval. While this significantly accelerates the convergence to a steady state [Miguel-Brebion et al., 2016, Scholl et al., 2016], it is equivalent to lowering the solid's heat capacity and can lead to an overestimation of thermal fluctuations. This concept of leveraging system properties to speed up convergence has been explored further in other acceleration methods [Koren et al., 2017a,b].

Another class of methods, waveform iterations, reconciles the different time scales by solving the subproblems separately on a specified time window [Meisrimel and Birken, 2022, Kotarsky and Birken, 2025]. The subsystems are solved independently, and the results are used to update the boundary conditions. This process is repeated iteratively until convergence is achieved for the time window.

Other researchers looked directly into the time integration schemes, Kazemi-Kamyab et al. [2014a] examined high-order implicit time integration techniques, such as explicit first-stage singly diagonally implicit Runge-Kutta (ESDIRK) methods, to improve the efficiency of unsteady CHT simulations. Implicit methods mitigate time-step restrictions caused by system stiffness, which may result from the governing equations or grid properties. Their study introduced a strongly coupled algorithm, with stability analysis aligning well with numerical results. Similarly, Ortega et al. [2021] investigated first- to third-order BDF schemes for thermally coupled incompressible flows, finding that higher-order schemes, especially third-order, enable larger time steps and capture a broader range of frequencies. This significantly reduces CPU time while preserving solution accuracy, highlighting the critical role of time integration scheme order in achieving accurate dynamic solutions.

A fundamentally different approach is to solve both the fluid and solid domains in the frequency domain. Frequency-based solvers generally require fewer computational resources than traditional time-marching methods, particularly for periodic unsteady turbomachinery flows, as only a single blade passage is needed [Wang and di Mare, 2019]. Adapting existing Fourier-based codes for conjugate heat transfer problems requires two key modifications: a solution for the temperature field within the solid and harmonic fluctuations, along with an interface condition at the boundary between the solid and fluid Mehdizadeh et al. [2017]. He and Oldfield [2011] implemented a hybrid coupling approach. Their model is based on a time-marching technique for the fluid domain and a frequency-based for the solid domain, with a continuously updating Fourier transform implemented at the interface. Similarly, Knapke and David [2015] using a harmonic balance approach to conjugate heat transfer with a quasi-Newton solver. It showed that harmonic balance is an effective technique for performing accurate conjugate heat transfer problems with periodic unsteady simulations. This was confirmed by Hodges [2018], who presented a similar method and validated it for an internally cooled turbine blade.

In addition to the time scale mismatch, the solid and fluid domains also exhibit different spatial scales. As will be shown in section 4.2, the thermal boundary layer thicknesses in these domains are related by the ratio of thermal conductivities, as expressed in Equation 2.6. For an air-steel system, this ratio is approximately 100, emphasising the significant differences in boundary layer heights between the two domains.

$$\frac{\delta_S}{\delta_F} = \mathcal{O}\left(\frac{\kappa_s}{\kappa_f}\right) \tag{2.6}$$

Coupling strategies

Coupling strategies are employed to manage the interaction between fluid and solid domains in CHT simulations, determining how heat transfer information is exchanged at their interface. In the literature, these strategies are broadly divided into two categories: weak and strong (or fully coupled) coupling approaches.

- **Weakly coupled:** The fluid and solid domains are solved separately and at the conjugate interface continuity of temperature and heat flux is imposed, Equation 2.7.
$$\begin{cases} T_f = T_s & \text{on } \Gamma \\ \kappa_f \nabla T_f \cdot \vec{n} = \kappa_s \nabla T_s \cdot \vec{n} & \text{on } \Gamma \end{cases} \tag{2.7}$$
The fluid and solid solvers are called sequentially, and the boundary conditions of each solver are updated explicitely between the coupling timesteps. This communicating interface is the key consideration of the implementation of a weakly coupled CHT algorithm, it controls the coupling sequence, the coupling timestep and needs to ensure precise matching of boundary points at the solid-fluid interface, [Errera, 2025]. The advantage is the ability to use existing specialised algorithms that have been validated for the individual domains. The main drawback is the added coupling algorithm which can potentially create stability and accuracy problems depending on the interpolation and communication procedures. In general, loosely coupled methods are suitable when the temperature gradients between fluid and solid are not extreme or when the steady-state heat transfer dominates the system [John et al., 2018, Verstraete and Scholl, 2016]. Weakly coupled approaches are widely used in practice due to their flexibility, allowing modifications to the interface conditions to address challenges like the time scale mismatch, [Duchaine et al., 2009, Scholl et al., 2016].

- **Strongly coupled:** The fluid and solid domains are combined, and the solver integrates the entire set of governing equations as a single system, meaning the fluid and solid domains are not physically distinguished but are mathematically solved together instead. This is facilitated in practice by the fact that the unsteady heat conduction equation has fundamentally the same structure as the flow equations. The fully coupled approach maintains high accuracy and stability but has a limited application range since it requires the same unified numerical approach to solve both fluid and solid domains [John et al., 2018, Rahman et al., 2005, Kotarsky and Birken, 2025].

It can be shown that, from a purely mathematical point of view, the two coupling strategy are equivalent [Quarteroni and Valli, 1999].

In general, weakly coupled methods can be categorised based on the iteration scheme between the flow and heat conduction solver.

A commonly used iteration scheme is the Neumann-Dirichlet boundary coupling, which results in algebraic coupling equations [Giles, 1997]. In this approach, the boundary conditions are staggered and exchanged post-convergence, the fluid solver applies a Dirichlet boundary condition at the interface, while the solid solver employs a Neumann condition. Such approach has been applied successfully in multiple CHT studies [Keyes and et. al., 2013, Miller et al., 2017]. Verdicchio et al. [2001] introduced the Flux Forward Temperature Back scheme, which is a modified version of the method developed by Giles [1997] where the process is now staggered, the interface temperature field is imposed to the fluid solver and the updated heat flux distribution is used as a Neumann boundary condition for the solid. Heidmann et al. [2003] proposed the Temperature Forward Flux Back approach which is similar to the Flux Forward Temperature Back but the where the flow solver is submitted to a Neumann boundary condition and the solid solver is closed with a Dirichlet boundary. Other methods are described in Montenay et al. [2000], Verstraete and Braembussche [2009]

On the other hand, strongly coupled methods are essential for scenarios involving significant transient heat transfer effects or substantial temperature gradients between the fluid and solid, requiring precise boundary interactions for accurate thermal modelling, [Kazemi-Kamyab et al., 2014a].

Using fully coupled methods for high fidelity CHT simulations, Oh et al. [2021] focused on a ribbed cooling passage using LES with the immersed boundary method. They showed that the time scale disparity between turbulent fluid flow and heat conduction in the solid can be overcome by using an artificially high solid thermal diffusivity, similarly to Duchaine et al. [2009], Koren et al. [2017a]. Their predictions are compared with experiments and other LES studies, showing good agreement on the top and back faces of the rib, but differences are present on the front face due to the need for higher grid resolution in that region. At even higher fidelity, Kuwata et al. [2020] highlighted the effects of a permeable porous wall on momentum and heat transfer by conducting conjugate DNS of airflow through a rectangular duct partially filled with a porous material. The findings reveal that the porous wall enhances turbulence and secondary flow, significantly boosting momentum and heat transfer. Notably, the dispersion and turbulent heat fluxes play crucial roles in heat transfer within the porous medium.

Stability and accuracy of the coupling

The stability and accuracy of the coupling are critical aspects of CHT simulations, particularly in the context of unsteady flows. Giles [1997] described, in a key paper for coupled systems, how the choice of coupling strategy, time-stepping method, and grid resolution can significantly impact the convergence and accuracy of the solution.

Following Giles [1997], Verstraete and Scholl [2016], Joshi and Leyland [2014], a simple analysis on a coupled domain can be done to assess the stability of the coupling and the influence of the different parameters.

Considering a 1D problem composed of two semi-infinite domains Ω_S and Ω_F. The interface is located at $x = 0$ and $\Omega_S \in]-\infty, 0]$ while $\Omega_F \in [0, +\infty[$. Both farfield boundary conditions are of Dirichlet type and are constant in time:

$$T(x \to -\infty, t) = T_{s,\infty} \quad \& \quad T(x \to +\infty, t) = T_{f,\infty} \tag{2.8}$$

Considering a uniformly spaced grid in both domains with grid size $\Delta_{x,s}$ and $\Delta_{x,f}$ with cell-centered discretisation, as shown in Figure 2.3. Both domains are described by the same equation, Equation 2.4, but with different material properties. The

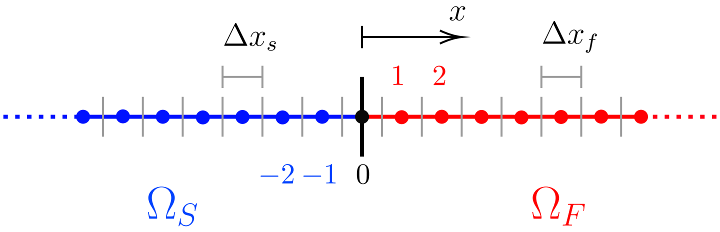

Figure 2.3: Schematic of the 1D CHT problem with both domains using a cell-centred discretisation

chosen scheme is a finite volume formulation that uses explicit schemes in time and space. The fluxes at the interface between two adjacent cells are computed using a centered difference scheme.The discretised equation for the interior nodes of the coupled system are:

$$\frac{T_i^{n+1} - T_i^n}{\Delta t} = \frac{\kappa_f}{c_f \Delta x_f^2} \left(T_{i+1}^n - 2T_i^n + T_{i-1}^n \right) \quad \text{for } i > 0 \tag{2.9}$$

$$\frac{T_i^{n+1} - T_i^n}{\Delta t} = \frac{\kappa_s}{c_s \Delta x^2} \left(T_{i+1}^n - 2T_i^n + T_{i-1}^n \right) \quad \text{for } i < 0 \tag{2.10}$$

Where T_i^n is the temperature at the node i at time step n, Δt is the time step, κ is the thermal diffusivity. The interface condition (at spatial index 0) in Equation 2.7 can be written as:

$$\frac{1}{2} \left(c_s \Delta x_s \right) \frac{T_0^{n+1} - T_0^n}{\Delta t} = q_w + \frac{\kappa_s}{\Delta x_s} \left(T_{-1}^n - T_0^n \right) \quad \text{For } \Omega_S \tag{2.11}$$

$$T_0 = T_w \quad \text{For } \Omega_F \tag{2.12}$$

Where T_w is the temperature at the wall, q_w is the heat flux from the fluid to the solid, given as boundary condition. This configuration was studied by Giles [1997] and they showed that the stability of this weakly coupled scheme is a function of the heat capacity ratio and the numerical Fourier number d of each domain. While on the other hand the fully coupled method with the same discretisation is stable as long as the the requirement for the numerical stability of the individual schemes are satisfied.

$$\frac{c_f \Delta x_f}{c_x \Delta x_s} < \frac{\sqrt{1 - 2d_s}}{1 - \sqrt{1 - 2d_f}} \qquad \text{with } d = \frac{\kappa \Delta t}{c \Delta x^2} \tag{2.13}$$

This highlights the importance of the coupling strategy and the numerical methods used in CHT simulations, as they can significantly impact the stability and accuracy of the solution.

Another aspect to consider is the discretisation methods used. For example, a node-based finite element formulation on Ω_S can be chosen as Errera and Chemin [2013], Joshi and Leyland [2014] have done, shown in Figure 2.4. Considering a lumped mass approach for the solid domain in order to keep the time integration

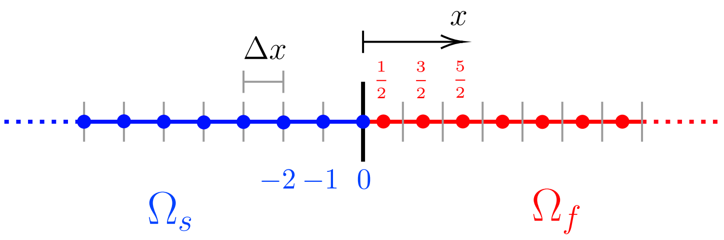

Figure 2.4: Schematic of the 1D CHT problem with a node based discretisation on Ω_s

explicit. The discretised equation for the interior nodes of the coupled system are:

$$\frac{T_i^{n+1} - T_i^n}{\Delta t} = \frac{\kappa_f}{c_f \Delta x_f^2}\left(T_{i+1}^n - 2T_i^n + T_{i-1}^n\right) \quad \text{for } i > 1/2 \tag{2.14}$$

$$\frac{T_{1/2}^{n+1} - T_{1/2}^n}{\Delta t} = \frac{\kappa_f}{c_f \Delta x^2}\left(T_{3/2}^n - 3T_{1/2}^n - 2T_0^n\right) \tag{2.15}$$

$$\frac{T_i^{n+1} - T_i^n}{\Delta t} = \frac{\kappa_s}{\rho_s c_s \Delta x^2}\left(T_{i+1}^n - 2T_i^n + T_{i-1}^n\right) \quad \text{for } i < 0 \tag{2.16}$$

The interface condition Equation 2.7 can be written as:

$$c_s \Delta x_s \frac{T_0^{n+1} - T_0^n}{\Delta t} = \frac{\kappa}{\Delta x_s}\left(T_{-1}^n - T_0^n\right) + q_w \quad \text{For } \Omega_s \tag{2.17}$$

$$T_0 = T_w \quad \text{For } \Omega_f \tag{2.18}$$

The stability analysis of the FEM-FVM combination has been studied by Joshi and Leyland [2014]. The condition for stability is given by Equation 2.19

$$\frac{c_f \Delta x_f}{c_x \Delta x_s} < \frac{\sqrt{1 + 2d_s}}{2 - 2\sqrt{1 - 2d_f}} \qquad \text{with } d = \frac{\kappa \Delta t}{c \Delta x^2} \tag{2.19}$$

Figure 2.5 shows the contour of the upper limit of the stability condition for the heat capacity ratios. With the FVM only, the stability condition is given by Equation 2.13 and the FEM-FVM combination is given by Equation 2.19. Highlighting how the stability conditions can be significantly different depending on the discretisation method used.

2.3 Applications of CHT

Since the works of Perelman [1961], conjugate heat transfer has emerged as a critical field of analysis in modern engineering, particularly as many systems increasingly

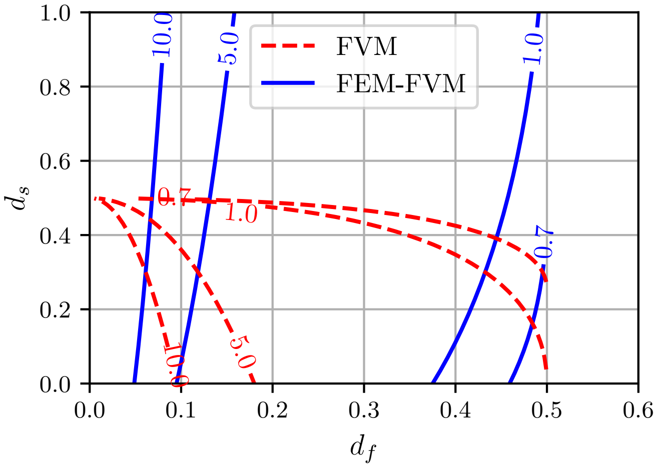

Figure 2.5: Contour of the upper limit of the stability condition for the heat capacity ratios.

operate at the thermal thresholds of their constituent materials. Nowadays, gas turbine engines, hypersonic vehicles, and advanced combustion systems all face significant thermal challenges that directly impact their reliability, efficiency, and service life. As manufacturers push designs to extract maximum performance, the simultaneous consideration of conduction, convection, and, in some cases, radiation has become essential for maintaining operational integrity and efficiency in high-performance applications.

2.3.1 CHT in turbomachinery

Turbomachines generate up to 80% of all the electricity in the world and power all large commercial aircraft. Increasing their efficiency to reduce emissions and costs is a key factor in overcoming the environmental challenges the world is currently facing.

Most turbomachines operate on an open Brayton cycle, extracting energy from the flowing air and fuel to generate usable work. The ideal thermal efficiency of the Brayton cycle η is given by:

$$\eta = 1 - \frac{T_{\text{exhaust}}}{\text{TET}} \quad \text{[Langston, 2004]} \tag{2.20}$$

Where T_{exhaust} is the exhaust temperature and TET is the turbine entry temperature. Consequently, increasing the TET constitutes an effective approach to improving thermodynamic performance. At the time of writing, TET values well above the melting temperature of the alloys used for the turbine components are commonplace [Nourin and Amano, 2021], necessitating the implementation of advanced cooling systems to maintain blade metal temperatures within acceptable operational range.

From a material science perspective for example, maximum allowable temperatures are increased through the development of advanced alloys, while thermal loads from the flow are lowered using thermal barrier coatings applied to blade surfaces. From a fluid mechanics standpoint, cooling flow bled from the upstream compressor is used to cool the blade metal. Turbine thermal design has evolved substantially over recent decades, progressing from rudimentary cooling and thermal management systems to complex integrated solutions incorporating convection, impingement, and film cooling techniques. These technological advancements have enabled a doubling of TET values over the past sixty years.

Blade cooling technology

The high-pressure turbine is the turbomachinery component subject to the most challenging operating conditions. The combustor exit flow, at the highest temperature of the cycle, combined with the cooling flow, result in significant heat transfer with the blade metal.

At present, turbine blade cooling systems are mainly divided into two main categories: internal and external cooling systems. Internal cooling systems extract heat from within the blade structure through various heat transfer enhancement techniques. These include convection cooling, which involves passing cooling air through multiple channels inside the blade [Holland and Thake, 1980, Thakur et al., 1999]. Advanced configurations such as pin fins are used to further enhance heat transfer, through a greater surface area and increased turbulence [Horbach et al., 2011, Liang et al., 2021]. Additionally, impingement cooling is used in regions subjected to the highest thermal loads. This technique functions by directing high-velocity air jets to strike the inner surface of the blade directly. The impinging jets significantly increase local heat transfer coefficients compared to conventional convection cooling, making this approach particularly valuable for critical areas like the leading edge, where temperature and heat flux reach maximum values.

External cooling methods complement internal approaches by forming protective thermal barriers on the outer surface of the blade, directly shielding it from hot gas exposure. Film cooling stands as the predominant external cooling strategy in contemporary turbine designs, offering the best compromise between cooling effectiveness and operational efficiency penalties, Gao et al. [2008]. Transpiration cooling represents an advanced variation of this approach, wherein the blade surface incorporates porous materials that allow cooling air to permeate uniformly through countless microscopic passages, creating a more continuous and effective thermal barrier than discrete film cooling holes while potentially reducing the overall cooling flow requirement, Wang et al. [2004].

While these advanced cooling technologies enable operation at higher temperatures and thus greater thermodynamic efficiency, they come with a number of drawbacks. Firstly, the cooling air is bled from the compressor resulting in a loss of thermodynamic cycle performance. Valuable high-pressure flow is diverted for cooling purposes instead of being expanded to generate power. Furthermore, cooled blades make the aerodynamic design more complex and less efficient. For example, film cooling holes interact with the main flow causing additional losses. Another example is trailing edge cooling that requires wider sections which increases mixing, [Yang and Hu, 2012]. Cooling design is therefore the result of a trade-off between increased turbine inlet temperature and lower aerodynamic performance. Lastly, the cost of machining, casting and testing a cooled blade is greater than an uncooled design because of the structural complexity of the design.

In these conditions, it is crucial to have detailed data about heat transfer and temperature distributions of the components. The harsh operating environments limit experimental testing to research or high technology readiness level industrial cases which makes CHT simulations a valuable approach for these situations. In fact, numerical methods are widely used to model conjugate heat transfer and have proven to be a powerful and cost-effective tool for the design of cooling systems.

Turbine blade research into CHT started with studies by Hylton et al. [1983], Turner et al. [1985]. They used 2D test cases of turbine blades to compare and taylor analytical and numerical models to match experimental data, including internal temperature distribution. The ability to perform conjugate analysis shed light on the shortcomings in predicting the flow over the blade and temperature distribution without considering CHT. Bohn et al. [1997] presented a 3D conjugate simulation to assess the influence of leading edge cooling gas ejection on the temperature distribution in the vane material. Their objective was to optimise the location of cooling holes to use the lowest possible cooling mass flow. It was shown that stagnation line position significantly influences the distribution of cooling fluid along the vane surface and therefore the thermal load of the vane. Moreover, Heidmann et al. [2003] found that in a realistic film-cooled turbine vane, conjugate heat transfer cases generally have a lower outer wall temperature than the adiabatic wall convection solutions. However, due to thermal conduction from the outer wall to the plenum, secondary effects were observed, such as zones with higher local temperatures caused by a change in the direction of the heat flux at the wall on the outer surface.

The previously mentionned studies have primarily focused on steady-state methods. However, Fransen et al. [2012] and Schmidt and Starke [2015] highlight the importance of coupled simulations that account for the time-dependent nature of the flow field. A typical conjugate heat transfer problem that cannot be fully understood without considering the unsteady effects is the prediction of metal temperatures at the leading edge of turbine blades. The unsteadiness may arise from the spatially and temporally non-uniform combustor exit flow, external cooling jets, or wakes from upstream NGVs. Schmidt and Starke [2015] reported differences in thermal loads when time-dependent flow physics were included, with Nusselt numbers increasing by about 30% and local temperature variations of 30 to 40 K. Similarly, Hwang et al. [2016] observed that the surface temperature of the blade was strongly influenced by unsteadiness, with the stagnation point at the leading edge shifting over time, highlighting the need for cooling designs that can accommodate these dynamic effects.

From a modelling perspective, Fransen et al. [2012] demonstrated that various RANS models fail to accurately predict flow within internal cooling passages, which substantially impacts the thermal distribution in the solid. As a result, there has been a shift toward higher-fidelity methods, with LES currently being the most widely used approach in research for conjugate heat transfer problems. For instance, Duchaine et al. [2013] investigated a low-pressure water-cooled turbine vane with a coupled LES solver, successfully capturing key heat transfer mechanisms such as the separation bubble on the suction side and the separated region on the pressure side. These coupled simulations outperformed isothermal cases, particularly in challenging areas like the trailing edge, where Newton's law of cooling does not hold. Likewise, Shum-Kivan et al. [2014] used conjugate LES to study a round impinging jet at a moderate Reynolds number. The LES approach effectively identified key flow features driving heat transfer but also underscored the stringent mesh requirements (e.g., $y^+ \approx 1$) necessary for accurate predictions, as sub-grid modeling tended to overestimate shear layer fluctuations.

Combustor

Combustor flows are another example of a complex thermal environment within turbomachinery where CHT analysis is essential. In combustors, heat transfer management governs critical phenomena such as flame-wall interactions, coolant film effectiveness, and thermal stress distribution, which ultimately determine the lifespan of the combustor [Janicka et al., 2012]. The cooling air strategy, including the number and location of film cooling slots, size of effusion patches, and use of cooling tiles, is largely dictated by the need to achieve desired maximum metal surface temperatures with minimal cooling air [Luff and McGuirk, 2001]. Key developments in modern combustor design include high-fidelity turbulence-resolving simulations and multi-physics coupling strategies. Studies demonstrate that CHT analysis substantially improves temperature prediction accuracy on combustor liner walls, coolant flow effectiveness, and combustion efficiency. In comparative studies between CHT and adiabatic wall models, CHT simulations have demonstrated much better agreement with experimental measurements, [Cui and Bose, 2022, Zong et al., 2022]. However, challenges persist in managing computational costs for large-scale geometries and reconciling multiscale phenomena across fluid and solid domains.

One of the early CHT analysis of combustors was performed by Duchaine et al. [2008], they studied a wall flame interaction by coupling explicitely a reactive LES code and a solid conduction code. It was demonstrated that accurate heat transfer predictions require synchronisation at the smallest time scales present in the coupled problem. Later, Kim et al. [2010] analysed temperature distributions within a gas turbine combustion liner to identify potential weak points in hot components. Their findings concluded that LES results which incorporated thermal radiation and conjugate heat transfer demonstrated better alignment with experimental data compared to LES results that excluded these effects. Combustor simulations bring an additional difficulty in that thermochemistry effects could be significant however only few studies are available Ferguson et al. [2021], Gonçalves dos Santos et al. [2008], Abbassi et al. [2021] because it considerably increases the model complexity and the simulation cost.

2.3.2 CHT in high-speed flows

Hypersonic vehicle design faces significant challenges due to operating in extreme thermal environments. In addition to substantial energy fluxes from convective and radiative heating, high temperatures critically influence pressure distributions and skin friction forces on the aircraft surface [Bertin and Cummings, 2006]. With respect to turbomachinery, aerodynamic heating is an additional effect that must be taken into account Murty et al. [2013]. During ascent and reentry phases, the high-velocity vehicle converts kinetic energy from stationary air into thermal energy, a phenomenon scaling quadratically with the Mach number. To mitigate excessive heat transfer to the vehicle, advanced thermal protection systems (TPS) are employed to maintain structural temperatures within operational limits [Johnson and

Rubesin, 1949]. However, for hypersonics, a purely fluid-thermal coupled analysis is insufficient for addressing these challenges. Thermal loads also induce structural deformations, necessitating a fully coupled fluid-thermal-structural approach for accurate design predictions.

Conjugate heat transfer analysis has been widely adopted in supersonic and hypersonic applications, particularly for TPS design. Given the prohibitive costs of space missions, exhaustive physical testing is impractical, underscoring the importance of integrated CHT and thermal-structural simulations for reducing design iterations.

Dechaumphai et al. [1989] conducted pioneering work in fluid-thermal-structural analysis for hypersonic flows, focusing on heated leading edges and active cooling strategies. Later, Rafla [2019] developed a transient heat transfer model integrating classical fluid dynamics, aeroheating correlations, and a 2-D structural heat transfer framework. Their approach accounts for convective, radiative, and conductive heat transfer mechanisms, validated against Space Shuttle STS-3 flight data. Recent advancements include Le et al. [2021], who utilized CHT to optimise sandwich-structured TPS for hypersonic vehicles.

Emerging areas of CHT research include transpiration cooling techniques Bandivadekar and Minisci [2020], Brody et al. [2024] and thermochemical effects Clarke et al. [2022], both critical for managing extreme thermal loads in hypersonic systems.

2.3.3 Other applications of CHT

As highlighted in the introductory paragraph of the literature review, CHT analysis finds broad applicability across diverse fields. The following non-exhaustive examples underscore its versatility.

In the context of electric mobility, the rapid growth of electric vehicles, driven by the increasing demand for sustainable transportation and lower running costs, necessitates effective thermal management. In these systems, electric motors operate at high power densities and therefore generate considerable heat. Insufficient cooling may lead to the demagnetization of permanent magnets and the breakdown of winding insulation, [Tosetti et al., 2014, Boscaglia et al., 2019].

Within the battery industry, CHT simulations are routinely employed to predict temperature distributions within battery cells and modules. High operating temperatures can compromise battery efficiency and lifespan. Consequently, optimising the cooling system is critical to ensuring that the battery functions within a safe thermal range. For example, Chalise et al. [2018] demonstrated that enhancing the thermal conductivity of individual Li-ion cells can significantly reduce the required coolant flow rate, thereby improving both safety and performance.

In nuclear reactor technology, robust cooling mechanisms are essential to prevent overheating of the reactor core, ensuring safe operation, and avoiding potential catastrophic failures [Ho et al., 2019]. The nuclear fission process generates immense heat, and inadequate cooling may result in dangerously high temperatures that could lead to a core meltdown and the subsequent release of radioactive materials. Thus, the implementation of effective cooling systems—employing water or gas coolants—is essential, as extensively documented in the literature Piro and Leitch [2014], Uribe et al. [2013], Lu et al. [2021].

In Biomedicine, Abdoli et al. [2014] used CHT to demonstrate a feasibility of a heart perfusion concept to extend the viability of the transplant heart. The study showed that the heart could be cooled faster if a cooled solution is pumped through, which could extend the viability of the heart transplant.

Chapter 3 Divergence-free turbulent inflow data from realistic covariance tensor

Contents

The growing availability of computational resources has made flow simulations increasingly accessible. However, ensuring that these simulations accurately reflect real-world conditions remains a challenge, especially when it comes to modelling turbulent flows. Within this challenge, generating realistic turbulent inflow conditions is particularly critical.

Turbulent inflow generation refers to methodologies for prescribing fluctuations in flow variables at the boundaries of the computational domain for scale-resolving simulations. These fluctuations must adhere to targeted statistical properties, including Reynolds stress distributions and energy spectra, while maintaining appropriate spatial correlations. Furthermore, inflow generation methodologies should preserve physical consistency with fundamental governing equations, particularly the conservation of mass principle.

In practical engineering scenarios such as flow around aerodynamic surfaces, within combustion chambers, or through turbomachinery passages, the incoming flow frequently exhibits fully-developed turbulence.The absence of appropriately represented time-dependent fluctuation at domain inlets can result in substantial inaccuracies in the prediction of key flow parameters, including wall shear stress distributions and heat transfer rates.

3.1 Preface : Turbulent inflow generation

Turbulent inflow generation is necessary across a spectrum of applications, from renewable energy systems to urban air quality assessments, where upstream turbulence directly governs downstream flow physics, structural loading, and operational performance. The fidelity of inflow turbulence generation methodologies determines the reliability of simulations in replicating real-world flow complexities.

3.1.1 Turbulent inflow requirements across diverse CFD applications

A classical example of the importance of inflow conditions is the simulation of a backward-facing step. Research by Le et al. [1997] and Kanchi et al. [2013] revealed that simulations without appropriate inflow conditions significantly overpredict flow reattachment length by approximately 20%. While implementing turbulent inflow generation techniques reduced this discrepancy to within 4% of experimental measurements. The error made without turbulent inflow generation can be attributed to boundary layer dynamics. When flow enters the computational domain with artificially low turbulence intensity, the absence of turbulent structures impairs mixing between the high-momentum freestream and the low-momentum recirculation region within the shear layer separating from the step edge. The resulting reduction in momentum transfer across the shear layer delays the flow reattachment point, at which sufficient momentum reaches the near-wall region to overcome the adverse pressure gradient. Their research further established that inflow conditions influence power spectra in downstream turbulent regions over considerable distances, underscoring the far-reaching impact of initial flow conditions on simulation accuracy.

The spatially-developing boundary layer represents another fundamental case demonstrating the necessity of turbulent inflow conditions. Research by Lund et al. [1998], Xu and Martin [2004], Jewkes et al. [2011], Yousif et al. [2023] has established that proper turbulent inflow specification prevents non-physical development lengths and wasteful readjustment behaviour of the flow. When inflow conditions lack adequate turbulence characteristics, the flow may initially exhibit laminar properties before transitioning to turbulence further downstream. This creates a significant discrepancy between simulation results and physical reality, particularly in scenarios where fully developed turbulence should be present from the beginning of the domain.

The importance of turbulent inflow generation extends beyond fundamental turbulence cases to practical engineering applications. In wind energy systems, atmospheric boundary layer flows contain multiscale turbulence with spatially correlated velocity fluctuations that directly impact rotor dynamics and wake interactions which are essential for predicting blade fatigue loads, power output variability within wind farms. Contemporary scale-resolving studies of wind energy aerodynamics consistently incorporate turbulent inflow methodologies, for example Munters et al. [2016], Wu et al. [2020], Mansouri et al. [2022]. In other domains, Xue et al. [2024] investigated how turbulent inflow affects aerodynamic load characteristics of trains and their surrounding flow fields, identifying variations of 5-10% in side force coefficients between uniform and turbulent inlet conditions. Additional examples can be found in different fields such as wind effects on buildings [Zhang et al., 2022], film cooling effectiveness [Ellis and Xia, 2022] or heat transfer characteristics [Kanani et al., 2021, Bacci et al., 2021].

Turbulence plays also a significant role in influencing heat transfer characteristics. The impact of freestream turbulence on heat transfer rates has been widely investigated. For instance, Kestin [1966], Hancock and Bradshaw [1983] developed correlations that relate heat transfer enhancement to both freestream turbulence intensity and Reynolds number. In the context of immersed bodies, early experimental work by Comings et al. [1948] demonstrated how turbulence intensity affects the average Nusselt number around a cylinder in crossflow. Their results showed a 25%

increase in the average Nusselt number at a Reynolds number of 5800 when the turbulence intensity was raised from 1% to 7%. Subsequent studies have consistently reported enhanced heat transfer rates with increasing turbulence levels in cylinder flows [Giedt, 1951, Griffiths and Awbery, 1933, Lowery and Vachon, 1975]. Similarly, the influence of inflow turbulence on heat transfer in stagnation point flows has been the focus of extensive research. Several studies Van Fossen et al. [1995], Sutera [1965], Hoogendoorn [1977], Bae et al. [2000] have identified the turbulence intensity and turbulence length scale as key parameters in accurately correlating stagnation point heat transfer.

3.1.2 Existing inflow generation methods

The inflow realisations must be unsteady, but it is not sufficient to simply superimpose uncorrelated and spectrally uniform randomness on top of a mean flow field. Because turbulence is inherently characterised by a broad spectrum of scales, ranging from large, energy-containing eddies to smaller dissipative scales, fluctuations generated as such will get damped out, not developing into turbulence and leading to inaccurate results. Therefore, several methods have been developed by researchers to generate realistic turbulent inflow conditions.

Two primary categories of inflow generation methods exist: deterministic techniques and synthetic techniques. Each category has its strengths and limitations, reflecting trade-offs between computational cost, physical accuracy, and adaptability to different flow configurations.

- Synthetic Turbulence Generation: Synthetic methodologies employ mathematical frameworks to produce artificial representations of turbulent flow characteristics without resolving the complete underlying physics. These approaches are widely used in both industry and research for their computational efficiency and implementation flexibility. An essential design consideration for these generators is their ability to function with readily available or computationally inexpensive turbulence statistics.

In practical applications, the synthetic turbulence boundary plane is positioned a short distance upstream of the primary simulation domain.While these methods should aim to achieve immediate agreement with first-order statistics at the boundary, the accurate reproduction of covariance properties typically requires a development region. Within this region, the synthetic structures evolve into physically realistic turbulence that satisfies the governing Navier-Stokes equations. The required development length serves as a meaningful performance metric for evaluating both the effectiveness of the methodology and the validity of its underlying assumptions. Among the most prevalent approaches in contemporary computational fluid dynamics are digital filtering techniques, the synthetic eddy method, and spectral-based approaches. See Fukami et al. [2019], Di Mare et al. [2006], Kempf et al. [2005], Yousif et al. [2022] for references.

- Deterministic techniques: These represent physically consistent methodologies that solve some form of flow equations on a secondary domain, ensuring high fidelity in terms of statistical properties and spatial correlations rather than approximating its statistical properties. The resulting data are then mapped onto the inflow plane of the main simulation.

  One of most intuitive approach are turbulence inducing techniques which simulate the turbulent transition upstream of the domain of interest, see for example Rai and Moin [1993].

  One alternative approach is a precursor simulation, wherein a separate, auxiliary simulation generates fully developed turbulent flow that subsequently serves as inlet conditions for the primary domain of interest, Lund et al. [1998], Mukha and Liefvendahl [2017]. The implementation typically involves a simplified geometry, often a periodic channel or box, allowing turbulence to develop naturally under appropriate boundary conditions. This auxiliary simulation continues until statistical stationarity is achieved, ensuring the turbulence characteristics have stabilised. Time-dependent flow field data is then extracted from a cross-sectional plane and applied as the inlet boundary condition for the main simulation, providing physically accurate turbulent structures that inherently satisfy the Navier-Stokes equations.

Another category is recycling methods which operate on the principle of extracting flow data from a downstream location within the simulation domain and reintroducing it at the inlet, creating a semi-autonomous system that maintains realistic turbulence characteristics without requiring separate precursor simulations [Morgan et al., 2011, Liu and Pletcher, 2006]. The implementation process involves establishing a recycling plane at a sufficient distance downstream from the inlet, where the flow has developed the desired turbulent properties. The velocity field data from this plane undergoes appropriate scaling to account for boundary layer growth and is then applied as the inlet boundary condition. This creates a feedback loop that sustains physically consistent turbulence throughout the simulation duration. A primary advantage of recycling methods is their ability to maintain spatial and temporal coherence of turbulent structures while significantly reducing computational requirements compared to traditional precursor simulations.

Deterministic techniques are relatively straightforward to implement and the generated fields at the inflow are realistic but rely on an extended numerical domain of some sort and consequently bring a considerable additional computational and memory cost. However, they perform better in terms of accuracy: the turbulent structures introduced at the inlet require minimal or no development length, eliminating artificial transition regions. Additionally, these methods naturally preserve higher-order statistics, coherent structures, and anisotropic characteristics that synthetic methods often struggle to replicate. See Lund et al. [1998], Rai and Moin [1993], Urbin and Knight [2001], Stevens et al. [2014] for references.

For a more comprehensive analysis of the inflow turbulence generation methods refer to Dhamankar et al. [2018] or Wu [2017].

3.2 Divergence-free turbulent inflow data from realistic covariance tensor

The present section contains a copy of the research paper "Divergence-free turbulent inflow data from realistic covariance tensor," published in the February 2023 issue of *Physics of Fluids*, available at `https://doi.org/10.1063/5.0136568`.

This paper introduces a methodology for generating divergence-free turbulent inflow data. The approach is categorised among synthetic inflow generators and employs the digital filter technique, which is comprehensively explained in Appendix A. Building upon previous work by Hao et al. [2022], the present work extends existing frameworks by constructing a full correlation tensor instead of using only the diagonal components, ensuring that the filters satisfy the divergence-free condition and removing the need for an approximate exponential expression of the filter by considering the spectrum of the fluctuations. By incorporating the off-diagonal Reynolds stress components and strictly enforcing the divergence-free condition, this methodology generates a more physically realistic anisotropic turbulence structure. This directly improves simulation accuracy by eliminating non-physical fluctuations. Consequently, the required flow development region is shortened by approximately 30 % compared to Hao et al. [2022] while keeping the same computational overhead to generate the fluctuations, leading to a substantial reduction in computational cost and faster convergence to statistically steady results.

RESEARCH ARTICLE | FEBRUARY 09 2023

Divergence-free turbulent inflow data from realistic covariance tensor

Yann Dreze ; Muting Hao (郝苜婷) ; Luca di Mare

Physics of Fluids 35, 025120 (2023)
https://doi.org/10.1063/5.0136568

Physics of Fluids ARTICLE scitation.org/journal/phf

Divergence-free turbulent inflow data from realistic covariance tensor

Cite as: Phys. Fluids **35**, 025120 (2023); doi: 10.1063/5.0136568
Submitted: 27 November 2022 · Accepted: 24 January 2023 ·
Published Online: 9 February 2023

Yann Dreze,[a)] Muting Hao (郝苜婷), and Luca di Mare

AFFILIATIONS

Department of Engineering Science, Oxford Thermofluids Institute, University of Oxford, Oxford OX2 0ES, United Kingdom

[a)]Author to whom correspondence should be addressed: yann.dreze@wadham.ox.ac.uk

ABSTRACT

Scale-resolving computational fluid dynamics (CFD) methods require carefully constructed boundary conditions to produce accurate results. The inflow data should be unsteady and the successive realizations must follow specific statistics while ideally having a particular correlation in both space and time. A method for generating synthetic correlated stochastic data from uncorrelated sequences is detailed and applied to the problem of inflow turbulence generation for CFD simulations. The technique constructs divergence-free anisotropic random fields with the sensible spectrum and complete complex correlation in space and time. A realistic two-point correlation tensor is inferred from first and second moments and a set of heuristic recommendations based on turbulent flow observations. These statistics are readily available in most practical cases making the technique highly versatile. The approach is computationally efficient with the use of eigendecomposition to reduce the resources required depending on the accuracy needed. Demonstration of the method is provided with the simulation of a turbulent channel flow and a square duct flow, and validation is done against existing numerical data.

I. LITERATURE SURVEY

Over the years, the development of computer capabilities has increased the popularity of large-eddy simulations (LES) and direct numerical simulations (DNS). For such scale-resolving techniques, while the precision is dictated by the computational resources available, the accuracy of the result is strongly influenced by the boundary conditions imposed, especially at the inlet. The inflow realizations must be unsteady, but it is not sufficient to superimpose uncorrelated and spectrally uniform randomness on top of a mean flow field. Because turbulent flow fields are highly correlated at small separations and have a wide range of length scales, the fluctuations generated as such will get damped out, not developing into turbulence and leading to inaccurate results. For instance, Lund *et al.* (1998) showed that specifying random uncorrelated fluctuations at the inflow of a spatially developing boundary layer leads to large underpredictions of the boundary layer characteristics downstream. The same conclusion was drawn by Le *et al.* (1997) in the simulation of a backward-facing step, highlighting the strong influence of the inflow on the result; hence, the boundary realizations should follow the specific turbulent properties of the problem studied.

Various approaches are available to generate inlet turbulence. The present section provides a brief overview of the main techniques, for a more comprehensive analysis refer to Dhamankar *et al.* (2018) or Wu (2017). Traditionally, inflow methods can be divided into two main categories: synthetically generated turbulence under which the proposed method falls, and deterministic techniques such as turbulence-inducing simulations and inflows using precursor or concurring simulations. Turbulence-inducing techniques simulate the turbulent transition upstream of the domain of interest, hence not requiring the generation of correlated random data, see, for example, Rai and Moin (1993). Alternatively, a second simulation can be run *a priori* or concurrently to generate turbulent data for the main simulation. These approaches are relatively straightforward to implement, and the generated fields at the inflow are realistic but rely on an extended numerical domain of some sort and consequently bring a considerable additional computational and memory cost. Synthetic methods alleviate this issue by constructing turbulence-like fluctuations from uncorrelated data and known target properties. Preferably, synthetic generators should rely only on turbulence statistics that are readily available or inexpensive to compute. The boundary plane is placed a short distance upstream of the simulation model to allow for the synthetic turbulence to settle. The fields generally match first-order statistics immediately, but the correct covariance is usually reached only after a short distance from the boundary. The synthetic field morphs into a physical turbulent flow, satisfying the Navier–Stokes equations. This development distance is a good indicator on the performance of a method and the validity of the assumptions made.

In recent years, novel hybrid approaches have emerged. Spille-Kohoff and Kaltenbach (2001), Meux *et al.* (2015), and Ketterl and Klein (2018) proposed a method based on a linear forcing term and a precursor simulation. The forcing term is used to control the fluctuations in order to achieve the desired turbulence characteristics while still being realistic as the Navier–Stokes equations are solved. Another approach studied is the application of machine learning to synthetic turbulence. In recent years, machine learning techniques have been used to better understand and predict turbulence. For inflow generation, machine learning algorithms can be trained on data collected from simulations or high-definition experiments, and can then be used to generate synthetic fluctuations that closely resemble the physical phenomenon. Fukami *et al.* (2019) used DNS data of a turbulent channel flow to produce inflow fields for the same case properties. A similar approach was followed by Kim and Lee (2020), and they successfully generated inflow boundaries at different Reynolds numbers. More recently, Yousif *et al.* (2022) used deep learning to generate instantaneous velocity fields for a developing boundary layer. Although machine learning models are able to accurately match turbulence statistics for various flow regimes over an extended period, their reliance on high-order statistics for training limits their current practical applications.

Synthetic methods continue to be widely used among the available options due to their versatility and relatively low computational cost. Apart from attempts based on uniformly distributed series, the earliest proposed approaches relied on a Fourier decomposition of turbulence following the well-known Kolmogorov spectra, as done by Kondo *et al.* (1997), who successfully simulated decaying isotropic turbulence. A second type of decomposition frequently used is orthogonal decomposition, which transform a flow field into an orthogonal basis sorted based on energy and can be applied to nonperiodic signals. The eigenfunctions represent coherent patterns present in the function of interest. The energy of each mode is scaled by its eigenvalue, offering a direct way to reduce the data needed while keeping the main features of the correlation. The estimation of how many terms in the series are necessary for an accurate representation is dependent on the length scales resolvable by the mesh and the computational method used. Eigendecompostion is useful for studying turbulent flows; Bakewell and Lumley (1967) applied it to extract the main structures present in the viscous sublayer of a turbulent pipe flow. Moin and Moser (1989) and Nawab and di Mare (2018) decomposed a DNS simulation of a turbulent channel using POD to understand the different eddy structures present.

A related technique was proposed by Klein *et al.* (2003) and followed by di Mare *et al.* (2006), and it employs digital filters to generate inflow data. Random uncorrelated data are filtered with a set of coefficients to obtain the prescribed one-point first- and second-order statistics as well as two-point correlation function. In most cases, the filters have a Gaussian shape to simplify the relations between the filter coefficients and the velocity correlation. Advantages of filtering digitally random data are the ability to generate prescribed statistics while keeping the signal non-periodic unlike Fourier-based inflows. Later, Hao *et al.* (2022) extended the method by combining the use of a digital filter and eigendecomposition. The correlation tensor is decomposed into modes that capture the variations of the flow quantities on the inflow plane while preserving a prescribed correlation. Finally, a digital filter was created for each mode to enforce a two-time correlation. The procedure was applied to a developing boundary layer and a turbulent channel flow, and it was found to require significantly shorter development lengths compared to previous synthetic generation techniques. Efforts are also ongoing to further improve the computational performance and broaden the scope of applications for digital filtering techniques. Treleaven *et al.* (2020) applied a proper orthogonal decomposition to the generated filter to compress the data needed to reconstruct the filter, making the method up to eight times faster. Moreover, Dhamankar *et al.* (2018) has adapted the original filtering method to curvilinear grids instead of uniform grids only, extending the scope of the technique. The present method builds up on the work of Hao *et al.* (2022), seeking more realistic fluctuations while maintaining a computational cost similar to the original filtering technique. To achieve this, the extension utilizes a complete complex correlation function rather than a diagonal tensor and ensures the divergence-free condition is met by the filters. Additionally, the method removes the need for an approximate exponential expression of the filter by considering the spectrum of the fluctuations. Overall, significant performance improvements in terms of development length are achieved.

II. METHOD

This section describes the procedure used to generate correlated data from uncorrelated sequences based on the decomposition of the covariance tensor. In addition, a discussion about the structure of the two-point correlation tensor in turbulent wall-bounded flows is made based on observations. From there, recommendations are drawn and an approximation technique based on first-order statistics and the divergence-free condition is detailed.

A. Prescribed covariance

Correlated data a_i can be generated synthetically from an uncorrelated random set ϕ_i and some appropriately chosen coefficients. As explained by di Mare and Jones (2005), any symmetric factorization s_{ih} of a covariance tensor r_{ij} is an appropriate choice of coefficients. Given a random uncorrelated sequence ϕ_i, with covariance tensor δ_{ij}, the stochastic correlated data can be generated by the following equation:

$$\begin{aligned} \langle a_i a_j^* \rangle = \langle s_{ih}\phi_h s_{jk}^* \phi_k^* \rangle &= \langle \phi_h \phi_k^* \rangle s_{ih} s_{jk}^*, \\ &= \delta_{hk} s_{ih} s_{jk}^*, \\ &= s_{ih} s_{jh}^*, \\ &= r_{ij}. \end{aligned} \tag{1}$$

Using Einstein's convention, $.^*$ indicates the complex conjugate. To avoid periodicity in the generated data due to the finite size of the correlation tensor support, Klein *et al.* (2003) preferred the use of a convolution instead of multiplying the data coefficients

$$a_i = \sum_{h=-N}^{N} s_{ih}\phi_{i+h}. \tag{2}$$

This filter technique is capable of generating three-dimensional correlated data that can be used as inflow data if the Taylor hypothesis is made. It has been applied successfully by Klein *et al.* (2003) and Hoepffner *et al.* (2011) to generate inflow conditions for impinging jet flows and free shear layers. However, the filter coefficients were obtained based on assumed exponential expressions; the present work alleviates these by constructing a realistic correlation tensor based on spectral and variance data.

The statistical method to reproduce correlated data relies on the ability to factorize the correlation tensor of the targeted signal in every dimension of the problem studied. An efficient way to obtain a symmetric factorization of a tensor is using an orthogonal decomposition. As explained in Sec. I, eigenanalysis linearly decomposes the turbulent flow into modes representing the coherent structure present in the data. The special case of a homogeneous direction must be treated carefully. In such an instance, the correlation tensor is circulant and eigenanalysis leads to trigonometric eigenvectors, shortening the information needed in the periodic direction to only an energy distribution. Nevertheless, as elaborated in Lumley (1981), trigonometric functions differ fundamentally from typical eigenfunctions as their spatial extent is not limited. Another difference in that case is that the modes do not represent specific structures present in the flow, rather the spectral distribution of the flow. It must be noted that other decompositions are available and can preserve the features of shape and spatial extent, see Lumley (1981).

B. Construction of the covariance tensor

A turbulent flow can be statistically described by its two-point one-time velocity correlation tensor $R_{i,j}(\mathbf{x}^{(1)},\mathbf{x}^{(2)}) = \langle u_i(\mathbf{x}^{(1)})u_j^*(\mathbf{x}^{(2)})\rangle$, with the symmetry property $R_{i,j}(\mathbf{x}^{(1)},\mathbf{x}^{(2)}) = R^*_{j,i}(\mathbf{x}^{(2)},\mathbf{x}^{(1)})$.

In most practical cases, the complete covariance tensor is not directly available. A reasonable estimation can be obtained based on first and second moments, directly available from an inexpensive steady RANS simulation. Klein *et al.* (2003) and Hao *et al.* (2022) proposed an expression dependent on an exponential decay function of the separation and an appropriate length scale.

$$R_{i,j}(\mathbf{x}^{(1)},\mathbf{x}^{(2)}) = (-1)^{\delta_{ij}}\sqrt{\langle u_{i'}u_{j'}\rangle(\mathbf{x}^{(1)})\langle u_{i'}u_{j'}\rangle(\mathbf{x}^{(2)})} \times \exp\left(-\frac{||(\mathbf{x}^{(1)}-\mathbf{x}^{(2)})||^2}{L(\mathbf{x}^{(1)})\cdot L(\mathbf{x}^{(2)})}\right). \tag{3}$$

The continuity equation constrains the correlation tensor as

$$\frac{\partial}{\partial x_j^{(2)}} R_{i,j}(\mathbf{x}^{(1)},\mathbf{x}^{(2)}) = 0. \tag{4}$$

In the case of a homogeneous inflow direction, which is the case for most simulations as the inflow turbulent properties are likely to be constant or at least periodic, the flow can be decomposed in Fourier series. The correlations between the complex series coefficients have been studied for a turbulent channel and a square duct. Multiple observations have been made:

- The envelope of the correlation decays as an exponential or a Gaussian shape. In some cases, the decay reaches negative values, which are necessary for the divergence-free condition to be respected. A Gaussian modulated with a cosine is well suited to approximate the behavior of the correlation.
- The imaginary part of the normal components must be anti-symmetric as per the definition of the correlation.
- The exponential decay constant is proportional to the position in the non-periodic directions and the wavelength of the mode.
- The symmetries of the correlation are dictated by the non-periodic direction—the correlation follows the symmetries present in the velocity variances.

The complete correlation tensor is Hermitian thanks to the symmetry properties, which ensures real eigenvalues. For the purpose of factorization, only the positive eigenvalues are kept as the others are non-realizable—these arise when the correlation prescribed spreads too far in space.

III. RESULTS

In this section, the method described above is applied to two test cases and the results are compared with DNS data. Particular attention is given to the settlement length needed for the synthetic fluctuations to transform into physical turbulence.

The flow equations are solved using the code H4X (Hao *et al.*, 2022; Hope-Collins and di Mare, 2023). The code is a cell-centered finite volume code based on a multiblock grid arrangement. The flow field is represented by the viscous variables: velocities, temperature, and pressure. The equations of motion for a compressible fluid are solved in conservative form. The spatial discretization is third-order accurate in space for the inviscid fluxes. Third-order accuracy is achieved on a compact stencil by using variable extrapolation. No limiter is applied. The extrapolation is based on weighted least-square gradients. The gradient stencil contains all the face neighbors of each cell. For the purpose of variable extrapolation onto a cell interface, the gradient stencil is biased by removing the contributions from the neighbor on the other side of the interface. The numerical fluxes are adapted to low Mach numbers (Hope-Collins and di Mare, 2023), and a modified pressure flux is employed. The viscous fluxes are evaluated using a second-order discretization. Advancement in time is performed using a formally second-order accurate implicit scheme. The implicit iterations are based on a dual-time stepping formulation. The code is parallelized by partitioning the blocks of the multiblock grid among the available MPI ranks. Within each rank, block operations are parallelized using OpenMP. Computations and communications are overlaid to hide the latency of the network fabric.

A. Channel flow case

The first test case is a fully developed turbulent channel flow, rendered in Fig. 1. With turbulent channels being one of the most fundamental test cases in anisotropic turbulence, a great deal of knowledge has been gained on the flow dynamics over a large range of regimes. Direct numerical simulations have enabled researchers to obtain detailed statistical characteristics such as flow spectra and two-point correlations.

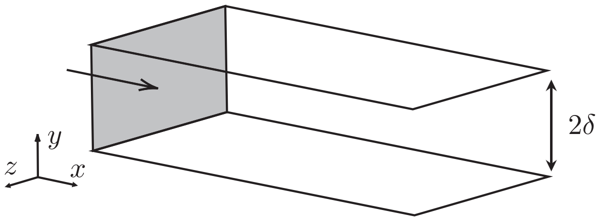

FIG. 1. Channel flow case and coordinate system.

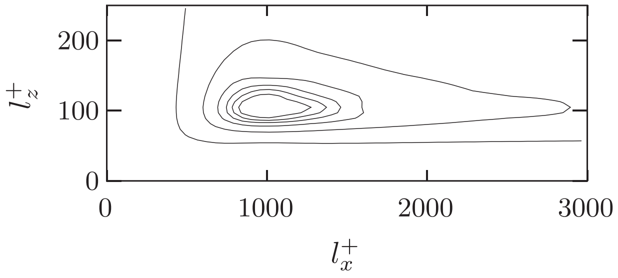

FIG. 2. Contour plot of the two-dimensional velocity spectrum imposed.

The averaged flow field is non-homogeneous in the wall-normal direction, symmetric with respect to the mid-channel and homogeneous in the streamwise and spanwise directions. Knowing that, the inflow data for a turbulent channel can be formally represented by

$$u_i'(x,y,z) = \sum_{k_x}\sum_{k_z}\sum_{l} \sqrt{C(k_x,k_z)\,\lambda(l)}\,q_i(k_x,k_z,l,y) \times e^{\imath(k_x x + k_z z)}\,\phi(j,k,l), \quad (5)$$

where k_x and k_z are the wavenumbers in the homogeneous directions, l is the wall-normal mode index, q is the wall-normal eigenmode, λ is the eigenvalue, C is the spectrum imposed, and ϕ is a random number.

The three-dimensional digital filters $f_{k_z,l}$ are obtained by taking the inverse transform in the streamwise direction of Eq. (5)

$$f_{k_z,l}(x,y,z) = \sum_{k_x} \sqrt{C(k_x,k_z)\,\lambda(l)}\,q_i(k_x,k_z,l,y)\,e^{\imath(k_x x + k_z z)}. \quad (6)$$

Finally, the three-dimensional signal, of which each spanwise-wall-normal slice will be used as an inflow realization, is obtained by convoluting the filters with a random signal

$$u_i'(x,y,z) = \sum_{k_z}\sum_{l}(f_{k_z l} \circledast \phi)(x,y,z). \quad (7)$$

Subsections III A 1 and III A 2 explain the procedure followed to construct the filters for the channel case, highlighting the approximations made to obtain a shape estimation of the correlation tensor and the power spectrum.

1. Velocity spectrum in periodic directions

As explained in Sec. II A, an energy distribution is needed for each of the homogeneous directions. Turbulent flows contain a wide range of length scales, but most of the energy is often located within a limited scope. In isotropic turbulence, the well-known Kolmogorov spectrum with the energy proportional to a power law of the wavenumber can be used. For a channel case, multiple DNS analyses are available, see Andrade *et al.* (2018), Mizuno (2016), and Lee and Moser (2019). The main concentration of energy is located at wavenumber ratios $k_z/k_x \gtrsim 10$, corresponding to elongated structures present in the channel. Various wall-normal spectral regimes have been identified in Lee and Moser (2019) and Mizuno (2016), highlighting the wavelength variations of the channel streaks with the wall-normal direction. However, a reasonable assumption can be made by considering a uniform spectrum in the wall-normal direction. Figure 2 shows the spectrum with a maximum spanwise wavelength of $l_z^+ = 100$ and a ratio $l_x/l_z = 10$.

2. Wall-normal autocorrelation

The construction of the wall-normal covariance tensor as a function of the wavenumber is guided by previous research from Townsend (1976), Kim *et al.* (1987), and Nawab and di Mare (2018). Writing the one-dimensional correlation tensor $R_{i,j}(y^{(1)},y^{(2)}) = \langle u_i(y^{(2)})u_j^*(y^{(1)})\rangle$, the continuity equation for a periodic channel in wavenumber space is

$$\begin{cases} \imath k_x R_{1,1}(y^{(1)},y^{(2)},k_x,k_z) + \imath k_z R_{1,2}(y^{(1)},y^{(2)},k_x,k_z) \\ \quad + \dfrac{\partial}{\partial y^{(2)}} R_{1,3}(y^{(1)},y^{(2)},k_x,k_z) = 0, \\ \imath k_x R_{2,1}(y^{(1)},y^{(2)},k_x,k_z) + \imath k_z R_{2,2}(y^{(1)},y^{(2)},k_x,k_z) \\ \quad + \dfrac{\partial}{\partial y^{(2)}} R_{2,3}(y^{(1)},y^{(2)},k_x,k_z) = 0, \\ \imath k_x R_{3,1}(y^{(1)},y^{(2)},k_x,k_z) + \imath k_z R_{3,2}(y^{(1)},y^{(2)},k_x,k_z) \\ \quad + \dfrac{\partial}{\partial y^{(2)}} R_{3,3}(y^{(1)},y^{(2)},k_x,k_z) = 0. \end{cases} \quad (8)$$

The continuity constraint combined with the symmetry condition of the two-point correlation leaves three components of the tensor to be specified. The three normal components could be chosen, but then a

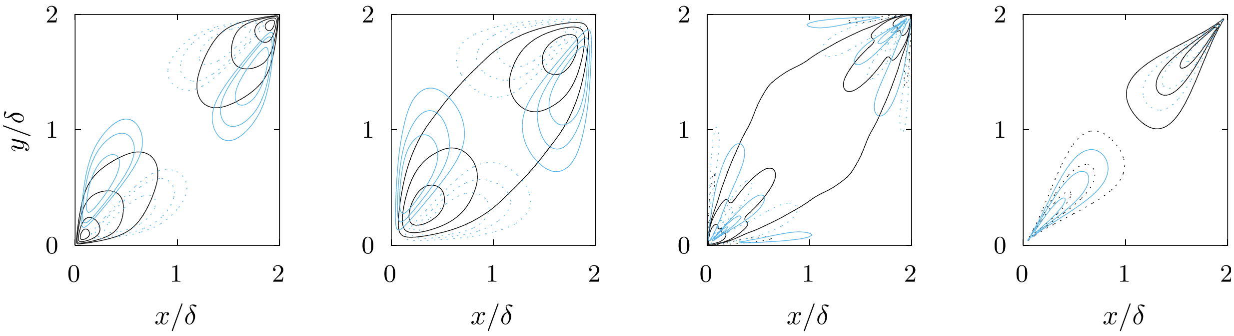

(a) R_{11} (b) R_{33} (c) R_{22} (d) R_{13}

FIG. 3. Contour plots of the two-point velocity correlation tensor. Black contours represent the real part; blue contours represent the imaginary part; and dashed lines represent negative values.

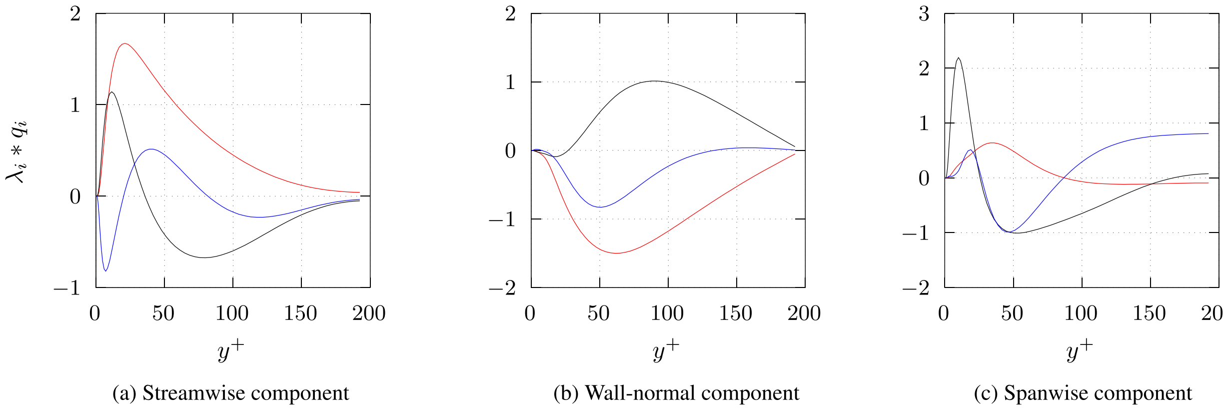

(a) Streamwise component (b) Wall-normal component (c) Spanwise component

FIG. 4. Real part of the first three wall-normal eigenfunctions at peak spectrum. Red curve—first mode; black curve—second mode; and blue curve—third mode.

linear system of differential equations must be solved. The system is likely to have an infinite number of solutions and must be solved in a least squares fashion. Taking another approach, if two normal and one non-diagonal components are specified, the system can be solved immediately by substitution. The equations suggest that the approximations of the correlation must be complex. The imaginary part controls the phase of the velocity field, which is related to the structure and shape of the turbulent eddies, see Keating *et al.* (2004). Nawab and di Mare (2018) give an idea of the full shape of the correlation tensor.

The covariance tensor is built from the exponential expression given in Eq. (3) with the characteristic length scale chosen to be the harmonic average of the turbulent length scale and the wavelength of the mode considered. One assumption made is that the wall-normal variance profile does not change with the wavenumber considered, and only the extent in space of the correlation is changing. This is not the case as shown in Lee and Moser (2019), but there does not exist enough data on the subject to make a better representation. Figure 3 shows the contours of the velocity correlation tensor for spanwise wavelengths of $l_z^+ = 50$ and streamwise wavelengths of $l_x^+ = 500$, and the real and imaginary components follow correctly the trends present in the data from Nawab and di Mare (2018).

The first three one-dimensional eigenfunctions for different velocity components are plotted in Fig. 4. The modes represent the influence on the velocity fluctuations of the turbulent structures present in the flow. The eigenfunctions for the streamwise velocity have most of the energy near the wall, whereas for the other components, the overall peak energy is located further away from the wall. The streamwise and wall-normal components compare well with the results from Moin and Moser (1989). The modes for the spanwise components on the other side are imperfect, and this is because all the spanwise velocity correlation components are solved for through the divergence equation, and therefore, no variance data for the spanwise component have been used. The study of the eigenmodes showed the need for a complete expression of the correlation tensor—if components are missing, the remaining components become uncorrelated and the relative amplitude and phase between the modes are not correct.

The three-dimensional shape of the eigenfunctions is dictated by the homogeneous directions, and the modes will have an oriented periodic eddy structure corresponding to their wavenumber, as detailed by Ball *et al.* (1991).

3. Simulation setup

Strictly speaking, the geometry of a channel flow is completely defined by the channel height, 2δ. However, the computational domain has to be of finite size, leading to the introduction of the streamwise and spanwise lengths, L_x and L_z. The flow is simulated between two viscous walls, and periodic boundaries are applied in spanwise directions. The Reynolds number Re_τ, based on the friction velocity and the channel half-width investigated, is 180 at a Mach number $Ma = 0.3$.

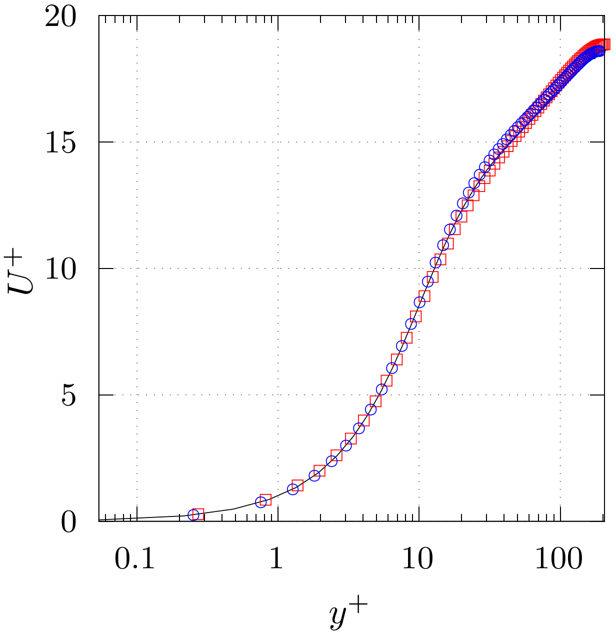

FIG. 5. Mean velocity profiles. Black curve—DNS data from Moser *et al.* (1999), blue circles—periodic channel, and red squares—channel with inflow at $x/\delta = 2$.

The computational domain size in the streamwise and spanwise directions is $(8\pi\delta, 4/3\pi\delta)$, found by Kim *et al.* (1987) to be enough for the flow variables to become uncorrelated at maximum streamwise and spanwise separation. The grid size is (256 × 144 × 128) with a grid stretching in the wall-normal direction detailed in Pirozzoli and Orlandi (2021). To capture the physics, the first cell is in the viscous sub-layer, $\Delta y^+\mathcal{O}(1)$, and having $\Delta x^+\mathcal{O}(10)$ and $\Delta z^+\mathcal{O}(5)$ is sufficient to resolve small-scale structures near the walls.

The simulation with the inflow generator will be compared against DNS data available from Kim *et al.* (1987) and against a streamwise periodic channel run with the same setup as the channel with turbulent inflow. The mass flow of the periodic channel was kept constant with the addition of an artificial body force.

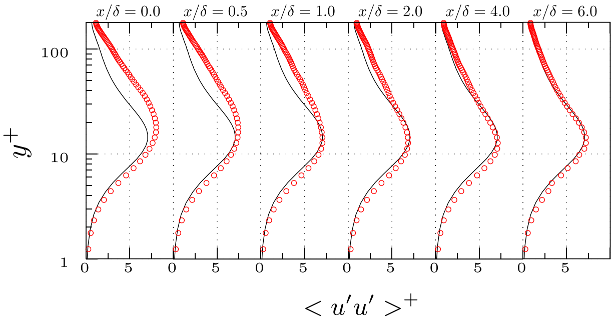

(a) Streamwise component

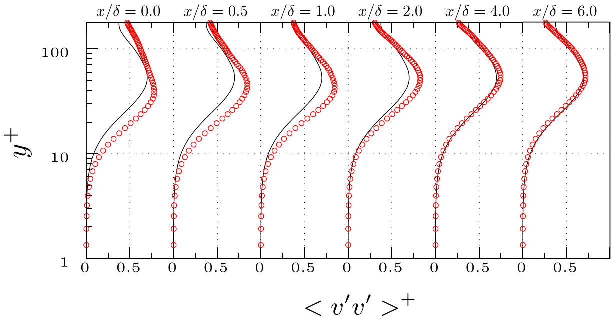

(b) Wall-normal component

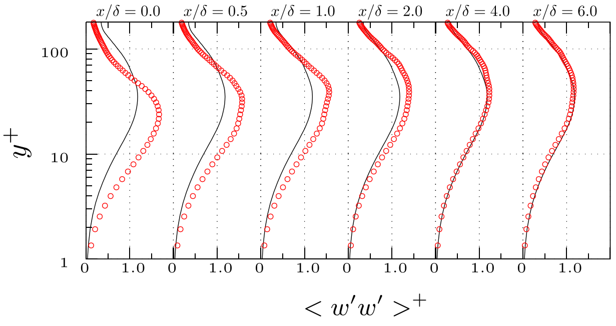

(c) Spanwise component

FIG. 6. Streamwise development of the dimensionless time-averaged velocity variances.

4. *Mean quantities*

Figure 5 plots the mean velocity profiles made dimensionless by the wall-shear velocity. The profile of the simulation with inflow correctly matches the well-known DNS results. This is expected as the profile imposed came from DNS calculations, but it shows that the mean quantities downstream of the inlet plane are not altered by the introduced fluctuations. The periodic channel case was initialized with a simple randomized parabolic profile. The correct prediction of the mean streamwise velocity profile shows the ability of the solver and the mesh to resolve appropriately the scales of interest.

5. *Velocity fluctuations*

To evaluate the development length, the velocity variances are compared with Kim *et al.* (1987) at different streamwise locations. Figure 6 shows the streamwise evolution of the Reynolds normal stresses. Overall, a very good fit is reached after $x/\delta \simeq 6$, less than 5% RMS error, but less than 10% RMS deviation is reached after $x/\delta \simeq 3$. While the guessed shape for the streamwise and spanwise component is close to the actual profile for the streamwise and wall-normal component, the fit and amplitude is less accurate for the spanwise component—as explained in Sec. III A 4. This is a result of the divergence condition that was applied. The streamwise profile at the inflow is overestimated toward the mid-channel but recovers slowly until $x/\delta \simeq 6$. The spanwise and wall-normal profiles have inaccurate near-wall behavior but reach a better agreement near the mid-channel.

Figure 7 plots the spanwise correlation at two different wall-normal positions, near the wall and near mid-channel. At the inflow, it can be seen that the realizations are correlated and the sinc shape is in accordance with the spectrum prescribed, with a negative peak at small separation. The decay for $x/\delta = 6$ follows the same trend as the correlations available in Kim *et al.* (1987) and Abe *et al.* (2001). At the inlet, the failure to capture the correct spanwise correlation away from the

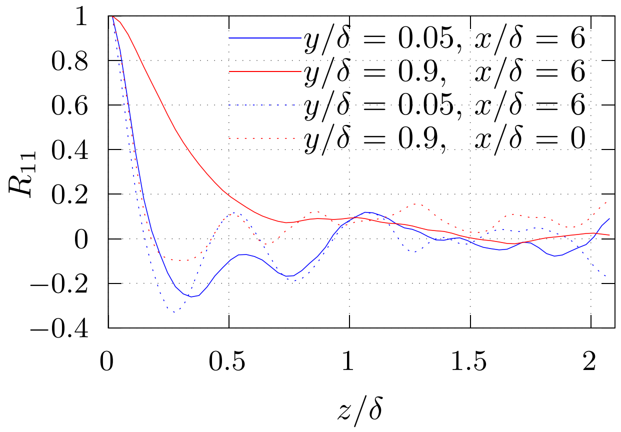

FIG. 7. Spanwise two-point correlation at selected streamwise and spanwise locations.

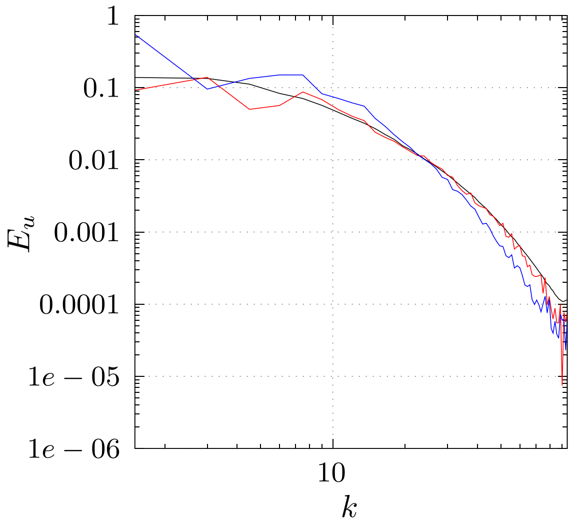

FIG. 8. Normalized spanwise spectrum of the streamwise velocity component at mid-channel averaged over $x/\delta = [0.6–0.7]$. Black curve—DNS data from Moser *et al.* (1999); red curve—reference inflow run, energy cutoff = 0.95; and blue curve—energy cutoff = 0.6.

wall comes from the assumption that the streamwise–spanwise spectrum is constant in the wall-normal direction.

6. Inflow parameters and performance

The inflow technique relies on a number of turbulent parameters that must be carefully chosen in order to obtain accurate inflow realization.

First, the streamwise extent of the inflow domain should be greater than the integral timescale of the flow field, which is necessary to ensure the field becomes uncorrelated.

In the exponential expression chosen to estimate the wall-normal correlation, the extent of the wall-normal correlation is dictated by the magnitude of the decay constant. If the decay is excessively swift, the covariance matrix becomes virtually diagonal and the fluctuations uncorrelated. On the contrary, the variables become too correlated at large separations and the inflow realizations will resemble a set of bands in the wall-normal direction. The top and bottom sides of the channel will become too correlated, which is not physical.

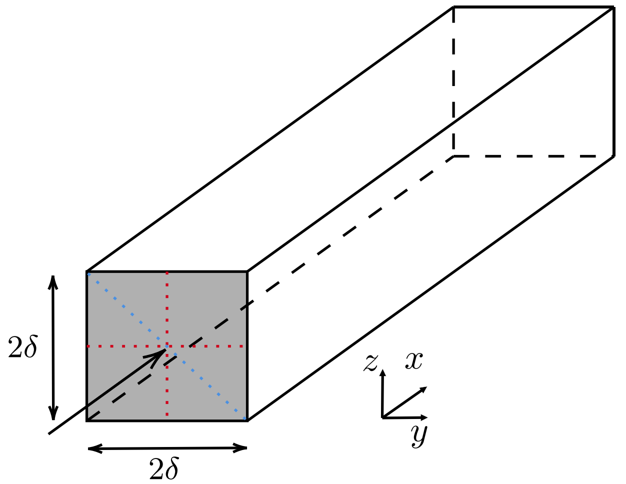

FIG. 9. Square duct diagram and coordinate system.

Eigenanalysis allows for a direct sorting of the modes based on energy. The energy cutoff should be proportional to the scales resolvable by the mesh of the main simulation. It is desirable to retain as much energy as possible, but it adds a memory and computational overhead to store and reconstruct all the length scales. The spectral content of the generated fields is important for the Reynolds stress budget equation. As explained in Keating *et al.* (2004), the production rate term is a function of the mean flow field and the Reynolds stress; hence, from Fig. 6, it can be assumed that the magnitude is sensible even close to the inflow plane. However, to correctly model the dissipation term, the spectral content in the flow field must follow the distribution of a real turbulent flow along the wall-normal direction. If only large scales are present in the flow, the kinetic energy dissipation

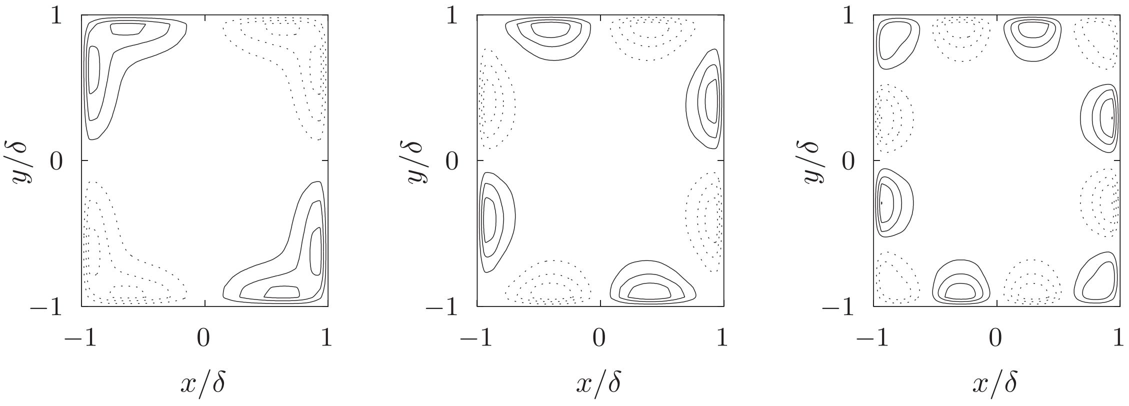

(a) First mode (b) Second mode (c) Third mode

FIG. 10. Contour plots of streamwise component of the first three modes. Dashed lines represent negative values.

will be largely underestimated. The correct distribution will be reached further downstream once the large structures have broken down and the balance between production and dissipation is restored. Figure 8 illustrates this by comparing the spanwise spectrum downstream of the inflow for different energy cutoffs, one where nearly all the length scales are represented and a second case where only the dominant scales are kept. The case with lower energy cutoff does not have the correct decay unlike the case with higher energy threshold. The performance of the inflow generator depends on several factors, including the size of the filter, the number of grid points at the inlet, and the number of modes retained. To prioritize runtime performance or ensure repeatability, the inflow fields can be generated prior the simulation and simply read at runtime. In terms of resources, the entire inflow generation process uses 4%–8% of the total simulation time, depending on the energy cutoff chosen. While the proposed method requires additional resources compared to the original filter method by Klein *et al.* (2003), it remains significantly lighter than precursor simulations and hybrid volumetric forcing simulations. The performance of the algorithm can be further enhanced by applying techniques outlined in Kempf *et al.* (2012), for example.

B. Square duct flow

The second test case studied is a straight duct with a square cross section at a Reynolds number based on the friction velocity of 220 and a bulk Mach number of 0.2. There has been a strong interest in rectangular duct flows mainly because of the cross-sectional motions (Fig. 9). The time-averaged flow has four statistically symmetric quadrants, each containing a pair of counter rotating vortices. These turbulence-born secondary flows, named of Prandtl's second kind, will test the ability of the inflow method to generate coherent structures capable of reproducing the gradients in the Reynolds stresses to produce the vorticity necessary to drive the secondary flows, Brundrett and Baines (1964). Multiple DNS studies on duct flows are available, see, for example, Gavrilakis (1992) or Pirozzoli *et al.* (2018).

1. Streamwise turbulent kinetic energy spectra

Square ducts have only one homogeneous direction, and the streamwise kinetic energy spectra can be approximated by simple Kolmogorov spectra, agreeing with results from Khan *et al.* (2020) and Huser and Biringen (1993).

2. Spanwise and wall-normal correlation

The correlation tensor is constructed using the expression in Eq. (3). Similarly to Sec. III A 2, only three components of the tensor are guessed and the remaining are set through the divergence-free condition and the symmetries of the problem. The symmetries of the problem imply that each eigenmode comes in quartet. The streamwise component of the first three families of modes is plotted in Fig. 10.

3. Mean quantities

The contours of mean velocity are plotted in Fig. 11(a), and the secondary flows are highlighted using velocity vectors. While the magnitude of the secondary flows is not of the same order of that of the mean axial flow, they are responsible for the swelling of mean axial velocity contours toward the corners, as observed by Brundrett and Baines (1964). The mean velocity profile on the wall bisector is plotted on Fig. 11(b) and matches well the data from Pirozzoli *et al.* (2018).

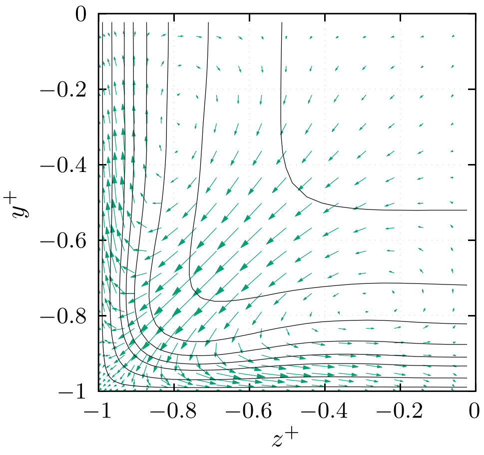

(a) Vector plot of the cross-section mean velocity and contours of the streamwise component

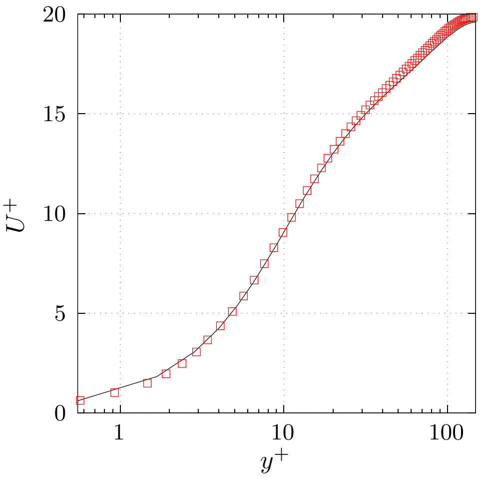

(b) Mean dimensionless streamwise velocity profiles. Black curve - data from Pirozzoli et al. (2018), red squares - square duct with inflow

FIG. 11. Mean quantities for the square duct case.

C. Fluctuating quantities

Figure 12 plots the development of the time-averaged velocity variances. It is observed again that, while not perfect, a close agreement is reached after a length of 6δ, RMS error of 6%. The spanwise component, which was obtained mainly through the divergence-free condition, is largely overpredicted at the inflow but quickly settles downstream.

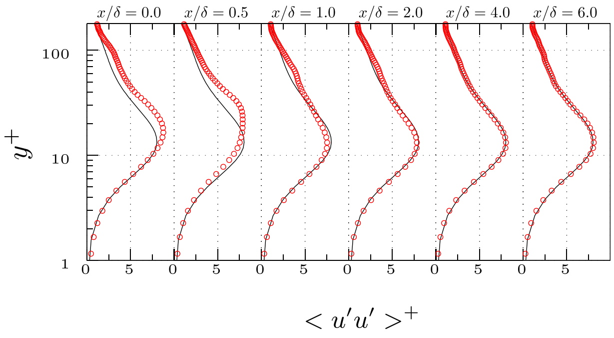

(a) Streamwise component

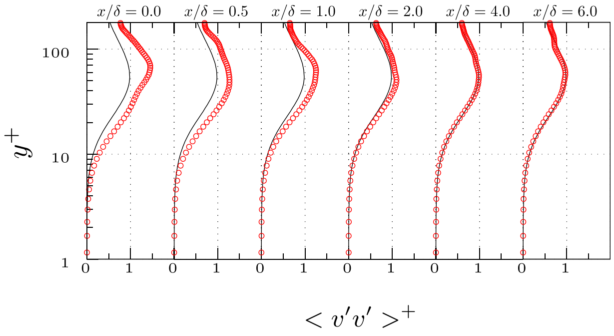

(b) Wall-normal component

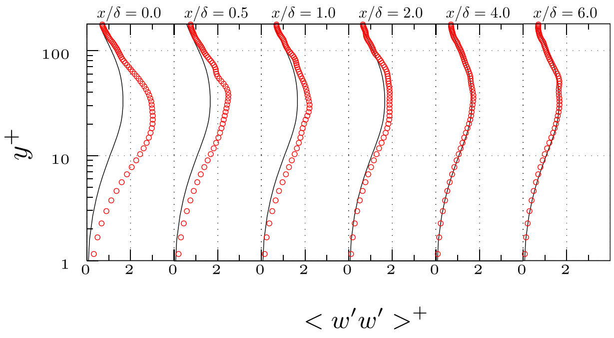

(c) Spanwise component

FIG. 12. Development of dimensionless time-averaged velocity variances.

IV. CONCLUSION

The current work presented an extension to a filter-based method for generating statistically realistic divergence-free turbulent data. The procedure is built around the factorization of the covariance tensor and the conservation of mass. In the non-homogeneous directions, an approximation of the complex correlation tensor is constructed from variance data combined with an exponential decay. The incompressible continuity equation was enforced to lower the number of components to be guessed and to ensure the generated field is divergence-free. The periodic directions are assembled with trigonometric functions based on an appropriate energy distribution.

The method was tested on two wall-bounded turbulence cases and showed good agreement with existing data. The eigenmodes for both cases capture the regions of high variance. The inflow generator was able to generate realistic fluctuations for the reproduction of the second moments within a short distance of the inlet plane while keeping a constant first moment. The reconstructed second moments at the inflow plane have a realistic shape and adjust quickly to the targeted profile. Only the components solved with the continuity equation gave less accurate approximations in the variance of the realizations. The assumption of constant properties in the wall-normal direction leads to acceptable results while being the source of most inaccuracies—further developments should take the different wall regimes into account. Component-wise spectra could also be introduced.

The main interest of the proposed method is the ability to generate realistic data for scale-resolving simulations with a short development length from readily available statistics. The approach has a small computational cost overhead compared to other inflow techniques and is highly versatile. The performance has been proven and potential further development highlighted.

ACKNOWLEDGMENTS

The authors are grateful for the support from Rolls-Royce PLC and the EPSRC Center for Doctoral Training in Future Propulsion and Power. The authors would also like to acknowledge the use of the University of Oxford Advanced Research Computing (ARC, Richards, 2015), facility in carrying out this work.

AUTHOR DECLARATIONS

Conflict of Interest

The authors have no conflicts to disclose.

Author Contributions

Yann Drèze: Investigation (lead); Methodology (equal); Software (lead); Validation (lead); Writing – original draft (lead); Writing – review & editing (lead). **Muting Hao:** Methodology (lead); Software (supporting); Supervision (supporting); Writing – review & editing (supporting). **Luca di Mare:** Investigation (supporting); Methodology (equal); Resources (lead); Supervision (lead); Writing – review & editing (lead).

DATA AVAILABILITY

The data that support the findings of this study are available from the corresponding author upon reasonable request.

REFERENCES

Abe, H., Kawamura, H., and Matsuo, Y., "Direct numerical simulation of a fully developed turbulent channel flow with respect to the Reynolds number dependence," J. Fluids Eng. **123**(2), 382–393 (2001).

Andrade, J. R., Martins, R. S., Mompean, G., Thais, L., and Gatski, T. B., "Analyzing the spectral energy cascade in turbulent channel flow," Phys. Fluids **30**(6), 065110 (2018).

Bakewell, H. P. and Lumley, J. L., "Viscous sublayer and adjacent wall region in turbulent pipe flow," Phys. Fluids **10**(9), 1880–1889 (1967).

Ball, K. S., Sirovich, L., and Keefe, L. R., "Dynamical eigenfunction decomposition of turbulent channel flow," Int. J. Numer. Methods Fluids **12**, 585–604 (1991).

Brundrett, E. and Baines, W. D., "The production and diffusion of vorticity in duct flow," J. Fluid Mech. **19**(3), 375–394 (1964).

Dhamankar, N. S., Martha, C. S., Situ, Y., Aikens, K. M., Blaisdell, G. A., Lyrintzis, A. S., and Li, Z., "Digital filter-based turbulent inflow generation for jet aeroacoustics on non-uniform structured grids," AIAA Paper No. 2014-1401, 2014.

Dhamankar, N. S., Blaisdell, G. A., and Lyrintzis, A. S., "Overview of turbulent inflow boundary conditions for large-eddy simulations," AIAA J. **56**(4), 1317–1334 (2018).

di Mare, L. and Jones, W., "Algebraic and operator methods for generation of inflow data for LES and DNS," in *Fourth International Symposium on Turbulence and Shear Flow Phenomena* (Begell House Inc., 2005).

di Mare, L., Klein, M., Jones, W. P., and Janicka, J., "Synthetic turbulence inflow conditions for large-eddy simulation," Phys. Fluids **18**(2), 025107 (2006).

Fukami, K., Nabae, Y., Kawai, K., and Fukagata, K., "Synthetic turbulent inflow generator using machine learning," Phys. Rev. Fluids **4**, 064603 (2019).

Gavrilakis, S., "Numerical simulation of low-Reynolds-number turbulent flow through a straight square duct," J. Fluid Mech. **244**, 101–129 (1992).

Hao, M., Hope-Collins, J., and di Mare, L., "Generation of turbulent inflow data from realistic approximations of the covariance tensor," Phys. Fluids **34**, 115140 (2022).

Hoepffner, J., Naka, Y., and Fukagata, K., "Realizing turbulent statistics," J. Fluid Mech. **676**, 54–80 (2011).

Hope-Collins, J. and di Mare, L., "Artificial diffusion for convective and acoustic low Mach number flows. I. Analysis of the modified equations, and application to Roe-type schemes," J. Comput. Phys. **475**, 111858 (2023).

Huser, A. and Biringen, S., "Direct numerical simulation of turbulent flow in a square duct," J. Fluid Mech. **257**, 65–95 (1993).

Keating, A., Piomelli, U., Balaras, E., and Kaltenbach, H.-J., "*A priori* and *a posteriori* tests of inflow conditions for large-eddy simulation," Phys. Fluids **16**(12), 4696–4712 (2004).

Kempf, A., Wysocki, S., and Pettit, M., "An efficient, parallel low-storage implementation of Klein's turbulence generator for LES and DNS," Comput. Fluids **60**, 58–60 (2012).

Ketterl, S. and Klein, M., "A band-width filtered forcing based generation of turbulent inflow data for direct numerical or large eddy simulations and its application to primary breakup of liquid jets," Flow, Turbul. Combust. **101**, 413 (2018).

Khan, H., Anwar, S., Hasan, N., and Sanghi, S., "The organized motion of characterized turbulent flow at low Reynolds number in a straight square duct," SN Appl. Sci. **2**, 763 (2020).

Kim, J. and Lee, C., "Deep unsupervised learning of turbulence for inflow generation at various Reynolds numbers," J. Comput. Phys. **406**, 109216 (2020).

Kim, J., Moin, P., and Moser, R., "Turbulence statistics in fully developed channel flow at low Reynolds number," J. Fluid Mech. **177**, 133–166 (1987).

Klein, M., Sadiki, A., and Janicka, J., "A digital filter based generation of inflow data for spatially developing direct numerical or large eddy simulations," J. Comput. Phys. **186**(2), 652–665 (2003).

Kondo, K., Murakami, S., and Mochida, A., "Generation of velocity fluctuations for inflow boundary condition of LES," J. Wind Eng. Ind. Aerodyn. **67**–**68**, 51–64 (1997).

Le, H., Moin, P., and Kim, J., "Direct numerical simulation of turbulent flow over a backward-facing step," J. Fluid Mech. **330**, 349–374 (1997).

Lee, M. and Moser, R. D., "Spectral analysis of the budget equation in turbulent channel flows at high Reynolds number," J. Fluid Mech. **860**, 886–938 (2019).

Lumley, J. L., "Coherent structures in turbulence," in *Transition and Turbulence* (Academic Press, 1981), pp. 215–242.

Lund, T. S., Wu, X., and Squires, K. D., "Generation of turbulent inflow data for spatially developing boundary layer simulations," J. Comput. Phys. **140**(2), 233–258 (1998).

Meux, B., Audebert, B., Manceau, R., and Perrin, R., "Anisotropic linear forcing for synthetic turbulence generation in LES and hybrid RANS/LES modeling," Phys. Fluids **27**, 035115 (2015).

Mizuno, Y., "Spectra of energy transport in turbulent channel flows for moderate Reynolds numbers," J. Fluid Mech. **805**, 171–187 (2016).

Moin, P. and Moser, R. D., "Characteristic-eddy decomposition of turbulence in a channel," J. Fluid Mech. **200**, 471–509 (1989).

Moser, R. D., Kim, J., and Mansour, N. N., "Direct numerical simulation of turbulent channel flow up to $Re_\tau = 590$," Phys. Fluids **11**(4), 943–945 (1999).

Nawab, A. and di Mare, L., "Re scaling of pod modes in plane channel flow," Phys. Fluids **30**(5), 055109 (2018).

Pirozzoli, S., Modesti, D., Orlandi, P., and Grasso, F., "Turbulence and secondary motions in square duct flow," J. Fluid Mech. **840**, 631–655 (2018).

Pirozzoli, S. and Orlandi, P., "Natural grid stretching for DNS of wall-bounded flows," J. Comput. Phys. **439**, 110408 (2021).

Rai, M. M. and Moin, P., "Direct numerical simulation of transition and turbulence in a spatially evolving boundary layer," J. Comput. Phys. **109**(2), 169–192 (1993).

Richards, A. (2015). "University of Oxford advanced research computing," Zenodo. 10.5281/zenodo.22558

Spille-Kohoff, A. and Kaltenbach, H.-J., "Generation of turbulent inflow data with a prescribed shear-stress profile," Report No. ADP013648 (2001).

Townsend, A. A., *The Structure of Turbulent Shear Flow*, 2nd ed. (Cambridge University Press, 1976).

Treleaven, N., Staufer, M., Spencer, A., Garmory, A., and Page, G., "Application of the PODFS method to inlet turbulence generated using the digital filter technique," J. Comput. Phys. **415**, 109541 (2020).

Wu, X., "Inflow turbulence generation methods," Annu. Rev. Fluid Mech. **49**(1), 23–49 (2017).

Yousif, M. Z. G., Zhang, M.-T., Yu, L., Vinuesa, R., and Lim, H., "A transformer-based synthetic-inflow generator for spatially developing turbulent boundary layers," arXiv:2206.01618 (2022).

3.3 Remarks and potential extensions

The method presented in section 3.2 relies on several assumptions, most of which are directly related to the reconstruction of the two-points velocity correlation. Addressing these assumptions could lead to a more accurate and versatile method.

First, the method assumes that the velocity spectra in the isotropic directions remain constant along the anisotropic directions. In principle, this assumption may not always hold, as the spectra are expected to vary along anisotropic directions. Such variations may arise due to geometric features, such as struts or vanes, or from proximity to walls, where smaller wavelength structures become more prominent. Nevertheless, for relatively simple incoming flows, this approximation appears reasonable and effective.

Second, the current treatment of the isotropic directions employs a Fourier decomposition to represent the spectrum. While this approach accurately captures the spectral content, the resulting mode shapes have infinite spatial support and may not reflect localised features inherent to the flow. As discussed by Lumley [1981], alternative decomposition techniques exist that preserve both the shape and spatial extent of the modes, making this a promising direction for future work.

In addition, in the current setup, the fluctuations generated are imposed on the ghost cells adjacent to the inflow, where a local one-dimensional inviscid (LODI) [Poinsot and Lelef, 1992] non-reflecting boundary condition is enforced. Because the present LODI formulation prioritizes low reflections, a portion of the injected turbulence is unavoidably attenuated. More sophisticated non-reflecting treatments for compressible solvers can mitigate this dissipation; see, e.g., Gloerfelt and Le Garrec [2008], Guézennec and Poinsot [2009], Moguen et al. [2014].

Finally, a key to unlocking the full potential of the method lies in understanding the relationship between flow features and the velocity correlation. This relationship can be formulated as a regression problem, which is particularly well suited for data-driven techniques. In practice, machine learning algorithms could be employed to map the relationship between the two-point correlation and the physical parameters that characterise the flow while physics-based models enforce known constraints in the correlation tensor (e.g., symmetries, conservation laws). Several studies have applied machine learning to the generation of synthetic turbulent flow fields [Yousif et al., 2022, Yu et al., 2022, Shinde and Johnsen, 2018], most of these approaches directly target velocity fields. In contrast, focusing on the two-point correlation—which is sufficient for many applications—remains largely unexplored. For instance, training a model to use RANS quantities as inputs and compute invariants of the mean flow along the eddy viscosity at the preprocessing stage. The model could be trained on available DNS data in different configurations to predict the diagonal components of the two-point correlation tensor, making use of the divergence-free approximation and the symmetry of the tensor to predict the remaining components. Such an approach would potentially enable the simulation of more complex geometries, including separated flows.

3.4 Statement of authorship

- Title of the paper: *Divergence-free turbulent inflow data from realistic covariance tensor*
- Publication status: Published
- Publication details: Dreze Y., Hao M. and di Mare L. "Divergence-free turbulent inflow data from realistic covariance tensor" (2023), *Physics of Fluids* 35, 025120. `doi.org/10.1063/5.0136568`
- Student Confirmation:
  - Student name: Yann Drèze
  - Contribution to the paper: I wrote all the code for the inflow generation based on the method from Hao et al. [2022], I obtained the numerical resources to run the simulations and I also performed the numerical simulations presented in the paper. Finally, I wrote the paper manuscript.

  - Date and signature: , September 26, 2025

- Supervisor Confirmation:

  By signing the Statement of Authorship, you are certifying that the candidate made a substantial contribution to the publication, and that the description described above is accurate.

  - Supervisor name and title: Luca di Mare, Associate Professor
  - Supervisor comments: I confirm that the candidate's statement is an accurate description of his contribution to this publication.
  - Signature and date: , September 26, 2025

Chapter 4 Unsteady Conjugate Heat Transfer modelling

Contents

The importance of conjugate heat transfer has been established in chapter 2, highlighting its critical role in the design of many thermally dominated systems. However, it also shed light on the limitations of prevailing approaches for unsteady CHT. In particular, commonly used methods are either computationally prohibitive or rely on restrictive modelling assumptions that can bias predictions in regimes where interfacial feedback are essential.

High-fidelity time-marching strategies, whether fully coupled or partitioned, can resolve accurately the approach to steady-state but at a steep cost. Stability and accuracy constraints force the timestep to track the fastest physics (often on the fluid side), while the solid may evolve on much longer diffusive timescales. The resulting stiffness inflates wall-clock time and memory footprint, making parametric exploration, control-oriented studies, and uncertainty quantification impractical.

To avoid that cost, many workflows assume a quasi- or fully steady solid, solving the steady conduction problem once and coupling it to a transient fluid. This decoupling suppresses thermal storage and phase-lag effects in the solid, which can be unacceptable whenever the Biot number is moderate to large, volumetric heating is present, or start-up/shut-down transients dominate the use case.

A second class of state-of-the-art methods recasts the unsteady problem in the frequency domain via a truncated Fourier decomposition (e.g., harmonic balance or time-spectral formulations). While effective for strictly periodic forcing, these approaches struggle with broadband or intermittent transients: convergence can be slow, many modes are required to capture sharp events, and Gibbs-type artifacts can corrupt interfacial fluxes and temperatures. Moreover, accommodating nonstationary boundary conditions or mixed time scales often defeats the efficiency gains that motivate the frequency-domain route in the first place.

In this chapter we address these shortcomings by developing an unsteady CHT framework that (i) retains full unsteady dynamics in both fluid and solid without assuming a steady solid, (ii) reduces cost relative to naive time marching by separating fast and slow processes where possible, and (iii) avoids global Fourier expansions by using separating the scale only using the algebraic properties of the numerical system so that nonperiodic transients and localized events are captured directly in time. The approach is demonstrated on canonical benchmarks and application-relevant cases, emphasizing accuracy at the interface and predictable computational cost.

Subsequently, an applied study on the effects of unsteady conjugate heat transfer on flow characteristics is presented, published in Dreze and di Mare [2025].

4.1 Multiscale Unsteady Conjugate Transfer via Modal Projection

The following section contains a draft of a journal paper titled "Multiscale Unsteady Conjugate Transfer via Modal Projection", which was submitted to the *Journal of Computational Physics* on April 25, 2025, and is currently under review.

This work aims to address the main challenges of unsteady conjugate heat transfer simulations presented in subsection 2.2.1. The paper presents a novel approach to CHT simulations that leverages modal projection to address the time scale mismatch between the fluid and solid domains. The paper demonstrates the effectiveness of the proposed method through a series of numerical experiments, highlighting its ability to accurately capture the transient thermal behaviour while maintaining computational efficiency.

Highlights

Multiscale Unsteady Conjugate Transfer via Modal Projection

Yann Dreze, Muting Hao, Luca di Mare

- A modal decomposition of the solid temperature field is proposed, which allows for an efficient representation of the unsteady heat conduction problem.
- The modal representation reduces the solid domain to a set of uncoupled, single-degree-of-freedom ordinary differential equations, which require only surface integrals to be computed
- To address the timescale challenge, the thermal transients of the modal equations are accelerated individually based on the respective time constants of the modes.
- The method shows a fourfold reduction in time to steady state for the slowest modes, with an associated error of 6%.

Multiscale Unsteady Conjugate Transfer via Modal Projection

Yann Dreze[a,*], Muting Hao[a], Luca di Mare[a]

[a]*Department of Engineering Science, Oxford University, Oxford Thermofluids Institute, Southwell Building , Oxford, OX20ES, United Kingdom*

Abstract

This paper presents a multiscale methodology for efficient unsteady conjugate heat transfer simulations. The solid domain is modelled by coupling a global representation of the temperature field, based on the eigenfunctions of the unsteady heat conduction equation, with a local, fine-scale-resolving solution of the heat conduction equation at the conjugate interface. To address the disparate time scales and enhance convergence, the decoupled modal equations are leveraged to enable targeted acceleration of the longest thermal time scales. One-dimensional analyses validate the properties of the scheme, while scale-resolving simulations demonstrate its practical application for steady and unsteady problems. Notably, the method achieves up to a fourfold reduction in computational time to reach steady thermal conditions compared to conventional conjugate simulations, without introducing significant computational overhead or error, offering an accurate and accelerated framework for unsteady thermal analysis.

Keywords: Conjugate heat transfer modelling, Unsteady conjugate heat transfer, Thermal transients

---

1. Introduction

Over the years, the development of computer capabilities has increased the popularity of large-eddy simulations (LES) and direct numerical simulations (DNS). For such scale-resolving techniques, while the precision is dictated by the computational resources available, the physical accuracy of the result is strongly influenced by the boundary conditions imposed. Simple boundary conditions, such as constant Dirichlet or Neumann may not be sufficient to accurately model real-world problems which often involve interactions across multiple physical domains. Indeed, in recent years, the scope of CFD has evolved recognising the importance of fluid-structure interactions [1, 2, 3, 4].

In the context of the thermal boundary condition, most of the fluid prediction methods frequently used in research and in industry do not take into account conjugate heat transfer (CHT) — the thermal interaction between fluid and ajacent solid. The boundary conditions between solid walls and the fluid domain are usually specified as a fixed heat flux or a fixed temperature. However, there is a direct interest in metal temperature distribution in presence of fluid flow with large temperature variations. This is because the heat transfer and the temperature gradients between the fluid and solid can significantly influence the flow and the simple specifications commonly used are not accurate. A classic example is that of high pressure turbines rows, where accurate modelling of the thermal operating conditions requires a conjugate heat transfer analysis as shown by [5, 6, 7].

Since the pionerring works of Perelman [8], CHT has now become a critical aspect of many engineering applications. Its significance spans from microscopic levels, such as near-wall turbulence [9] or the use of nanofluids for improved heat transfer [10], to macroscale systems such as thermal management in spacecraft, insulation in nuclear reactors, cooling of turbine blades, and thermal regulation in battery technology, [11, 12].

Coupling domains with distinct governing equations presents significant modeling challenges. These challenges stem from the different physical processes, conduction dominated in solids and convection dominated in most fluids,

---

[*] yann.dreze@engs.ox.ac.uk

Nomenclature

α	Thermal diffusivity
χ, η, ζ	Local geodesic coordinates
χ_a	scaling factor for SFD
Δr^+	Wall-normal grid spacing in radial direction
Δy^+	Wall-normal grid spacing in viscous sub-layer
δ	Channel half-width
δ_b	Boundary layer thickness
Γ	Boundary
κ	Thermal conductivity
λ	Eigenvalue
$\mathcal{L}$	Laplace operator
μ	Dynamic viscosity
Ω	Domain
ω	Angular frequency
ϕ	Angle
ρ	Density
σ	Acceleration factor
τ	Time scale
CFEA	Combined Finite Element Accelerated
CFE	Combined Finite Element Solution
FE	Finite Element Solution
MFE	Modal Finite Element Solution
M	Mach number
Pr	Prandtl number
Re_τ	Reynolds number based on friction velocity
Re_D	Reynolds number based on pipe diameter
Θ	Transformed temperature
$\vec{n}$	Normal vector
ξ	Dimensionless coordinate
c_p	Specific heat capacity
$C_{f,\theta}$	Local skin friction coefficient
F	Shape function
F_{str}	Strouhal Frequency
H	Laplace transfer function
L_x	Streamwise length
L_y	Transversal length
L_z	Spanwise length
Q_s	Heat source
R_c	Radius of curvature
s	Laplace variable
T	Temperature
T_∞	Outer flow temperature
U	Modal coefficients
x, y, z	Global Cartesian coordinates
CFD	Computational Fluid Dynamics
CHT	Conjugate Heat Transfer
DNS	Direct Numerical Simulation
LES	Large Eddy Simulation
N-S	Navier-Stokes equations
Nu_θ	Local Nusselt number
$\mathrm{R_{in}}$,$\mathrm{R_{out}}$	Inner and outer radius
SFD	Selective Frequency Damping
St	Stanton number
Str	Strouhal number
URANS	Unsteady Reynolds-averaged N-S

which operate on different spatial and temporal scales. This disparity complicates the achievement of accurate and efficient simulations.

Firstly, in transient CHT problems, approach to a steady-state takes place at significantly different rates in the solid and fluid domain, the mismatch in time scales being potentially very large. [13] presented a dimensional analysis of the time scales in CHT problems. The analysis demonstrates that the timescale ratio τ_s/τ_f between convection and conduction is given by the following Equation 1:

$$\frac{\tau_s}{\tau_f} = \frac{\kappa_f \rho_f c_{p,f}}{\kappa_s \rho_s c_{p,s}} \mathrm{St}\,\mathrm{Re}^a \Big/ \left(\frac{\mathrm{Re}^{-1+2a}}{\mathrm{Pr}} \right) \tag{1}$$

The timescale ratio τ_s/τ_f is a function of the thermal effusivity $\kappa\rho c_p$, which characteristices the rate at which heat is absorbed, stored, and conducted away from an interface, [14, 15]. The timescale ratio also depends on the Stanton number (St), the Prandtl number (Pr). The properties of the boundary layer near the solid/fluid interface also affect the timescale ratio through the scaling law of the thickness of the thermal boundary layer (Re^a). For a typical air-steel system, $\tau_s/\tau_f \approx 10^4$. Similarly, large values are found in most gas/metal interfaces of practical interest. Large values of the ratio τ_s/τ_f indicate that progress towards the attainement of a steady temperature distribution in the conjugate system is dominated by the thermal transient in the metal. In conjugate heat transfer simulations with large solid domains, this may require very long simulation times for a true steady state to be reached [16, 17]. Reconciling these timescales to ensure a statistical steady state remains problematic.

Secondly, the temperature distribution in the solid and fluid domains may exhibit drastically different length scales. The thermal boundary layers thicknesses in the solid and fluid domains stand in a ratio dictated by the ratio of the thermal conductivities [14, 13], as shown in Equation 2:

$$\frac{\delta_s}{\delta_f} \simeq O\left(\frac{\kappa_s}{\kappa_f}\right) \tag{2}$$

As an example, for the same air-steel system the ratio is about 100, higlighting the differences in thermal boundary layer heights ($\frac{\delta_s}{\delta_f}$). The concept of thermal penetration depth is also widely used in the literature to describe the spatial scales of temperature variations in the solid domain for unsteady CHT problems. There are various definitions of the thermal penetration depth, but for periodic cases the most common is the distance over which the temperature fluctuations from a harmonic forcing decrease by a factor of $1/e$. The thermal penetration depth is given by Equation 3, where ω is the angular frequency of the temperature oscillations.

$$\delta_P = \sqrt{2\alpha_s/\omega} \tag{3}$$

Because most current simulation methods rely on a time-marching approach, such as URANS or LES, the small timesteps required, combined with the strict grid requirements for the solid domain, make these simulations resource-intensive when conducted over timescales relevant to the solid.

From a computational implementation perspective, coupling strategies are used to manage how the heat transfer information is exchanged at the interface between the fluid and solid regions during a simulation. There are two primary categories of coupling strategies: weakly coupled and strongly coupled (or fully coupled). The coupling strategy can lead to additional modelling error, such as interpolation errors if the grids for both methods are different and interpolation is needed.

1.1. Strategies to efficiently solve CHT problems

The fundamental challenge of the disparity in timescales between the fluid and solid domains and its impact on the complexity of initialising and conducting unsteady conjugate heat transfer analyses is widely recognised [13, 16, 18]. Various methods have been proposed to accelerate the initial transient towards the statistical steady-state, while still enabling accurate time-dependent solutions for temperature fluctuations in the solid domain.

One of the most straightforward approaches is to alter the solid properties to try to realign the fluid and solid time scales. Oh et al. [19] focused on a ribbed cooling passage using LES with the immersed boundary method. They showed that the timescale disparity can be overcome by using an artificially high solid thermal diffusivity while maintaining a constant Biot number. The higher Fourier number allowed for a faster approach to statistical steady-state. Once statistical steady-state is reached, the solid thermal properties were changed back to their original values and the simulation ran until stationary steady-state was achieved again with the original values. Their predictions are compared with experiments and other LES studies, however, the simulation time remains high due to the convergence of two successive steady-states separated by a discontinuous change in solid properties. Similarly, Shi et al. [20] modified the solid thermal properties and calculation time based on a Biot and Fourier number scaling of the equations. While the scaling is correct for the standalone unsteady heat equations, the scaling breaks the similarity principle for fluid convection. It allowed for a reduction of the simulation time by an arbitrary factor, but lead to errors in the predictions of both the mean and fluctuating temperature fields.

Another type of approach relies on frequency-based decomposition to address the timescale mismatch between the fluid and solid domains. He and Oldfield [18] implemented a hybrid coupling approach based on a time-marching technique for the fluid domain and a frequency-based for the solid domain, with a continuously updating Fourier transform implemented at the interface. This method also has the advantage of directly answering the timescale mismatch by solving the solid region in the frequency domain. Since this work, frequency based approaches have been used frequently for unsteady CHT simulations. Knapke and David [21] used a harmonic balance approach to with a quasi-Newton solver for CHT simulations. They showed that harmonic balance is an effective technique for performing accurate conjugate heat transfer problems with periodic unsteady simulations. This was confirmed by Hodges

[22], who presented a similar method and validated it for an internally cooled turbine blade. Another frequency-based decomposition, the non-linear harmonic method has also been used for CHT simulations. Mehdizadeh et al. [23] extended an existing commercial harmonic code to conjugate heat transfer. They used an updated harmonic equation with the addition of the harmonic source term to update the wall temperature at each timestep and on each side of the thermal interface. Further studies including [24, 16] refined the method and adapted it for multiscale thermal systems.

Aside from frequency-based methods, other decomposition approaches have been used. Białecki et al. [25] proposed a POD decomposition to tackle more efficiently transient heat transfer problems with fixed thermal boundary conditions. They used a combination of a time marching technique for the initial transient and then POD decomposition is used to reduce the dimensionality of the problem. Blanc et al. [26] applied a similar reduced order model to the complete conjugate heat transfer problem. In addition, discrete Green function approaches have been applied to decouple conjugate heat transfer problems with any temperature variations as done in [27, 28]. Discrete Green functions decompose the temperature field into a set of functions independent of the thermal boundary condition. The functions describe the relationship between surface temperature and convective heat transfer, relating heat transfer from each element of the source surface to temperature rise on all other elements of the target surface. This approach allows direct, non-iterative calculation of heat transfer for any temperature distribution, irrespective of thermal boundary conditions.

Eigenanalysis has also been applied to tackle heat transfer problems. Shih and Skladany [29] applied it to transient heat conduction, demonstrating its accuracy and computational efficiency compared to classical implicit and explicit time-marching numerical schemes, particularly for long-duration and large-domain transient problems. Quéméner et al. [30] used modal analysis on advection diffusion problems with time-dependent parameters, achieving a significant computational time reduction compared to the finite elements model, by efficiently selecting influential modes and minimising the error between the reduced and physical models. Other applications can be found in [31, 32, 33]. Eigenanalysis has been also applied to CHT problems by Knupp et al. [34]. They used an integral transform approach to the solution of the problem on conjugate heat transfer. They achieved a significant improvement in convergence rate for a transient two-dimensional incompressible channel flow case.

Finally, when the behavior of the long thermal transient is of interest, the coupling conditions can be loosened to obtain efficient results. Sun et al. [35] proposed a method based on the consideration that for these transients the fluid flow time scales are much shorter than those for the solid heat conduction and therefore the influence of unsteadiness in fluid regions is negligible on the longer thermal transients. Their technique employs iterative procedures and steady CFD calculations to ensure continuity of temperature and heat flux. The procedure allows for defining CFD models at key time points and offers a "frozen flow" option for improved computational efficiency. Maffulli et al. [36] developed a loosely coupled CHT methodology using a source-term based modelling approach and adaptive time stepping. The technique demonstrated comparable accuracy to fully coupled unsteady simulations, but with significantly reduced computational costs. The technique was tested on predictions of turbine thermal loads during fast startup/shutdown cycles.

As demonstrated in the literature overview, achieving efficient CHT simulations is a complex task. The key challenge lies in addressing the interplay between time and length scales in both the metal and the fluid. Simple dimensional arguments indicate that these scales are inherently linked, making it impossible to treat spatial and temporal scale separation independently. In most practical cases, what is desired is an acceleration of the large-scale, slow varying transients of the solid temperature field. Simple techniques such as alterations of the solid properties inevitably affect all length scales simultaneously and ultimately compromise either computational efficiency or physical accuracy. Methods based on orthogonal decompositions of the temperature field seeem better placed to achieve the twin goals of preserving accuracy and improving computational performance of unsteady CHT simulations.

In this paper, we build on the work of [31, 30, 34] by employing a modal decomposition approach for the solid temperature field. A modal basis can represent a given temperature field within a prescribed error with the smallest number of degrees of freedom. A modal basis also inherently preserves the natural relationships between large-scale, slow-evolving features and small-scale, fast-evolving features of the temperature distribution [37]. Since the modes are formally mutually uncoupled, a modal representation reduces the solid domain to a set of uncoupled, single-degree-of-freedom ordinary differential equations, which require only surface integrals to be computed. Additionally, by recognising the linear nature of heat conduction, we show that eigendecomposition provides an effective alternative for handling different scales individually—both in the numerical scheme and in the deliberate manipulation of time constants. We demonstrate a method to selectively modify the behavior of the modes responsible for the time/length scale reconciliation problem. We show that only a small subset of modes should be accelerated and establish an appropriate modal truncation criterion. Finally, we introduce a turbulent resolving grid at the interface to capture the remaining fluctuations

2. Method

This section develops the theoretical framework for the proposed strategy to efficiently solve an unsteady conjugate heat transfer problem.

2.1. Problem specification and governing equations

Consider a conjugate heat transfer problem over a domain Ω composed of the union of subdomains Ω_s and Ω_f. The interface between the subdomains Ω_s and Ω_f is denoted as Γ and the exterior boundaries are Γ_{ext}. The governing equations are the compressible Navier-Stokes (N-S) equations on Ω_f and the unsteady heat conduction equation for Ω_s. This leads to the formal formulation of the CHT problem:

$$\begin{cases} \text{N-S equations} & \text{on } \Omega_f \\ \rho_s c_{p,s}\dfrac{\partial T}{\partial t} = \nabla\cdot(\kappa_s \nabla T) + Q_s & \text{on } \Omega_s \\ T_f = T_s & \text{on } \Gamma \\ \kappa_f \nabla T_f \cdot \vec{n} = \kappa_s \nabla T_s \cdot \vec{n} & \text{on } \Gamma \\ g(\vec{x}, T, \nabla T) = 0 & \text{on } \Gamma_{\text{ext}} \\ T(\vec{x}, 0) = T_0(\vec{x}) & \text{on } \Omega \end{cases} \tag{4}$$

Where Q_s is a heat source, g the boundary condition on the exterior boundary and the subscripts f and s refer to subdomains Ω_f and Ω_s, respectively. The initial condition is given by T_0.

2.2. Modal representation of the heat conduction problem

The unsteady heat conduction problem in Equation 4 can be written in a finite element formulation:

$$\mathbf{M}\frac{d\mathbf{T}}{dt} = -\mathbf{K}\mathbf{T} + \mathbf{G}(t) \tag{5}$$

Considering only natural boundary conditions gives the following expression for the matrices :

$$M_{ij} = \int_{\Omega_s} \rho c_p F_i F_j \, dS \tag{6}$$

$$K^h_{ij} = \int_{\Omega_s} \kappa \frac{\partial F_i}{\partial x_k}\frac{\partial F_j}{\partial x_k} dS \tag{7}$$

$$G^{ij} = \int_{\Gamma,\Gamma_{ext}} F_i \kappa \frac{\partial F_j}{\partial n} dS + \int_{\Omega_s} F_i Q_s \, dS \tag{8}$$

Where F_i are the shape functions.
For the purpose of the following developments, it is useful to state certain general assumptions made about the structure of the fluid solution. It is assumed that the fluid solution is obtained through a finite volume solver with cell

centred variables, so that a straightforward algebraic relation exists between the numerical surface heat flux and linear combinations of a small number of solid surface temperatures with a small number of gas near-wall temperatures. It should be stressed that whereas this assumption appears in the diagrams and in some of the derivations, it is by no means essential. A different structure of the fluid solution, e.g. a discontinuous Galerkin solver with non-comformal discretisation at the element boundary would still express the surface flux as a linear combination of surface solid and fluid temperature, but the expression would involve a larger number of degrees of freedom.
Invoking a general mixed type boundary condition in Equation 9. With $h(x)$ being the thermal law of the wall coefficient and $q_r(x,t)$ a heat flux that is not influenced by the presence of the gas (e.g. radiation) and T_g being the boundary temperature from subdomain Ω_f, yields Equation 10.

$$-\kappa\frac{\partial T}{\partial n} = h(x)\left(T - T_g(x,t)\right) + \beta(x,t) \qquad \text{on } \Gamma_{\text{ext}} \text{ and on } \Gamma \tag{9}$$

$$\mathbf{M}\frac{d\mathbf{T}}{dt} = -\left(\mathbf{K^h} + \mathbf{K^b}\right)\mathbf{T} + \mathbf{G(t)} \tag{10}$$

$$K^b_{ij} = \int_{\Gamma,\Gamma_{ext}} h(x)F_iF_j dS \tag{11}$$

$$G_i = \int_{\Omega_s} F_iQ_s\,dS + \int_{\Gamma,\Gamma_{ext}} \left(h(x)T_g(x,t) - q_r(x,t)\right)F_i\,dS \tag{12}$$

This shows that the matrix **K** is composed of symmetric positive blocks.
Considering the homogeneous part of the system Equation 10, solutions of the following type are sought:

$$\mathbf{T} = \mathbf{Z}e^{-\lambda t} \tag{13}$$

where **Z** is time independent. This yields to the modified eigenvalue problem for the homogeneous part of the system.

$$\lambda\mathbf{MZ} = \mathbf{KZ} \tag{14}$$

The eigenvectors **Z** can be normalised in such a way that

$$\mathbf{Z}^\top\mathbf{MZ} = \mathbf{I} \tag{15}$$

$$\mathbf{Z}^\top\mathbf{KZ} = \mathbf{\Lambda} \tag{16}$$

$$\mathbf{ZU} = \mathbf{T} \tag{17}$$

With **U** being the modal amplitude.
Now returning to the inhomogeneous problem of Equation 5

$$\mathbf{M}\frac{d\mathbf{T}}{dt} = -\mathbf{KT} + \mathbf{G}(t) \tag{18}$$

$$\mathbf{Z}^\top\mathbf{MZ}\frac{d\mathbf{U}}{dt} = -\mathbf{Z}^\top\mathbf{KZU} + \mathbf{Z}^\top\mathbf{G}(t) \tag{19}$$

$$\frac{d\mathbf{U}}{dt} = -\mathbf{\Lambda U} + \mathbf{Z}^\top\mathbf{G}(t) \tag{20}$$

Since the matrix $\mathbf{\Lambda}$ is diagonal, the equations describing the evolution of the modal amplitudes are decoupled. For each mode, a scalar equation needs to be solved for the modal amplitude, with $\mathbf{\Lambda}$ and $\mathbf{Z}^\top$ as inputs.

In practical implementation, the modes are only needed at the boundaries where the scalar product $\mathbf{Z}^\top\mathbf{G}(t)$ will not vanish. This greatly reduces the memory requirements for a simulation as only the boundary values have to be stored instead of the full eigenvector matrix. Additionally, depending on the coupling methodology used, the solution to the eigenproblem of Equation 14 is usually only needed once, for instance if the coupling is done through an inhomogeneous Neumann boundary condition. However, in some cases the influence of the coupling on the mass and conductance matrix is expected to vary greatly during the simulation span, for instance through a varying heat transfer coefficient. For these cases, if the variation of properties with temperature is mild and can be represented with a linearized relation, then the structure of the eigenvalue problem is unchanged, which limits the need to recompute the eigendecomposition again.

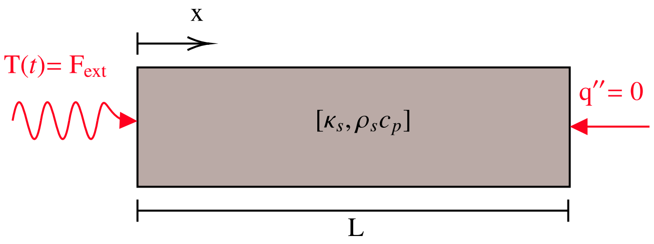

Figure 1: Sketch of the 1D domain with boundary conditions and coordinate system

2.3. *Acceleration techniques*

Modal decomposition (subsection 2.2) decouples the heat conduction equation, inherently enabling targeted acceleration strategies. Previous methods (discussed in subsection 1.1) often introduced errors by altering solid characteristics or accelerating time integration across all scales. In contrast, the present approach leverages the modal basis to selectively accelerate only the slowest thermal modes within the solid domain—those corresponding to long low-energy time scales. This targeted modification minimises the impact on solution accuracy compared to prior techniques while still providing significant computational acceleration.

Concerning the practical ways Equation 20 can be accelerated to statistical steady-state, most of the techniques mentioned in subsection 1.1 can be applied to the modal equations. For example, a harmonic or Fourier formulation can be done on the individual modes. If nonlinear interactions between the modes are neglected it would make the assumptions of the Fourier transform stronger when applied on the decoupled modal equations. While it would be interesting to test the performance of these various methods in the modal context, the current paper will focus mostly on one strategy that arise naturally from the decomposition.

The following subections introduce the proposed acceleration technique and assesses its performance on simple test cases. This is followed by a discussion on the properties of the temperature eigenmodes and the possible truncation of the modal basis.

2.3.1. *One dimensional - Single mode analysis*

To illustrate how the proposed method tackles the problem of the disparity in timescales between the fluid and solid domains, we consider a simple 1D solid domain of length L with constant thermal diffusivity α_s. On one end the solid is submitted to external thermal excitation, similar to the thermal Stokes problem and adiabatic conditions are set on the other end. A sketch of the domain can be found in Figure 1. The domain is discretised into N elements using a finite element approach and temporal advancement is performed using an implicit Euler scheme.

The unsteady heat conduction equation (Equation 4) can be written in non-dimensional form by introdusing the Fourier number Fo, the normalised temperature $\Theta = (T - T_m)/(T_{max} - T_m)$ and the dimensionless coordinate $\xi = x/L$ where T_m is the mean temperature and $T_{\max}$ the maximum temperature.

$$\frac{\partial \Theta}{\partial \mathrm{Fo}} = \frac{\partial^2 \Theta}{\partial \xi^2} \tag{21}$$

With the prescribed boundary conditions, the finite element system can be written as:

$$\mathbf{M}\frac{d\mathbf{\Theta}}{d\mathrm{Fo}} = -\mathbf{K^h}\mathbf{\Theta} + \mathbf{G}(t) \tag{22}$$

And the modal equation is:

$$\frac{d\mathbf{U}}{d\mathrm{Fo}} = \mathbf{\Lambda}\mathbf{U} + \mathbf{Z}^T\mathbf{G}(t) \qquad \text{with} : \mathbf{\Theta} = \sum_i \mathbf{z}_i U_i \tag{23}$$

In the first test case, the prescribed temperature is represented by a sine wave with zero mean, an amplitude of $T_{\max}$ and a dimensionless angular frequency $\tilde{\omega} = 10\pi$. The temperature response of the system at different depths is plotted in Figure 2a, with the initial condition set to the time-averaged value. The curves exhibit the classical exponential decay found in transient heat conduction in a slab, [38]. As explained by Hickling and He [16], due to the nature of the external excitation (a step function modulated by a harmonic function), the initial response of the solid exhibits an overshoot before gradually approaching a steady state. The closer to the interface, the faster the convergence until $\xi = 1$ that takes approximately 1 Fo to reach the steady-state. This behavior is seen also in Figure 2b, which shows the time evolution of the modal amplitudes, U_i. Notably, only the first few modes, those associated with the longest time constants, converge to a steady state over an extended period. It can be seen that the first mode shape needs approximately 1 Fo to reach steady-state, similarly to the direct simulation, in Figure 2a. Thus, in practice, only a limited subset of modes, those with the longest timescales, require acceleration.

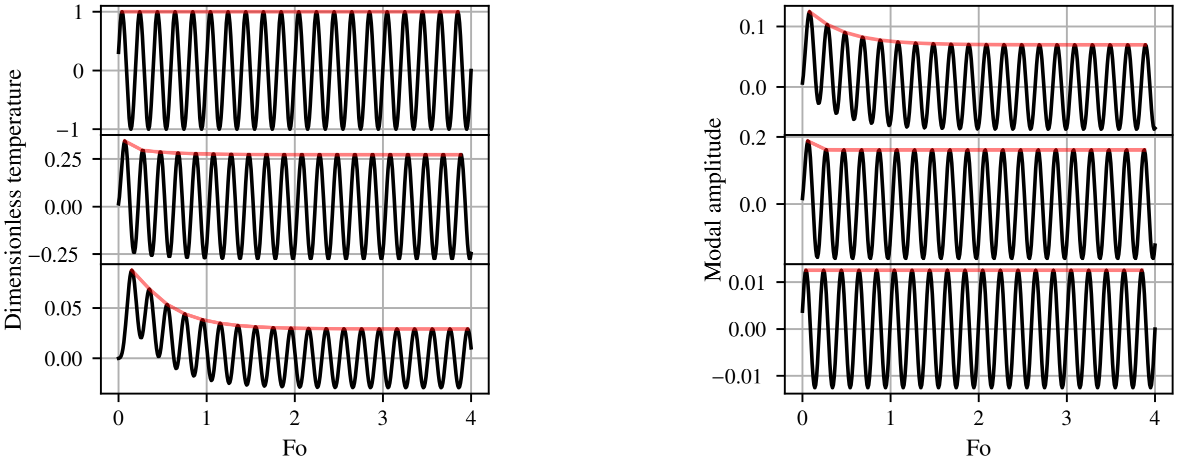

(a) Time trace of the temperature (black line) and upper envelope (red line) at selected locations. From top to bottom: $\xi = [0, 0.3, 0.9]$

(b) Time trace of the modal amplitude (black line) and upper envelope (red line) for selected modes. From top to bottom: U_1, U_2, U_{30}.

Figure 2: Time evolution of the temperature and modal amplitudes for the 1D isolated domain

To gain a deeper understanding of how does the unsteady heat conduction equation behave, we seek an analytical solution to Equation 23 considering a single mode. As the external heat flux $G(t)$ is a sine wave of angular frequency $\tilde{\omega}$ with zero mean, Equation 23 becomes Equation 24 where β, σ are scaling factors and ϕ an arbitrary phase. The subscript has been omitted for clarity.

$$\frac{dU}{d\text{Fo}} = -\lambda U + G(\text{Fo}) = -\lambda U + \sin(\tilde{\omega}\text{Fo} + \phi) \tag{24}$$

The transfer function $H(s)$ of the system is given by Equation 25. For sinusoidal inputs the system acts as a type of low-pass filter with a cut-off frequency of λ.

$$H(s) = \frac{U(s)}{G(s)} = \frac{1}{\lambda + s} \tag{25}$$

The solution of Equation 24 to a harmonic forcing of angular frequency $\tilde{\omega}$ with zero mean is given by Equation 26.

$$U(\text{Fo}) = \frac{\tilde{\omega}\cos(\phi) - \lambda\sin(\phi)}{\omega^2 + \lambda^2} e^{-\lambda\text{Fo}} + \frac{\lambda\sin(\tilde{\omega}\text{Fo} + \phi) - \omega\cos(\tilde{\omega}\text{Fo} + \phi)}{\omega^2 + \lambda^2} \tag{26}$$

Inspecting the terms, the exponential term is the initial transient response similar to the classical transient heat equation problem. The decaying behavior arises from the initial condition because to have steady state a balance in the function's value and its first derivative is necessary. A phase portrait is shown in Figure 3a, it has been initialised with $U(\text{Fo} = 0) = 0$ and $\lambda = 1$. It shows the solution path slowly converging $\{U(0), U'(0)\} = \{0, 0\}$ to its steady-state

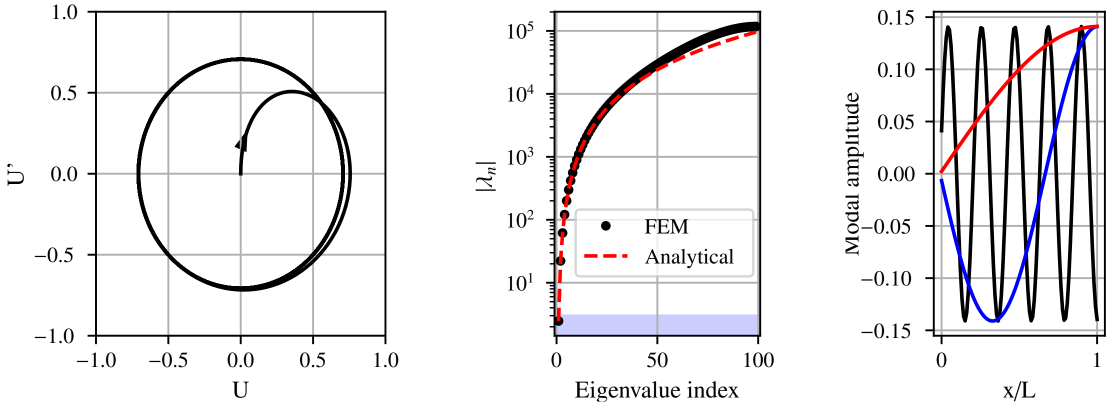

(a) Phase portrait of Equation 24 with initial condition $U(0) = 0$

(b) Eigenvalues and the light blue zone corresponds to $|\lambda_n| < 3$

(c) Selected mode shapes. Red: first mode, blue: second mode, black: 20th mode

Figure 3: Analysis for the 1D domain test case

solution on the circle. Equation 26 explains the slow steady-state convergence of modes with the lowest eigenvalues (longest time constants), as illustrated in Figure 2b, and notably reveals that their decay constants are independent of excitation frequency.

Figures 3b and 3c show the eigenvalues and selected eigenvectors of the problem. For a slab problem formulated in dimensionless variables with the prescribed boundary conditions, the analytical eigenvalues of the Laplace operator are given by [39]:

$$\lambda_n = \left(\frac{(2n-1)\pi}{2}\right)^2 \qquad n = 1, 2, 3, ... \tag{27}$$

Figure 3b shows that the finite element space accurately captures the eigenmodes that are well resolved by the mesh, while the higher-frequency modes are less well resolved, resulting in inaccuracies in the corresponding eigenvalues. Equation 26 showed that the decay of the transient behavior for each mode depends solely on the product of its eigenvalue and the Fourier number. Therefore, the eigenvalues provide insight into which modes require acceleration based on the Fourier number of the simulation, which characterises the allowed simulation time. For example, with an allowable Fourier number of 1 and a target threshold for the decay is 95 % (approximately $\exp(-3)$), any mode with an eigenvalue less than 3 Fo will not have decayed sufficiently, this is illustrated by the light blue region in Figure 3b. Consequently, in the present case, only the first eigenmode has not decayed to the threshold level by Fo = 1, as also visible by Equation 26. This type of analysis allows one to determine a priori which modes need to be accelerated, depending on the total simulation time and a threshold number for the transient to decay to acceptable levels. This is the key advantage of the current targeted acceleration approach; typically, only a few modes require acceleration because the eigenvalues increase rapidly with mode number $\lambda_n \propto n^2$. Furthermore, as shown in Figure 3c, lower eigenvalues correspond to large-scale spatial patterns, confirming that larger temperature fluctuations take longer to approach steady state.

To accelerate the approach to steady state, two direct techniques can be inferred from Equation 26. The first involves scaling the time update by an arbitrary factor β, as done Koren et al. [17]. The second option is to artificially increase the eigenvalue by a factor σ. Equation 28 shows the modified equation for a periodic excitation which has now a non-zero mean, Ψ, where β and σ are scaling factors. The solution of Equation 28 is given in Equation 29, where C is a constant. From Equation 29, it can be concluded that both techniques amplify heat flux fluctuations received by the solid interface, as both frequency and response amplitude are modified proportionally to β or σ. However, there are regimes where one technique is more advantageous than the other.

$$\frac{1}{\beta}\frac{dU}{d\text{Fo}} = -\sigma\lambda U + (\Psi + \sin(\tilde{\omega} + \phi)) \tag{28}$$

$$U(\mathrm{Fo}) = \frac{\Psi}{\sigma\lambda} + Ce^{-\sigma\lambda\beta\mathrm{Fo}} + \frac{\sigma\lambda\sin(\tilde{\omega}\mathrm{Fo}+\phi) - \tilde{\omega}/\beta\cos(\tilde{\omega}\mathrm{Fo}+\phi)}{\tilde{\omega}^2/\beta^2 + \sigma^2\lambda^2} \tag{29}$$

Typically, the eigenvalues of the modes that require acceleration are smaller than $\tilde{\omega}$. The lowest dimensionless frequency resolved by the simulation is $\tilde{\omega} = 1/\mathrm{Fo}$ and the modes that require acceleration have λ Fo $\ll 1$, which leads to $\lambda \ll \tilde{\omega}$. Therefore, altering the eigenvalue through the σ factor has lower influence on the temporal solution once statistical steady-state has been reached compared to modifying β, according to Equation 29. Figure 4a illustrates the comparative performance of a β and a σ scaling using λ_1 from Equation 27 and $\tilde{\omega} = 10\pi$, leading to $\tilde{\omega}/\lambda_1 \gg 1$. Analysis of the upper envelope of the signal demonstrates that while both β and σ modifications improve convergence rates, $\beta-$alterations proportionally modifies the amplitude of the response's leading term, for the chosen ratio $\tilde{\omega}/\lambda_1$. In contrast, σ-modifications primarily influence the solution's minor term as long as $\tilde{\omega}$ is greater than λ which is precisely the modal regime targeted for acceleration, as depicted Figure 3b.

On the other hand, when the forcing signal has some content at lower frequency than the eigenvalue ($\lambda > \tilde{\omega}$) or if the forcing has a nonzero mean, the steady state time-averaged solution $\bar{U}$ is given in Equation 30.

$$\bar{U} = \frac{\Psi}{\sigma\lambda} \tag{30}$$

Figure 4b compares β and σ alterations for a case when the forcing signal is constant in time, $\tilde{\omega}/\lambda \ll 1$. As expected, altering the stiffness properties of the system through the eigenvalue will impact the steady-state time-averaged solution.

To avoid this issue, a Selective Frequency Damping (SFD) approach is used. SFD is a technique coming from system control theory that aims to accelerate the transient decay of specific frequency components in a system while preserving the dynamics of others. SFD has notably been used in the context of CFD simulations to accelerate the convergence of the flow equations, [40, 41, 42]. The approach consists of adding a linear forcing term to Equation 24 in order to achieve frequency-selective damping via coupled low-pass filtering and high-frequency feedback. The modified equation is given in Equation 31 where U_{LP} is a low-pass filtered solution. The modified differential equation written for an arbitrary forcing $G(\mathrm{Fo})$ with mean Ψ is given in Equation 31.

$$\frac{dU}{d\mathrm{Fo}} = -\lambda U + G(\mathrm{Fo}) - \chi_a\left(U - U_{LP}\right) \tag{31}$$

Here, $\chi_a > 0$ is a feedback gain parameter, effectively increasing the effective decay rate of the higher frequencies to $\lambda + \chi_a$, thereby speeding up the approach to the steady state. The steady state remains unchanged because the additional term vanishes when considering the time-averaged system. To keep a consistent notation we will write the feedback parameter as $\sigma = 1 - \chi_a/\lambda$. The low-pass filtered solution U_{LP} can be accelerated through the β parameter as done in Equation 28. Figure 4c plots the different acceleration techniques for a forcing with a finite mean amplitude superimposed with a higher frequency signal and the initial condition is kept at $U(0) = 0$. From this point onward, the β modifications are applied exclusively to the low-pass filtered solution U_{LP}, whereas the σ modifications are applied to the high-pass component, defined as $U - U_{LP}$. It can be seen that the unmodified system needs similar time to reach the steady state compared to Figure 4a as expected because the decay constant is not a function of frequency. The modified equations converge significantly faster than the unmodified system without loss in accuracy in both the mean and fluctuating components.

2.3.2. Coupled domains - Complete thermal field analysis

The next test case involves two coupled one-dimensional domains, each governed by the unsteady heat equation, as illustrated in Figure 5. This configuration has been previously analyzed by Koren et al. [17], and the thermal properties of both domains, shown in Table 1, match those presented in their study. The domains are discretised using finite elements and explicit time integration is used. This test case evaluates whether the proposed acceleration technique influences a coupled system with significantly lower thermal capacity. The outer boundaries are subject

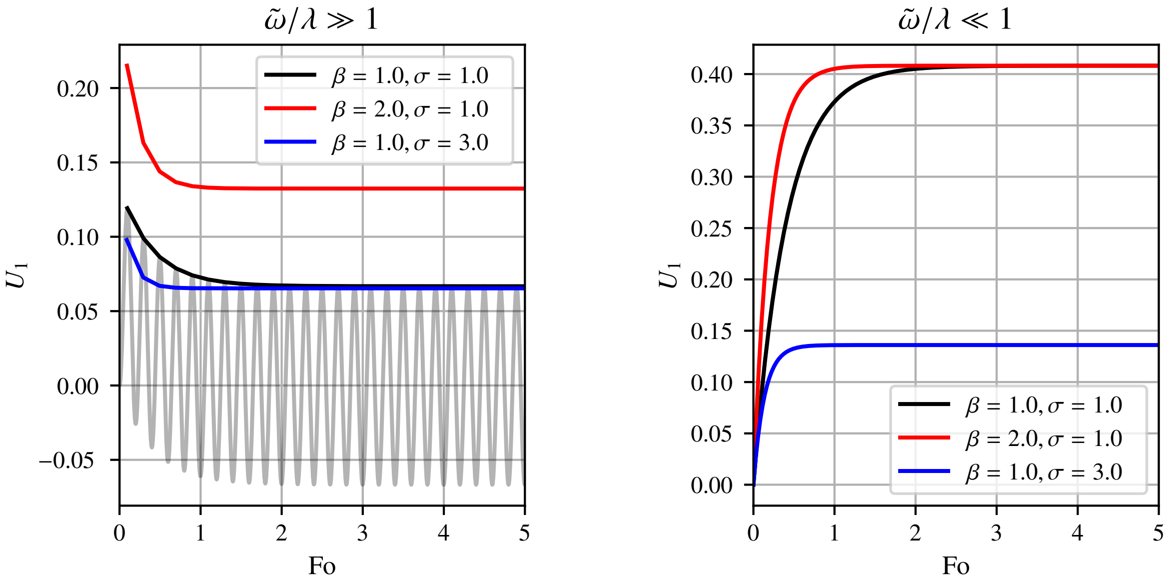

(a) Illustration of different acceleration techniques for $\tilde{\omega}/\lambda \gg 1$ via upper envelope, with signal time trace for reference case.

(b) Illustration of different acceleration techniques for $\tilde{\omega}/\lambda \ll 1$.

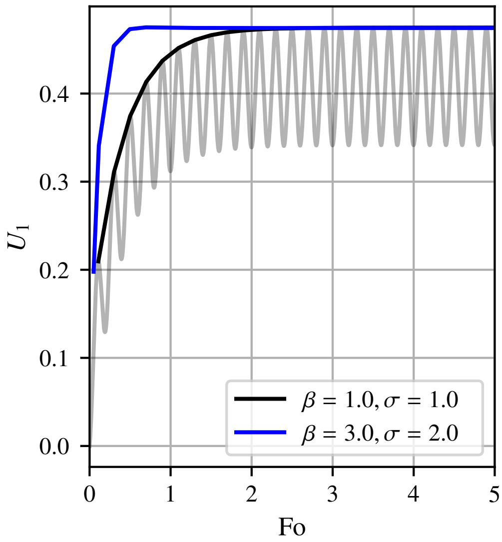

(c) Illustration of the SFD technique via upper envelope, with signal time trace for reference case. The forcing signal has a nonzero mean and oscillating component at $\tilde{\omega}/\lambda \gg 1$.

Figure 4: Illustrations of acceleration techniques for the 1D domain test case

to Neumann boundary conditions. Here, the coupling is modeled as convective, with the heat flux at the interface computed using Newton's law of cooling, assuming a heat transfer coefficient of $h = 10$ W/(m^{2}K). This condition makes the system similar to real life scenarios, such as a turbine with a metal casing surrounded by insulating material. Focusing on the solid s in Figure 5, the combination of Robin and Neumann boundary conditions makes the domain less stiff, leading to lower eigenvalues compared to the case in subsubsection 2.3.1, which was subjected to a Dirichlet boundary condition. These lower eigenvalues are expected to require a longer time to reach steady-state than those in subsubsection 2.3.1, making the need for acceleration more pronounced in this case.

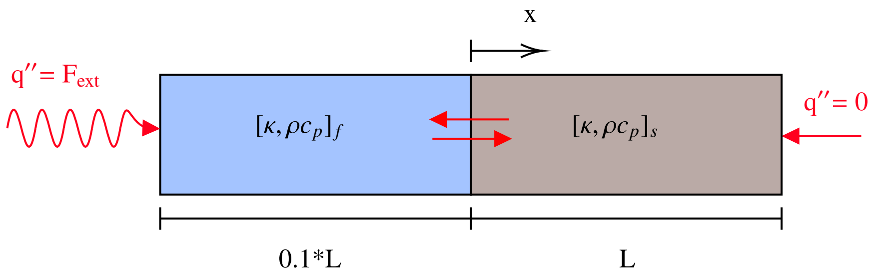

Figure 5: Sketch of the system of two solids with boundary conditions and coordinate system

Table 1: Thermal properties of the coupled domains

	κ [W/(mK)]	ρc_p[J/(m^{3}K)]	L [m]	N[−]
Domain s	7.3	4500*570	0.005	100
Domain f	0.158	1738*3.65	0.0005	100

The signal imposed at the boundary of domain f is more realistic than the one used in subsubsection 2.3.1. It consists of a series of harmonics with random phase. The spectrum is made of a plateau until 1 Hz after that a $-5/3$ power law is applied to the higher frequencies. As shown in Table 1, the length of the domain where the excitation force is applied has also been divided by 10, minimising the damping of high-frequency content reaching the interface. The system has one eigenvalue lower than the highest dominant forcing frequency that is 1 Hz. The corresponding eigenvector is the constant mode, which will therefore require acceleration. The constant solid temperature mode has a non vanishing eigenvalue because of the Robin boundary condition a the interface with the fluid domain. Two acceleration levels have been tested using the SFD technique, one with the acceleration factors σ and β set to $1/\lambda_1$ and the other with an intermediate factor set to $0.1/\lambda_1$, where λ_1 is the eigenvalue of the constant mode.

The results are shown in Figure 6. The bar levels represent the time required to reach steady-state for the thermal field at different levels within the solid domain. The interface corresponds to $x/L = 0$. Three simulations are compared, the first one is the original non-accelerated system, in dark grey. In blue is the accelerated system, with acceleration factor set to $1/\lambda$. Finally, in red is the intermediate acceleration level. It can be seen that the acceleration factor has a significant impact on the approach to steady-state of the system. The time required to reach steady-state is reduced by a factor of 10 and 70 for the intermediate and high acceleration levels, respectively.

The error made in the standard deviation through the acceleration factors is shown in the line plots in Figure 6. The dashed lines correspond to the relative error in the standard deviation while the solid line is the error in the standard deviation relative to the standard deviation at the interface, i.e. the maximum amplitude. The relative error has a maximum of 2.5 % and 13 % for the intermediate and high acceleration levels, respectively. The error is more pronounced towards the far end of the solid domain, where the low-frequency modes are more dominant. The error relative to the interface fluctuations is less than 3 % for the high acceleration level and less than 0.7 % for the intermediate acceleration level. Showing that compared to the interface fluctuations, the error remains low.

In conclusion, this section showed briefly some capabilities of the proposed approach in terms of reducing the time required to reach steady-state. It proved to have a low impact on the steady-state mean and fluctuating components of the solution while improving the convergence time greatly, as long as most of the energy is not contained close to the pole of the transfer function. At the pole, the error made directly correlates with the acceleration factor. As stated at the beginning of this section, the modal approach is not limited to the acceleration technique presented here. It can be used with most of the acceleration techniques presented in subsection 1.1. The main advantage of the modal decomposition is that it allows for a targeted acceleration. This is in contrast to the other acceleration techniques,

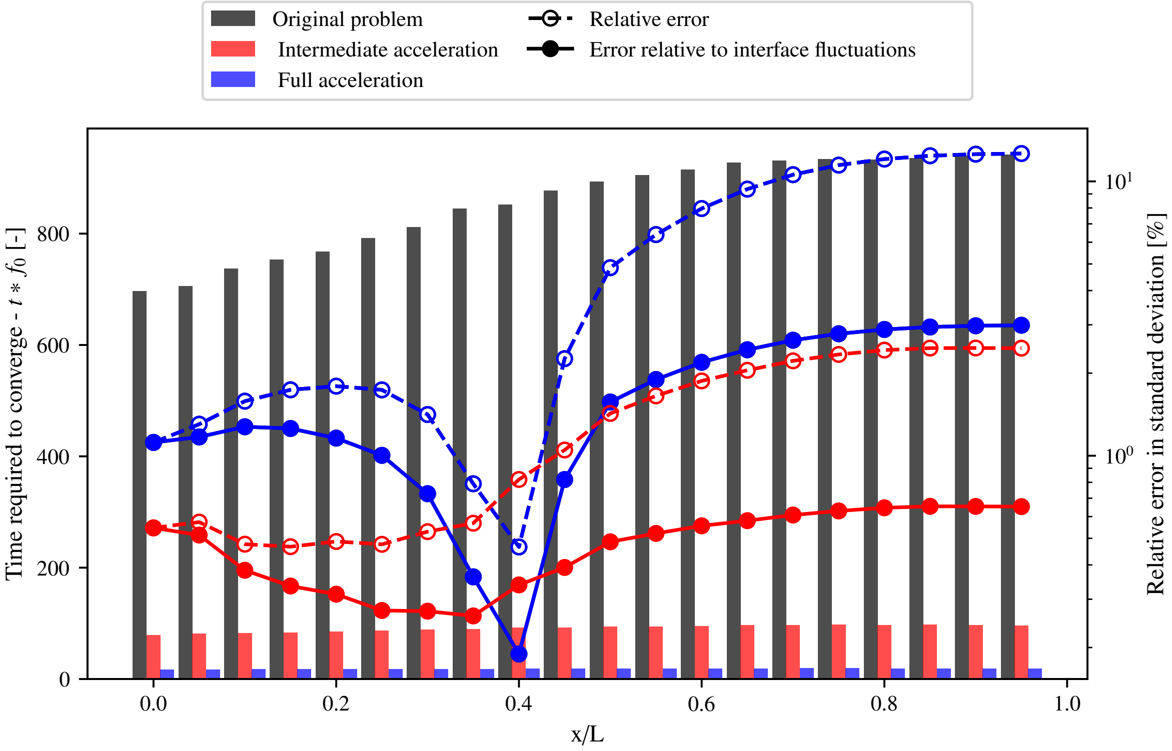

Figure 6: Convergence time and relative error in standard deviation for the solid s of the system of two solids. The interface corresponds to $x/L = 0$. The bar levels represent the convergence time for the thermal field at different depths within the solid s (corresponding axis is on the left-hand side). The dashed lines correspond to the relative error while the solid line is the error in the standard deviation relative to the interface standard deviation (corresponding axis is on the right-hand side).

which modify the entire system.

2.4. *Solving complex multiscale heat conduction problems*

Having demonstrated the advantages of the modal decomposition to speed up the approach to steady-state of unsteady CHT problems, it is important to understand the properties of the temperature eigenmodes. This section will delve into the spatial distribution of the eigenmodes and the practical implementation of the modal method for more complex scenarios beyond the simple 1D cases discussed in subsection 2.3.

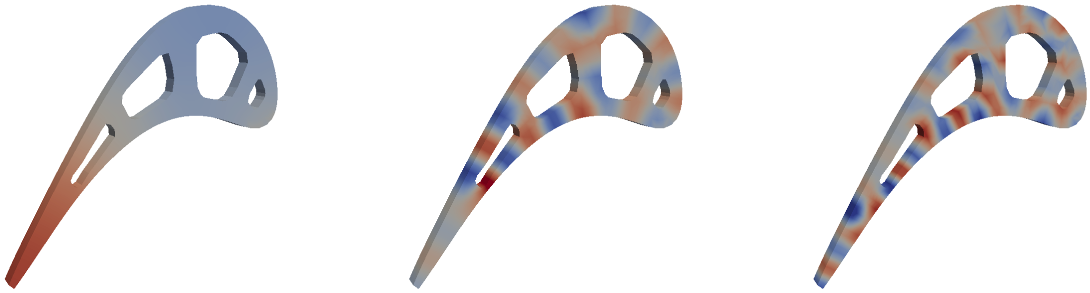

(a) (b) (c)

Figure 7: Temperature modes for a typical turbine section. The eigenvalue increases from left to right and the color scale is symmetrical around zero with red being positive and blue negative.

2.4.1. *Timescale selection and truncation of the modal basis*

Figure 7 displays three eigenmodes for a typical turbine blade section, with the eigenvalue magnitude increasing from left to right. Each eigenmode corresponds to a specific timescale, which is inversely proportional to its eigenvalue. The timescale determines the spatial extent of the mode, directly related to its penetration depth. The mode in Figure 7c exhibits more localized features, while the mode in Figure 7a demonstrates a broader, global trend. In practical scenarios involving complex three-dimensional geometries, it is neither feasible nor necessary to retain a large modal basis during a simulation. Additionally, high-frequency modes are often physically unrealisable because they are dominated by the discretisation error of the method that was used to build the mass and conductivity matrix. Therefore, to achieve optimal efficiency it is beneficial to operate in practice with a truncated modal basis. Truncating the modal basis comes with two main advantages. First, it reduces interpolation errors, particularly for high-frequency or purely numerical modes that are discarded. Second, when performing eigenanalysis on a large system, various algorithms can efficiently compute a subset of the eigenvalues and eigenvectors, such as those with the lowest magnitude.

The selection of time scales and truncation of the modal basis is a critical step in the analysis process. Only the scales that can be resolved by the simulation should be considered. One important factor to consider is the time evolution of slow modes. These modes might exhibit time scales longer that the simulation and may have minimal impact on the overall behaviour of the system within the given computation length. Consequently, including them in the analysis may not be necessary for obtaining accurate results. By carefully considering these factors, an appropriate selection and truncation of the modal basis can be achieved. This enables an efficient and accurate analysis of the system while balancing computational constraints and the need for reliable results.

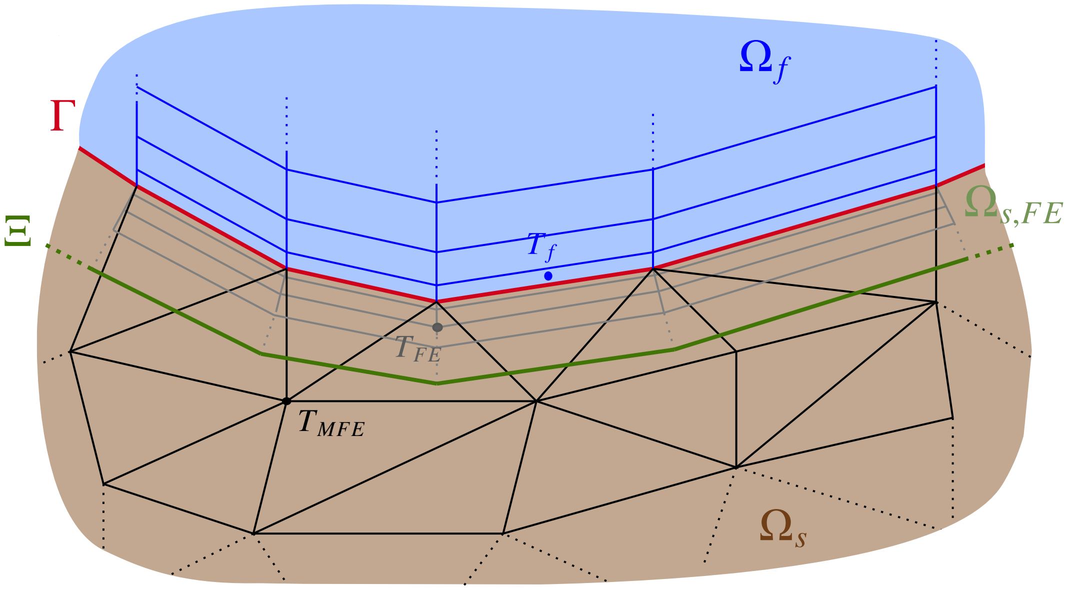

Figure 8: Partition of solid degrees of freedom near an interface boundary in a conjugate heat transfer problem. Γ is the interface between Ω_s and Ω_f. Ξ is the interface between Ω_s and $\Omega_{s,\mathrm{FE}}$.

2.4.2. *Treatment of the residual modal flux*

The truncation of the modal basis results in higher-order frequencies not being captured by the modal decomposition. This residual flux is expected to have a small penetration depth. Therefore, to capture it we propose using a finite-element grid of relatively small thickness compared to the overall thickness of the solid domain. This local grid is referred to as the *FE* solution.
A sketch of the different grids used is available in Figure 8. The body-following grid (in blue) represents the classical cell-centered CFD mesh solving for T_f, the coarser grid (black lines, T_{MFE}) corresponds to the node-based modal grid defined on Ω_s, referred to as the *MFE* solution, used to capture the large scale thermal field and drive it to statistical steady-state. The finer grid (in light grey, T_{FE}) is the node-based *FE* grid, defined on $\Omega_{s,\mathrm{FE}} \in \Omega_s$. Finally, the interface between Ω_f and Ω_s is noted Γ while the remaining interface between Ω_s and $\Omega_{s,FE}$ is Ξ

The *FE* grid is directly extruded from the normal at the interface Γ due to its conduction-dominated nature, see [13]. This technique avoids the requirements of generating manually an additional mesh and as well as the overheads related to separate data structures for the solid grid and provisions for interpolation of temperatures and fluxes between the two grids. The *FE* grid solves the unsteady heat equation using a finite element approach with local geodesic coordinates (ξ, η, ζ). The equivalent equations are available in Equation 32 (2D) and Equation 33 (3D), under the approximation of a small penetration depth and a smooth surface. Further developments and assumptions for the Laplace operator in geodesic coordinates are available in Appendix A.

$$\text{2D:} \qquad \frac{\partial T}{\partial t} = \alpha\left(\frac{\partial^2 T}{\partial \chi^2} + \frac{\partial^2 T}{\partial \eta^2} + \frac{1}{R_c}\frac{\partial T}{\partial \eta}\right) \tag{32}$$

$$\text{3D:} \qquad \frac{\partial T}{\partial t} = \alpha\left(\frac{\partial^2 T}{\partial \chi^2} + \frac{\partial^2 T}{\partial \eta^2} + \frac{\partial^2 T}{\partial \zeta^2} + \frac{1}{R_c}\frac{\partial T}{\partial \zeta}\right) \tag{33}$$

where $\frac{1}{Rc}$ is the local harmonic mean curvature of the surface and α is the thermal diffusivity.

For the domain $\Omega_{s,\mathrm{FE}}$, the overlap between the *MFE* and the *FE* field is handled by solving the unsteady heat conduction equation for the combination $(T_{FE} + T_{MFE})$. Written in global coordinates for clarity, the compatibility equation is:

$$\rho c_p \frac{\partial (T_{FE} + T_{MFE})}{\partial t} = \kappa \left(\frac{\partial^2}{\partial x^2} + \frac{\partial^2}{\partial y^2} + \frac{\partial^2}{\partial z^2} \right) (T_{FE} + T_{MFE}) \tag{34}$$

The coupling strategy applies a Dirichlet boundary condition to the fluid side while a Robin boundary condition is applied on the solid solution. This approach was proven to be stable by Giles [43]. This give the following boundary conditions at the interface Γ between Ω_s and Ω_f:

$$-\kappa \frac{\partial}{\partial n} (T_{FE} + T_{MFE}) = h(x) \big((T_{FE} + T_{MFE}) - T_g(x,t) \big) + \beta(x,t) \qquad \text{on } \Gamma \tag{35}$$

The weak form of the equation is obtained by multiplying by a test function F_i and integrating over the *FE* domain $\Omega_{s,\mathrm{FE}}$:

$$\rho c_p \int_{\Omega_{s,\mathrm{FE}}} F_i \frac{\partial}{\partial t} (T_{FE} + T_{MFE}) \, d\Omega = \kappa \int_{\Omega_{s,\mathrm{FE}}} F_i \frac{\partial^2}{\partial x_k \partial x_k} (T_{FE} + T_{MFE}) \, d\Omega \tag{36}$$

Integrating by parts yields and describing the thermal field with the shape functions of the *FE* grid:

$$\begin{aligned} \rho c_p \left(\int_{\Omega_{s,\mathrm{FE}}} F_i F_j d\Omega \right) \frac{\partial T^j_{FE}}{\partial t} = & -\kappa \left(\int_{\Omega_{s,\mathrm{FE}}} \frac{\partial F_i}{\partial x_k} \frac{\partial F_j}{\partial x_k} d\Omega \right) T^j_{FE} + \kappa \int_\Gamma F_i \frac{\partial}{\partial n} (T_{FE} + T_{MFE}) \, dS \\ & + \kappa \int_\Xi F_i \frac{\partial}{\partial n} (T_{FE} + T_{MFE}) \, dS - \rho c_p \int_{\Omega_{s,\mathrm{FE}}} F_i \frac{\partial T_{\mathrm{MFE}}}{\partial t} d\Omega - \kappa \int_{\Omega_{s,\mathrm{FE}}} \frac{\partial F_i}{\partial x_k} \frac{\partial T_{\mathrm{MFE}}}{\partial x_k} d\Omega \end{aligned} \tag{37}$$

Substituting the boundary condition

$$\begin{aligned} \rho c_p \left(\int_{\Omega_{s,\mathrm{FE}}} F_i F_j d\Omega \right) \frac{\partial T^j_{FE}}{\partial t} = & -\kappa \left(\int_{\Omega_{s,\mathrm{FE}}} \frac{\partial F_i}{\partial x_k} \frac{\partial F_j}{\partial x_k} d\Omega + \int_\Gamma h(x) F_i F_j dS \right) T^j_{FE} + \int_\Gamma F_i \left(h(x) \left(T_g - T_{MFE} - T_{FE} \right) + \beta \right) dS \\ & + \kappa \int_\Xi F_i \frac{\partial}{\partial n} (T_{FE} + T_{MFE}) \, dS - \rho c_p \int_{\Omega_{s,\mathrm{FE}}} F_i \frac{\partial T_{\mathrm{MFE}}}{\partial t} d\Omega - \kappa \int_{\Omega_{s,\mathrm{FE}}} \frac{\partial F_i}{\partial x_k} \frac{\partial T_{\mathrm{MFE}}}{\partial x_k} d\Omega \end{aligned} \tag{38}$$

Equation 38 shows that the surface perturbation temperature field is driven by the gas temperature reduced by the modal contribution to the solid temperature. The left-hand side and the first two terms on the right-hand side of Equation 38 represent the usual mass and conductivity matrix for the finite element problem in the surface layer $\Omega_{s,FE}$. The remaining terms contain the modal temperature field and its derivatives weighted by the shape functions of the surface finite element space and represent forcing terms. The functional form of these terms also indicates that the temperature mode shapes are only needed at the numerical integration points of the surface layer grid and its boundary. Alternatively, if the modal flux at the interface Ξ is assumed to be exact, the correction terms could be neglected, allowing the thermal field within the thin layer domain to be entirely described by the FE solution, overriding the *MFE* field. This assumption makes the *FE* implementation more straightforward, as the modal field is only used to provide the boundary conditions for the *FE* solution.

The extent of the *FE* domain should be chosen according to the frequency range present at the interface as well as the frequency range that the remaining modal basis is able to capture. As an example, we can study the error made by a coarse truncated modal basis as a function of the surface layer extent δ_{FE}. For that purpose, the problem of subsubsection 2.3.1 is studied again with a harmonic external forcing. The reference solution is a finite element solution with a grid resolution able to capture well the forcing. On the other hand, the grid for the modal basis is purposefully coarse, with five grid points within $[0, \delta_P]$. Finally, the *FE* grid has the same resolution as the reference solution. Figure 9 shows the relative energy error with the thin layer extend and the modal truncation level. As expected, the error decreases with the thin layer extend. The slope of the error is greater closer to the interface where the higher density captures better the fluctuations until $\delta_{\mathrm{FE}}/\delta_P \approx 1$ where the slope decreases. The error is also dependent on the truncation level of the modal basis. For this case, omitting half of the modes introduces a relative error less than 1%. However, the error increases exponentially with further truncations. Finally, the case where the *FE* solution overrides the *MFE* solution is plotted using the dotted line in Figure 9 with 70% of the modes kept. When the *FE* grid does not extend far enough within the solid, the error made by the modal solution invalidates the assumption and therefore the model performs worst. However, when $\delta_{FE}/\delta_P \gtrapprox 3$, neglecting the additional terms offers similar level of performance.

2.5. Time integration

Advancement in time for the solid (*FE* and *MFE* solution) and fluid equations is carried out using a formally second-order accurate semi-implicit scheme, with implicit iterations based on a dual-time stepping formulation, originally proposed by Jameson and Shankaran [44]. Convergence in pseudo-time is further accelerated using techniques such as local time stepping, residual smoothing, low-Mach number preconditioning. More details on the acceleration techniques implemented can be found in [45].

On top of the intrinsic advantages of a dual-time scheme such as improved stability or increased efficiency, directly coming from the use of implicit time integration schemes while maintaining stability and convergence properties typically associated with explicit schemes, the dual-time framework is advantageous for unsteady problems with multiple time scales, such as CHT problems. It allows for the separation of these scales, enabling each domain to be resolved appropriately without the need for excessively small physical time steps. The physical time-step selection can be based on physical considerations alone, regardless of numerical stability considerations, as numerical stability is managed by the pseudo-time integration process.

With this scheme, both domains are coupled within each inner iteration and the criterion for both system to have converged to the desired tolerance is enforced. This allows to reduce greatly the temperature discontinuity coming from the solid-fluid coupling, [43].

2.6. Numerical implementation of the flow solver

The flow equations in Equation 4 are solved using the code H4X [46, 47, 48, 13]. It is a cell-centered finite volume code based on a multiblock grid arrangement. The flow field is represented by the viscous variables: velocity, temperature and pressure and the equations of motion for a compressible fluid are solved in conservative form. The spatial discretisation is third-order accurate in space for the inviscid fluxes. Third-order accuracy is achieved on a compact stencil by using variable extrapolation. No limiter is applied to the vorticity and entropy fields. The extrapolation is based on weighted least-square gradients. The gradient stencil contains all the face neighbors of each cell. For the purpose of variable extrapolation onto a cell interface, the gradient stencil is biased by removing the contributions from the neighbor on the other side of the interface. The numerical fluxes are adapted to low Mach numbers and a modified pressure flux is employed, [46]. The viscous fluxes are evaluated using a second-order discretisation. The code is parallelised by partitioning the blocks of the multiblock grid among the available MPI ranks. Within each rank, block operations are parallelised using OpenMP. Computations and communications are overlaid to hide the latency of the network fabric.

The modal portion of the conjugate solver is done using the `FENICSX` library and the eigenmodes are computed using the `SLEPc` library.

3. Results

In this section, the unsteady CHT method described is applied to two three-dimensional test cases. Both test cases are first validated with reference data and then the acceleration technique is analysed.

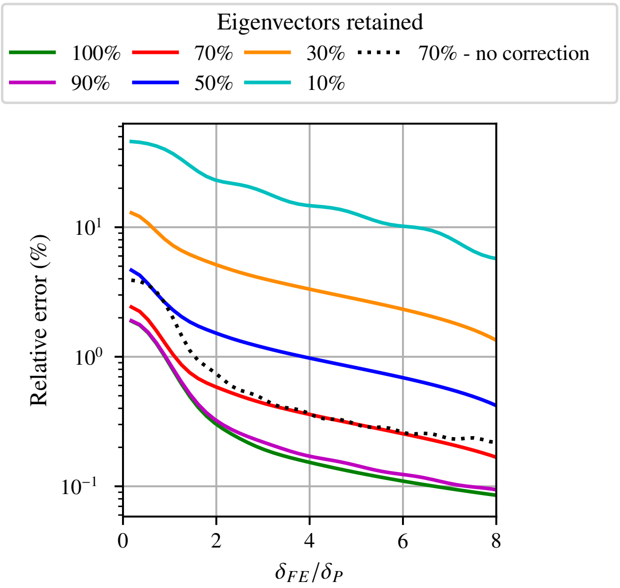

Figure 9: Relative error with the thin layer extend and the modal truncation level for the problem in subsubsection 2.3.1. The thin layer extend δ_{FE} is normalised by the characteristic penetration depth δ_P

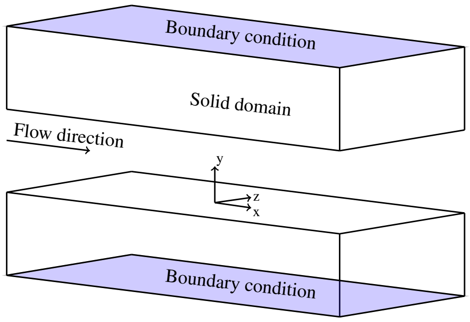

Figure 10: Turbulent channel flow case and coordinate system

3.1. Conjugate channel flow case

The first test case considered is a fully developed turbulent channel flow with conducting walls, illustrated in Figure 10. With turbulent channels being one of the most fundamental test cases in anisotropic turbulence, a great deal of knowledge has been gained on the flow dynamics over a large range of regimes. The numerical solver H4X has been validated for channel flows under different flow regimes in terms of mean and fluctuating velocity quantities, as detailed in [47]. High-resolution conjugate heat transfer simulations in channel flows have been conducted by Flageul et al. [49], Tiselj et al. [50] and Tiselj and Cizelj [15], among others. This test case is used to validate the different solution approaches for the solid domain—including a directly coupled finite element method, a coupled modal-finite element, and an accelerated procedure—against existing reference data.

3.1.1. Numerical setup

A channel flow is characterised by the channel height, 2δ as well as the streamwise and spanwise domain lengths, L_x and L_z. The flow is simulated between two viscous walls, with periodic boundaries applied in the streamwise and spanwise directions. To maintain a constant mass flow in the channel, an artificial body force is introduced. The solid domains have a thickness of δ and with Neumann thermal boundary condition applied at the far end to balance the energy dissipated by the fluid. The Reynolds number Re_τ, based on the friction velocity and the channel half-width investigated, is 150 at a Mach number $M = 0.1$. The Prandtl number is 0.71. The fluid-solid ratio of thermal conductivities and thermal diffusivities is set to 1, to have a significant effect of convection and conduction coupling at the interface, [49].

The computational domain size in the streamwise and spanwise directions is $(8\pi\delta,\ 4/3\pi\delta)$, found by Kim et al. [51] to be enough for the flow variables to become uncorrelated at maximum streamwise and spanwise separation. The grid size is (256×144×128) with a grid stretching in the wall-normal direction detailed in [52]. To capture the physics, the first cell is in the viscous sub-layer, $\Delta y^+ O(1)$ and having $\Delta x^+ O(10)$ and $\Delta z^+ O(5)$ is sufficient to resolve small-scale structures near the walls. The initial condition for the fluid was taken from an isothermal case and the solid was initialised from the steady-state solution. The simulation was run until the first and second moment of the temperature converged in both domains and then statistics have been computed for 10 flow-through times.

Table 2: Computational parameters for the turbulent channel flow simulation

Re_τ	(N_x, N_y, N_z)	$\min(\Delta y^+)$	$(\Delta x^+,\Delta z^+)$
149.2	(256,144,128)	0.23	(14.52, 4.71)
M	Pr	κ_f/κ_s	α_f/α_s
0.1	0.71	1	1

The conjugate channel flow serves as a benchmark for the different modelling strategies used for the solid domain. Firstly, a finite element approach for the directly coupled conjugate solution is used, and this solution is referred to as the *FE* solution. The finite element grid has the same resolution in the harmonic directions as the fluid mesh in Table 2 and the resolution is higher in the wall-normal direction, $N_{y,s} = 144$ for both domains. Then a combined solution strategy is also introduced, labeled *CFE* solution for combined finite element. The *CFE* has a local finite element grid that spans 10% of the overall thickness of the solid domain and maintains the *FE* mesh density, this thickness was chosen because, the amplitude of the fluctuations is expected to have diminished by a factor $1/e$ at that depth. A modal mesh complements the finite element mesh. The resolution $N_{x,s} = 64$, $N_{y,s} = 36$, $N_{z,s} = 32$ and the truncation threshold is set to 70 % of the total energy. A third strategy is employed, labeled *CFEA* solution, for combined finite element accelerated. The *CFEA* solution has the same grid arrangement and resolution as the *CFE* solution, but the acceleration factors σ and β are set to 2.0 for the first twenty eigenmodes.

Figure 11 and Figure 12 show the mean temperature relative to the interface temperature in wall units, θ^+, and standard deviation profiles, θ^+_{rms}. The figures compare the results from Flageul et al. [49] with the three modeling strategies proposed. For the *FE* solution, although a small discrepancy is seen towards the middle of the channel for the mean flow and the RMS fluctuations are slightly underpredicted at the interface, the general agreement in both domains validates the accuracy of the present code. The *CFE* solution features the same discrepancies as the *FE* solution and in addition the RMS fluctuations are underpredicted at the far end of the solid domain. This is due to the modal truncation and coarser mesh used. Overall, the alignment of this approach with other curves demonstrates its effective implementation. Finally, the *CFEA* solution shows good agreement for the mean value and the RMS fluctuations. However, the modal fluctuations are underpredicted at the far end as a result of the acceleration factor making the eigenvectors stiffer and therefore the fluctuations' amplitude will decrease.

3.2. Pipe flow case

The turbulent channel flow case validated the ability of the solver to accurately handle conjugate heat transfer using different solution strategies. However, due to the limited large-scale temperature fluctuations, the transient behaviour of the temperature field was not very pronounced.

This second test case consists of a pipe in crossflow, as illustrated in Figure 13a. The pipe is subjected to an internal longitudinal flow and an external crossflow which are at different mean temperatures. This configuration serves as a fundamental example of crossflow heat exchanger operation and can provide a first-order approximation of the leading edge of an internally cooled turbine. This test case is particularly relevant to benchmark the proposed method because, when the pipe operates in the shedding regime, periodic fluctuations in heat transfer occur. To ensure the formation of a fully turbulent vortex street, the outer flow is characterised by a Reynolds number of $Re_D = 5000$, based on the tube's outer diameter. The Mach number is set to 0.1. The inner flow is characterised by a Reynolds number of $\mathrm{Re}_{D,\mathrm{in}} = 4500$ based on the pipe inner diameter while the temperature is set to be twice the outer temperature. The turbulence intensity for both inner and outer flow is set to 5%. The thickness of the pipe is set to 20% of its radius. The Prandtl number is 0.71 and the ratio of thermal diffusivities α_f/α_s is 9.

The main source of thermal excitation on the outside of the pipe will come from the vortex shedding. The dominant shedding frequency is set by the Strouhal frequency $\mathrm{F}_{\mathrm{Str}}$. The depth at which the amplitude of the temperature

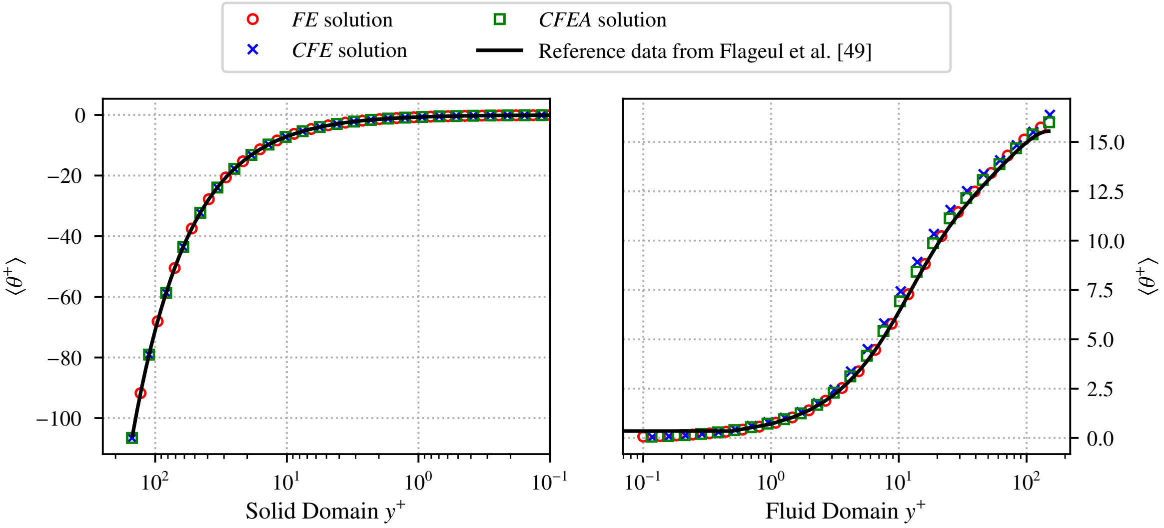

Figure 11: Mean temperature profiles for the conjugate channel flow case. The symbols do not match the mesh used.

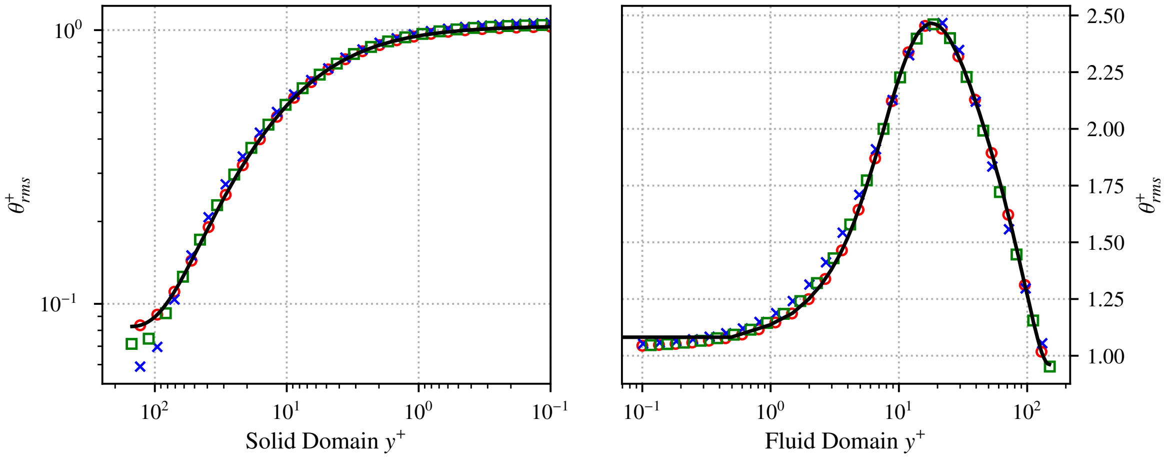

Figure 12: Temperature fluctuation profiles for the conjugate channel flow case. The black line represents the reference data from [49]. Symbols are defined in Figure 11 and do not correspond to the mesh used.

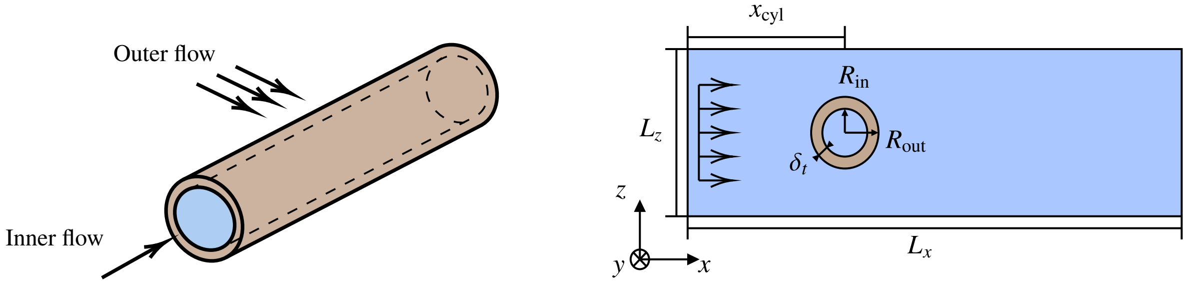

(a) Sketch of the pipe flow case

(b) Detail of the computational domain and coordinate system

Figure 13: Pipe flow case and computational domain.

fluctuation is reduced to roughly 95% of its surface value is:

$$\delta_{P,95\%} = 3\delta_P = 3\sqrt{2}\sqrt{\frac{\alpha_s}{2\pi F_{\text{Str}}}} = 3\sqrt{2}\sqrt{\frac{2\alpha_s R_{\text{out}}}{2\pi \text{Str} U}} = 3\sqrt{2}\sqrt{\frac{4R_{\text{out}}^2}{2\pi \text{Re Str Pr}}\frac{\alpha_s}{\alpha_f}} = 3\sqrt{2}\sqrt{\frac{2(\delta_t/0.2)^2}{\pi \text{Re Str Pr}}\frac{\alpha_s}{\alpha_f}} = 0.215\,\delta_t \tag{39}$$

The fluctuations are expected to extend approximately 20 % of the pipe thickness, allowing for a significant penetration of the temperature fluctuations into the solid domain, to be captured by the modal *MFE* solution.

To understand how long the thermal transient is expected to last, the system can be simplified by considering a one dimensional case with the limit case of Dirichlet boundary conditions on both sides, corresponding the best case scenario in terms of approach to steady state. In dimensionless form, the first eigenvalue of the laplacian for the heat equation is $\lambda_1 = \pi^2$. To determine the number of Strouhal periods N_{Str} required for the transient of the first mode to decay by 95%, the following condition must be satisfied:

$$\lambda_1 \text{Fo} > 3 \implies \lambda_1 \frac{\alpha_s N}{\delta_t^2 F_{\text{Str}}} > 3 \implies N > 19.4$$

Highlighting that in practice the convergence of the lower modes will likely require many Strouhal periods. Furthermore, because the boundary conditions are not Dirichlet but Robin, the transient response will be longer.

3.2.1. Computational setup

Strictly speaking, the geometry of the problem is completely defined by the inner and outer pipe radii R_{in} and R_{out} along with the pipe length L_y. However, since the computational domain must be finite, additional parameters such as the streamwise and spanwise length L_x and L_z and the streamwise position of the cylinder within the domain, x_{cyl} are introduced. These geometrical parameters are sketched in Figure 13b. The inner radius and the length of the cylinder are set to $R_{\text{in}} = 0.8R_{\text{out}}$ and $L_y = 6R_{\text{out}}$. To determine the optimal value of the parameters a sensitivity study on the drag coefficient of the cylinder is performed at a fixed mesh density. The range spanned by the parameters is $L_x/R_{\text{out}} \in [10, 50]$, $L_z/R_{\text{out}} \in [10, 50]$, $x_{\text{cyl}}/L_x \in [0.2, 0.5]$. Guiding values for scale resolving simulations of cylinders in crossflows at low Reynolds number can be found in [53, 54, 55]. A summary of the tested scenarios is available in Table 3. The final values of the parameters are $L_x = 30R_{\text{out}}$, $L_z = 20R_{\text{out}}$, $x_{\text{cyl}} = 0.35L_x$. The fluid computational grid is a block-structured h-type with local refinement around the viscous surfaces.

On the solid side, two *FE* meshes are extruded from the pipe surfaces on the inner and outer fluid domains. The *FE* meshes extend across 10% of the radial extend of the pipe and the radial resolution at the wall is approximately twice the resolution from the fluid side. A modal mesh *MFE*, which spans the entire solid domain, is employed to thermally couple the two fluid domains using a coarser discretisation. The mesh details are provided in Table 4, with a total node count of 8.4×10^6.

Table 3: Drag coefficient C_D for different geometrical parameters

L_x/R_{out}	L_z/R_{out}	$x_{\text{cyl}}/R_{\text{out}}$	C_D
10	5	0.4	1.120
20	10	0.3	1.110
20	20	0.4	1.075
30	20	0.35	1.073
50	40	0.35	1.073
40	30	0.25	1.074

Table 4: Details of the different numerical grids used in the pipe flow case.

Domain	Node count	N_y	N_r	max(Δr^+)
Inner	2.11×10^6	120	-	0.53
Outer	5.04×10^6	72	-	0.43
Solid *FE*	6.15×10^5 [1]	72	24	0.14
Solid *MFE*	13824	24	18	5.61

At the inflow boundary of both inner and outer domains, synthetic turbulence is generated using the method described by Dreze et al. [47]. This technique uses modified uniformly distributed random sequences to construct divergence-free anisotropic random fields with sensible spectrum and complete complex correlation in space and time. To allow for the turbulence to develop, the domain detailed above is extended by 4 diameters before entering the mixing domain of interest. Each simulation is run for 40 Strouhal periods once the shedding regime has been established.

3.2.2. Validation

The solver is validated against reference data of [56, 57, 58, 59, 60]. To match the boundary conditions of the reference data, these simulations only included the outer domain at the target Reynolds number with a constant heat flux or constant temperature on the cylinder surface for the validation of the skin friction and local Nusselt number respectively. Figure 14 shows the time-averaged skin friction coefficient $\langle C_{f_\theta} \rangle$ and the time-averaged Nusselt number $\langle Nu \rangle$. The local angle ϕ is starting from the stagnation point on the cylinder surface. For the skin friction coefficient, the solver predicts separation for ϕ slightly below 90 degrees, which is in line with the experimental data at the studied Reynolds number, [61].

Regarding the local Nusselt number in Figure 14b, the global trend is well captured, but the curves move away from each other on the rear side of the cylinder, multiple factors explain this discrepancy. First, the simulations are at slightly different Reynolds numbers. This will mostly impact the rear side of the cylinder, the greater the Reynolds number the greater the heat transfer coefficient on the rear side of the cylinder. Similarly, the local Nusselt number on the rear of the cylinder is also influenced by turbulence intensity, which is challenging to replicate accurately the wind tunnel conditions. Additionally, the discrepancy at $\phi = 0$ is due to the difference in the ratio k_s/k_f. van Meel [60] used a ratio of approximately 50, whereas in the present case and in the experiment by Nakamura and Igarashi [59], the ratio is closer to 9000. As the ratio decreases, the local Nusselt number varies, particularly on the forward side of the cylinder. However, since the ratios are all greater than 20, their influence is confined to the forward side of the cylinder, as noted by Sundén [62].

Qualitatively, the thermal response of the pipe flow is displayed in Figure 15. It shows thermal slices at multiple radii within the domain, from left to right the slices correspond to the fluid in the vicinity of the outer surface of the cylinder, the outer surface of the cylinder, the start of the *MFE* solution at $0.9R_{\text{out}}$ and finally the fluid in the vicinity of the inner section of the pipe $r^+ \approx 5$. The figure highlights that deeper into the solid, the temperature fluctuations exhibit larger scales, which are directly related to the penetration depth. Additionally, it reflects the difference in the nature of the perturbations originating from the inner and outer surfaces, duct streaks for the inner section and shedding regime for the outer region.

3.2.3. Unsteady thermal behavior

To study the unsteady behavior, the thermal solution was initialised with a uniform temperature corresponding to the respective freestream temperature, while the solid pipe was initialised at the inner freestream temperature. The

---

[1] Node count includes both *FE* grids.

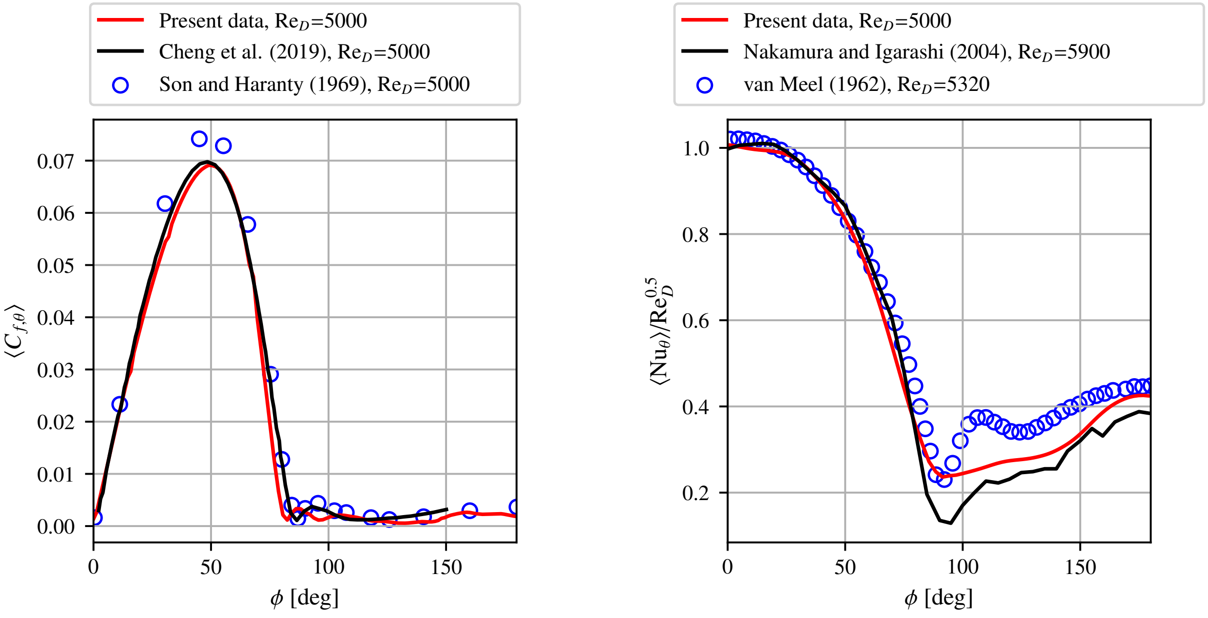

(a) Local skin friction coefficient

(b) Local Nusselt number

Figure 14: Validation results for the pipe flow case

time trace of the modal amplitude has been recorded and is shown in Figure 16. The figure presents the normalised modal amplitudes for selected modes against time normalised by the Strouhal frequency f_{St}. The figure also illustrates the time required to reach a steady state. Mode 0 stabilises after approximately 0.4 Fo, while the other modes converge more rapidly as the mode index increases. Mode 0 represents the constant mode characterised by a uniform amplitude in the circumferential direction and participating mainly to the mean solution. In contrast, the other modes plotted have a zero mean along the circumferential direction and are therefore more associated with the fluctuating behavior of the temperature field, as seen by the more pronounced fluctuating behavior in their time trace matching the Strouhal frequency.

A second simulation is performed, this time initialising the flow field from an instantaneous snapshot of the shedding cylinder. The modal amplitudes are set initially to the mean values of the time traces from Figure 16, excluding the initial 10 Strouhal periods. An example of a time trace when restarted from the mean value is shown in

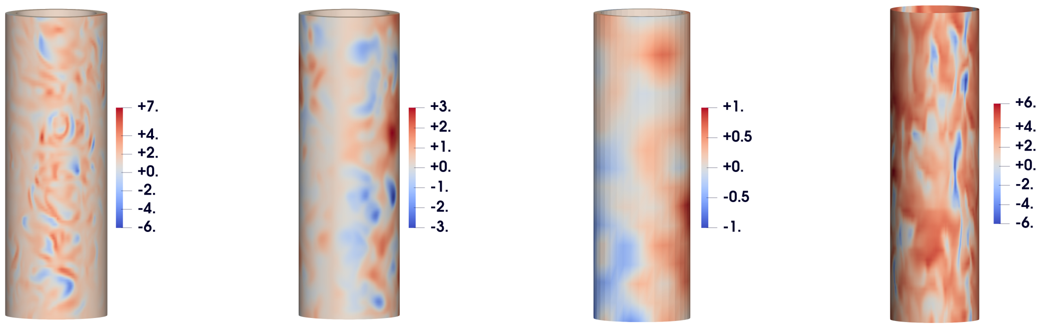

(a) $r^+ = 3$

(b) $r^+ = 0$, start of the FE solution

(c) Edge of the MFE solution

(d) $r^+ = 5$ inside the pipe

Figure 15: Dimensionless temperature fluctuations at different depths in the domain

Table 5: Strouhal periods to reach steady-state and aboslute percent error in standard deviation for different acceleration factors for selected modes

$\lambda/\omega_{\mathrm{Str}}$	0.0242	0.0247	0.0872	0.7604	2.606	10.331
$\beta = 1.0, \sigma = 1.0$	19.7, 0.00%	19.3, 0.00%	5.47, 0.00%	0.63, 0.00%	0.18, 0.00%	0.046, 0.00%
$\beta = 2.0, \sigma = 2.0$	9.86, 2.72%	9.66, 2.91%	2.73, 3.32%	0.31, 6.87%	0.09, 4.41%	0.023, 1.28%
$\beta = 4.0, \sigma = 4.0$	4.93, 6.27%	4.83, 5.48%	1.36, 6.71%	0.16, 13.1%	0.05, 9.39%	0.012, 2.32%
$\beta = 8.0, \sigma = 8.0$	2.47, 15.7%	2.42, 10.9%	0.68, 12.8%	0.08, 27.2%	0.03, 19.5%	0.006, 5.95%

Figure 17 with the black line. The curve exhibit similar behaviour than Figure 2, even if the mode is initialised with the statistical steady state value the amplitude of the mode goes through a transient before stabilising. It should be noted that not all the modes exhibit such a significant transient, it is a function of the phase between the initial state in the solid and the flow. Alongside, three additional simulation have been run with different acceleration factors. A summary of the performance of the different simulations is available in Table 5. Table 5 shows, for multiple modes, the estimated time required to reach a steady state and the absolute percent error in standard deviation once the steady state is reached. It can be seen that for the lowest mode shapes, a time-to-steady state divided by four can be achieved with an error just above 6%. This error is done on the modal amplitude of long-time low energy modes and does not have a significant impact on the interface fluctuations on both sides of the pipe, which remain constant for all acceleration factors tested, however deeper in the solid, the behavior is dominated by these modes and therefore the error in the standard deviation directly correlates with the modal amplitude error. In Table 5, it is interesting to note that for the modes that are close to the Strouhal frequency ($\lambda/\omega_{\mathrm{Str}} = 0.7604\,\&\,2.606$), the error in the standard deviation is significantly higher than for the other modes. This is because the main forcing frequency for these modes will be close to the pole of the transfer function and therefore the error in the amplitude will be larger with the SFD method used.

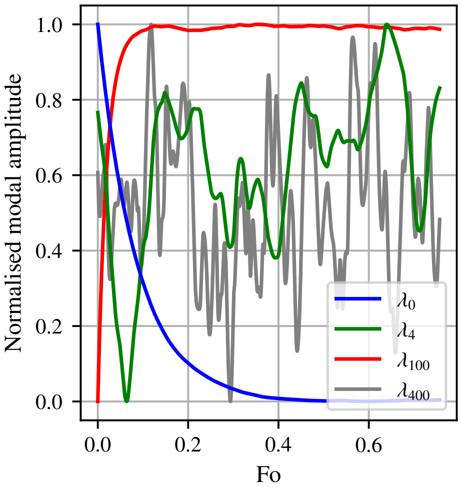

Figure 16: Normalised modal time trace with uniform temperature field initialization

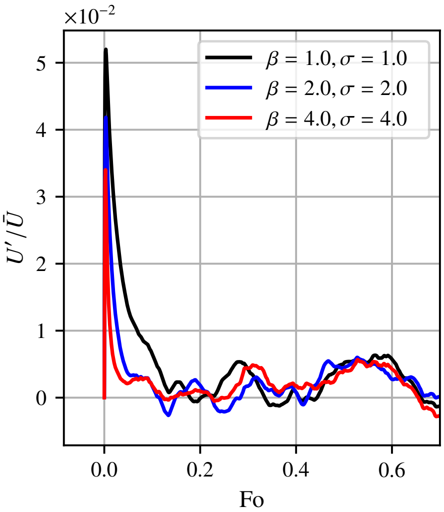

Figure 17: Modal time trace for mode 100 with a temperature field initialised with steady-state solution

4. Conclusion

In this work, we have presented the theoretical foundation of a multiscale framework for efficient unsteady high-fidelity conjugate transfer simulations. The proposed method addresses the common challenge of mismatched time and length scales in CHT problems by combining a modal decomposition with a scale-resolving mesh at the fluid-solid interface.

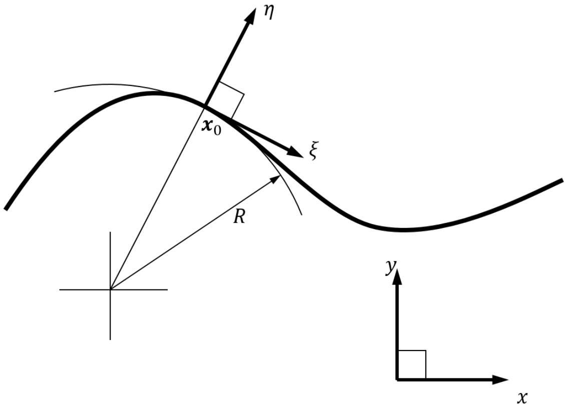

Figure A.18: Surface frame of reference

This hybrid approach enables the separation of long and short scale thermal fluctuations within the solid domain. Large-scale thermal behavior is captured through the modal projection, while finer, near-interface features are resolved using a scale-resolving mesh. Continuity of both temperature and heat flux is maintained across the fluid-solid interface, as well as across the region where the scale-resolving mesh overlaps with the modal projection, ensuring the accuracy of the method.

The timescale mismatch is addressed by leveraging the uncoupled modal equations, the approach to steady state of the overall solution can be accelerated without significant error by only altering the mode whose approach to steady-state is longer than the allowable simulation time. In this study, the acceleration strategy is implemented by adjusting the coefficients of the modal equations; however, it is worth noting that other acceleration techniques can also be integrated effectively within the modal decomposition framework. The method has been rigorously validated against DNS data for a turbulent channel flow and a pipe in cross flow. Results from the pipe case demonstrate that the acceleration technique can reduce the time to steady state for the slowest modes by up to a factor of 8, with the associated error kept within 16%.

5. Acknowledgements

The authors are grateful for the support from Rolls-Royce PLC and the EPSRC Center for Doctoral Training in Future Propulsion and Power. The authors would also like to acknowledge the use of the Cirrus UK National Tier-2 HPC Service at EPCC (`http://www.cirrus.ac.uk`) funded by the University of Edinburgh and EPSRC (EP/P020267/1).

Appendix A. Heat conduction in thin layers

Appendix A.1. Two dimensions space

Consider a two-dimensional space with a curved boundary. The global coordinates are denoted by (x, y) and the local surface bound coordinate are (ξ, η), see Figure A.18. Consider a position vector $\mathbf{x}$ = in the surface-bound frame of reference:

$$\mathbf{x} = \mathbf{x}_0\left(\xi\right) + \eta\mathbf{n} \tag{A.1}$$

Defining the unit tangent and normal vectors as

$$\mathbf{t} = \begin{bmatrix} t_x \\ t_y \end{bmatrix} \qquad \mathbf{n} = \begin{bmatrix} -t_y \\ t_x \end{bmatrix} \tag{A.2}$$

For a curve with radius of curvature R, the change of the tangent and normal vectors with respect to ξ is:

$$\frac{\partial \mathbf{t}}{\partial \xi} = \frac{1}{R}\begin{bmatrix} t_y \\ -t_x \end{bmatrix} \qquad \frac{\partial \mathbf{n}}{\partial \xi} = \frac{1}{R}\mathbf{t} \tag{A.3}$$

Differentiating the position vector $\mathbf{x}$ with respect to ξ and η yields

$$d\mathbf{x} = \frac{d\mathbf{x}_0}{d\xi}\, d\xi + \eta\, \frac{d\mathbf{n}}{d\xi}\, d\xi + \mathbf{n}\, d\eta. \tag{A.4}$$

Since the derivative of the boundary position is the tangent vector $\frac{d\mathbf{x}_0}{d\xi} = \mathbf{t}$ and using $\frac{d\mathbf{n}}{d\xi} = \frac{1}{R}\,\mathbf{t}$, we obtain

$$\begin{aligned} d\mathbf{x} &= \left[\mathbf{t} + \frac{\eta}{R}\,\mathbf{t}\right] d\xi + \mathbf{n}\, d\eta \\ &= \left(1 + \frac{\eta}{R}\right) \mathbf{t}\, d\xi + \mathbf{n}\, d\eta. \end{aligned} \tag{A.5}$$

Defining

$$\varrho = 1 + \frac{\eta}{R}, \tag{A.6}$$

this can be written as

$$d\mathbf{x} = \varrho\, \mathbf{t}\, d\xi + \mathbf{n}\, d\eta. \tag{A.7}$$

$$d\begin{bmatrix} x \\ y \end{bmatrix} = \begin{bmatrix} \varrho t_x & -t_y \\ \varrho t_y & t_x \end{bmatrix} d\begin{bmatrix} \xi \\ \eta \end{bmatrix} \tag{A.8}$$

The scaling factor

$$\varrho = 1 + \frac{\eta}{R}$$

accounts for the curvature of the boundary. At a distance η away from the boundary in the normal direction, the effective tangential length changes because the curves parallel to the boundary have different radii. At the boundary (i.e., when $\eta = 0$), we have $\varrho = 1$ and the mapping is simply given by the tangent and normal directions. However, away from the boundary, the scaling factor ϱ modifies the $d\xi$ component accordingly.

Inverting to get the derivatives of the local coordinates with respect to the global coordinates yields

$$\begin{bmatrix} \frac{\partial \xi}{\partial x} & \frac{\partial \xi}{\partial y} \\ \frac{\partial \eta}{\partial x} & \frac{\partial \eta}{\partial y} \end{bmatrix} = \begin{bmatrix} \frac{t_x}{\varrho} & \frac{t_y}{\varrho} \\ -t_y & t_x \end{bmatrix} \tag{A.9}$$

Differentiating each entry in A.9 to get the second derivatives of ξ and η with respect to x and y yields

$$\frac{\partial^2 \xi}{\partial x^2} = \frac{\partial}{\partial \xi}\left(\frac{\partial \xi}{\partial x}\right)\frac{\partial \xi}{\partial x} + \frac{\partial}{\partial \eta}\left(\frac{\partial \xi}{\partial x}\right)\frac{\partial \eta}{\partial x} = -\frac{\varrho'}{\varrho^3}t_x^2 + \frac{2}{R\varrho^2}t_x t_y \tag{A.10}$$

$$\frac{\partial^2 \xi}{\partial y^2} = \frac{\partial}{\partial \xi}\left(\frac{\partial \xi}{\partial y}\right)\frac{\partial \xi}{\partial y} + \frac{\partial}{\partial \eta}\left(\frac{\partial \xi}{\partial y}\right)\frac{\partial \eta}{\partial y} = -\frac{\varrho'}{\varrho^3}t_y^2 - \frac{2}{R\varrho^2}t_x t_y \tag{A.11}$$

$$\frac{\partial^2 \eta}{\partial x^2} = \frac{\partial}{\partial \xi}\left(\frac{\partial \eta}{\partial x}\right)\frac{\partial \xi}{\partial x} + \frac{\partial}{\partial \eta}\left(\frac{\partial \eta}{\partial x}\right)\frac{\partial \eta}{\partial x} = \frac{1}{R\varrho}t_x^2 \tag{A.12}$$

$$\frac{\partial^2 \eta}{\partial y^2} = \frac{\partial}{\partial \xi}\left(\frac{\partial \eta}{\partial y}\right)\frac{\partial \xi}{\partial y} + \frac{\partial}{\partial \eta}\left(\frac{\partial \eta}{\partial y}\right)\frac{\partial \eta}{\partial y} = \frac{1}{R\varrho}t_y^2 \tag{A.13}$$

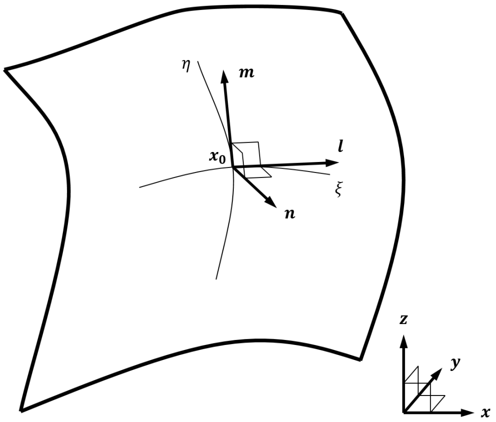

Figure A.19: Geodesic coordinates on a surface

with ϱ' denoting $\dfrac{d\varrho}{d\xi}$. Combining A.10-A.13 yields

$$\begin{aligned}\frac{\partial^2\xi}{\partial x^2}+\frac{\partial^2\xi}{\partial y^2}=\mathcal{L}(\xi) &= \frac{\varrho'}{\varrho^3}=\frac{\eta R'}{R^2\varrho^3} && \text{(A.14)}\\ \frac{\partial^2\eta}{\partial x^2}+\frac{\partial^2\eta}{\partial y^2}=\mathcal{L}(\eta) &= \frac{1}{R\varrho} && \text{(A.15)}\end{aligned}$$

Finally, using the chain rule for the Laplacian operator

$$\begin{aligned}\mathcal{L}(T) &= \mathcal{L}(\xi)\frac{\partial T}{\partial\xi}+\mathcal{L}(\eta)\frac{\partial T}{\partial\eta}+2\left(\frac{\partial\xi}{\partial x}\frac{\partial\eta}{\partial x}+\frac{\partial\xi}{\partial y}\frac{\partial\eta}{\partial y}\right)\frac{\partial^2T}{\partial\xi\partial\eta}+\left(\left(\frac{\partial\xi}{\partial x}\right)^2+\left(\frac{\partial\xi}{\partial y}\right)^2\right)\frac{\partial^2T}{\partial\xi^2}\\ &+ \left(\left(\frac{\partial\eta}{\partial x}\right)^2+\left(\frac{\partial\eta}{\partial y}\right)^2\right)\frac{\partial^2T}{\partial\eta^2}\end{aligned}$$

yields

$$\mathcal{L}(T)=\frac{1}{\varrho^2}\frac{\partial^2T}{\partial\xi^2}+\frac{\partial^2T}{\partial\eta^2}+\frac{1}{R\varrho}\frac{\partial T}{\partial\eta}+\frac{\eta R'}{R^2\varrho^3}\frac{\partial T}{\partial\xi} \tag{A.16}$$

At small distances from a smooth surface $\eta\approx 0$, $\varrho\approx 1$ and $\eta R'\approx 0$, so that

$$\mathcal{L}(T)=\frac{\partial^2T}{\partial\xi^2}+\frac{\partial^2T}{\partial\eta^2}+\frac{1}{R}\frac{\partial T}{\partial\eta} \tag{A.17}$$

For a cylindrical surface of radius R, $\eta=r-R$, $R\varrho=r$, $\xi=R\theta$, $R'=0$ hence the equation above reduces to the familiar Laplacian in cylindrical coordinates

$$\mathcal{L}(T)=\frac{1}{r^2}\frac{\partial^2T}{\partial\theta^2}+\frac{\partial^2T}{\partial r^2}+\frac{1}{r}\frac{\partial T}{\partial r} \tag{A.18}$$

Appendix A.2. Three dimensions space

Geodesic coordinates

For the three-dimensional case, a pair of geodesic coordinates ξ,η is introduced on the surface so that a point $\mathbf{x}$ in a thin layer adjacent to the surface may be mapped as follows:

$$\mathbf{x}=\mathbf{x}_0(\xi,\eta)+\mathbf{n}\zeta \tag{A.19}$$

On the surface, the tangent vectors are defined as:

$$\mathbf{l} = \frac{\partial \mathbf{x}_0}{\partial \xi} \qquad \mathbf{m} = \frac{\partial \mathbf{x}_0}{\partial \eta} \tag{A.20}$$

with **l**,**m** and **n** mutually orthogonal and $|\mathbf{l}| = |\mathbf{m}| = |\mathbf{n}| = 1$ (See Figure A.19).

Because of the normalization of the vectors

$$\mathbf{l} \cdot \left(\frac{\partial \mathbf{l}}{\partial \xi} d\xi + \frac{\partial \mathbf{l}}{\partial \eta} d\eta \right) = 0 \tag{A.21}$$

$$\mathbf{m} \cdot \left(\frac{\partial \mathbf{m}}{\partial \xi} d\xi + \frac{\partial \mathbf{m}}{\partial \eta} d\eta \right) = 0 \tag{A.22}$$

For equations A.21,A.22 to hold for any value of $d\xi$ and $d\eta$ the following must hold

$$\mathbf{l} \cdot \frac{\partial \mathbf{l}}{\partial \xi} = \mathbf{l} \cdot \frac{\partial \mathbf{l}}{\partial \eta} = 0 \tag{A.23}$$

$$\mathbf{m} \cdot \frac{\partial \mathbf{m}}{\partial \xi} = \mathbf{m} \cdot \frac{\partial \mathbf{m}}{\partial \eta} = 0 \tag{A.24}$$

By virtue of equations A.23,A.24, the following representations are possible for the derivatives of **l** and **m**:

$$\frac{\partial \mathbf{l}}{\partial \xi} = \alpha \mathbf{m} + \beta \mathbf{n} \tag{A.25}$$

$$\frac{\partial \mathbf{l}}{\partial \eta} = \delta \mathbf{m} + \epsilon \mathbf{n} \tag{A.26}$$

$$\frac{\partial \mathbf{m}}{\partial \xi} = \phi \mathbf{l} + \chi \mathbf{n} \tag{A.27}$$

$$\frac{\partial \mathbf{m}}{\partial \eta} = \psi \mathbf{l} + \omega \mathbf{n} \tag{A.28}$$

The scalars α, β, δ, ϵ, ϕ, χ, ψ and ω describe how the local basis vectors change with respect to the geodesic coordinates.

Similar conditions are obeyed by **n** and its derivatives. By comparing equations A.26 and A.27 one finds

$$\frac{\partial \mathbf{l}}{\partial \eta} = \frac{\partial \mathbf{m}}{\partial \xi} = \frac{\partial^2 \mathbf{x_0}}{\partial \xi \partial \eta} \tag{A.29}$$

$$\delta \mathbf{m} + \epsilon \mathbf{n} = \phi \mathbf{l} + \chi \mathbf{n} \tag{A.30}$$

which implies $\delta = \phi = 0$ and $\epsilon = \chi$.

Furthermore :

$$\frac{\partial}{\partial \xi} (\mathbf{l} \cdot \mathbf{m}) = \mathbf{l} \cdot \frac{\mathbf{m}}{\partial \xi} + \frac{\partial \mathbf{l}}{\partial \xi} \cdot \mathbf{m} = 0 \tag{A.31}$$

Substituting equations A.25 and A.26 into A.31 yields $\alpha = 0$. Similarly, combining orthogonality with equations A.27 and A.28 yields $\psi = 0$. The derivatives of the base vectors **l** and **m** are therefore:

$$\frac{\partial \mathbf{l}}{\partial \xi} = \beta \mathbf{n} \tag{A.32}$$

$$\frac{\partial \mathbf{l}}{\partial \eta} = \epsilon \mathbf{n} \tag{A.33}$$

$$\frac{\partial \mathbf{m}}{\partial \xi} = \epsilon \mathbf{n} \tag{A.34}$$

$$\frac{\partial \mathbf{m}}{\partial \eta} = \omega \mathbf{n} \tag{A.35}$$

The functions β, ϵ and ω are the components of the curvature tensor. The selection $\epsilon = 0$ identifies the geodesic coordinates ξ,η as the unique pair of coordinates aligned with the principal directions of the curvature tensor.

Heat conduction in a thin surface layer

Differentiating the position vector

$$d\mathbf{x} = \mathbf{l}d\xi + \mathbf{m}d\eta + \mathbf{n}d\zeta + \zeta\left(\frac{\partial \mathbf{n}}{\partial \xi}d\xi + \frac{\partial \mathbf{n}}{\partial \eta}d\eta\right) \tag{A.36}$$

Taking scalar products by **l**, **m** and **n** yields

$$\mathbf{l}\cdot d\mathbf{x} = d\xi + \zeta\mathbf{l}\cdot\left(\frac{\partial \mathbf{n}}{\partial \xi}d\xi + \frac{\partial \mathbf{n}}{\partial \eta}d\eta\right) \tag{A.37}$$

$$\mathbf{m}\cdot d\mathbf{x} = d\eta + \zeta\mathbf{m}\cdot\left(\frac{\partial \mathbf{n}}{\partial \xi}d\xi + \frac{\partial \mathbf{n}}{\partial \eta}d\eta\right) \tag{A.38}$$

$$\mathbf{n}\cdot d\mathbf{x} = d\zeta \tag{A.39}$$

Note that:

$$\mathbf{l}\cdot\frac{\partial \mathbf{n}}{\partial \xi} + \mathbf{n}\cdot\frac{\partial \mathbf{l}}{\partial \xi} = 0 \tag{A.40}$$

therefore:

$$\mathbf{l}\cdot\frac{\partial \mathbf{n}}{\partial \xi} = -\beta \tag{A.41}$$

by virtue of A.32.
Similarly:

$$\mathbf{l}\cdot\frac{\partial \mathbf{n}}{\partial \eta} = -\epsilon \qquad \mathbf{m}\cdot\frac{\partial \mathbf{n}}{\partial \xi} = -\epsilon \qquad \mathbf{m}\cdot\frac{\partial \mathbf{n}}{\partial \eta} = -\omega \tag{A.42}$$

hence, with $\epsilon = 0$

$$\mathbf{l}\cdot d\mathbf{x} = (1-\zeta\beta)\,d\xi \tag{A.43}$$

$$\mathbf{m}\cdot d\mathbf{x} = (1-\zeta\omega)\,d\eta \tag{A.44}$$

The metrics are

$$\begin{bmatrix} \dfrac{\partial \xi}{\partial x} & \dfrac{\partial \xi}{\partial y} & \dfrac{\partial \xi}{\partial z} \\ \dfrac{\partial \eta}{\partial x} & \dfrac{\partial \eta}{\partial y} & \dfrac{\partial \eta}{\partial z} \\ \dfrac{\partial \zeta}{\partial x} & \dfrac{\partial \zeta}{\partial y} & \dfrac{\partial \zeta}{\partial z} \end{bmatrix} = \begin{bmatrix} \dfrac{l_x}{\varrho_\xi} & \dfrac{l_y}{\varrho_\xi} & \dfrac{l_z}{\varrho_\xi} \\ \dfrac{m_x}{\varrho_\eta} & \dfrac{m_y}{\varrho_\eta} & \dfrac{m_z}{\varrho_\eta} \\ n_x & n_y & n_z \end{bmatrix} \tag{A.45}$$

where ϱ_ξ and ϱ_η are defined as

$$\varrho_\xi = 1 - \zeta\beta \qquad \varrho_\eta = 1 - \zeta\omega \tag{A.46}$$

The Laplacian of a scalar field in the coordinates ξ, η, ζ requires the Laplacians of ξ, η and ζ with respect to x,y,z. These can be found differentiating each entry in equation A.45. As an example, for the coordinate ξ:

$$\frac{\partial^2 \xi}{\partial x^2} = \left(\frac{\partial \xi}{\partial x}\frac{\partial}{\partial \xi} + \frac{\partial \eta}{\partial x}\frac{\partial}{\partial \eta} + \frac{\partial \zeta}{\partial x}\frac{\partial}{\partial \zeta}\right)\frac{\partial \xi}{\partial x} \tag{A.47}$$

$$\frac{\partial^2 \xi}{\partial y^2} = \left(\frac{\partial \xi}{\partial y}\frac{\partial}{\partial \xi} + \frac{\partial \eta}{\partial y}\frac{\partial}{\partial \eta} + \frac{\partial \zeta}{\partial y}\frac{\partial}{\partial \zeta}\right)\frac{\partial \xi}{\partial y} \tag{A.48}$$

$$\frac{\partial^2 \xi}{\partial z^2} = \left(\frac{\partial \xi}{\partial z}\frac{\partial}{\partial \xi} + \frac{\partial \eta}{\partial z}\frac{\partial}{\partial \eta} + \frac{\partial \zeta}{\partial z}\frac{\partial}{\partial \zeta}\right)\frac{\partial \xi}{\partial z} \tag{A.49}$$

Substituting

$$\frac{\partial^2 \xi}{\partial x^2} = \frac{l_x}{\varrho_\xi^2}\left(\frac{\partial l_x}{\partial \xi} - \frac{l_x}{\varrho_\xi}\frac{\partial \varrho_\xi}{\partial \xi}\right) + \frac{m_x}{\varrho_\eta \varrho_\xi}\left(\frac{\partial l_x}{\partial \eta} - \frac{l_x}{\varrho_\xi}\frac{\partial \varrho_\xi}{\partial \eta}\right) \tag{A.50}$$

$$\frac{\partial^2 \xi}{\partial y^2} = \frac{l_y}{\varrho_\xi^2}\left(\frac{\partial l_y}{\partial \xi} - \frac{l_y}{\varrho_\xi}\frac{\partial \varrho_\xi}{\partial \xi}\right) + \frac{m_y}{\varrho_\eta \varrho_\xi}\left(\frac{\partial l_y}{\partial \eta} - \frac{l_y}{\varrho_\xi}\frac{\partial \varrho_\xi}{\partial \eta}\right) \tag{A.51}$$

$$\frac{\partial^2 \xi}{\partial z^2} = \frac{l_z}{\varrho_\xi^2}\left(\frac{\partial l_z}{\partial \xi} - \frac{l_z}{\varrho_\xi}\frac{\partial \varrho_\xi}{\partial \xi}\right) + \frac{m_z}{\varrho_\eta \varrho_\xi}\left(\frac{\partial l_z}{\partial \eta} - \frac{l_z}{\varrho_\xi}\frac{\partial \varrho_\xi}{\partial \eta}\right) \tag{A.52}$$

Adding equations A.50-A.52 and performing similar operations on the variables η and ζ, finally yields

$$\mathcal{L}(\xi) = -\frac{1}{\varrho_\xi^3}\frac{\partial \varrho_\xi}{\partial \xi} = \frac{\zeta\beta'}{\varrho_\xi^3} \tag{A.53}$$

$$\mathcal{L}(\eta) = -\frac{1}{\varrho_\eta^3}\frac{\partial \varrho_\eta}{\partial \eta} = \frac{\zeta\omega'}{\varrho_\eta^3} \tag{A.54}$$

$$\mathcal{L}(\zeta) = -\left(\frac{\beta}{\varrho_\xi} + \frac{\omega}{\varrho_\eta}\right) \tag{A.55}$$

The Laplacian of a scalar quantity T with respect to the coordinates ξ,η,ζ, therefore is

$$\begin{aligned}\mathcal{L}(T) = {} & \mathcal{L}(\xi)\frac{\partial T}{\partial \xi} + \mathcal{L}(\eta)\frac{\partial T}{\partial \eta} + \mathcal{L}(\zeta)\frac{\partial T}{\partial \zeta} + \left(\left(\frac{\partial \xi}{\partial x}\right)^2 + \left(\frac{\partial \xi}{\partial y}\right)^2 + \left(\frac{\partial \xi}{\partial z}\right)^2\right)\frac{\partial^2 T}{\partial \xi^2} \\ & + \left(\left(\frac{\partial \eta}{\partial x}\right)^2 + \left(\frac{\partial \eta}{\partial y}\right)^2 + \left(\frac{\partial \eta}{\partial z}\right)^2\right)\frac{\partial^2 T}{\partial \eta^2} + \left(\left(\frac{\partial \zeta}{\partial x}\right)^2 + \left(\frac{\partial \zeta}{\partial y}\right)^2 + \left(\frac{\partial \zeta}{\partial z}\right)^2\right)\frac{\partial^2 T}{\partial \zeta^2} \\ & + \left(\frac{\partial \xi}{\partial x}\frac{\partial \eta}{\partial x} + \frac{\partial \xi}{\partial y}\frac{\partial \eta}{\partial y} + \frac{\partial \xi}{\partial z}\frac{\partial \eta}{\partial z}\right)\frac{\partial^2 T}{\partial \xi \partial \eta} + \left(\frac{\partial \xi}{\partial x}\frac{\partial \zeta}{\partial x} + \frac{\partial \xi}{\partial y}\frac{\partial \zeta}{\partial y} + \frac{\partial \xi}{\partial z}\frac{\partial \zeta}{\partial z}\right)\frac{\partial^2 T}{\partial \xi \partial \zeta} \\ & + \left(\frac{\partial \eta}{\partial x}\frac{\partial \zeta}{\partial x} + \frac{\partial \eta}{\partial y}\frac{\partial \zeta}{\partial y} + \frac{\partial \eta}{\partial z}\frac{\partial \zeta}{\partial z}\right)\frac{\partial^2 T}{\partial \eta \partial \zeta}\end{aligned} \tag{A.56}$$

$$\mathcal{L}(T) = \frac{1}{\varrho_\xi^2}\frac{\partial^2 T}{\partial \xi^2} + \frac{1}{\varrho_\eta^2}\frac{\partial^2 T}{\partial \eta^2} + \frac{\partial^2 T}{\partial \zeta^2} + \frac{\zeta\beta'}{\varrho_\xi^3}\frac{\partial T}{\partial \xi} + \frac{\zeta\omega'}{\varrho_\eta^3}\frac{\partial T}{\partial \eta} - \left(\frac{\beta}{\varrho_\xi} + \frac{\omega}{\varrho_\eta}\right)\frac{\partial T}{\partial \zeta} \tag{A.57}$$

At small distances from a smooth surface $\varrho_\xi \approx 1$, $\varrho_\eta \approx 1$ and $\zeta\beta' = \zeta\omega' \approx 0$ so that

$$\mathcal{L}(T) = \frac{\partial^2 T}{\partial \xi^2} + \frac{\partial^2 T}{\partial \eta^2} + \frac{\partial^2 T}{\partial \zeta^2} + \frac{1}{R}\frac{\partial T}{\partial \zeta} \tag{A.58}$$

where

$$\frac{1}{R} = \omega + \beta \tag{A.59}$$

is the local harmonic mean curvature of the surface.

References

[1] Y. Hou, M. Cheng, Z. Sheng, J. Wang, Unsteady conjugate heat transfer simulation of wall heat loads for rotating detonation combustor, International Journal of Heat and Mass Transfer 221 (2024) 125081.

[2] X. Fan, J.-X. Wang, Differentiable hybrid neural modeling for fluid-structure interaction, Journal of Computational Physics 496 (2024) 112584. URL: `https://www.sciencedirect.com/science/article/pii/S0021999123006794`. doi:`https://doi.org/10.1016/j.jcp.2023.112584`.

[3] M. Lomele, A. S. Smyth, X. Chen, R. H. Willden, Aerodynamic damping assessment on wind turbine blades using 2d and 3d computational fluid dynamics, AIAA Scitech 2025 Forum (2025). URL: https://arc.aiaa.org/doi/abs/10.2514/6.2025-1236. doi:10.2514/6.2025-1236. arXiv:https://arc.aiaa.org/doi/pdf/10.2514/6.2025-1236.

[4] A. Mourato, R. Valente, J. Xavier, M. Brito, S. Avril, J. C. de Sa, A. Tomas, J. Fragata, Computational modelling and simulation of fluid structure interaction in aortic aneurysms: a systematic review and discussion of the clinical potential, Applied Sciences 12 (2022) 8049.

[5] A. Heselhaus, A Hybrid Coupling Scheme and Stability Analysis for Coupled Solid/Fluid Turbine Blade Temperature Calculations Volume 4: Heat Transfer; Electric Power; Industrial and Cogeneration (1998). URL: https://doi.org/10.1115/98-GT-088. doi:10.1115/98-GT-088.

[6] R. Maffulli, L. He, Wall temperature effects on heat transfer coefficient for high-pressure turbines, Journal of Propulsion and Power 30 (2014) 1080–1090. doi:10.2514/1.B35126.

[7] M. G. Dunn, Convective Heat Transfer and Aerodynamics in Axial Flow Turbines Volume 4: Heat Transfer; Electric Power; Industrial and Cogeneration (2001).

[8] T. Perelman, On conjugated problems of heat transfer, International Journal of Heat and Mass Transfer 3 (1961) 293–303. doi:https://doi.org/10.1016/0017-9310(61)90044-8.

[9] S. Sharma, M. Shadloo, A. Hadjadj, Turbulent flow topology in supersonic boundary layer with wall heat transfer, International Journal of Heat and Fluid Flow 78 (2019) 108430. URL: https://www.sciencedirect.com/science/article/pii/S0142727X18306027. doi:https://doi.org/10.1016/j.ijheatfluidflow.2019.108430.

[10] S. U. Choi, J. A. Eastman, Enhancing thermal conductivity of fluids with nanoparticles (1995). URL: https://www.osti.gov/biblio/196525.

[11] M. T. Lewis, J.-P. Hickey, Conjugate heat transfer in high-speed external flows: A review, Journal of Thermophysics and Heat Transfer 37 (2023) 697–712. URL: https://doi.org/10.2514/1.T6763. doi:10.2514/1.T6763. arXiv:https://doi.org/10.2514/1.T6763.

[12] B. John, P. Senthilkumar, S. Sadasivan, Applied and theoretical aspects of conjugate heat transfer analysis: A review, Archives of Computational Methods in Engineering 2 (2018) 475–489.

[13] Y. Dreze, L. di Mare, Unsteady conjugate heat transfer effects on flow characteristics in transonic flow, International Journal of Heat and Mass Transfer (2025).

[14] D. L. Schultz, Heat transfer measurements in short-duration hypersonic facilities, AGARD 165. (1973).

[15] I. Tiselj, L. Cizelj, Dns of turbulent channel flow with conjugate heat transfer at prandtl number 0.01, Nuclear Engineering and Design 253 (2012) 153–160.

[16] T. Hickling, L. He, A multiscale framework for unsteady conjugate heat transfer with turbulence resolving methods — with application to rotating cavities, International Journal of Heat and Fluid Flow 103 (2023) 109174. URL: https://www.sciencedirect.com/science/article/pii/S0142727X23000735. doi:https://doi.org/10.1016/j.ijheatfluidflow.2023.109174.

[17] C. Koren, R. Vicquelin, O. Gicquel, Self-adaptive coupling frequency for unsteady coupled conjugate heat transfer simulations, International Journal of Thermal Sciences 118 (2017) 340–354. URL: https://www.sciencedirect.com/science/article/pii/S1290072916305932. doi:https://doi.org/10.1016/j.ijthermalsci.2017.04.023.

[18] L. He, M. Oldfield, Unsteady conjugate heat transfer modeling, Journal of turbomachinery 133 (2011).

[19] T. K. Oh, D. K. Tafti, K. Nagendra, Fully Coupled Large Eddy Simulation-Conjugate Heat Transfer Analysis of a Ribbed Cooling Passage Using the Immersed Boundary Method, Journal of Turbomachinery 143 (2021) 041012. URL: https://doi.org/10.1115/1.4050111. doi:10.1115/1.4050111. arXiv:https://asmedigitalcollection.asme.org/turbomachinery/article-pdf/143/4/041012/6669694/turbo_143_4_041012.pdf.

[20] Y. Shi, S. Ding, T. Qiu, C. Liu, S. Zhang, Bi-fo time scaling method in the numerical simulation of transient conjugate heat transfer, Propulsion and Power Research 10 (2021) 209–223. URL: https://www.sciencedirect.com/science/article/pii/S2212540X21000353. doi:https://doi.org/10.1016/j.jppr.2021.05.005.

[21] R. D. Knapke, R. David, High-Order Unsteady Heat Transfer with the Harmonic Balance Method, PhDT (2015).

[22] J. Hodges, Gas turbine blade heat transfer via unsteady flow mechanisms using harmonic balance conjugate heat transfer simulation (2018).

[23] O. Mehdizadeh, S. Vilmin, B. Tartinville, C. Hirsch, Nonlinear harmonic method applied to turbine conjugate heat transfer analysis for efficient simulation of hot streak clocking and unsteady heat transfer, 2017. doi:10.1115/GT2017-63622.

[24] L. He, Closely coupled fluid-solid interface method with moving-average for les based conjugate heat transfer solution, International Journal of Heat and Fluid Flow 79 (2019). doi:10.1016/j.ijheatfluidflow.2019.108440.

[25] R. A. Białecki, A. J. Kassab, A. Fic, Proper orthogonal decomposition and modal analysis for acceleration of transient fem thermal analysis, International Journal for Numerical Methods in Engineering 62 (2005) 774–797. doi:10.1002/nme.1205.

[26] T. J. Blanc, M. R. Jones, S. E. Gorrell, Reduced-Order Modeling of Conjugate Heat Transfer Processes, Journal of Heat Transfer 138 (2016). URL: https://doi.org/10.1115/1.4032453. doi:10.1115/1.4032453. arXiv:https://asmedigitalcollection.asme.org/heattransfer/article-pdf/138/5/051703/6211779/ht_138_05_051703.pdf, 051703.

[27] J. Hacker, J. Eaton, Measurements of heat transfer in a separated and reattaching flow with spatially varying thermal boundary conditions, International Journal of Heat and Fluid Flow 18 (1997) 131–141. URL: https://www.sciencedirect.com/science/article/pii/S0142727X96001427. doi:https://doi.org/10.1016/S0142-727X(96)00142-7, selected Papers from the Engineering Foundation Turbulent Heat Transfer Conference.

[28] D. W. Hoffman, J. K. Eaton, Conjugate Heat Transfer Analysis Using the Discrete Green's Function, Journal of Heat Transfer 143 (2021) 031401. URL: https://doi.org/10.1115/1.4048992. doi:10.1115/1.4048992. arXiv:https://asmedigitalcollection.asme.org/heattransfer/article-pdf/143/3/031401/6621841/ht_143_03_031401.pdf.

[29] T. M. Shih, J. T. Skladany, An eigenvalue method for solving transient heat conduction problems, Numerical Heat Transfer 6 (1983) 409–422. URL: https://doi.org/10.1080/01495728308963097. doi:10.1080/01495728308963097. arXiv:https://doi.org/10.1080/01495728308963097.

[30] O. Quéméner, F. Joly, A. Neveu, The generalized amalgam method for modal reduction, International Journal of Heat and Mass Transfer

55 (2012) 1197–1207. URL: https://www.sciencedirect.com/science/article/pii/S0017931011005485. doi:https://doi.org/10.1016/j.ijheatmasstransfer.2011.09.043.

[31] Y. Gerstenmaier, G. Wachutka, Time dependent temperature fields calculated using eigenfunctions and eigenvalues of the heat conduction equation, Microelectronics Journal 32 (2001) 801–808. doi:https://doi.org/10.1016/S0026-2692(01)00066-0.

[32] J. Zhong, L. C. Chow, W. SOON CHANG, A finite element eigenvalue method for solving transient heat conduction problems, International Journal of Numerical Methods for Heat & Fluid Flow 2 (1992) 243–259.

[33] J. V. Palmieri, K. A. Rathjen, Cave3: A general transient heat transfer computer code utilizing eigenvectors and eigenvalues (1978).

[34] D. Knupp, R. Cotta, C. Naveira-Cotta, Conjugate heat transfer: Analysis via integral transforms and eigenvalue problems, Journal of Engineering Physics and Thermophysics 93 (2020) 60–73.

[35] Z. Sun, J. W. Chew, N. J. Hills, K. N. Volkov, C. J. Barnes, Efficient Finite Element Analysis/Computational Fluid Dynamics Thermal Coupling for Engineering Applications, Journal of Turbomachinery 132 (2010). URL: https://doi.org/10.1115/1.3147105. doi:10.1115/1.3147105. arXiv:https://asmedigitalcollection.asme.org/turbomachinery/article-pdf/132/3/031016/5535970/031016_1.pdf, 031016.

[36] R. Maffulli, L. He, P. Stein, G. Marinescu, Fast Conjugate Heat Transfer Simulation of Long Transient Flexible Operations Using Adaptive Time Stepping, Journal of Turbomachinery 140 (2018). URL: https://doi.org/10.1115/1.4040997. doi:10.1115/1.4040997, 091005.

[37] S. Vlase, M. Marin, A. Öchsner, Eigenvalue and eigenvector problems in applied mechanics, Springer, 2019.

[38] J. H. Lienhard, A heat transfer textbook, Phlogistron, 2005.

[39] H. Gottlieb, Eigenvalues of the laplacian with neumann boundary conditions, The ANZIAM Journal 26 (1985) 293–309.

[40] G. Cunha, P.-Y. Passaggia, M. Lazareff, Optimization of the selective frequency damping parameters using model reduction, Physics of Fluids 27 (2015).

[41] E. Åkervik, L. Brandt, D. S. Henningson, J. Hœpffner, O. Marxen, P. Schlatter, Steady solutions of the navier-stokes equations by selective frequency damping, Physics of Fluids 18 (2006) 068102. URL: https://doi.org/10.1063/1.2211705. doi:10.1063/1.2211705. arXiv:https://pubs.aip.org/aip/pof/article-pdf/doi/10.1063/1.2211705/13564379/068102_1_online.pdf.

[42] J. Casacuberta, K. J. Groot, H. J. Tol, S. Hickel, Effectivity and efficiency of selective frequency damping for the computation of unstable steady-state solutions, Journal of Computational Physics 375 (2018) 481–497. URL: https://www.sciencedirect.com/science/article/pii/S0021999118305898. doi:https://doi.org/10.1016/j.jcp.2018.08.056.

[43] M. B. Giles, Stability analysis of numerical interface conditions in fluid-structure thermal analysis, International Journal for Numerical Methods in Fluids 25 (1997) 421–436.

[44] A. Jameson, S. Shankaran, An assessment of dual-time stepping, time spectral and artificial compressibility based numerical algorithms for unsteady flow with applications to flapping wings, in: 19th AIAA computational fluid dynamics, 2009, p. 4273.

[45] J. Hope-Collins, Low mach number numerical methods and dns of turbulent heat transfer (2022).

[46] J. Hope-Collins, L. di Mare, Artificial diffusion for convective and acoustic low mach number flows i: Analysis of the modified equations, and application to roe-type schemes, Journal of Computational Physics 475 (2023) 111858. URL: https://www.sciencedirect.com/science/article/pii/S0021999122009214. doi:https://doi.org/10.1016/j.jcp.2022.111858.

[47] Y. Dreze, M. Hao, L. di Mare, Divergence-free turbulent inflow data from realistic covariance tensor, Physics of Fluids 35 (2023) 025120. URL: https://doi.org/10.1063/5.0136568. doi:10.1063/5.0136568.

[48] M. Hao, L. di Mare, Reynolds stresses and turbulent heat fluxes in fan-shaped and cylindrical film cooling holes, International Journal of Heat and Mass Transfer 214 (2023) 124324. URL: https://www.sciencedirect.com/science/article/pii/S0017931023004702. doi:https://doi.org/10.1016/j.ijheatmasstransfer.2023.124324.

[49] C. Flageul, S. Benhamadouche, É. Lamballais, D. Laurence, Dns of turbulent channel flow with conjugate heat transfer: Effect of thermal boundary conditions on the second moments and budgets, International Journal of Heat and Fluid Flow 55 (2015) 34–44.

[50] I. Tiselj, R. Bergant, B. Mavko, I. Bajsic, G. Hetsroni, Dns of turbulent heat transfer in channel flow with heat conduction in the solid wall, Journal of Heat Transfer 123 (2001) 849–857. URL: https://doi.org/10.1115/1.1389060. doi:10.1115/1.1389060. arXiv:https://asmedigitalcollection.asme.org/heattransfer/article-pdf/123/5/849/5733971/849_1.pdf.

[51] J. Kim, P. Moin, R. Moser, Turbulence statistics in fully developed channel flow at low reynolds number, Journal of Fluid Mechanics 177 (1987) 133–166. doi:10.1017/S0022112087000892.

[52] S. Pirozzoli, P. Orlandi, Natural grid stretching for dns of wall-bounded flows, Journal of Computational Physics 439 (2021) 110408. URL: https://www.sciencedirect.com/science/article/pii/S002199912100303X. doi:https://doi.org/10.1016/j.jcp.2021.110408.

[53] M. E. Young, A. Ooi, Comparative assessment of les and urans for flow over a cylinder at a reynolds number of 3900, 2007.

[54] D. Lysenko, I. Ertesvåg, K. E. Rian, Large-eddy simulation of the flow over a circular cylinder at reynolds number 3900 using the openfoam toolbox, Flow, Turbulence and Combustion 89 (2012). doi:10.1007/s10494-012-9405-0.

[55] A. G. Kravchenko, P. Moin, Numerical studies of flow over a circular cylinder at red=3900, Physics of Fluids 12 (2000) 403–417. URL: https://doi.org/10.1063/1.870318. doi:10.1063/1.870318. arXiv:https://pubs.aip.org/aip/pof/article-pdf/12/2/403/19139241/403_1_online.pdf.

[56] W. Cheng, D. I. Pullin, R. Samtaney, W. Zhang, W. Gao, Large-eddy simulation of flow over a cylinder with re_D from 3.9×10^3 to 8.5×10^5: a skin-friction perspective, Journal of Fluid Mechanics 820 (2017) 121–158. doi:10.1017/jfm.2017.172.

[57] J. S. Son, T. J. Hanratty, Velocity gradients at the wall for flow around a cylinder at reynolds numbers from 5×10^3 to 10^5, Journal of Fluid Mechanics 35 (1969) 353–368. doi:10.1017/S0022112069001157.

[58] G. Lowery, R. Vachon, The effect of turbulence on heat transfer from heated cylinders, International Journal of Heat and Mass Transfer 18 (1975) 1229–1242. URL: https://www.sciencedirect.com/science/article/pii/0017931075902318. doi:https://doi.org/10.1016/0017-9310(75)90231-8.

[59] H. Nakamura, T. Igarashi, Unsteady heat transfer from a circular cylinder for reynolds numbers from 3000 to 15,000, International Journal

of Heat and Fluid Flow 25 (2004) 741–748. Selected papers from the 4th International Symposium on Turbulence Heat and Mass Transfer.

[60] D. van Meel, A method for the determination of local convective heat transfer from a cylinder placed normal to an air stream, International Journal of Heat and Mass Transfer 5 (1962) 715–722. URL: `https://www.sciencedirect.com/science/article/pii/0017931062902016`. doi:`https://doi.org/10.1016/0017-9310(62)90201-6`.

[61] H. Jiang, Separation angle for flow past a circular cylinder in the subcritical regime, Physics of Fluids 32 (2020) 014106. URL: `https://doi.org/10.1063/1.5139479`. doi:10.1063/1.5139479. `arXiv:https://pubs.aip.org/aip/pof/article-pdf/doi/10.1063/1.5139479/15801892/014106_1_online.pdf`.

[62] B. Sundén, Conjugated heat transfer from circular cylinders in low reynolds number flow, International Journal of Heat and Mass Transfer 23 (1980) 1359–1367. URL: `https://www.sciencedirect.com/science/article/pii/0017931080902100`. doi:`https://doi.org/10.1016/0017-9310(80)90210-0`.

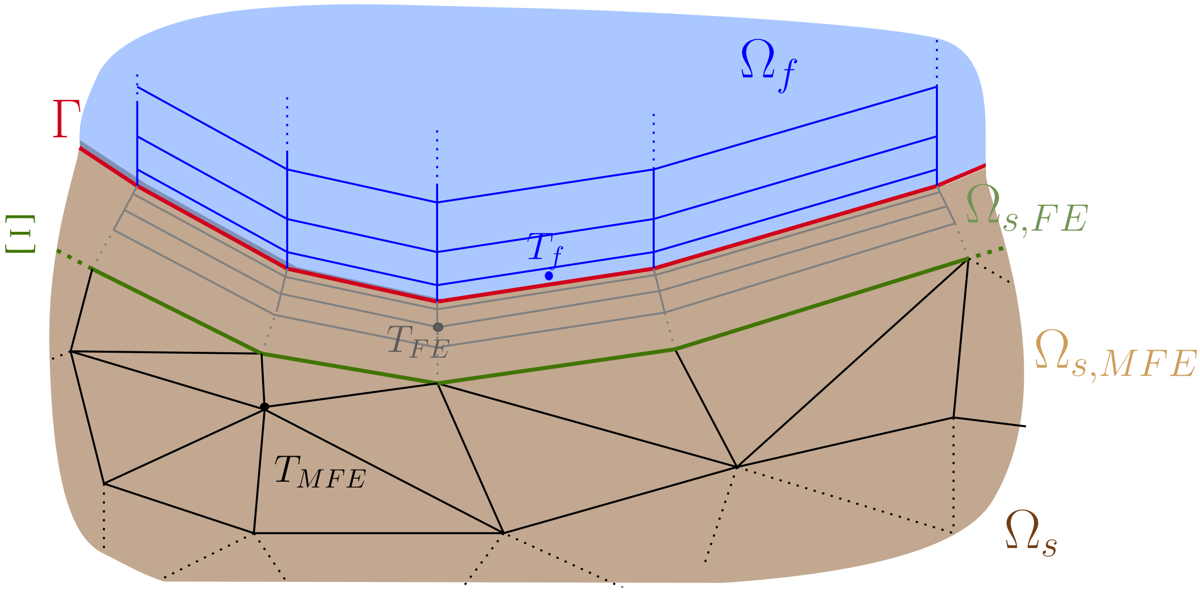

Figure 4.1: Partition of the degrees of freedom near an interface boundary in a conjugate heat transfer problem. Γ is the interface between Ω_s and Ω_f. Ξ is the interface between $\Omega_{s,\mathrm{FE}}$ and $\Omega_{s,\mathrm{MFE}}$.

4.1.1 Additional material and possible extensions

Overlap of the modal and surface temperature fields

In the paper, the overlap between the modal $\Omega_{s,MFE}$ and the local field $\Omega_{s,FE}$ is handled by using the local field to correct the truncated modal solution. However, alternative strategies exist for addressing this overlap, as explored in this section.

One such alternative involves redefining the domains $\Omega_{s,FE}$ and $\Omega_{s,MFE}$ to eliminate their overlapping regions. If $\Omega_{s,MFE}$ is defined on Ω_s excluding the surface domain $\Omega_{s,FE}$, as sketched in Figure 4.1, it avoids the overlap and allows for the $\Omega_{s,FE}$ domain to be described by the classical FEM formulation of the heat conduction equation instead of the combined formulation presented in the paper (Equation (38) in the paper). The main drawback of this approach is that the modal solution is not defined on a clearly specified solid domain but rather on an arbitrary surface defined by the outer surface of the $\Omega_{s,FE}$ domain. Additionally, the boundary treatment at the interface Ξ between $\Omega_{s,FE}$ and $\Omega_{s,MFE}$ is not straightforward.

Alternative ways of accelerating the equations

Section 2.4 of the paper discusses various techniques to accelerate the convergence of the initial transient. It examines the natural acceleration methods derived from the modal projection, modifying the eigenvalues and time updates of modes associated with the longest time scales. Another alternative is to employ a Fourier-based approach. Unlike prior studies by Mehdizadeh et al. [2017], He and Oldfield [2010], Hodges [2018], this method applies discrete Fourier transforms directly to the modal equations.

The modal equation for the temperature field is given by:

$$\frac{dU}{d\mathrm{Fo}} = \lambda U + G(\mathrm{Fo}) \tag{4.1}$$

Assuming that both the modal amplitude and the forcing signal are periodic functions over the sampling interval, Equation 4.1 can be represented as a Fourier series:

$$U(\mathrm{Fo}) = \sum_{n=0}^{N} \hat{U}_n e^{i\omega_n \mathrm{Fo}} \qquad G(\mathrm{Fo}) = \sum_{n=0}^{N} \hat{G}_n e^{i\omega_n \mathrm{Fo}} \tag{4.2}$$

Where $\hat{U}_n$ and $\hat{G}_n$ are the Fourier coefficients of the modal amplitude and the forcing signal, respectively. The angular dimensionless frequency ω_n is defined as $\omega_n = \frac{2\pi n}{T}$, where T is the non-dimensional period of the forcing signal.
Inserting Equation 4.2 into Equation 4.1 gives:

$$\hat{U}_n = \hat{G}_n/(i\omega_n - \lambda) \tag{4.3}$$

The Fourier method will be evaluated using the same test case as presented in Figure 1 and Table 1 of the paper. The test case involves a simple 1D solid domain with constant thermal properties. One end of the solid is subjected to external thermal excitation, while adiabatic conditions are applied at the other end. The boundary signal imposed on the domain is a square wave with a dimensionless frequency of 1, shown in green in Figure 4.2.

The results are available in Figure 4.2. When the signal is known beforehand or if the solver uses a Fourier-based formulation of the flow variables, the Fourier-based approach directly converges to the statistical steady-state solution, as indicated by the red line in Figure 4.2. However, for most fully coupled time-marching CHT simulations, a Fourier transform must be performed dynamically, represented by the blue line in Figure 4.2. The simple dynamic Fourier transform does not perform better than the original problem.

While the Fourier transform approach demonstrates potential performance improvements, its accuracy heavily depends on hyperparameters such as the sampling period, the windowing algorithm (which typically requires multiple periods to minimise frequency leakage), and the number of harmonics retained. Careful tuning of these parameters is essential to ensure solution accuracy, and at least one complete period is necessary for the discrete Fourier transform to converge.

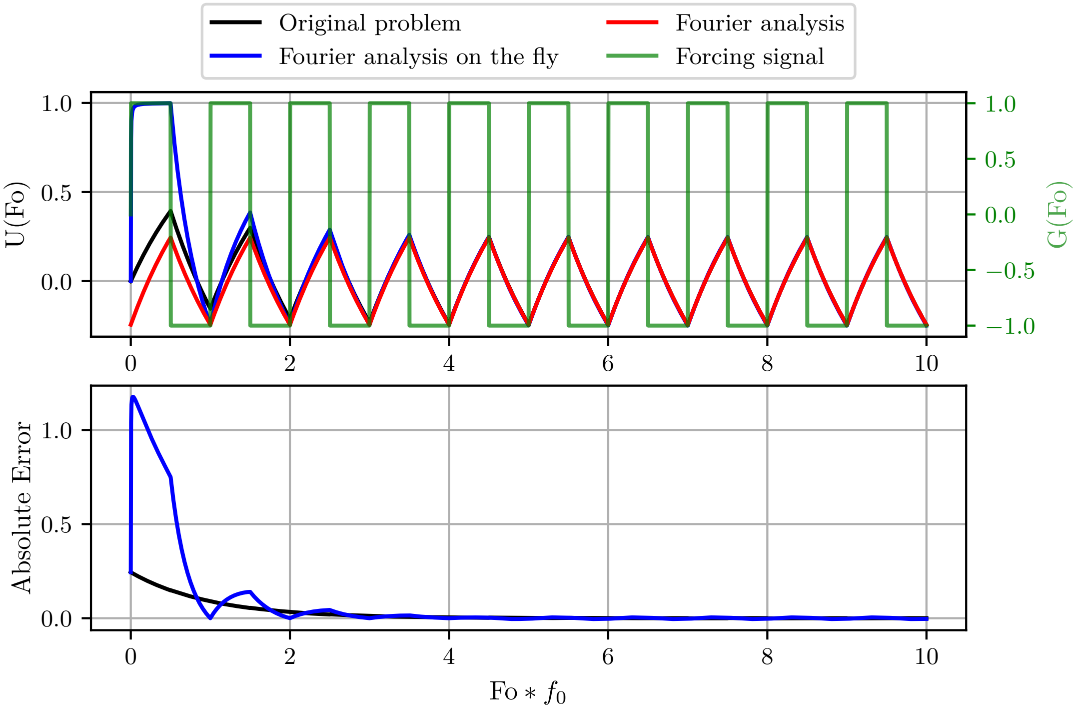

Figure 4.2: Acceleration of the modal equations using Fourier-based approach.

Mesh quality for the pipe flow case

Supplementary data are presented in the following to complement the discussion on mesh quality for the cylinder flow case, offering further insights into the mesh characteristics and wall refinement. The mesh of the outer flow is a structured

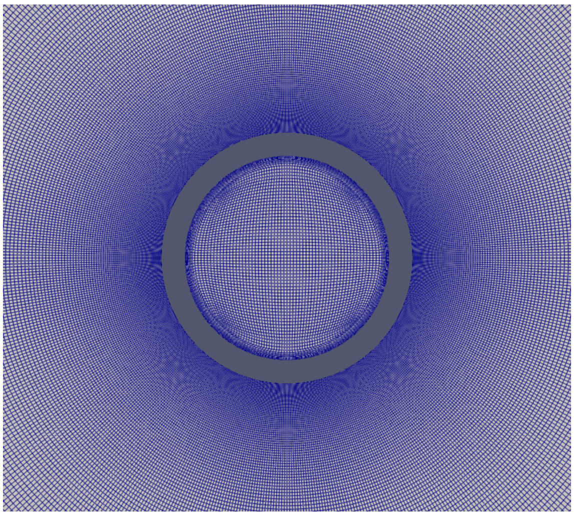

Figure 4.3: Sectional view of the mesh in the vicinity of the pipe.

H-type mesh with an O-grid in the vicinity of the cylinder and the mesh of the inner flow is also block-structured with a refinement near the conjugate interface. Figure 4.3 shows a sectional view of both meshes in the vicinity of the cylinder. The mesh quality is assessed by the variation of the first grid point in the outer section of the pipe, shown in Figure 4.4. The mesh keeps a value of Δr^{+} lower than 0.5 wall units along the circumference of the cylinder. The inner section maintains a value of Δr^{+} in the range of 0.41 to 0.53 wall units.

The modal mesh for the pipe domain is constructed as a structured grid, derived directly from the block mesh of the fluid domain to minimise interpolation errors.

Analysis of the thermal modes for the pipe flow case

To gain deeper insights into the thermal behavior of the pipe flow case, an analysis of the thermal modes is conducted. The eigenvalues of these thermal modes, which provide a quantitative measure of their temporal response, are presented in Figure 4.5.

Because of the structured nature of the chosen modal grid, the eigenvalues exhibit a distinct grouping pattern, forming plateaux that correspond to the radial extent of the modes. The first group of modes, up to approximately index 250 in Figure 4.5, represents modes that are constant in the radial direction, as shown in Figures 4.6b and 4.6c. The second group consists of modes with a sign change in the radial direction (Figure 4.6d), and this pattern continues for subsequent

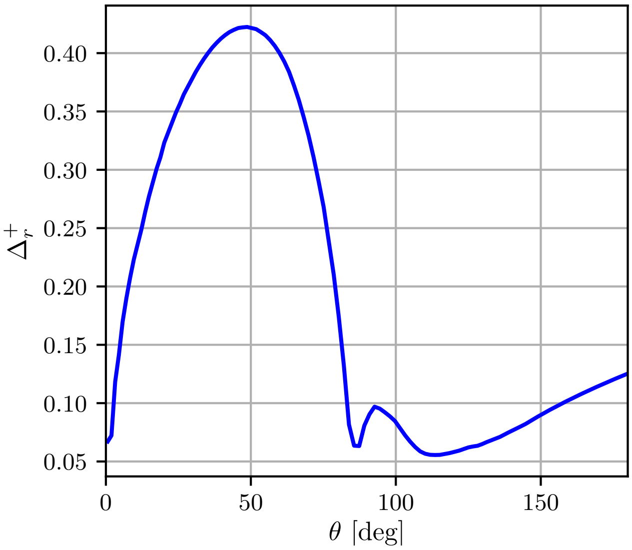

Figure 4.4: Variation of Δr^+ of the first grid point along the outer section of the pipe.

plateaux. Within each plateau, the first mode is constant along the circumference, as illustrated in Figure 4.6a. The red line in Figure 4.5 indicates the amplitude of the response to a constant excitation, showing that all other modes have a zero mean along the circumference (Figures 4.6b to 4.6d). The remaining modes within a plateau correspond to progressively smaller circumferential extents, as seen in Figure 4.6. The significant increase in eigenvalues with radial order is consistent with the penetration depth of the modes, emphasising that circumferential perturbations are more naturally induced by external excitation, while radial perturbations are more difficult to excite, as being a feature of the solid thermal properties solely.

Time traces of the temperature field in the cylinder

The time traces of the forcing signals applied to the modes provide valuable insights into the expected transient behavior of the system. Figure 4.7 shows the time traces of the modal amplitudes for two modes that have reached steady state. The traces correspond to modes with comparable eigenvalue magnitude but different types of eigenmode patterns. The blue curve in Figure 4.7 correspond to an eigenmode that is symmetrical with respect to the $x - y$ plane and whose eigenmode is plotted in Figure 4.8. While the red curve corresponds to an asymmetrical mode and is plotted

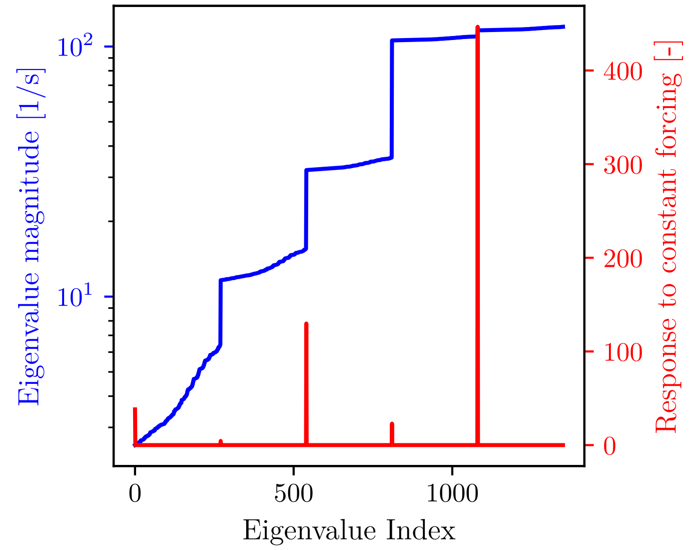

Figure 4.5: Example eigenvalue distribution for the cylinder case. The red line indicates the amplitude of the modal response to a constant excitation.

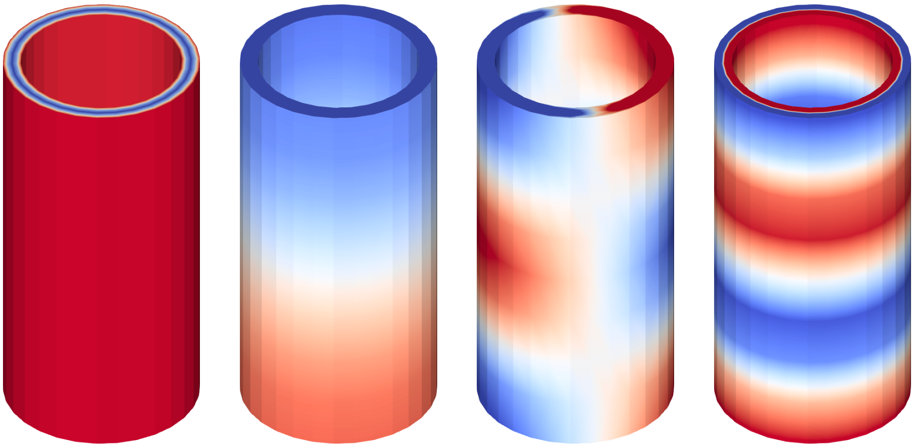

(a) Mode 0 **(b)** Mode 1 **(c)** Mode 7 **(d)** Mode 283

Figure 4.6: Selected thermal modes

in Figure 4.9. This pattern causes anti-symmetric modes to be more excited by the shedding phenomenon, the high frequency content visible in the time trace is in phase with the Strouhal number of the flow, around 0.2 at $\mathrm{Re}_D = 5000$. Because the Strouhal frequency is higher than the eigenfrequency of the mode, this is the cause of the long thermal transient observed in the temperature field. Similar heat flux time traces have been observed for a pipe in crossflow by Scholten and Murray [1998] using an experimental setup.

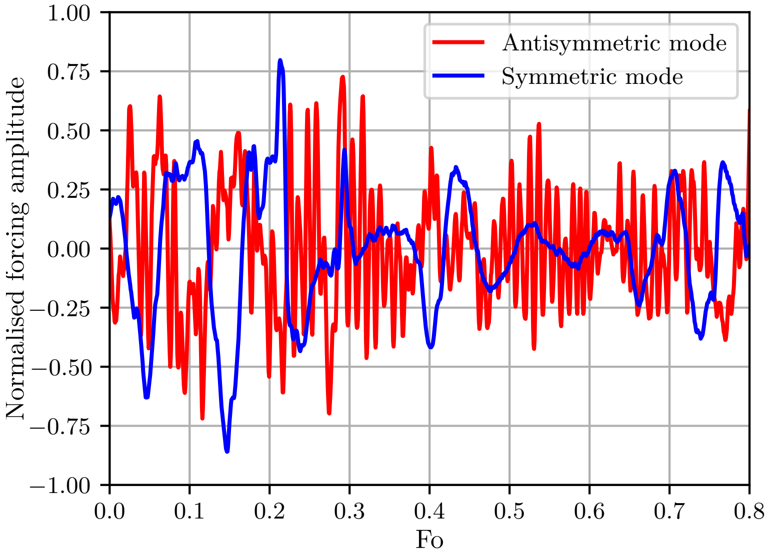

Figure 4.7: Normalised forcing signal of a symmetric and an asymmetric mode.

Scaling of the transient behaviour of the modal traces

Since the transient behaviour of the modes is proportional to $\lambda\mathrm{Fo}$, the time traces of the modal amplitudes can be normalised by the eigenvalue λ to demonstrate that the transient behaviour is independent of the eigenvalue. By replotting Figure 16 from the paper with the x-axis normalised by $\mathrm{Fo} * \lambda$, Figure 4.10 illustrates the time traces of the modal amplitudes for a set of modes exhibiting significant transient behaviour. Once the time axis is normalised by the eigenvalue, the time traces collapse onto each other, as predicted by Equation (29) in the paper.

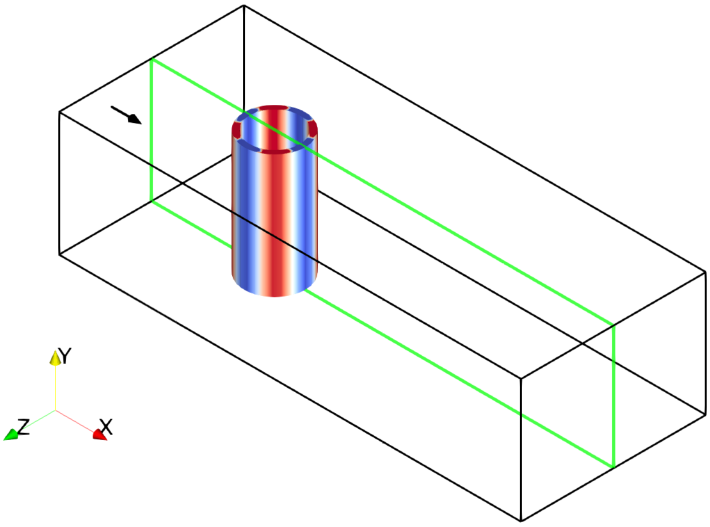

Figure 4.8: Symmetric mode shape of the temperature field around the $x-y$ plane (in green).

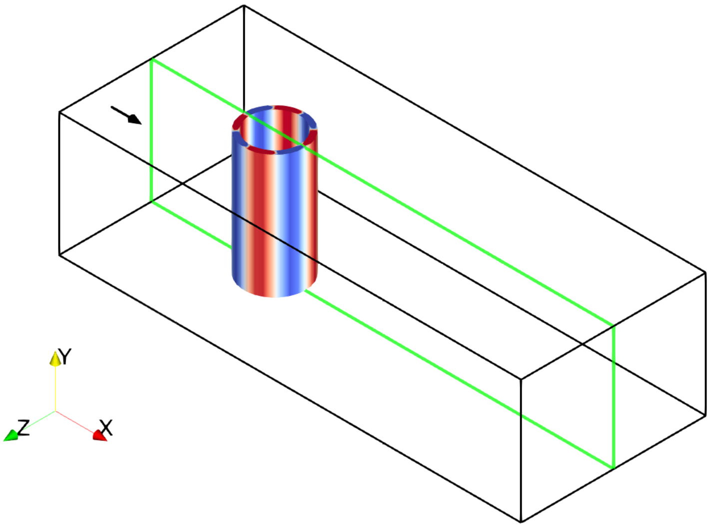

Figure 4.9: Asymmetric mode shape of the temperature field around the $x-y$ plane (in green).

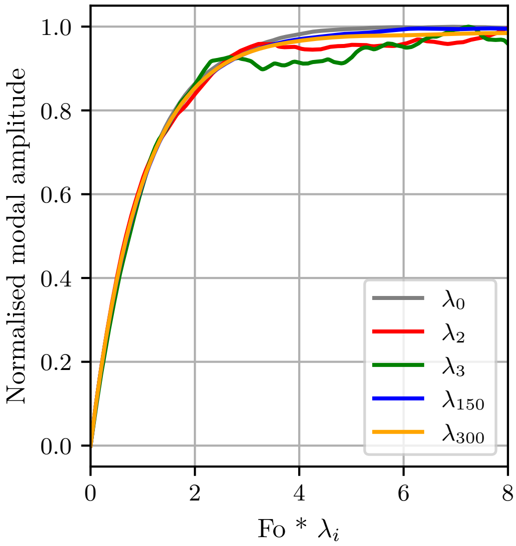

Figure 4.10: Normalised modal amplitude time traces

4.1.2 Statement of authorship

- Title of the paper: *Multiscale Unsteady Conjugate Transfer via Modal Projection*
- Publication status: Submitted for publication and in the review process
- Publication details: Dreze Y., Hao M. and di Mare L. "Multiscale Unsteady Conjugate Transfer via Modal Projection"
- Student Confirmation:
  - Student name: Yann Dreze
  - Contribution to the paper:

    I wrote all the code presented in the manuscript, I developed most of the methodology and theoretical analysis. I performed the numerical simulations presented in the paper and I wrote the paper manuscript.
  - Date and signature: , September 26, 2025
- Supervisor Confirmation:

  By signing the Statement of Authorship, you are certifying that the candidate made a substantial contribution to the publication, and that the description described above is accurate.

- Supervisor name and title: Luca di Mare, Associate Professor
- Supervisor comments: I confirm that the candidate's statement is an accurate description of his contribution to this publication.
- Signature and date: , September 26, 2025

4.2 Unsteady Conjugate Heat Transfer Effects on Flow Characteristics

This section presents a study that was undertaken to illustrate some of the effects CHT can have on flow behaviour and resulted in a journal article published in the *International Journal of Heat and Mass Transfer*, titled "Unsteady Conjugate Heat Transfer Effects on Flow Characteristics", [Dreze and di Mare, 2025]. The study investigates the influence of the thermal time scale disparity between conduction and convection on flow characteristics. In numerous experimental, numerical, and practical scenarios, thermal equilibrium between the media is not reached, and the system operates in a pseudo-steady state. In a few cases, some researchers have used models to account for this transient behaviour [Reiss et al., 1998, Ma et al., 2016]. This study demonstrates that until thermal steady-state is achieved, all flow quantities experience drift which follows a characteristic exponential decay. It should be mentioned that because the transient behaviour of the system is of interest, the conjugate model employed was not the modal projection method presented in section 4.1 but rather a classical time-accurate method. Additionally, the study discusses the integration of simplified models into engineering design workflows and evaluates their impact in terms of computational efficiency relative to classical simulations and acceptable error margins.

International Journal of Heat and Mass Transfer 246 (2025) 127036

Contents lists available at ScienceDirect

International Journal of Heat and Mass Transfer

journal homepage: www.elsevier.com/locate/hmt

Unsteady conjugate heat transfer effects on flow characteristics in transonic flow

Yann Dreze *, Luca di Mare

Department of Engineering Science, Oxford University, Oxford Thermofluids Institute, Southwell Building, Oxford, OX20ES, United Kingdom

ARTICLE INFO

Keywords:
Conjugate heat transfer
Unsteady conjugate heat transfer
Thermal transients
Capacity measurement

ABSTRACT

We present a detailed study into compressible flows in presence of unsteady conjugate heat transfer to the walls. The investigation reveals that all flow quantities experience drift until thermal steady state is achieved in both fluid and solid domains. The drift follows a characteristic exponential decay, and we demonstrate that the heat transfer process between the two domains is ruled by the ratio of thermal capacity and the Stanton number that characterises the interface. To illustrate these effects, we numerically analyse the influence of slow thermal transients due to conjugate heat transfer on discharge characteristics of non-adiabatic nozzles. A transonic nozzle with thermally conducting walls is simulated using numerical methods with different fidelity, from one-dimensional reduced-order models to large eddy simulations, and the transient evolution of mass flow rate is monitored. Additionally, it is observed that while preheating does not affect the decaying time constant of the drift, the bounds of the decay are directly proportional to the initial temperature difference.

1. Introduction

Conjugate heat transfer (CHT), the thermal interaction between fluid flow and solid bodies, plays a crucial role in understanding and optimising the performance of many fluid dynamics domains. Its significance spans from microscopic levels, such as near-wall turbulence [1] or the use of nanofluids for improved heat transfer [2], to macroscale systems such as thermal management in spacecraft, insulation in nuclear reactors, cooling of turbine blades, and thermal regulation in battery technology, [3,4].

In turbomachinery, CHT is a critical aspect when designing the hot parts in high-pressure turbines [5,6]. This is particularly important when considering the increased inlet temperatures of next-generation aero-engines, which can exceed the melting points of current turbine blade materials. These components therefore require complex thermal cooling system and accurate thermal analysis is needed to ensure their longevity and safety.

1.1. Effects of steady conjugate heat transfer through the external walls on flow characteristics

The present work examines the transient impact of the external thermal boundary on non-isentropic internal flows. However, before looking at transient effects, let us first consider with an example the steady effects that external heat transfer can have on global flow characteristics.

A Rayleigh flow describes a frictionless, non-adiabatic flow through a constant area duct with heat transfer. Using isentropic relations, the dimensional mass flow rate in the duct is given by the following equation:

$$\dot{m} = \frac{A\,p_t}{\sqrt{T_t}}\sqrt{\frac{\gamma}{R}}\,M\left(1+\frac{\gamma-1}{2}M^2\right)^{-\frac{\gamma+1}{2(\gamma-1)}} \tag{1}$$

For the traditional Rayleigh flow setup, the inlet Mach number and stagnation temperature are fixed along with the outlet static pressure. Therefore, for a given entropy rise, the mass flow rate is proportional to the total pressure at the inlet.

The total pressure can be found using the outlet pressure and a closed-form solution for internal compressible flows with an arbitrary combination of area change, heat addition. Details of the implementation can be found in Appendix A. The development lead to Eq. (2) which is a second-order equation for the exit Mach number based on an inlet Mach number and a stagnation temperature ratio. This approach provides a tool for analysing the steady effects of heat transfer on flow characteristics in a quasi-one-dimensional setting.

$$\frac{(1+\frac{A_1}{A_2}+2\gamma M_1^2)}{(1+\frac{A_2}{A_1}+2\gamma M_2^2)}\sqrt{\frac{T_{t,1}\,f(M_2)}{T_{t,2}\,f(M_1)}}\,\frac{M_2}{M_1}-1=0 \tag{2}$$

When looking at the enthalpy-entropy diagram for a Rayleigh flow, on the subsonic branch the entropy change will lead to a change in total

---

* Corresponding author.
E-mail address: yann.dreze@engs.ox.ac.uk (Y. Dreze).

https://doi.org/10.1016/j.ijheatmasstransfer.2025.127036
Received 12 September 2024; Received in revised form 24 March 2025; Accepted 26 March 2025

Nomenclature

α	Thermal diffusivity
δ_f	Thermal boundary layer thickness
δ_s	Thermal penetration depth in the solid
$\dot{m}$	Mass flow rate
Γ	Capacity
γ	Ratio of specific heats
μ	Dynamic viscosity
ρ	Density
τ	Characteristic time
θ	Dimensionless temperature
ξ, ζ, η	Geodesic coordinates
A	Area
a	Speed of sound
c_p	Specific heat capacity at constant pressure
c_v	Specific heat capacity at constant volume
F_{fx}	Friction force acting on the control volume projected in the streamwise direction
h	Specific enthalpy
h_f	Heat transfer coefficient
k	Thermal conductivity
M	Mach number
p	Pressure
Q	Heat transferred into the control volume
R	Specific gas constant
s	Specific entropy
T	Temperature
T'	Temperature perturbation
T_w	Temperature at the conjugate interface
U	Streamwise velocity magnitude
u, v, w	Velocity components
W_i	Characteristic variables
Ec	Eckert number
MA	Moving average
Pr	Prandtl number
Re	Reynolds number
Re_τ	Reynolds number based on the friction velocity
St	Stanton number

Subscripts and superscripts

x^*	Reference condition
x^+	Dimensionless distance
x_f	Related to the fluid
x_s	Related to the solid
x_t	Stagnation quantity
x_{SS}	Steady state value

pressure and Mach number that follows the direction of the entropy change. The opposite holds on the supersonic branch. Fig. 1 shows this phenomenon graphically by plotting the contours of the dimensional mass flow change with respect to adiabatic conditions for different inlet Mach number and total temperature increase. At low Mach number ($M_1 < 0.6$), the change in mass flow rate relative to adiabatic condition is less than proportional to the change in total temperature, i.e. a change of 1% in $T_{t,2}$ will lead to a change in mass flow rate less than 1% with respect to the adiabatic case. For $0.6 < M_1 < 1$, the change in mass flow rate becomes more than proportional to $T_{t,2}/T_{t,1}$. As the fluid continues to be heated, the flow eventually becomes thermally choked, resulting in smaller changes in mass flow rate. The unshaded area represents the thermally choked region. On the supersonic side, for most of the Mach number range tested, the change in mass flow rate is more than proportional to the stagnation temperature change. The greatest change in capacity occurs near sonic conditions where $\|\frac{dM}{ds}\|$ is maximum.

Practical examples of how heat transfer can influence flow characteristics can be found in numerous research areas. For instance, in combustor flows [7,8], in transonic compressors [9], and in hypersonic flows [3,10].

1.2. Effects of unsteady conjugate heat transfer through the external walls on flow characteristics

Having reviewed and demonstrated some steady state effects of conjugate heat transfer on a system, we now turn to the impact of unsteadiness. For instance, Fig. 2 sketches the time evolution of a flow quantity for an experiment involving the flow of a hot fluid through equipment of large thermal capacity, initially at room temperature, when CHT is taken into account. The initial transient phase corresponds to the fluid accelerating from rest to a quasi-steady state value from the perspective of fluid time scales. This state, denoted as Γ_{iso}, represents a system with isothermal walls since the large thermal capacity of the metal causes the interface to act as an isothermal boundary. After reaching this point, the variable gradually drifts as the metal approaches thermal steady state, Γ_{SS}. The time required to reach steady state depends on the thermal time scales of the solid.

A practical example can be found in aeroengines, where the time required to reach thermal equilibrium after startup often constitutes a significant portion of the flight envelope, leading to changes in the thermodynamic flow path, as described by Lazareff et al. [11]. Similar transient heat transfer conditions occur during engine start-up and shutdown in rocket propulsion systems. During these transients, the chamber or nozzle walls can reach temperatures higher than those observed during steady state operation and may experience substantial temperature gradients [12]. As a result, cooling systems designed for nominal engine conditions may be inadequate to ensure overall safety and structural integrity. Wang et al. [13] studied the cold start warm-up process of a steam turbine control valve, observing significant changes in temperature and heat flux throughout the startup process.

Hypersonic flows also are highly influenced by heat transfer, and it is widely recognised that outer walls do not reach thermal equilibrium during typical testing due to the rapid nature of the flow. As a result, walls are often modeled as isothermal, based on the assumption that they cannot respond quickly enough within the experiment's duration [14]. However, as reviewed by Lewis and Hickey [3], at high speeds, non-adiabatic wall temperatures significantly affect both the characteristics of the turbulent boundary layer and its transitional behaviour. Griffin et al. [10] proposed a scaling law for the transitional boundary layer thickness in hypersonic flows, emphasising the importance of accounting for non-adiabatic wall temperatures in such cases. Recently, [15] studied the mechanisms governing the unsteady interactions between a showckwave and a boundary layer.

Another area where thermal transients are of significant interest is experimental testing. Often, the temperature field of the test section is not matched to the target conditions. For example, turbine testing typically involves cooler test chamber walls compared to actual turbine walls. This mismatch can result in spurious temperature gradients and heat transfer from external surfaces, potentially compromising measurement accuracy. A practical example of this was observed by Adams et al. [16] during the design of a swirler for a transonic test turbine facility. They reported a 6% reduction in the mass-mean total temperature at the turbine inlet, which was attributed to convective heat transfer to the metal components.

From a transient perspective, many test facilities operate for a short duration, typically on the order of a few seconds. This limited

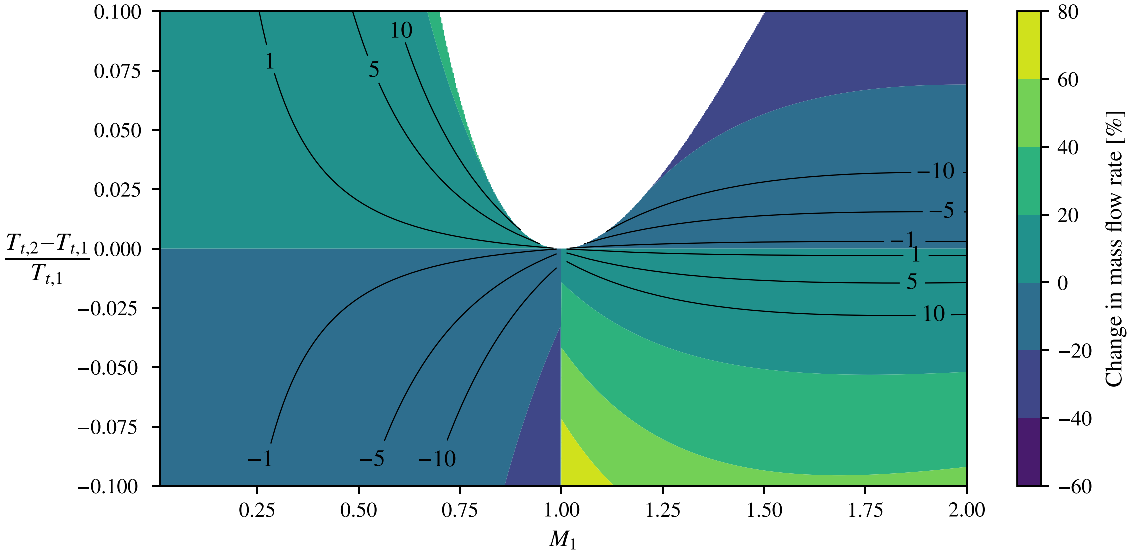

Fig. 1. Contours of the relative change in dimensional mass flow rate with respect to adiabatic conditions at fixed stagnation temperature and Mach number.

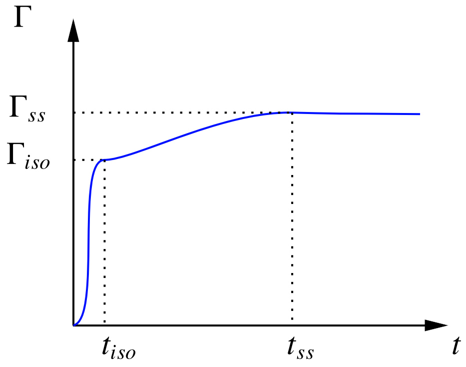

Fig. 2. Sketch of the typical unsteady behaviour of a global flow quantity with external heat transfer.

timeframe frequently proves often insufficient for solid components to achieve thermal equilibrium with the fluid. Measurements taken during this period would correspond to t_{iso}, as shown in Fig. 2. These slow thermal transients can significantly impact flow dynamics in high-temperature applications, particularly when tests are conducted in quick succession. Amend et al. [17] addressed this issue in their study of a lean-burn combustor simulator by implementing a transient effectiveness correction to account for convective heat loss to the endwalls.

Similarly, when calibrating total temperature probes, Englerth [18] found that repeatability and sensor performance were highly dependent on the thermal state of the stainless steel facility. To ensure accurate measurements, they ran the facility until the nozzle reached a steady state temperature, minimising heat transfer between the fluid and the structure, which otherwise affected total temperature readings and sensor accuracy. Achieving steady state conditions greatly improved measurement repeatability.

In transient heat transfer studies, thermal transients have been shown to affect external wall heat transfer characteristics. Bianchi et al. [19] studied unsteady heat conduction in nozzles and its impact on erosion. Their results indicated that the steady state condition was achieved near the throat region, while regions farther from the throat — experiencing lower heating rates — remained far from steady state. Xue et al. [20] developed a transient measurement technique for heat transfer that accounts for linear temperature variations in the main flow during the measurement window due to cooling.

These examples underscore the importance of unsteady heat transfer effects in practical situations, as they can significantly alter both local and global flow parameters. Researchers must be aware that their experiments capture either Γ_{iso} or Γ_{SS}; otherwise, time-dependent modeling errors may be introduced. These steady and unsteady phenomena are often overlooked in standard testing procedures, where measurements rarely account for the influence of external heat transfer.

A similar argument can be made from a computational perspective. Most numerical methods do not account for CHT; the interface between solid walls and fluid domains is typically modeled using simplified thermal boundary conditions, such as fixed heat flux or constant temperature. The isothermal boundary condition represents rapid transients, where swift changes in state parameters preclude significant heat transfer. This assumption implies that the surrounding environment has infinite heat capacity, corresponding to the Γ_{iso} state from Fig. 2. Conversely, constant heat flux boundaries, particularly the limiting case of adiabatic flow, assume that the gas has achieved thermal equilibrium with its surroundings. This condition is usually associated with slow, time-dependent processes. Except for high-temperature cases, the adiabatic or isothermal boundary assumptions are widely adopted as default boundary condition in numerical simulations for blade and end walls. Only for thermal assessments of turbine blades or combustors is heat transfer to the solid taken into account, and even then, it is often done in a steady state manner. This simplification represents a significant limitation that must be carefully considered during the validation or calibration of CFD results against experimental data.

The reason time-accurate conjugate heat transfer is rarely accounted for in numerical simulations is because it faces significant challenges. These arise primarily due to the substantial disparity between thermal time scales of solids and fluids. Conventional numerical methods, such as URANS or LES, rely on time-marching approaches with small timesteps. When combined with stringent grid requirements for the solid domain, these methods become computationally intensive for conjugate simulations spanning solid thermal time scales.

Reduced-order models offer a promising alternative for capturing both steady and transient CHT effects. These models can provide rapid insights, enabling efficient analysis of CHT impacts and facilitating the development of mitigation strategies. This study will then also aim to assess the ability of simplified models to get order of magnitude estimates and to explore potential mitigation strategies of the slow transients effect.

To further understand the parameters that govern the approach to steady state of the coupled fluid-solid system, we propose a simple

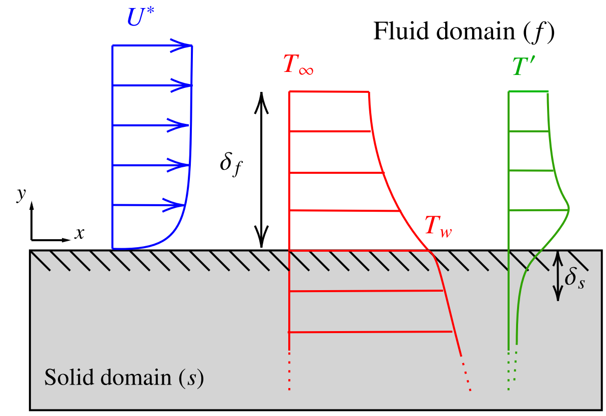

Fig. 3. Sketch of the fluid boundary layer and solid domain.

dimensional analysis of a boundary layer flow. The problem of interest consist of a semi-infinite solid domain in contact with a fluid. The fluid has a streamwise freestream velocity U^* and freestream temperature T_∞. The fluid has some arbitrary temperature fluctuation profile T' associated with a thermal penetration depth δ_s in the solid. A sketch of the problem is available in Fig. 3.

The energy equation for an incompressible boundary layer in coordinates aligned with the surface is given by:

$$\rho_f c_{p,f}\left(\frac{\partial T}{\partial t}+u\frac{\partial T}{\partial x}+v\frac{\partial T}{\partial y}\right)=k_f\frac{\partial^2 T}{\partial y^2}+\mu\left(\frac{\partial u}{\partial y}\right)^2 \tag{3}$$

where u and v are velocity components in x and y directions respectively, t is time, T is temperature, k_f is the thermal conductivity of the fluid, μ is the dynamic viscosity, ρ_f is the density of the fluid and $c_{p,f}$ is the specific heat capacity at constant pressure. The dissipation term is included to ensure the analysis is applicable to both subsonic and transonic flows.

On the solid side, the unsteady heat equation applies. Assuming that the streamwise characteristic length scale is much larger than the transversal one, the streamwise heat diffusion can be neglected. The energy equation for the solid is then given by:

$$\rho_s c_{p,s}\left(\frac{\partial T}{\partial t}\right)=k_s\frac{\partial^2 T}{\partial y^2} \tag{4}$$

where k_s is the thermal conductivity of the solid, ρ_s is the density of the solid and $c_{p,s}$ is the specific heat capacity.

At the interface, we have the continuity of both the heat flux and the temperature:

$$k_s\left.\frac{\partial T}{\partial y}\right|_s=k_f\left.\frac{\partial T}{\partial y}\right|_f \quad \& \quad T|_s=T|_f \tag{5}$$

On the fluid side, introducing the following dimensionless variables:

$$\tilde{u}=\frac{u}{U^*},\ \tilde{v}=\frac{v}{U^*},\ \tilde{t}=t\frac{U^*}{L^*},\ \tilde{x}=\frac{x}{L^*},\ \tilde{y}=\frac{y}{\delta_f},\ \tilde{T}=\frac{T-T_\infty}{T_w-T_\infty}$$

Where L^* is a characteristic length scale in the streamwise direction, U^* is the characteristic streamwise velocity, T_w is the interface temperature and δ_f is the thermal boundary layer thickness of the fluid domain.

$$\frac{\partial\tilde{T}}{\partial\tilde{t}}+\tilde{u}\frac{\partial\tilde{T}}{\partial x^*}+\tilde{v}\frac{\partial\tilde{T}}{\partial y^*}=\frac{1}{\mathrm{Re\,Pr}}\left(\frac{L^*}{\delta_f}\right)^2\frac{\partial^2\tilde{T}}{\partial\tilde{y}^2}+\frac{\mu L^*}{\rho_f c_{p,f}U^*(T_w-T_\infty)}\left(\frac{U^*}{\delta_f}\right)^2\left(\frac{\partial\tilde{u}}{\partial\tilde{y}}\right)^2 \tag{6}$$

Introducing the Eckert number Ec:

$$\frac{\partial\tilde{T}}{\partial\tilde{t}}+\tilde{u}\frac{\partial\tilde{T}}{\partial x^*}+\tilde{v}\frac{\partial\tilde{T}}{\partial y^*}=\frac{1}{\mathrm{Re\,Pr}}\left(\frac{L^*}{\delta_f}\right)^2\frac{\partial^2\tilde{T}}{\partial\tilde{y}^2}+\frac{\mathrm{Ec}}{\mathrm{Re}}\left(\frac{L^*}{\delta_f}\right)^2\left(\frac{\partial\tilde{u}}{\partial\tilde{y}}\right)^2 \tag{7}$$

Eq. (7) can be further simplified using the desired scaling for the Reynolds number and the streamwise to transversal characteristic length scale ratio $\left(\frac{L^*}{\delta_f}\right)\sim\mathrm{Re}^{\,a}$.

$$\text{General BL:}\quad \frac{\partial\tilde{T}}{\partial\tilde{t}}+\tilde{u}\frac{\partial\tilde{T}}{\partial x^*}+\tilde{v}\frac{\partial\tilde{T}}{\partial y^*}=\frac{\mathrm{Re}^{-1+2a}}{\mathrm{Pr}}\frac{\partial^2\tilde{T}}{\partial\tilde{y}^2}+\mathrm{Ec}\mathrm{Re}^{-1+2a}\left(\frac{\partial\tilde{u}}{\partial\tilde{y}}\right)^2 \tag{8}$$

For instance, in a laminar boundary layer the proportionality relation is given by $\left(\frac{L}{\delta_f}\right)\sim\sqrt{\mathrm{Re}}$ which would lead to Eq. (9).

$$\text{Laminar BL:}\quad \frac{\partial\tilde{T}}{\partial\tilde{t}}+\tilde{u}\frac{\partial\tilde{T}}{\partial x^*}+\tilde{v}\frac{\partial\tilde{T}}{\partial y^*}=\frac{1}{\mathrm{Pr}}\frac{\partial^2\tilde{T}}{\partial\tilde{y}^2}+\mathrm{Ec}\left(\frac{\partial\tilde{u}}{\partial\tilde{y}}\right)^2 \tag{9}$$

In Eq. (8), the approach to a steady state is dominated by the diffusion coefficient, $\left(\frac{\mathrm{Re}^{-1+2a}}{\mathrm{Pr}}\right)$, in front of the second order term. The nonlinear term and the convective terms can also affect the approach to equilibrium especially at the initial state when the flow has not settled yet to a quasi-steady state, but the second-order derivative term is generally the dominant factor in determining the approach to steady state rate.

For the solid domain, we introduce the dimensionless transversal coordinate on the solid side $\tilde{y}_s=\frac{y}{\delta_s}$, based on the thermal boundary layer thickness. The interface condition can be rewritten as:

$$\frac{k_s}{\delta_s}\left.\frac{\partial\tilde{T}}{\partial\tilde{y}_s}\right|_s=\frac{k_f}{\delta_f}\left.\frac{\partial\tilde{T}}{\partial\tilde{y}}\right|_f \tag{10}$$

Assuming the gradients of the normalised temperature with respect to the dimensionless transversal coordinate specific to the individual domains are of the same order, we have:

$$\frac{\delta_s}{\delta_f}\sim\left(\frac{k_s}{k_f}\right) \tag{11}$$

Finally, the unsteady heat equation in the solid can be made dimensionless:

$$\frac{\partial\tilde{T}}{\partial\tilde{t}}=\frac{L^*}{U^*}\frac{\alpha_s}{\delta_s^2}\frac{\partial^2\tilde{T}}{\partial\tilde{y}_s^2} \tag{12}$$

Under the assumption that in the boundary layer $h_f=k_f/\delta_f$, we have:

$$\frac{\partial\tilde{T}}{\partial\tilde{t}}=\frac{L^*}{U^*}\frac{\alpha_f}{\alpha_f}\frac{\alpha_s}{\delta_s^2}\frac{\partial^2\tilde{T}}{\partial{\tilde{y}_s}^2}=\frac{\partial\tilde{T}}{\partial\tilde{t}}=\frac{L^*\delta_f}{\delta_s^2}\frac{\alpha_s}{\alpha_f}\mathrm{St}\frac{\partial^2\tilde{T}}{\partial{\tilde{y}_s}^2} \tag{13}$$

Using the proportionality found in the interface equation, we have the final equation for the solid side:

$$\frac{\partial\tilde{T}}{\partial\tilde{t}}=\frac{L^*}{\delta_s}\frac{\rho_f c_{p,f}}{\rho_s c_{p,s}}\mathrm{St}\frac{\partial^2\tilde{T}}{\partial{\tilde{y}_s}^2}=\frac{\delta_f}{\delta_s}\frac{\rho_f c_{p,f}}{\rho_s c_{p,s}}\frac{\mathrm{Re}^a}{\mathrm{St}}\frac{\partial^2\tilde{T}}{\partial{\tilde{y}_s}^2} \tag{14}$$

$$=\frac{k_f\rho_f c_{p,f}}{k_s\rho_s c_{p,s}}\frac{\mathrm{Re}^a}{\mathrm{St}}\frac{\partial^2\tilde{T}}{\partial{\tilde{y}_s}^2} \tag{15}$$

In Eqs. (8) and (15), the diffusion coefficients determine how quickly the system approaches steady state. On the fluid side from Eq. (8), shows that the diffusion coefficient is dependent on the Prandtl number and the Reynolds number scaling of the boundary layer height. On the solid side, Eq. (15), the approach to steady state depends on the thermal capacity ratio of the solid to the fluid, the ratios of heat conductivities, the Stanton number and again on the Reynolds number. In Eq. (15), the product $k\rho c_p$ appear which is characteristic of transient thermal analysis because it directly influences the rate at which heat is absorbed, stored, and conducted within a material, [21].

For a typical, fluid-solid coupled system of air and steel the following properties can be chosen. The metal specific heat is 465 J/kg K, thermal conductivity 54 W/(m K) and density 7800 $\mathrm{kg/m^3}$. The

Prandtl number of air is of order 1, thermal conductivity 3×10^{-2}W/(m K), density 1.293 kg/m^3 and specific heat capacity 1000 J/kg K. The Stanton number of the coupled system is $\approx\ 10^{-1}$ with a Reynolds number of 100,000.

Using these values, in a turbulent boundary layer, the ratio between the diffusion constants of the two equations become:

$$\frac{\frac{k_f \rho_f c_{p,f}}{k_s \rho_s c_{p,s}} \mathrm{St} \mathrm{Re}^a}{\left(\frac{\mathrm{Re}^{-1+2a}}{\mathrm{Pr}}\right)} \simeq 4 \cdot 10^{-4} \tag{16}$$

Eq. (16) shows that the ratio of the diffusion constants is of the order of 10^{-4}. Indicating that, if the system was decoupled, the fluid side would reach a steady state much faster than the solid side. However, in the coupled system, the solid side will influence the fluid side, and the system will reach a steady state at a rate determined by the solid side, forcing the simulation or experiment to be carried out for extended time periods. Besides the physical properties of the system, the main parameters that describe this ratio are the Stanton number, which directly describes the interface condition, and the Reynolds number. A similar result for the time scales' ratio was obtained by He and Oldfield [22], who noted that in typical operating conditions, the ratio of these time scales is approximately 10,000.

The aim of the paper is to illustrate the impact of unsteady CHT on global flow quantities. To this end, we will simulate numerically the transient flow through a nozzle with conducting walls. The global flow quantity of interest chosen is capacity, which will be recorded over time, similarly to Fig. 2, to see how it evolves. The transient evolution will be characterised by the parameters governing the approach to steady state of the coupled fluid-solid system.

1.3. Capacity prediction

Flow capacity can be defined as:

$$\Gamma = \frac{\dot{m}\sqrt{T_t}}{p_t} \tag{17}$$

In axial turbomachinery, accurate capacity measurements has been a long-standing challenge and area of research interest [23,24]. The capacity of the high-pressure nozzle guide vane (NGV) typically plays a critical role in design as it sets the overall engine capacity. Inaccurate prediction of engine capacity leads to mismatching of downstream stages, where even minor deviations from design conditions can significantly impact performance. Despite technological advancements, there remains a noticeable discrepancy between engine test capacity measurements and those obtained through alternative methods. Previous research has identified various potential sources for this discrepancy. From a numerical perspective, Fielding [25] provided insights on the relationship between irreversibilities and capacity measurements in gas turbines and introduced a correction factor to account for this effect. Afanasiev et al. [26] put forward the influence of 3D flow effects on capacity measurements by comparing 1D and 3D approaches. Experimentally, Povey [24] studied the effect of film cooling on capacity measurements. Burdett et al. [27] presented a novel technique for low uncertainty capacity measurements. CHT can significantly affect capacity measurements and predictions due to the extreme operating conditions of NGVs. These components typically function in high-pressure, high-temperature environments, often approaching 1500 °C.

2. Methodology

The present numerical study will use two methods to investigate the impact of unsteady conjugate heat transfer and these methods are outlines in this section. First, an unsteady quasi-one-dimensional analysis utilising the method of characteristics (MOC). This is used to get an estimate on the time scales and bounds of the CHT influence. It is anticipated that this reduced order method will adequately capture slow thermal transients, while the influence of turbulent perturbations on the system will not be captured. Then, fully coupled Large Eddy Simulations (LES) will serve as baseline cases.

2.1. Unsteady, quasi-one-dimensional compressible flow with heat transfer (MOC)

The method of characteristics provides a straightforward approach to solving the unsteady Euler equations [28–30]. It has also been successfully applied to simulate efficiently unsteady flows with heat transfer. Issa and Spalding [31] presented a procedure for solving one-dimensional, unsteady, compressible, frictional flows with heat transfer, demonstrating its effectiveness in simulating shock tube flows. Similarly, Huang [32] employed the method of characteristics to study unsteady flow in a heat exchanger. The unsteady Euler equations can be transformed into the characteristic expression written in Eq. (18), details of the derivation are available in Appendix B. The source vector of the conservative variables has been projected and behave as source terms for the entropy and the sounds waves.

$$\begin{aligned}
\frac{\partial W_1}{\partial t} &= -U & &\frac{\partial W_1}{\partial x} & &-(\gamma-1)\frac{\rho U}{a^2}\delta Q_x \\
\frac{\partial W_2}{\partial t} &= -(U+a) & &\frac{\partial W_2}{\partial x} - Ua\frac{1}{A}\frac{dA}{dx} & &+(\gamma-1)\frac{U}{a}\ \delta Q_x \\
\frac{\partial W_3}{\partial t} &= -(U-a) & &\frac{\partial W_3}{\partial x} + Ua\frac{1}{A}\frac{dA}{dx} & &-(\gamma-1)\frac{U}{a}\ \delta Q_x
\end{aligned} \tag{18}$$

The conjugate portion of the code solves the unsteady heat conduction equation in a 2D finite element framework fully coupled with the MOC. Unlike the MOC, wall-normal temperature variations are considered with both streamwise and wall-normal conduction solved for. The interface condition is imposed by continuity of the heat flux. The heat flux can be inferred from the temperature difference between the fluid and the solid and a correlation for the heat transfer coefficient, for instance the Dittus–Boelter equation for turbulent flows in tubes.

2.2. 3D Large Eddy Simulations (LES)

The flow equations are solved using the in-house code H4X [33–36]. The code is a cell-centred finite volume code based on a multiblock grid arrangement. The flow field is represented by the viscous variables: velocities, temperature, pressure. The equations of motion for a compressible fluid are solved in conservative form. The spatial discretisation is third-order accurate in space for the inviscid fluxes. Third-order accuracy is achieved on a compact stencil by using variable extrapolation. No limiter is applied to the entropy and vorticity fields whereas the sound waves are limited using a third order limiter introduced by [37]. The extrapolation is based on weighted least-square gradients. The gradient stencil contains all the face neighbours of each cell. For the purpose of variable extrapolation onto a cell interface, the gradient stencil is biased by removing the contributions from the neighbour on the other side of the interface. At low Mach numbers, the numerical fluxes are adapted following the work of Hope-Collins and di Mare [34] and a modified pressure flux is employed. The viscous fluxes are evaluated using a second-order discretisation. Advancement in time is performed using a formally second-order accurate implicit scheme. The implicit iterations are based on a dual-time stepping formulation. The dual-time framework is advantageous for unsteady problems with multiple time scales, such as CHT problems. It allows for the separation of these scales, enabling each to be resolved appropriately without the need for excessively small physical time steps. The code is parallelised by partitioning the blocks of the multiblock grid among the available MPI ranks. Within each rank, block operations are parallelised using OpenMP. Computations and communications are overlaid to hide the latency of the network fabric. The computations have been done on the Cirrus UK National Tier-2 HPC Service.

At the inflow boundary, synthetic turbulence is generated using the method described by Dreze et al. [33]. This technique uses modified uniformly distributed random sequences to construct divergence-free anisotropic random fields with sensible spectrum and complete complex correlation in space and time.

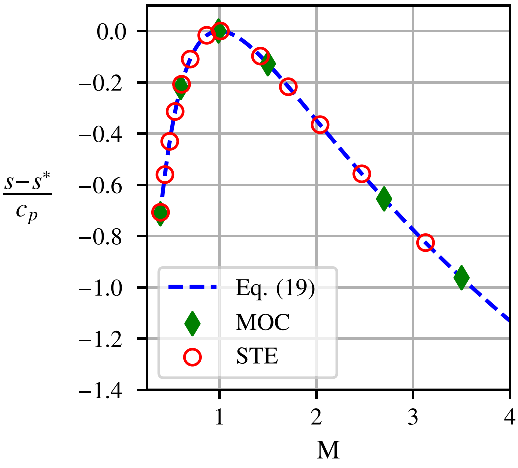

Fig. 4. Validation of the steady state Rayleigh flow for the STE and MOC methods.

The conjugate portion of the code solves the unsteady heat conduction equation in a fully-coupled fashion using a node-based finite element framework. The solid domain mesh is directly extruded from the interface surface and the mesh is scaled proportionally to the wall-normal mesh density of the fluid domain. This technique avoids the requirements of generating two separate meshes and as well as the overheads related to a separate data structures for the solid grid and provisions for interpolation of temperatures and fluxes between the two grids. The extrusion uses a thin layer approximation to form the heat conduction equation. The Laplacian of the temperature in a thin layer for geodesic coordinates on a smooth surface can be written as:

$$\mathcal{L}(T) = \frac{\partial^2 T}{\partial \xi^2} + \frac{\partial^2 T}{\partial \eta^2} + \frac{\partial^2 T}{\partial \zeta^2} + \frac{1}{R_c}\frac{\partial T}{\partial \zeta} \tag{19}$$

where $\frac{1}{R_c}$ is the local harmonic mean curvature of the surface.

3. Results

This section studies two different cases. First, a Rayleigh flow is used to validate the different conjugate methods. Then, as Fig. 1 showed that the effect of heat transfer on a discharge characteristic of quasi-one-dimensional flow is strongest near sonic conditions, a transonic nozzle is simulated and the transient evolution of capacity is recorded.

3.1. Channel with uniform heat flux

To validate the inviscid MOC and the steady approach proposed, a Rayleigh flow is used. The dimensionless change in entropy with respect to sonic conditions has been derived in Shapiro [38] and is shown in Eq. (20). Fig. 4 compares this theoretical solution with the different implementations to demonstrates agreement of the solutions for this reference case for the inviscid approaches. In all cases the entropy change has been applied as a constant uniform heat flux along the length of the domain.

$$\frac{s-s^*}{c_P} = \ln\left[M^2\left(\frac{\gamma+1}{1+\gamma M^2}\right)^{(\gamma+1)/\gamma}\right] \tag{20}$$

Table 1
Grid statistics for the channel flow simulation.

M_1	Re_τ	(N_x, N_y, N_z)	Δx^+	Δy^+	Δz^+
0.1	178.38	(312, 144, 128)	14.34	0.31	5.92

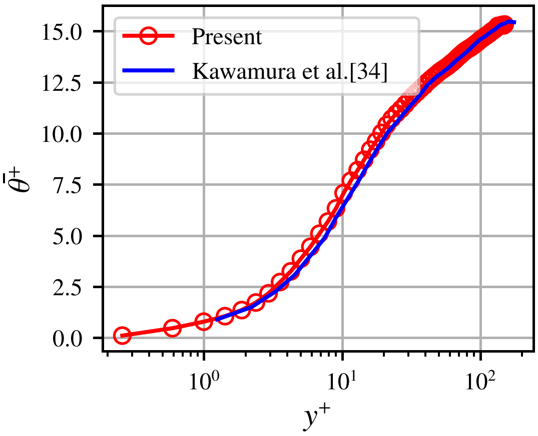

Fig. 5. Mean dimensionless temperature profile for the channel flow.

To validate the LES methodology, the present methodology is compared to simulations by Kawamura et al. [39]. They simulated heated channel flows with symmetrical heating from both walls. The heating is applied using a uniform constant heat flux. To keep the energy balanced, a negative source term is applied to the energy equation. The bulk Reynolds number is 5500 corresponding to a Reynolds number based on the friction velocity of 180 and the inlet Mach number is 0.1, to align best with the incompressible results from Kawamura et al. [39]. The Prandtl number is set to 0.71. The streamwise length of the computational domain is $8\pi\delta$ while the transversal length is $4/3\pi\delta$ where δ is the channel half-width. The first section of length $3\pi\delta$ section was used for the inflow generated fluctuations to settle, and the heat flux was only applied to the remaining of the domain. The grid has a stretching in the wall-normal directions detailed in [40] and grid statistics can be found in Table 1. The mean normalised temperature θ^+ profile is shown in Fig. 5 and shows good agreement with Kawamura et al. [39]. Towards the middle of the channel, the temperature profile is overpredicted by a maximum of 3.7%.

Now that both approaches have been validated, let us investigate the transient evolution of flow capacity. The channel was started from rest and the capacity was recorded. The transient evolution of the normalised capacity is shown in Fig. 6 , the time is normalised by the channel flow through time, defined as the length of the channel divided by the bulk velocity. In this case the time to reach steady state is relatively short in terms of fluid time scales because the boundary condition is time invariant. The capacity predictions by the quasi one-dimensional methods are accurate within a couple of percents and can be attributed to boundary layer blockage, effectively reducing the core flow area. This is a well-known phenomenon limitation and multiple correction methodologies to account for viscous effects and boundary layer growth have been proposed in the literature, [41,42].

3.2. Back nozzle

The transonic case examined is an axisymmetric convergent-divergent nozzle, originally studied by Back et al. [43]. The primary objective of their study was to collect experimental data on convective heat transfer in turbulent flows characterised by significant pressure gradients, where boundary layers where relatively thin compared to the channel cross-section.

The specific configuration involves a nozzle discharging a perfectly expanded isothermal free jet at Mach 2.4 for a Reynolds number based on the throat radius of Re= 4.1×10^4 and a Reynolds number based on the friction velocity $\mathrm{Re}_\tau = 993$, with a pressure ratio of 11. The boundary conditions at the nozzle inlet are set to a stagnation temperature of 833 K and a pressure of 10.34 bar. The freestream boundary condition is established at standard atmospheric pressure and room temperature. This case serves as an excellent test scenario due to the extensive available data on heat transfer. The nozzle external walls

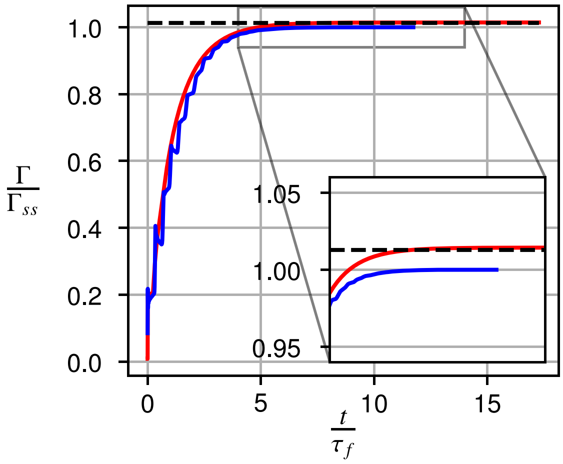

Fig. 6. Transient evolution of capacity normalised by the steady state capacity value of the LES. Black curve is steady method, red curve is MOC and blue curve is LES results. (For interpretation of the references to colour in this figure legend, the reader is referred to the web version of this article.)

Table 2
Global properties of the cases for the Back nozzle.

	Back et al.	LES	Finer LES (adiabatic)
M_2	2.45	2.42	2.41
St $\times 10^3$	1.58	1.50	1.53
$\Gamma \times 10^5$ $[m\sqrt{K}s]$	6.46	6.31	6.34

are made of 8 mm thick 502-type stainless steel and are assumed to be thermally insulated to the exterior.

The grid used for this case is a structured radial grid with a conformal elliptic transformation to an axisymmetric domain with a power law stretching at the walls. The grid size is (288 × 128 × 128). This leads to a grid spacing of Δy^+ in the range $[0.71, 3.27]$ on the fluid side and $[0.32, 1.46]$ on the solid side. The mesh on the solid side is finer at the wall because the lower penetration depth in the solid requires appropriate resolution to capture correctly the wall fluctuations, as per Eq. (11). The streamwise spacing was adjusted so that it lied in the range $\Delta x^+ \in [10, 45]$. The domain extends 3 nozzle diameters upstream of the nozzle inlet to allow for the synthetic turbulence to morph into the prescribed turbulent profiles. The profiles are fully turbulent following a 1/7-power-law curve as reported in [43]. Once thermal steady state reached for the combined system, the simulations were run for 10 flow-through times to record steady state statistics. CHT is not considered in the extended upstream domain.

Fig. 7 shows the convective heat-transfer coefficient of the LES results, and comparison to data extracted from Back et al. [43]. The largest difference between the experimental data and the LES results is downstream of the nozzle throat towards the exit of the nozzle where the relative difference is 19%. LES data is also compared with a finer grid of 288 × 160 × 160 with adiabatic walls, to show consistency and appropriate resolution. Even if the finer grid captures better the heat transfer coefficient peak at the throat the maximum difference between the two grids is less than 5% for the heat transfer coefficient. The difficulty in predicting the divergent section has been noted in previous studies [44–46] and despite some discrepancies, the main trend is well captured, reinforcing confidence in the overall results. Table 2 compares also macroscale properties of the different cases, confirming the ability of the chosen grid to simulate the desired setup.

For the MOC approach the heat transfer coefficients were directly taken from the experimental data.

The transient behaviour of the nozzle is shown in Figs. 8 and 9, the dark blue line correspond to a moving average (MA) value while the light blue is the instantaneous value. Fig. 8 shows the initial startup period that ends when the first pseudo steady state is reached. Fig. 9 then plots the slow capacity drift that occurs because of the external walls are heating up before reaching a final steady state. In both plots the dimensionless time has been normalised by the constants found in Section 1.2.

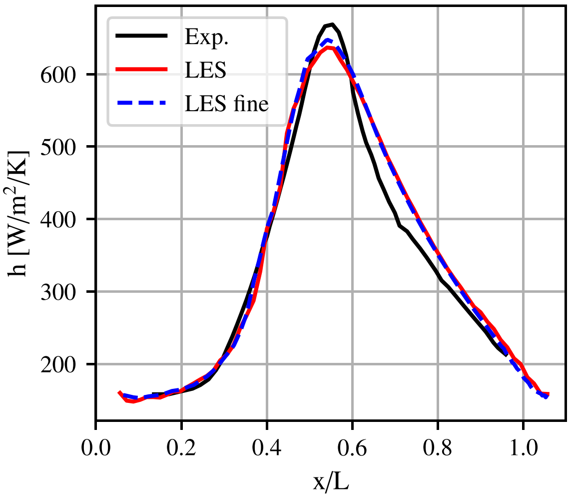

Fig. 7. Steady heat transfer coefficient for the Back nozzle.

For both the LES and the MOC, the capacity in the initial pseudo steady state is higher than the final steady state value. For instance, as seen in Fig. 9, the pseudo steady state value for the LES case is $\Gamma = 6.42 \times 10^{-5}$ while the final steady state value is $\Gamma = 6.11 \times 10^{-5}$. The overprediction comes from the fluid being overcooled because of the initial temperature difference between the walls and the flow. This leads to denser flow and therefore greater mass flux. Therefore, as per Fig. 9, if the external walls are not at thermal steady state, the capacity will be overpredicted by 1.7%. Looking at the comparison between the LES and MOC predictions for the final value of capacity, the quasi one dimensional method fall within 2% of the LES predictions. Similarly to Section 3.1, while the one-dimensional model fails to capture the boundary layer blockage effect, the differences in the predictions remain low due to the relatively simple geometry and thin boundary layers. But the transient behaviour of capacity is well captured by the MOC method. In terms of computational efficiency, the 1D MOC method completes within a minute on a standard laptop, whereas the full transient conjugate LES simulation requires access to large multicore facilities. This stark contrast underscores the practicality of MOC for rapid analysis.

The transient behaviour of capacity has the characteristic exponential decay of a preheated body cooled by convection. The characteristic time of the decay to steady state depends on the solid thermal properties and the heat transfer coefficient. When superimposed, one can see that the capacity decay in the LES case is lagging in time with respect to the one-dimensional model and has narrower bounds. This is because the boundary layer acts as a thermal resistance for heat transfer, slowing down the rate of heat transfer between the surface and the fluid. The fluid in direct contact with the cold surface quickly cools down and loses heat, while the faster-moving fluid above this layer does not lose heat as quickly. Resulting in additional time for the heat flux that is lost to the external wall to reach the mean flow, the amplitude is also lower because not all the heat transferred is reaching the mean flow. The thicker the boundary layer, the greater the resistance to heat transfer.

This phenomenon has been well-known and quantified for critical flow Venturi (CFV) nozzle, warmer, lower density gas near the CFV wall reduces mass flux through the CFV, an effect that increases in significance at lower Reynolds numbers. Wright et al. [47] proposed

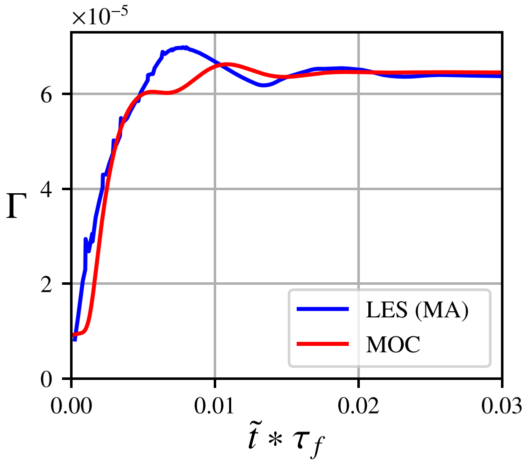

Fig. 8. Time evolution of the nozzle capacity starting from rest. (For interpretation of the references to colour in this figure legend, the reader is referred to the web version of this article.)

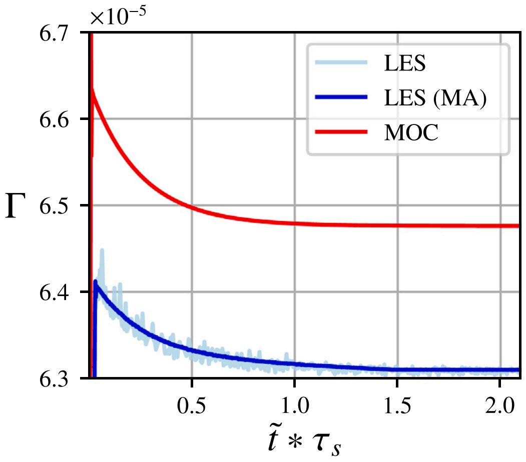

Fig. 9. Time evolution of the nozzle capacity after the initial startup transient. (For interpretation of the references to colour in this figure legend, the reader is referred to the web version of this article.)

a correction factor for the thermal boundary layer effect. Wang et al. [48],Ding et al. [49] also studied this effect experimentally and numerically and concluded that it can have great impact on the mass flow.

To reduce the time required for the thermal transient to vanish, one solution is to preheat the walls to try to lower the initial temperature difference. Fig. 10 plots a case where the external walls have been preheated to 75% of their steady state temperature rise.

During the thermal transient, the temperature difference in the metal decays exponentially, and the temperature distribution in the solid stays self-similar, if streamwise conduction can be ignored. This is because while the time constant of the solid is only related to the thermal properties of the system, the bounds of the decay are directly proportional to the fluid-solid temperature difference at the first pseudo-steady state.

4. Conclusion

This article has presented a comprehensive study of the existing research on the influence of external heat transfer on flow characteristics. Until thermal steady state is reached, all flow quantities are drifting, and this transient can be significant in case of high-temperature gradients between the initial solid thermal state and the steady state value. The study has focused on a practical application using capacity prediction to demonstrate these effects and to assess on the ability of simple models to predict the range of impact. For the transonic nozzle case, the error made if the external heat loss is not taken into account is about 2%. However, in other scenarios and quantity of interest it can have a greater impact, as reported by [16].

It was concluded that these methods are well suited to predict the global effects of heat loss. The literature survey showed that only few research items talk about this issue, but researcher could benefit with the use of 1D models to better design for this phenomenon. While for more complex cases, the predicted values might be offset because of unaccounted for 3D effects or other, the authors believe that the extent of the influence of CHT will still be well captured due to its intrinsic influence on the coreflow.

Finally, one strategy to minimise the effects of the slow thermal transients is to pre-heat the external walls to reduce the time to reach a steady state. While the exponential decay of the capacity will be self-similar, the amplitude of the decay will be directly proportional to the initial temperature difference.

A notable limitation of this study is the scarcity of experimental data for validation, as existing high-temperature experiments rarely comment on the thermal equilibrium or report time-resolved temperature fields. Future transient thermal tests cases would be valuable for cross-validating the numerical results.

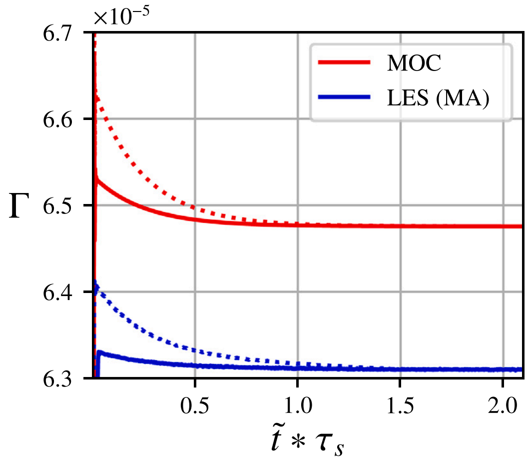

Fig. 10. Effect of preheating on the capacity evolution. Dotted lines are non-preheated cases, while solid lines are preheated cases.

CRediT authorship contribution statement

Yann Dreze: Writing – review & editing, Writing – original draft, Validation, Software, Methodology, Investigation. **Luca di Mare:** Writing – review & editing, Supervision.

Declaration of competing interest

The authors declare that they have no known competing financial interests or personal relationships that could have appeared to influence the work reported in this paper.

Acknowledgements

The authors are grateful for the support from Rolls-Royce PLC and the EPSRC Center for Doctoral Training in Future Propulsion and Power. The authors would also like to acknowledge the use of the Cirrus UK National Tier-2 HPC Service at EPCC (http://www.cirrus.ac.uk) funded by the University of Edinburgh, United Kingdom and EPSRC, United Kingdom (EP/P020267/1). The authors would like also to thank Andrew Oliva for their helpful advice.

Appendix A. Equations for steady, quasi-one-dimensional compressible flow with heat transfer (ste)

The equations for steady non-isentropic internal flows have long been a subject of theoretical interest. Classical cases such as Fanno and Rayleigh flows have analytical solutions [38,50] and multiple set of solutions for other types of flow have been proposed [51–53]. This paper adopts the methodology proposed by Oliva and Morris [54], who presented a closed-form solution for internal compressible flows with an arbitrary combination of area change, heat addition, friction, and non-uniform flow. Both friction forces and heat transfer are expected to influence the mass flow.

Consider a control volume with varying area, friction, and heat addition as illustrated in Fig. A.11, the following equations can be derived. Using averaged quantities, the mass and momentum conservation equations for this control volume can be derived as follows:

Mass conservation :

$$A_1\rho_1U_1 = A_2\rho_2U_2 \tag{A.1}$$

$$\Leftrightarrow\ \frac{p_2A_2}{p_1A_1}\sqrt{\frac{T_{t,1}f(M_2)}{T_{t,2}f(M_1)}}\frac{M_2}{M_1}-1=0 \tag{A.2}$$

$$\text{With } f(M)=1+\frac{\gamma-1}{2}M^2 \tag{A.3}$$

x-momentum conservation :

$$\rho_2U_2^2A_2-\rho_1U_1^2A_1=p_1A_1-p_2A_2+\int_{A_1}^{A_2}p\,dA-F_{fx} \tag{A.4}$$

The flow variables in the above equations are representative variables defined by the chosen averaging method. For a detailed discussion on this, refer to [54]. In Eq. (A.4), the streamwise integral for the resultant pressure force acting on the control volume can be simplified by assuming a linear pressure variation with area, as discussed by [54,55]. This allows to rewrite Eq. (A.4) as:

$$p_1A_1\left(1+\frac{A_2}{A_1}+2\gamma M_1^2\right)=p_2A_2\left(1+\frac{A_1}{A_2}+2\gamma M_2^2\right)-2F_{fx} \tag{A.5}$$

By combining the continuity and streamwise momentum equations, and neglecting friction forces, we obtain:

$$\frac{\left(1+\frac{A_2}{A_1}+2\gamma M_2^2\right)}{\left(1+\frac{A_1}{A_2}+2\gamma M_1^2\right)}\sqrt{\frac{T_{t,2}f(M_1)}{T_{t,1}f(M_2)}}\frac{M_1}{M_2}-1=0 \tag{A.6}$$

Eq. (A.6) is a second-order equation for the exit Mach number based on an inlet Mach number and a stagnation temperature ratio. This approach provides a tool for analysing the steady effects of heat transfer on flow characteristics in a quasi-one-dimensional setting. The solution procedure involves discretising the domain of interest into small control volumes and solving for each control volume sequentially. If the another property is to be specified at the inlet such as the complete stagnation state or entropy instead of the Mach number, an iterative approach is required to determine the inlet Mach number. For detailed solution methods, refer to [54].

We have shown that the Stanton number is a key parameter in the study of heat transfer in compressible flows. The total temperature ratio in Eq. (A.6) can be decomposed further to make the Stanton number appear explicitly.

$$T_{t,2}=T_{t,1}+\frac{Q}{c_p}=T_{t,1}+\mathrm{St}\,A_c\rho_1U_1T_1=T_{t,1}+\mathrm{St}\,A_c\frac{p_1U_1}{R} \tag{A.7}$$

Where Q is the heat transfer rate, c_p is the specific heat capacity at constant pressure, A_c is the external area, and R is the gas constant.

Aside from this approach, other recent research has expanded to include nonlinear analytical solutions for more generalised cases involving varying area. [52] derived the quasi-one-dimensional linearised Euler equations incorporating heat transfer, subsequently investigating a converging-diverging nozzle with constant heat transfer. Their findings revealed a strong dependence of the nozzle's acoustic and entropy transfer functions on heat transfer. [53] presented a generalised one-dimensional compressible flow analysis, accounting for heat addition and/or friction, for a prescribed pressure-area relation. Furthermore, [51] derived analytical solutions for one-dimensional steady state compressible viscous diabatic flow of an ideal gas through a constant cross-section pipe. While, [25,26] have highlighted limitations in predicting capacity using one-dimensional analysis, the purpose of this approach in our study is to understand the steady state sensitivity of external heat transfer on capacity measurements. The inaccuracies pointed arise from 3D effects or complex flows, but the heat transfer will directly influence the thermodynamic state the flow is in.

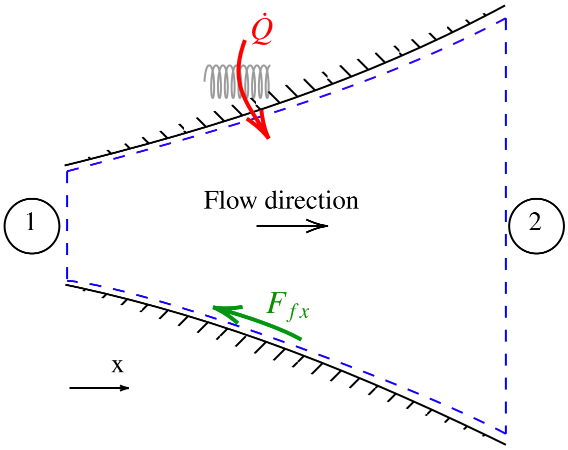

Fig. A.11. Sketch of a control volume with variable area, heat transfer and friction. Dashed lines define the control volume boundary.

Appendix B. Equations for unsteady, quasi-one-dimensional compressible flow with heat transfer (MOC)

The quasi-one-dimensional unsteady Euler equations with heat transfer, expressed in terms of primitive variables, can be written as:

$$\frac{\partial\rho}{\partial t}+U\frac{\partial\rho}{\partial x}+\rho\frac{\partial U}{\partial x}=-\frac{\rho U}{A}\frac{\partial A}{\partial x} \tag{B.1}$$

$$\frac{\partial U}{\partial t}+U\frac{\partial U}{\partial x}+\frac{1}{\rho}\frac{\partial p}{\partial x}=0 \tag{B.2}$$

$$\frac{\partial p}{\partial t}+U\frac{\partial p}{\partial x}+\frac{pU\gamma}{A}\frac{\partial A}{\partial x}+p\gamma\frac{\partial U}{\partial x}=Q\rho U(\gamma-1) \tag{B.3}$$

In matrix form:

$$\frac{\partial\mathbf{Q}}{\partial t}+\mathbf{M}\frac{\partial\mathbf{Q}}{\partial x}=\mathbf{S} \tag{B.4}$$

Where,

$$\mathbf{Q}=\begin{bmatrix}\rho\\U\\p\end{bmatrix} \tag{B.5}$$

$$\mathbf{M}=\begin{bmatrix}U&\rho&0\\0&U&\frac{1}{\rho}\\0&p\gamma&U\end{bmatrix}=\begin{bmatrix}U&\rho&0\\0&U&\frac{1}{\rho}\\0&\rho c^2&U\end{bmatrix} \tag{B.6}$$

$$\mathbf{S}=\begin{bmatrix}-\frac{\rho U}{A}\frac{\partial A}{\partial x}\\0\\-\frac{pU}{A}\gamma\frac{\partial A}{\partial x}+Q\rho U(\gamma-1)\end{bmatrix} \tag{B.7}$$

Decomposing $\mathbf{M}$ in its left and right eigenvectors, one can obtain the compatibility equations for the characteristic variables $\mathbf{W}$.

$$\frac{\partial\mathbf{W}}{\partial t}+\mathbf{\Lambda}\frac{\partial\mathbf{W}}{\partial x}=\mathbf{LS} \tag{B.8}$$

So the compatibility equations become

$$\frac{\partial W_1}{\partial t} = -U \frac{\partial W_1}{\partial x} -(\gamma-1)\frac{\rho U}{a^2}\delta Q_x \tag{B.9}$$

$$\frac{\partial W_2}{\partial t} = -(U+a) \frac{\partial W_2}{\partial x} - Ua\frac{1}{A}\frac{dA}{dx} +(\gamma-1)\frac{U}{a}\delta Q_x \tag{B.10}$$

$$\frac{\partial W_3}{\partial t} = -(U-a) \frac{\partial W_3}{\partial x} + Ua\frac{1}{A}\frac{dA}{dx} -(\gamma-1)\frac{U}{a}\delta Q_x \tag{B.11}$$

To model best the setup of interest, the boundary condition at the inlet should of type total enthalpy-entropy or fixing the stagnation properties. The following development is made under the assumption of no heat flux and constant area at the inlet but can be extended.

$$\partial W_1 = \partial\rho - \frac{1}{a^2}\partial p \tag{B.12}$$

$$\partial W_2 = \partial U + \frac{1}{\rho a}\partial p \tag{B.13}$$

$$\partial W_3 = \partial U - \frac{1}{\rho a}\partial p \tag{B.14}$$

However the variation of entropy is

$$ds = -\frac{\gamma c_v}{\rho}\left(d\rho - \frac{dp}{a^2}\right) \quad d\rho = -ds\frac{\rho}{\gamma c_v} + \frac{dp}{a^2}$$

Therefore

$$\partial W_1 = \partial\rho - \frac{1}{a^2}\partial p = -\frac{\rho}{\gamma c_v}\partial s \tag{B.15}$$

For the total enthalpy:

$$\begin{aligned} dh_t &= c_p dT + UdU \\ &= c_p T\frac{dT}{T} + UdU \\ &= c_p T\left(\frac{dp}{p} - \frac{d\rho}{\rho}\right) + UdU \\ &= c_p T\left(\frac{\rho a}{2p}(\partial W_2 - \partial W_3) - \partial W_1/\rho - \frac{\rho}{\rho 2a}(\partial W_2 - \partial W_3)\right) \\ &+ UdU \end{aligned} \tag{B.16}$$

$$\begin{aligned} &= c_p T\left((\partial W_2 - \partial W_3)(\frac{\rho a}{2p} - \frac{1}{2a}) - \partial W_1/\rho\right) \\ &+ \frac{u}{2}(\partial W_2 + \partial W_3) \\ &= -\frac{c_p T}{\rho}\partial W_1 + \partial W_2(\frac{\rho a c_p T}{2p} - \frac{c_p T}{2a} + \frac{U}{2}) \\ &+ \partial W_3(-\frac{\rho a c_p T}{2p} + \frac{c_p T}{2a} + \frac{U}{2}) \\ &= -\frac{a^2}{(\gamma-1)\rho}\partial W_1 + \partial W_2(\frac{ac_p}{2R} - \frac{a}{2(\gamma-1)} \\ &+ \frac{U}{2}) + \partial W_3(-\frac{ac_p}{2R} + \frac{a}{2(\gamma-1)} + \frac{U}{2}) \end{aligned} \tag{B.17}$$

A similar expression can be derived for prescribing the stagnation pressure. At the outlet, the static pressure is specified in case of subsonic outflow. To avoid the reflection of the characteristics at the outlet, a non-reflecting boundary condition is used [56].

As one of the focus of this study is the transient behaviour of the flow in transonic nozzles, it is expected that sonic conditions will be encountered. Numerical methods often encounter difficulties when dealing with sonic points. In these cases, a phenomenon known as the sonic glitch may occur. The sonic glitch manifests as a small, non-physical discontinuity or visible error in the computed solution around the sonic point [57]. To ensure a smooth transition as the flow accelerates through the sonic point, an entropy fix is implemented. This approach, as discussed by Va et al. [58], helps preserve the continuity of the solution across the sonic threshold. The entropy fix is particularly crucial in maintaining the accuracy and stability of our numerical simulations as the flow transitions from subsonic to supersonic regimes.

Data availability

Data will be made available on request.

References

[1] S. Sharma, M. Shadloo, A. Hadjadj, Turbulent flow topology in supersonic boundary layer with wall heat transfer, Int. J. Heat Fluid Flow 78 (2019) 108430, http://dx.doi.org/10.1016/j.ijheatfluidflow.2019.108430, URL: https://www.sciencedirect.com/science/article/pii/S0142727X18306027.

[2] S.U. Choi, J.A. Eastman, Enhancing thermal conductivity of fluids with nanoparticles, 1995, URL: https://www.osti.gov/biblio/196525.

[3] M.T. Lewis, J.-P. Hickey, Conjugate heat transfer in high-speed external flows: A review, J. Thermophys. Heat Transfer 37 (2023) 697–712, http://dx.doi.org/10.2514/1.T6763.

[4] B. John, P. Senthilkumar, S. Sadasivan, Applied and theoretical aspects of conjugate heat transfer analysis: A review, Arch. Comput. Methods Eng. 2 (2018) 475–489.

[5] T. Tu, S. Chen, C. Xu, Conjugated heat transfer simulation of flow mechanism and heat transfer characteristic of sweeping jet impinging on leading edge in turbine cascade, Appl. Therm. Eng. 236 (2024) 121839, http://dx.doi.org/10.1016/j.applthermaleng.2023.121839, URL: https://www.sciencedirect.com/science/article/pii/S1359431123018689.

[6] Q. He, W. Zhao, Z. Chi, S. Zang, Application of deep-learning method in the conjugate heat transfer optimization of full-coverage film cooling on turbine vanes, Int. J. Heat Mass Transfer 195 (2022) 123148.

[7] E.C. Okafor, M. Tsukamoto, A. Hayakawa, K.K.A. Somarathne, T. Kudo, T. Tsujimura, H. Kobayashi, Influence of wall heat loss on the emission characteristics of premixed ammonia-air swirling flames interacting with the combustor wall, Proc. Combust. Inst. 38 (2021) 5139–5146, http://dx.doi.org/10.1016/j.proci.2020.06.142, URL: https://www.sciencedirect.com/science/article/pii/S1540748920302224.

[8] S. Gövert, D. Mira, J.B.W. Kok, M. Vázquez, G. Houzeaux, The effect of partial premixing and heat loss on the reacting flow field prediction of a swirl stabilized gas turbine model combustor, Flow Turbul. Combust. 100 (2018) 503–534, http://dx.doi.org/10.1007/s10494-017-9848-4.

[9] D. Bruna, M.G. Turner, Isothermal boundary condition at casing applied to the rotor 37 transonic axial flow compressor, J. Turbomach. 135 (2013) 034501, http://dx.doi.org/10.1115/1.4007569.

[10] K.P. Griffin, L. Fu, P. Moin, Velocity transformation for compressible wall-bounded turbulent flows with and without heat transfer, Proc. Natl. Acad. Sci. 118 (2021) e2111144118, http://dx.doi.org/10.1073/pnas.2111144118, URL: https://www.pnas.org/doi/abs/10.1073/pnas.2111144118.

[11] M. Lazareff, R. Moretti, M.-P. Errera, Coupling methodology for thermal fluid-solid simulations through a full transient flight cycle, Int. J. Heat Mass Transfer 202 (2023) 123691, http://dx.doi.org/10.1016/j.ijheatmasstransfer.2022.123691, URL: https://www.sciencedirect.com/science/article/pii/S0017931022011590.

[12] M. Fiore, V. Barbato, F. Nasuti, Transient analysis of liquid rocket engine chill-down and startup by conjugate heat transfer approach, 2024, http://dx.doi.org/10.2514/6.2024-0353, URL: https://arc.aiaa.org/doi/abs/10.2514/6.2024-0353.

[13] P. Wang, F. Li, S. Xu, Y. Liu, Transient thermal behaviors of ultra-supercritical steam turbine control valves during the cold start warm-up process: Conjugate heat transfer simulation and field data validation, J. Heat Transf. 141 (2019) 122901, http://dx.doi.org/10.1115/1.4044834.

[14] J.R. Edwards, J.A. Boles, R.A. Baurle, Large-eddy/reynolds-averaged navier–stokes simulation of a supersonic reacting wall jet, Combust. Flame 159 (2012) 1127–1138, http://dx.doi.org/10.1016/j.combustflame.2011.10.009, URL: https://www.sciencedirect.com/science/article/pii/S0010218011003142.

[15] J. Muller, C. Johnson, M. Dutta, J.C. Oefelein, Analysis of shock-wave/boundary-layer interaction unsteadiness mechanisms using conjugate heat transfer and wall-modeled les, 2025, http://dx.doi.org/10.2514/6.2025-1892, URL: https://arc.aiaa.org/doi/abs/10.2514/6.2025-1892, http://arxiv.org/abs/https://arc.aiaa.org/doi/pdf/10.2514/6.2025-1892arXiv:https://arc.aiaa.org/doi/pdf/10.2514/6.2025-1892.

[16] M.G. Adams, T. Povey, B.F. Hall, D.N. Cardwell, K.S. Chana, P.F. Beard, Commissioning of a combined hot-streak and swirl profile generator in a transonic turbine test facility, J. Eng. Gas Turbines Power 142 (2020) 031008, http://dx.doi.org/10.1115/1.4044224.

[17] J. Amend, R. Lubbock, F. Ornano, T. Povey, Lean-burn combustor simulator for an engine-component test facility: An experimental and computational study, J. Turbomach. 145 (2023) 061014, http://dx.doi.org/10.1115/1.4056387.

[18] S.T. Englerth, An experimental conduction error calibration procedure for cooled total temperature probes, 2015, URL: https://api.semanticscholar.org/CorpusID:102301762.

[19] D. Bianchi, A. Turchi, F. Nasuti, M. Onofri, Coupled cfd analysis of thermo-chemical erosion and unsteady heat conduction in solid rocket nozzles, in: 48th AIAA/ASME/SAE/ASEE Joint Propulsion Conference & Exhibit, 2012, p. 4318.

[20] S. Xue, A. Roy, W.F. Ng, S.V. Ekkad, A novel transient technique to determine recovery temperature, heat transfer coefficient, and film cooling effectiveness simultaneously in a transonic turbine cascade, J. Therm. Sci. Eng. Appl. 7 (2015) 011016, http://dx.doi.org/10.1115/1.4029098.

[21] D.L. Schultz, Heat transfer measurements in short-duration hypersonic facilities, in: AGARD 165, 1973.

[22] L. He, M. Oldfield, Unsteady conjugate heat transfer modeling, J. Turbomach. 133 (2011).

[23] Analysis of high pressure turbine nozzle guide vanes considering geometric variations, in: Volume 2C: Turbomachinery of *Turbo Expo: Power for Land, Sea, and Air*, 2016, http://dx.doi.org/10.1115/GT2016-57502.

[24] T. Povey, Effect of film cooling on turbine capacity, J. Eng. Gas Turbines Power 132 (2009) 011901, http://dx.doi.org/10.1115/1.3026564.

[25] L. Fielding, The effect of irreversibility on the capacity of a turbine blade row, Proc. Inst. Mech. Eng. 195 (1981) 127–137.

[26] I.V. Afanasiev, A.V. Granovski, A.M. Kareline, M.K. Kostege, The problems of inaccuracy in flow capacity definition by using different numerical techniques, J. Therm. Sci. 13 (2004) 1–7, http://dx.doi.org/10.1007/s11630-004-0001-z.

[27] D. Burdett, C. Hambidge, T. Povey, Analysis of ultra-low uncertainty gas turbine flow capacity measurement techniques, Proc. Inst. Mech. Eng. Part A: J. Power Energy 235 (2021) 1053–1079, http://dx.doi.org/10.1177/0957650920909718.

[28] C. Hirsch, Numerical Computation of Internal and External Flows: The Fundamentals of Computational Fluid Dynamics, Elsevier, 2007.

[29] R.A. Delaney, P. Kavanagh, Transonic flow analysis in axial-flow turbomachinery cascades by a time-dependent method of characteristics, J. Eng. Power 98 (1976) 356–363, http://dx.doi.org/10.1115/1.3446181.

[30] M.J. Zucrow, J.D. Hoffman, Gas dynamics, in: Multidimensional Flow, Vol. 2, New York, 1977.

[31] R.I. Issa, D.B. Spalding, Unsteady one-dimensional compressible frictional flow with heat transfer, J. Mech. Eng. Sci. 14 (1972) 365–369.

[32] Y.M. Huang, Study of unsteady flow in a heat exchanger by the method of characteristics, J. Press. Vessel. Technol. 114 (1992) 459–463, http://dx.doi.org/10.1115/1.2929255.

[33] Y. Dreze, M. Hao, L. di Mare, Divergence-free turbulent inflow data from realistic covariance tensor, Phys. Fluids 35 (2023) 025120, http://dx.doi.org/10.1063/5.0136568.

[34] J. Hope-Collins, L. di Mare, Artificial diffusion for convective and acoustic low mach number flows i: Analysis of the modified equations, and application to roe-type schemes, J. Comput. Phys. 475 (2023) 111858, http://dx.doi.org/10.1016/j.jcp.2022.111858, URL: https://www.sciencedirect.com/science/article/pii/S0021999122009214.

[35] M. Hao, J. Hope-Collins, L. di Mare, Generation of turbulent inflow data from realistic approximations of the covariance tensor, Phys. Fluids 34 (2022) http://dx.doi.org/10.1063/5.0106664.

[36] M. Hao, L. di Mare, Budgets of reynolds stresses in film cooling with fan-shaped and cylindrical holes, Phys. Fluids 35 (2023) http://dx.doi.org/10.1063/5.0140670.

[37] M. Čada, M. Torrilhon, Compact third-order limiter functions for finite volume methods, J. Comput. Phys. 228 (2009) 4118–4145, http://dx.doi.org/10.1016/j.jcp.2009.02.020, URL: https://www.sciencedirect.com/science/article/pii/S0021999109000953.

[38] A.H. Shapiro, The dynamics and thermodynamics of compressible fluid flow, 1953.

[39] H. Kawamura, K. Ohsaka, H. Abe, K. Yamamoto, Dns of turbulent heat transfer in channel flow with low to medium-high prandtl number fluid, Int. J. Heat Fluid Flow 19 (1998) 482–491, http://dx.doi.org/10.1016/S0142-727X(98)10026-7, URL: https://www.sciencedirect.com/science/article/pii/S0142727X98100267.

[40] S. Pirozzoli, D. Modesti, P. Orlandi, F. Grasso, Turbulence and secondary motions in square duct flow, J. Fluid Mech. 840 (2018) 631–655, http://dx.doi.org/10.1017/jfm.2018.66.

[41] J.C. Sivells, Aerodynamic design of axisymmetric hypersonic wind-tunnel nozzles, J. Spacecr. Rockets 7 (1970) 1292–1299, http://dx.doi.org/10.2514/3.30160.

[42] J.C. Sivells, R.G. Payne, A Method of Calculating Turbulent-Boundary-Layer Growth at Hypersonic Mach Numbers, Vol. 59, Arnold Engineering Development Center, Air Research and Development Command ..., 1959.

[43] L. Back, P. Massier, H. Gier, Convective heat transfer in a convergent-divergent nozzle, Int. J. Heat Mass Transfer 7 (1964) 549–568, http://dx.doi.org/10.1016/0017-9310(64)90052-3, URL: https://www.sciencedirect.com/science/article/pii/0017931064900523.

[44] A.H.K. Bensayah, A. Bounif, Heat transfer in turbulent boundary layers of conical and bell shaped rocket nozzles with complex wall temperature, Numer. Heat Transf. Part A: Appl. 66 (2014) 289–314, http://dx.doi.org/10.1080/10407782.2013.873283.

[45] A. Makhija, K. Bodi, D. Chakraborty, Numerical estimation of convective heat transfer coefficient and heat flux for a supersonic rocket nozzle, Def. Sci. J. 74 (2024) 189–196, http://dx.doi.org/10.14429/dsj.74.19633.

[46] E. Zhalehrajabi, N. Rahmanian, N. Hasan, Effects of mesh grid and turbulence models on heat transfer coefficient in a convergent–divergent nozzle, Asia-Pac. J. Chem. Eng. 9 (2014) 265–271, http://dx.doi.org/10.1002/apj.1767, URL: https://onlinelibrary.wiley.com/doi/abs/10.1002/apj.1767, http://arxiv.org/abs/https://onlinelibrary.wiley.com/doi/pdf/10.1002/apj.1767arXiv:https://onlinelibrary.wiley.com/doi/pdf/10.1002/apj.1767.

[47] J.D. Wright, W. Kang, A.N. Johnson, V.B. Khromchenko, M.R. Moldover, L. Zhang, B. Mickan, Thermal boundary layers in critical flow venturis, Flow Meas. Instrum. 81 (2021) 102025, http://dx.doi.org/10.1016/j.flowmeasinst.2021.102025, URL: https://www.sciencedirect.com/science/article/pii/S095559862100131X.

[48] C. Wang, G. Wang, H. Ding, Thermal effect on body temperature distribution of the critical flow venturi nozzle, Exp. Therm. Fluid Sci. 79 (2016) 187–194, http://dx.doi.org/10.1016/j.expthermflusci.2016.07.012, URL: https://www.sciencedirect.com/science/article/pii/S0894177716301844.

[49] H. Ding, C. Wang, G. Wang, Transient conjugate heat transfer in critical flow nozzles, Int. J. Heat Mass Transfer 104 (2017) 930–942, http://dx.doi.org/10.1016/j.ijheatmasstransfer.2016.09.021, URL: https://www.sciencedirect.com/science/article/pii/S0017931016314065.

[50] Mitsuharu Masuda Kazuyasu Matsuo Yutaka Yamaguchi Miyazato, Masashi Kashitani, One—dimensional analysis of thermal choking in case of heat addition in ducts, 2000, URL: https://api.semanticscholar.org/CorpusID:108846797.

[51] A. Ferrari, Analytical solutions for one-dimensional diabatic flows with wall friction, J. Fluid Mech. 918 (2021) A32, http://dx.doi.org/10.1017/jfm.2021.278.

[52] S.R. Yeddula, J. Guzmán-Iñigo, A.S. Morgans, A solution for the quasi-one-dimensional linearised euler equations with heat transfer, J. Fluid Mech. 936 (2022) R3, http://dx.doi.org/10.1017/jfm.2022.101.

[53] W. Loh, A generalized one-dimensional compressible flow analysis with heat addition and/or friction in a non-constant area duct, Internat. J. Engrg. Sci. 8 (1970) 193–206, http://dx.doi.org/10.1016/0020-7225(70)90030-3, URL: https://www.sciencedirect.com/science/article/pii/0020722570900303.

[54] A.A. Oliva, S.C. Morris, Steady, quasi-one-dimensional, internal compressible flow with area change, heat addition and friction, J. Fluid Mech. 957 (2023) A15, http://dx.doi.org/10.1017/jfm.2023.44.

[55] M.J. Rahimi, H.K. Chelliah, Simplified approach to identify thermal choking limits of a dual-mode variable area combustor, AIAA J. 56 (2018) 2091–2095, http://dx.doi.org/10.2514/1.J055848.

[56] T. Poinsot, S. Lelef, Boundary conditions for direct simulations of compressible viscous flows, J. Comput. Phys. 101 (1992) 104–129, http://dx.doi.org/10.1016/0021-9991(92)90046-2.

[57] H. Tang, On the sonic point glitch, J. Comput. Phys. 202 (2005) 507–532, http://dx.doi.org/10.1016/j.jcp.2004.07.013, URL: https://www.sciencedirect.com/science/article/pii/S0021999104002967.

[58] B. Va, W.-T. Lee, K. Powell, Sonic-point capturing, 1989, http://dx.doi.org/10.2514/6.1989-1945, URL: https://arc.aiaa.org/doi/abs/10.2514/6.1989-1945.

4.2.1 Additional material

It should be noted that the local heat transfer coefficient presented in the paper has been calculated following the original formula of Back et al. [1964].

$$h = \frac{q_w}{T_{aw} - T_w} \tag{4.4}$$

Where T_{aw} is the adiabatic wall temperature, T_w is the wall temperature and q_w is the heat flux at the wall.

In the Introduction section of the presented paper, a steady CHT analysis was performed for a classical Rayleigh flow. The setup had a fixed inlet Mach number and total temperature as it is done traditionally for Rayleigh flows. It is possible to extend the analysis to a case where the inlet stagnation pressure and temperature are fixed, aligning better with boundary conditions from a large upstream reservoir typically found in propulsion systems or wind tunnel setups.
Starting from Equation (1) in section 4.2, the capacity Γ_m for such case is given by:

$$\Gamma_m = \frac{\dot{m}\sqrt{T_t}}{p_t} = A_x\sqrt{\frac{\gamma}{R}}M\left(1+\frac{\gamma-1}{2}M^2\right)^{-\frac{\gamma+1}{2(\gamma-1)}} \tag{4.5}$$

Under fixed inlet stagnation conditions and outlet pressure, the capacity depends solely on the Mach number. Figure 4.11 shows the contours of the capacity change compared to adiabatic conditions as a function of the total temperature change for different inlet isentropic Mach numbers. In this case, only at very low Mach numbers ($M_1 < 0.1$), the change in capacity with respect to adiabatic conditions is less than proportional to the total temperature change. For $0.1 < M_1 < 1$, the variation in mass flow rate is more than proportional to the total temperature variation. At high supersonic Mach numbers, the capacity is less sensitive to the entropy change. Looking at Equation 4.5, for $M \gg 1$ the capacity is proportional to $M^{\frac{-2}{\gamma-1}}$, implying that a large change in Mach number will have a small effect on the capacity when $M \gg 1$.

Despite this reduced sensitivity in capacity, other flow quantities can exhibit substantial variations at high Mach numbers, underscoring the complex interplay between flow conditions and heat transfer effects. For instance, Figure 4.12 plots the variation in inlet Mach number. In this case, the inlet Mach number is strongly influenced by the entropy change at high Mach number. Overall, the capacity is more sensitive to the entropy change in the transonic regime, where the capacity change is more than proportional to the total temperature variation.

The analysis is interesting because it shows that the effect of CHT is highly dependent on the flow boundary conditions and the flow quantity of interest. Figure 4.11 presents conclusions that are the very different to the ones presented in Figure 1 of Dreze and di Mare [2025] with constant inlet Mach number.

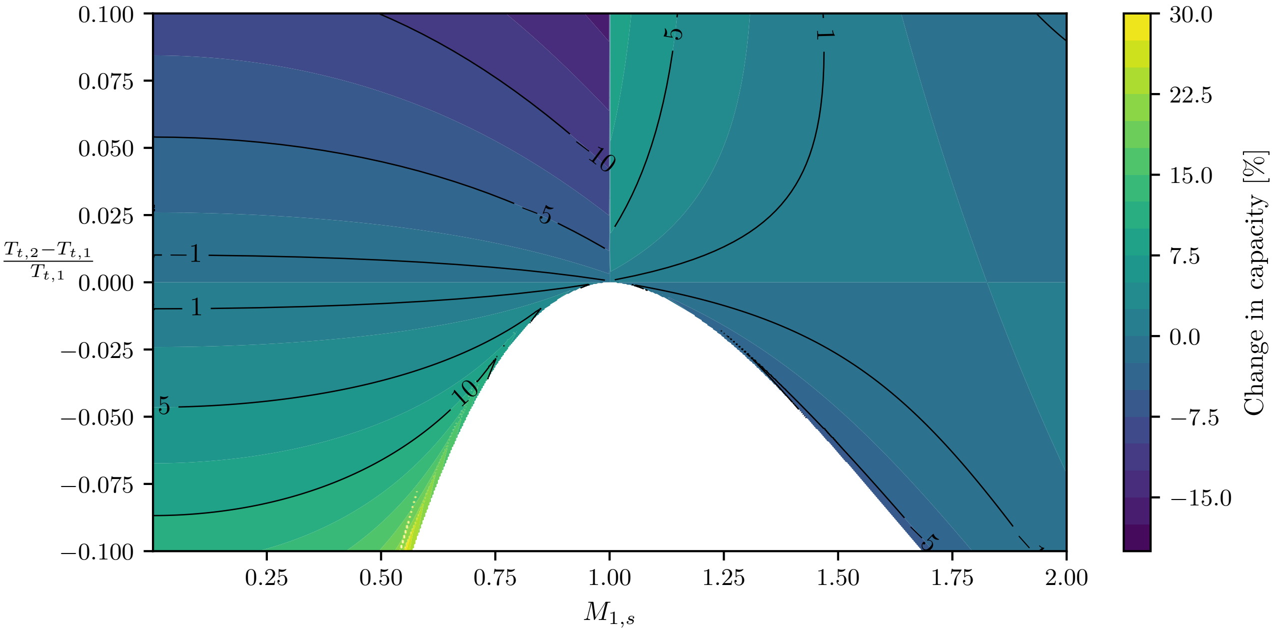

Figure 4.11: Contours of the relative change in capacity with respect to adiabatic conditions at fixed inlet stagnation pressure and temperature

4.2.2 Remarks and possible extensions

The primary limitation of the analysis presented in the paper is the absence of experimental data to validate the observed phenomenon. A thorough literature review revealed a scarcity of experimental studies that could corroborate these findings. Most high-temperature experimental campaigns do not explicitly state whether thermal equilibrium between the solid and fluid domains was achieved or how

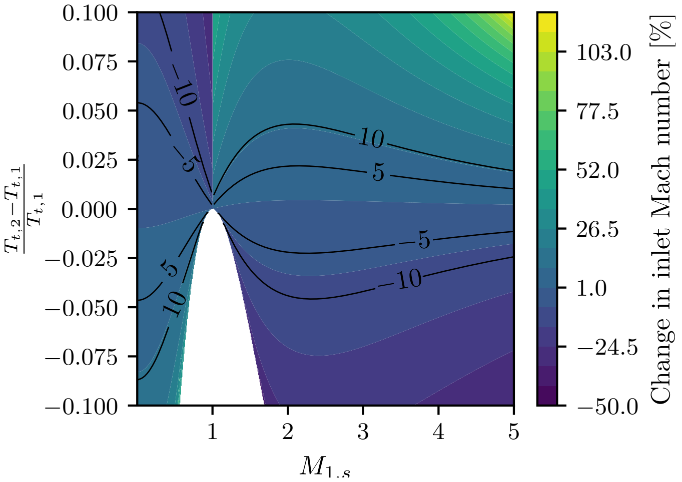

Figure 4.12: Contours of the relative change in outlet Mach number for different inlet Mach number and total temperature ratios

it was ensured. In one instance, the authors provided time traces of the temperature field in the solid domain, but the impact on flow quantities was not mentioned. Experimental data, such as transient thermal tests of high-pressure turbine nozzles, would be valuable for cross-validation with the numerical results.

Additionally, it would be worthwhile to investigate numerically or experimentally various preheating strategies, such as determining optimal preheating temperature ratios, and their practical implementation in scenarios like cold starts of rocket engines. A comparative analysis considering different materials, geometrical configurations (e.g. thin or thick walls), and flow conditions could provide further insights into the influence of thermophysical parameters on the time constant.

4.2.3 Statement of authorship

- Title of the paper: *Unsteady Conjugate Heat Transfer Effects on Flow Characteristics*
- Publication status: Published
- Publication details: Dreze Y. and di Mare L. "Unsteady Conjugate Heat Transfer Effects on Flow Characteristics" (2025), *International Journal of Heat and Mass Transfer*, `https://doi.org/10.1016/j.ijheatmasstransfer.2025.127036`

- Student Confirmation:
  - Student name: Yann Dreze
  - Contribution to the paper: I wrote all the code presented in the manuscript (1D methods and CHT capabilities of the LES solver) and I performed the numerical simulations presented in the paper. Finally, I wrote the paper manuscript.
  - Date and signature: , September 26, 2025
- Supervisor Confirmation:
  By signing the Statement of Authorship, you are certifying that the candidate made a substantial contribution to the publication, and that the description described above is accurate.
  - Supervisor name and title: Luca di Mare, Associate Professor
  - Supervisor comments: I confirm that the candidate's statement is an accurate description of his contribution to this publication.
  - Signature and date: , September 26, 2025

Chapter 5 Conclusions

This thesis has presented a comprehensive study of unsteady conjugate heat transfer modelling. The main contributions of this work are summarised below.

The first major part of this thesis, presented in chapter 3, focused on the development of a method for generating unsteady turbulent inflow conditions in scale-resolving simulations. This work served as a foundational step for achieving the subsequent objectives of the thesis. Building on the work of Hao et al. [2022], the proposed method advances the state of the art by eliminating the need for a user-defined correlation function. It generates divergence-free, anisotropic random fields with a physically consistent spectrum and fully defined spatial and temporal correlations. The algorithm infers a realistic velocity two-point correlation tensor from the first and second statistical moments, supported by heuristic guidelines derived from observations of turbulent flows. Since these statistics are commonly available in practical applications, the method offers broad applicability. Moreover, it is computationally efficient with the use of eigendecomposition to reduce the resources required depending on the accuracy needed. The method was validated against experimental data and showed improved performance compared to previously published methods.

Following the comprehensive literature review presented in chapter 2, the second major contribution of this thesis, detailed in chapter 4, focused on answering challenges in CHT modelling. Chapter 4 began with the implementation and development of a CHT simulation environment within the `H4X` framework. It then introduced a new modelling approach for unsteady CHT, addressing key challenges in the field by coupling a global representation of the solid temperature field—expressed through the eigenfunctions of the unsteady heat conduction problem—with a local, turbulent, scale-resolving solution. To reconcile the mismatches in time and length scales between the two domains, the method involves a careful selection of the modes to retain based on their associated time constants and thereby addressing slow convergence issues within the modal space. The capabilities of the proposed method were first demonstrated on simplified test cases, where it achieved an order-of-magnitude improvement in computational efficiency over conventional time-marching techniques. The method was subsequently applied to a more complex three-dimensional forced convection case, representative of heat exchanger applications in engineering. In this scenario, the method successfully captured the unsteady heat transfer phenomena with high accuracy and efficiency.

With the CHT method validated on both simplified and complex test cases, chapter 4 concluded with a practical application where unsteady CHT has implications. Specifically, it presented a detailed study into compressible flows in the presence of unsteady conjugate heat transfer to the walls. The investigation showed that all flow quantities undergo a transient drift until thermal steady-state is reached in both fluid and solid domains. This drift follows a characteristic exponential decay. The heat transfer dynamics are shown to be governed by the ratio of thermal capacity to the Stanton number, which characterises the interface behaviour. To illustrate these effects, a numerical analysis was performed on a transonic nozzle with thermally conducting walls, using simulation tools of varying fidelity. The transient evolution of the mass flow rate was monitored, demonstrating the impact of thermal transients. It was further observed that while preheating the system does not affect the decay time constant, the upper and lower bounds of the drift are directly proportional to the initial temperature difference between the solid and fluid domains.

5.1 Recommendations for future work

Future work in CHT should be directed toward several key areas that could enhance both physical realism and computational efficiency.

First of all, CHT should become the standard for the simulation of thermally influenced flows. However, even further, the importance of unsteady and transient effects is becoming increasingly evident. A primary challenge in this shift will be the development of robust coupling strategies that can efficiently manage models of different fidelities.

The field should also be influenced by artificial intelligence (AI) and machine learning (ML), which can augment and accelerate traditional simulation workflows. Rather than replacing fundamental physics, AI can act as a powerful accelerator by creating computationally inexpensive surrogate models. The great cost of high-fidelity transient simulations provides a strong incentive for this approach.

While mastering unsteady thermal-fluid coupling is a grand challenge, the ultimate future of CHT lies in its integration within a broader multiphysics context. In the most demanding engineering systems, thermal phenomena are deeply intertwined with structural mechanics (Fluid-Structure Interaction), material phase transitions, reacting flows, and multiphase physics. The full predictive power of UCHT will be realized when it is seamlessly coupled with these other domains, enabling a holistic simulation that captures the complex feedback loops governing system performance and reliability. Developing numerical frameworks to handle this multi-way coupling represents the next significant leap in computational engineering. A good example of this multiphysics complexity is aircraft icing and de-icing. This process involves a complex, unsteady energy balance between the cold airflow, impinging supercooled water droplets, a potential runback water film, the growing ice layer, and the heated aircraft skin. A comprehensive simulation requires UCHT to model the heat exchange but must also track the moving ice-water interface and account for the latent heat of fusion. This application perfectly illustrates how fully-integrated multiphysics analysis is essential for accurately predicting system behavior and solving critical engineering safety problems.

In addition, the following general remarks are made to guide future research that stems directly from the developments presented in this thesis:

- As explained in chapter 4, the unsteady CHT method presented is not limited to the acceleration method presented in this thesis. The modal framework is general and many other acceleration methods can be implemented. One of the more promising approaches is to cast the modal problem in Fourier space as illustrated in Figure 4.1.1.

- The method can be applied to additional unsteady conjugate heat transfer problems, such as those involving complex geometries or chemically reacting flows. In that perspective, the method could be implemented in the Rolls-Royce Plc. flow solver `Hydra` [Crumpton and Giles, 1996]. With the already implemented harmonic method [Lapworth, 2004], the method can be used to accelerate the convergence of periodic turbomachinery flows. Additionally, an implementation of the method could be pursued on open-source software such as `OpenFOAM` and `FENICSX`, which would allow for a wider dissemination of the method and its application to a broader range of problems.

- Finally, the modal CHT framework could be adapted to transient heat conduction problems, such as engine startup or shutdown, where the solid domain is subject to slow transients. The modal decomposition could be used to efficiently select the modes that are relevant for the transient heat conduction problem, allowing for a more efficient solution of the problem.

Appendices

Appendix A Inflow generation using the digital filter method

A.1 Inflow generation using the digital filter method

The generation of turbulent inflow involves creating a realistic field for a set of variables $\mathbf{q}$ at the inlet of the computational domain. These variables can be decomposed into a time-averaged $\overline{\mathbf{q}}$ and a fluctuating component $\mathbf{q}'$, as shown in Figure A.1.

$$\mathbf{q}(t) = \overline{\mathbf{q}} + \mathbf{q}'(t) \tag{A.1}$$

In most scenarios, the time-averaged value is known from experimental data, analytical solutions, or precursor simulations. Synthetic inflow generators are used to create the fluctuating part $\mathbf{q}'$ in a way that is consistent with the first and second statistical moments of $\mathbf{q}$. The present method relies on *digital filters* to transform a set of uncorrelated Gaussian random numbers into a field with a desired spatial and temporal correlation. Following the procedure explained in section 3.2, a 1D example is shown in Figure A.2. Starting with an uncorrelated signal ϕ, with time sequence and covariance shown in gray. The uncorrelated signal is then convoluted

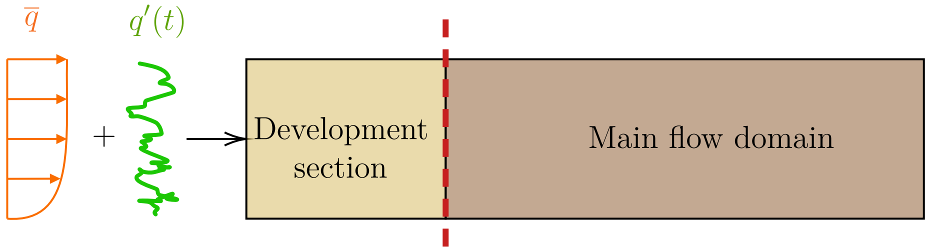

Figure A.1: Description of the boundaries in the computational domain.

using Equation A.2 with the filter s_{ih} to modify its covariance into a decaying exponential as shown in the orange in Figure A.2.

$$q_i = \sum_{l=-N}^{N} s_{ih}\phi_{h+l} \tag{A.2}$$

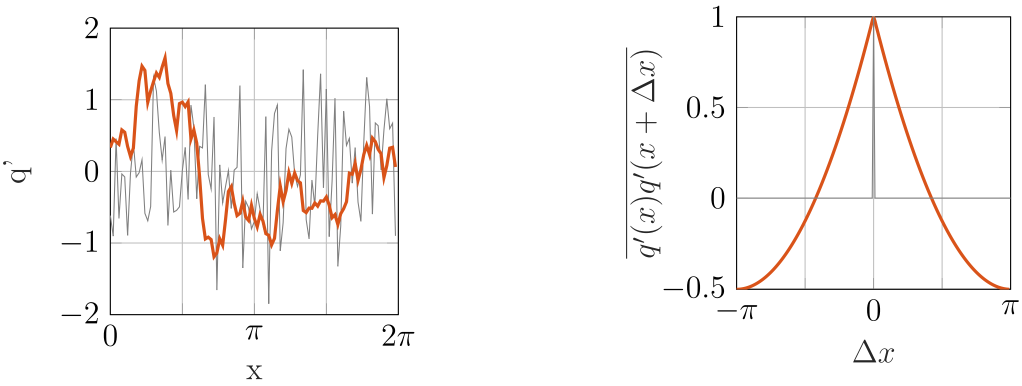

(a) Signal

(b) Covariance

Figure A.2: Time history and covariance of two signals. The gray line is the original random signal, and the orange line is the filtered signal.

A.1.1 Inflow generation procedure

An overview of the procedure is provided in Figure A.3. The inflow preprocessing, done before the main simulation, generates a set of 3D filters that will be used to produce the inflow planes during the simulation. The input parameters necessary for the preprocessing are:

- The target Reynolds number for the simulation case.
- The mean flow variables on the inflow plane and the Reynolds stress tensor. If unavailable, these are obtained through a precursor RANS simulation, as done in Hao et al. [2022].
- The streamwise length of the inflow plane L_I, i.e. its temporal extent. It should span at least an integral time scale of the simulation.
- An energy cutoff value, controlling the truncation of the filters.

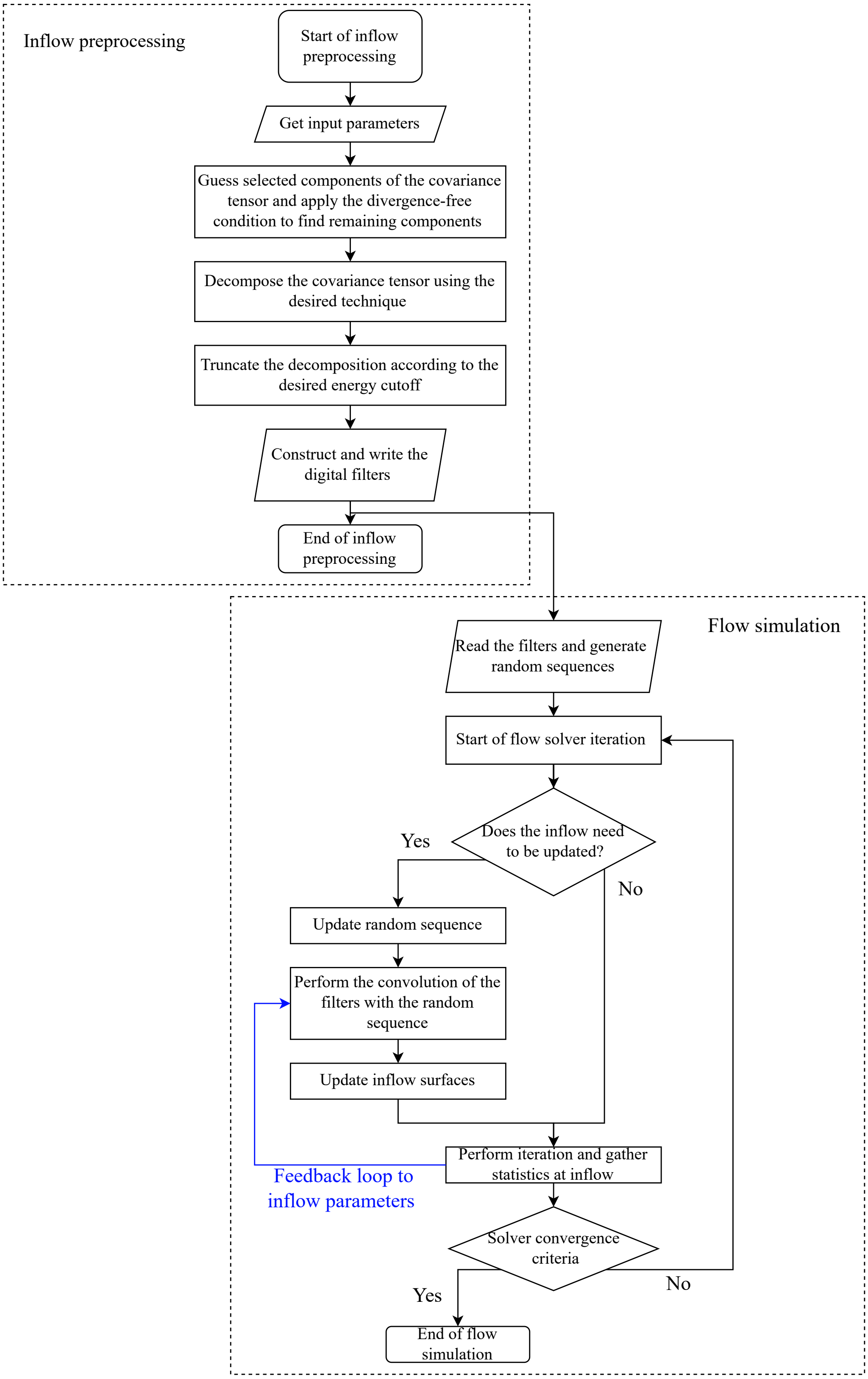

Figure A.3: Inflow generation preprocessing and simulation flowchart.

- A length scale function for the approximation of the correlation tensor.
- *Optional:* A mesh scaling factor to downsize the fluid mesh for the filter generation. This is useful to reduce the computational cost of the filter generation.

Details of the remaining preprocessing steps, including estimating the components of the correlation tensor and decomposing it, are given in the technical paper of section 3.2. The preprocessing phase produces a set of N_f filters. Looking at the flow simulation block in Figure A.3, at the start of a flow solver iteration the inflow surface is being updated. The update process is done by convoluting these three-dimensional filters with a random number array of dimensions $N_f \times L_I$. The convolution process is illustrated in Figure A.4. The convolution can either be done prior to the simulation and then the simulation loads the inflow planes directly, or it can be done on the fly during the simulation. It should be noted that storing directly the inflow planes is more memory intensive than storing the filters and generating the inflow planes on the fly. Finally, for compressible simulations, temperature and pressure fluctuations are also required. Using the strong Reynolds analogy Cebeci [2012], the velocity and temperature fluctuations are related to the mean temperature $\bar{T}$ and the velocity fluctuation u' through Equation A.3 as done in Schwartz and Garmann. The pressure fluctuations are assumed to be negligible compared to the velocity and temperature fluctuations.

$$T' = \frac{\bar{T}}{c_p} u' \tag{A.3}$$

During the simulation, a control or feedback plane is defined at the start of the main flow domain to monitor the inflow quality, dotted red lines in Figure A.1. The inflow quality is assessed by comparing the mean and fluctuating values of the variables at the inflow plane with the desired values. There is a feedback loop that adjusts the filters parameters and the individual velocity components to account for the dissipation occurring in the development section.

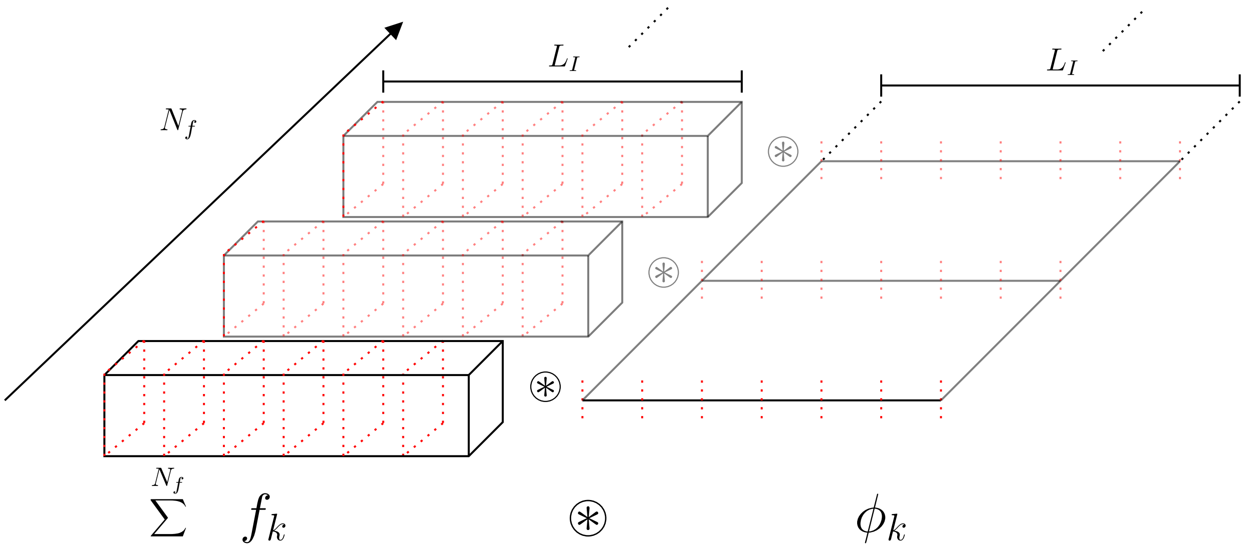

Figure A.4: Illustration of the convolution operation for the 3D filters f_k.

Appendix B Numerical methods for simulating low Mach number flows

B.1 Governing flow equations

The Navier-Stokes equations, which describe the dynamics of unsteady, viscous, and compressible flows, can be expressed in their conservative form as the following system of partial differential equations:

$$\frac{\partial \rho}{\partial t} + \nabla \cdot (\rho \mathbf{u}) = 0 \tag{B.1}$$

$$\frac{\partial (\rho \mathbf{u})}{\partial t} + \nabla \cdot (\rho \mathbf{u} \times \mathbf{u}) = -\nabla p + \nabla \cdot \boldsymbol{\tau} + \rho \mathbf{f} \tag{B.2}$$

$$\frac{\partial (\rho E)}{\partial t} + \nabla \cdot \left[(\rho E + p)\, \mathbf{u} \right] = \nabla \cdot (\mathbf{u} \cdot \boldsymbol{\tau}) + \nabla \cdot (\kappa \nabla T) + \rho \left(\mathbf{f} \cdot \mathbf{u} + Q \right) \tag{B.3}$$

Where the stress tensor $\boldsymbol{\tau}$ and the total energy E are given by:

$$\boldsymbol{\tau} = \mu \left(\nabla \mathbf{u} + (\nabla \mathbf{u})^{\top} \right) + \left(\lambda - \frac{2}{3}\mu \right) (\nabla \cdot \mathbf{u}) \mathbf{I} \tag{B.4}$$

$$E = e + \frac{1}{2} |\mathbf{u}|^2 \tag{B.5}$$

$\mathbf{u}$ is the velocity vector, ρ is the density, p is the pressure, T is the temperature, μ is the dynamic viscosity, λ is the second viscosity coefficient, κ is the thermal conductivity, and Q is the heat source term. The term $\mathbf{f}$ represents the body forces acting on the fluid, such as gravity.

The system of equations is closed by an equation of state, which relates the pressure, density, and temperature of the fluid. In the present case, the system is closed with the ideal gas law for compressible flows.

B.2 Numerical methods for the flow equations

`H4X` uses a Finite Volume Method (FVM) to solve the Navier-Stokes equations eqs. (B.1) to (B.3). The method begins by discretising the fluid domain into contiguous control volumes (cells). For each cell, the N-S equations are integrated over its volume, converting terms involving spatial derivatives into surface integrals via the divergence theorem. This step ensures local conservation by balancing fluxes (e.g., mass, momentum) across the cell's faces. By preserving conservation laws at the discrete level, FVM effectively captures complex flow phenomena, making it robust for compressible simulations, including turbulent multi-physics flows. Further details on the FVM formulation can be found in Ferziger et al. [2019], Blazek [2015].

The general integral form of the unsteady compressible Navier-Stokes equations over a domain Ω with outer boundary $\delta\Omega$ is:

$$\frac{\partial}{\partial t}\int_{\Omega}\mathbf{U}\,dV + \int_{\delta\Omega}\mathbf{F}_c(\mathbf{U})\cdot\vec{n}\,dS = \int_{\delta\Omega}\mathbf{F}_v(\mathbf{U},\nabla\mathbf{U})\cdot\vec{n}\,dS + \int_{\Omega}\mathbf{S}_{\mathbf{\Omega}}\,dV \tag{B.6}$$

Where:

- $\mathbf{U}$: vector of conserved variables
- $\mathbf{F}_c$: convective (inviscid) flux vector
- $\mathbf{F}_v$: viscous flux vector
- $\mathbf{S}_{\mathbf{\Omega}}$: optional source terms

Equation B.6 can be summarised into the compact form:

$$\frac{\partial\mathbf{U}_i}{\partial t} = \mathcal{R}_i(\mathbf{U},\nabla\mathbf{U}) \tag{B.7}$$

where $\mathcal{R}_i$ is the residual vector representing the net flux imbalance (convective and viscous) and source terms in cell i.

B.2.1 Spatial discretisation

The spatial discretisation for the inviscid fluxes used in `H4X` is third-order accurate. Third-order accuracy is achieved on a compact stencil by using variable extrapolation. Consider the following scalar advection equation as an example:

$$\frac{\partial u}{\partial t} + a\frac{\partial u}{\partial x} = 0, \tag{B.8}$$

where a is the constant advection velocity.

Using a finite volume discretisation, the semi-discrete equation for cell i is:

$$\frac{d\bar{u}_i}{dt} = -\frac{1}{\Delta x}\left(F_{i+\frac{1}{2}} - F_{i-\frac{1}{2}}\right), \tag{B.9}$$

where $\bar{u}_i$ is the cell-averaged solution, Δx is the mesh spacing and $F_{i\pm\frac{1}{2}}$ are the interface flux.

The numerical flux at the interface is defined as a function of the left and right states:

$$F_{i+\frac{1}{2}} = \frac{1}{2}\left(au_L + au_R\right) - \epsilon\frac{|a|}{2}\left(u_R - u_L\right), \tag{B.10}$$

where ϵ is a parameter that determines the amount of numerical diffusion applied. The reconstructed interface value is done by fitting a quadratic polynomial to the cell averages of three neighboring cells. The reconstructed value at the interface is then given by:

$$u^{\text{upwind}}_{i\pm\frac{1}{2}} = \frac{1}{6}\left(2\bar{u}_{i-1} + 5\bar{u}_i + 2\bar{u}_{i+1} - 3\bar{u}_{i\mp1}\right), \tag{B.11}$$

The combination of the flux and the reconstruction gives a third-order accurate scheme. The exact formulation of the diffusive terms of the inviscid fluxes for low Mach number flows is available in Hope-Collins and di Mare [2023].

Regarding the viscous fluxes, the gradients required for their computation are evaluated using the least squares method. This approach ensures improved accuracy and robustness, particularly on unstructured or highly skewed meshes, by minimising the error in gradient reconstruction based on surrounding cell values.

When dealing with the optional source term, it is assumed that the cell value represents the average value of the control volume. This simplifies the evaluation of the source term

$$\int_{\Omega_i} S_{\Omega_i}\, dV = S_{\Omega_i} V_i \tag{B.12}$$

B.2.2 Temporal discretisation

Advancement in time is carried out using a formally second-order accurate semi-implicit scheme, with implicit iterations based on a dual-time stepping formulation, originally proposed by Jameson and Shankaran [2009].

The dual-time stepping method can be derived by starting from the compact form of the N-S equations (Equation B.7) written for a scalar T:

$$\frac{\partial T}{\partial t} = \mathcal{R}(T) \tag{B.13}$$

The time integration is performed using the Crank-Nicolson method. This implicit scheme achieves second-order accuracy by evaluating the residual at the average of the current and next time steps. Although implicit methods allow for larger time steps compared to explicit methods, they require the solution of a nonlinear system of equations at each iteration. The Crank-Nicolson formulation of Equation B.13 is given by:

$$\frac{T^{n+1} - T^n}{\Delta t} = \frac{1}{2}\left(\mathcal{R}(T^{n+1}) + \mathcal{R}(T^n)\right) \tag{B.14}$$

Where the superscript n denotes the time level and Δt is the time step. The dual-time stepping approach introduces a pseudo-time derivative into Equation B.13 to solve the nonlinear system. If the system for the pseudo-time τ is driven to a steady state the solution will be equivalent to Equation B.14.

$$\frac{\partial T}{\partial \tau} = \mathcal{R}^*(T) \tag{B.15}$$

$$\text{where}: \mathcal{R}^*(T^n) = \frac{1}{2}\left(\mathcal{R}(T^{n+1}) + \mathcal{R}(T^n)\right) - \frac{T^{n+1} - T^n}{\Delta t} \tag{B.16}$$

The pseudo-time derivative is discretised using an explicit scheme, which does not require the system Jacobian or a linear solver. This explicit scheme is still subject to the CFL limit, but because time-accuracy is not required in the pseudo-time, various convergence acceleration techniques can be used to extend this limit considerably. The result is a scheme that allows large physical timesteps on the convective timescale without the need to directly solve an implicit system. Such a scheme allows the existing Runge-Kutta scheme implemented in `H4X` to be used to drive the pseudo-time convergence. A strong-stability-preserving Runge-Kutta (SSPRK) scheme, which is stable for large time steps and third-order accuracy, is employed for the pseudo-time derivative [Gottlieb, 2005]. To further accelerate pseudo-time convergence, methods such as multigrid techniques, local time stepping, residual smoothing, implicit relaxation, preconditioning, and residual scaling can be utilised. In this solver, three specific acceleration techniques are implemented: local time stepping, residual smoothing, and low Mach number preconditioning. Further details on these techniques are beyond the scope of this thesis and are available in Hope-Collins [2022].

B.3 Numerical methods for conjugate heat transfer simulations

B.3.1 Spatial discretisation

To solve numerically Equation 2.4, a discretisation method is required in space and time. In the present work, the spatial discretisation chosen for the solid domain is based on a finite element formulation.

Starting from Equation 2.4:

$$\rho_s c_{p,s} \frac{\partial T}{\partial t} = \frac{\partial}{\partial x_i} \left(\kappa_s \frac{\partial T}{\partial x_i} \right) + Q_s \tag{B.17}$$

In the following developments, the subscript S will be dropped for clarity.

To get the weak form, the continuous equation can be multiplied by an arbitrary test function N and integrated over the whole solid domain Ω_s.

$$\int_{\Omega_s} N \rho c_p \frac{\partial T}{\partial t} dV = \int_{\Omega_s} N \frac{\partial}{\partial x_i} \left(\kappa \frac{\partial T}{\partial x_i} \right) + NQ dV \tag{B.18}$$

Next, the second derivative of the temperature is transformed using integration by parts:

$$\int_{\Omega_s} N\frac{\partial}{\partial x_i}\left(\kappa\frac{\partial T}{\partial x_i}\right)dV = -\int_{\Omega_s}\frac{\partial N}{\partial x_i}\left(\kappa\frac{\partial T}{\partial x_i}\right)dv + \int_{\delta\Omega} N\left(\kappa\frac{\partial T}{\partial x_i}\right)dS + \int_{\Omega_s} NQdV \tag{B.19}$$

Invoking a general mixed type boundary condition in Equation B.20, with $h(x)$ and $\beta(x,t)$ as coefficients, yields Equation B.21. This general expression is used to keep the formulation broad and applicable to various boundary condition types: Robin boundary conditions, Neumann boundary conditions, and radiative boundary conditions through appropriate specification of the coefficients.

$$-\kappa\frac{\partial T}{\partial n} = h(x)\left(T - T_g(x,t)\right) + \beta(x,t) \qquad \text{on } \delta\Omega \tag{B.20}$$

$$\begin{aligned}\int_{\Omega} N\rho c_p\frac{\partial T}{\partial t}dV = &-\int_{\Omega}\frac{\partial N}{\partial x_i}\left(\kappa\frac{\partial T}{\partial x_i}\right)dV\\ &-\int_{\delta\Omega} h(x)\left(T - T_g(x,t)\right) + \beta(x,t)dS + \int_{\Omega} NQdV\end{aligned} \tag{B.21}$$

Introducing the Galerkin projection, discretising the domain using $T \simeq \sum_j T_j(t)N_j(x)$, the equation becomes

$$\begin{aligned}\sum_j \int_{\Omega} N_iN_j\rho c_p\frac{\partial T_j}{\partial t}dV = &-\int_{\Omega}\kappa\frac{\partial N_j}{\partial x_k}\frac{\partial N_i}{\partial x_k}T_jdV\\ &-\int_{\delta\Omega} h(x)\left(T_jN_j - T_g(x,t)\right) + \beta(x,t)dS + \int_{\Omega} N_iQdV\end{aligned} \tag{B.22}$$

The resulting linear system is symbolically:

$$\mathbf{M}\frac{d\mathbf{T}}{dt} = -\mathbf{K}\mathbf{T} + \mathbf{G}(t) \tag{B.23}$$

With M the mass matrix, K the stiffness matrix and G the forcing term.

$$\begin{aligned}\mathbf{M} : M_{ij} &= \int_{\Omega}\rho c_p N_iN_jdV\\ \mathbf{K} : K_{ij} &= \int_{\Omega}\kappa\frac{\partial N_i}{\partial x_k}\frac{\partial N_j}{\partial x_k}dV + \int_S hN_iN_jdS\\ \mathbf{G} : G_i &= \int_{\Omega} N_iQdV + \int_{\delta\Omega} h(x)\left(T_jN_j - T_g(x,t)\right) + \beta(x,t)dS\end{aligned}$$

B.3.2 Temporal discretisation

Time integration is carried out using a dual-time stepping scheme, described in subsection B.2.2. The time integration scheme is based on the Crank-Nicolson scheme, which has been used for the heat conduction equation in multiple studies [Henshaw and Chand, 2009, Kazemi-Kamyab et al., 2014b]. The scheme is adapted to the finite element formulation of the heat conduction equation. Starting from Equation B.14 written for Equation B.23 :

$$\mathbf{M}\frac{\delta \mathbf{T}}{\Delta t} = -\frac{\mathbf{K}}{2}\left(\mathbf{T}^{n+1} + \mathbf{T}^{n}\right) + \frac{\mathbf{G}^{n} + \mathbf{G}^{n+1}}{2} \tag{B.24}$$

$$\Leftrightarrow \mathbf{M}\frac{\delta \mathbf{T}}{\Delta t} = -\mathbf{K}\left(\mathbf{T}^{n} + \frac{1}{2}\delta\mathbf{T}\right) + \frac{\mathbf{G}^{n} + \mathbf{G}^{n+1}}{2} \tag{B.25}$$

Writing $\delta\mathbf{T} = \mathbf{T}^{n+1} - \mathbf{T}^{n}$. Introducing the pseudo-time derivative, the equation becomes:

$$\frac{\partial \mathbf{T}}{\partial \tau} + \mathbf{M}\frac{\delta \mathbf{T}}{\Delta t} = -\mathbf{K}\left(\mathbf{T}^{n} + \frac{1}{2}\delta\mathbf{T}\right) + \frac{\mathbf{G}^{n} + \mathbf{G}^{n+1}}{2} \tag{B.26}$$

$$\Leftrightarrow \frac{\partial \mathbf{T}}{\partial \tau} = -\left(\frac{\mathbf{M}}{\Delta t} + \frac{\mathbf{K}}{2}\right)\delta\mathbf{T} - \mathbf{K}\mathbf{T}^{n} + \frac{\mathbf{G}^{n} + \mathbf{G}^{n+1}}{2} \tag{B.27}$$

The pseudo-time derivative is discretised using a first-order Euler scheme and the residuals are evaluated using a semi-implicit method. Writing the pseudo-time iterations using the superscript m, the semi-implicit scheme becomes:

$$\frac{\delta \mathbf{T}^{*}}{\Delta \tau} = -\left.\left(\frac{\mathbf{M}}{\Delta t} + \frac{\mathbf{K}}{2}\right)\right|_{wn}\left(\delta\mathbf{T} + \delta\mathbf{T}^{*}\right) - \left.\left(\frac{\mathbf{M}}{\Delta t} + \frac{\mathbf{K}}{2}\right)\right|_{tg}\delta\mathbf{T} - \mathbf{K}\mathbf{T}^{n} + \frac{\mathbf{G}^{n} + \mathbf{G}^{n+1}}{2} \tag{B.28}$$

Where $\delta\mathbf{T}^{*} = \mathbf{T}^{n+1,m+1} - \mathbf{T}^{n+1,m}$. The semi-implicit scheme treats the wall-normal direction wn in an implicit manner, while the tangential directions tg are treated explicitly. This is done because in most CHT problems, the wall-normal gradients are expected to be the steepest, treating them implicitely in pseudo-time will enable the use of larger pseudo-time steps. The systems are solved independently along each wall-normal line, solving efficiently a tridiagonal system.

Rewriting gives:

$$\frac{\delta \mathbf{T}^*}{\Delta \tau} = -\left(\frac{\mathbf{M}}{\Delta t} + \frac{\mathbf{K}}{2}\right)\bigg|_{wn} (\delta \mathbf{T}^*) - \left(\frac{\mathbf{M}}{\Delta t} + \frac{\mathbf{K}}{2}\right) \delta \mathbf{T} - \mathbf{K}\mathbf{T}^n + \frac{\mathbf{G}^n + \mathbf{G}^{n+1}}{2} \tag{B.29}$$

$$\Leftrightarrow \left(1/\Delta \tau + \left(\frac{\mathbf{M}}{\Delta t} + \frac{\mathbf{K}}{2}\right)\bigg|_{wn}\right) \frac{\delta \mathbf{T}^*}{\Delta \tau} = -\left(\frac{\mathbf{M}}{\Delta t} + \frac{\mathbf{K}}{2}\right) \delta \mathbf{T} - \mathbf{K}\mathbf{T}^n + \frac{\mathbf{G}^n + \mathbf{G}^{n+1}}{2} \tag{B.30}$$

With this scheme, both domains are coupled within each inner iteration and the criterion for both system to have converged to the desired tolerance is enforced.

On top of the intrinsic advantages of a dual-time scheme such as improved stability or increased efficiency, coming from the use of implicit time integration schemes while maintaining stability and convergence properties typically associated with explicit schemes. The dual-time framework is advantageous for unsteady problems with multiple time scales, such as CHT problems as it allows for the separation of these scales, enabling each to be resolved appropriately without the need for excessively small time steps. The time step selection can be based on physical considerations alone, regardless of numerical stability considerations, as numerical stability is managed by the pseudo-time integration process.

Bibliography

Mohamed el Abbassi, Domenico Lahaye, and Kees Vuik. Modelling turbulent combustion coupled with conjugate heat transfer in openfoam. In Fred J. Vermolen and Cornelis Vuik, editors, *Numerical Mathematics and Advanced Applications ENUMATH 2019*, pages 1137–1145, Cham, 2021. Springer International Publishing. ISBN 978-3-030-55874-1.

Abas Abdoli, George S Dulikravich, Chandrajit Bajaj, David F Stowe, and M Salik Jahania. Human heart conjugate cooling simulation: Unsteady thermo-fluid-stress analysis. *International journal for numerical methods in biomedical engineering*, 30(11): 1372–1386, 2014.

Tommaso Bacci, Alessio Picchi, Tommaso Lenzi, Bruno Facchini, and Luca Innocenti. Effect of surface roughness and inlet turbulence intensity on a turbine nozzle guide vane external heat transfer: experimental investigation on a literature test case. *Journal of Turbomachinery*, 143(4):041006, 2021.

LH Back, PF Massier, and HL Gier. Convective heat transfer in a convergent-divergent nozzle. *International Journal of Heat and Mass Transfer*, 7(5):549–568, 1964.

Sungwon Bae, Sanjiva K Lele, and Hyung Jin Sung. Influence of inflow disturbances on stagnation-region heat transfer. *J. Heat Transfer*, 122(2):258–265, 2000.

Deep Bandivadekar and Edmondo Minisci. Modelling and simulation of transpiration cooling systems for atmospheric re-entry. *Aerospace*, 7(7), 2020. ISSN 2226-4310. doi: 10.3390/aerospace7070089. URL `https://www.mdpi.com/2226-4310/7/7/89`.

George Beckett, Josephine Beech-Brandt, Kieran Leach, Zöe Payne, Alan Simpson, Lorna Smith, Andy Turner, and Anne Whiting. Archer2 service description, December 2024. URL `https://doi.org/10.5281/zenodo.14507040`.

John J. Bertin and Russell M. Cummings. Critical hypersonic aerothermodynamic phenomena*. *Annual Review of Fluid Mechanics*, 38(Volume 38, 2006):129–157, 2006. ISSN 1545-4479. doi: https://doi.org/10.1146/annurev.fluid.38.050304.092041. URL `https://www.annualreviews.org/content/journals/10.1146/annurev.fluid.38.050304.092041`.

Jiri Blazek. *Computational fluid dynamics: principles and applications.* Butterworth-Heinemann, 2015.

D. Bohn, V. Becker, and Agnes U. Rungen. Experimental and numerical conjugate flow and heat transfer investigation of a shower-head cooled turbine guide vane. 1997.

Luca Boscaglia, Fabio Bonsanto, A. Boglietti, S. Nategh, and Claudio Scema. Conjugate heat transfer and cfd modeling of self-ventilated traction motors. *2019 IEEE Energy Conversion Congress and Exposition (ECCE)*, pages 3103–3109, 2019. doi: 10.1109/ECCE.2019.8913138.

Samuel Brody, Kin Sing Lau, Justin Clarke, Matthew McGilvray, and Di Mare Luca. *Numerical Simulation of Transpiration Cooling on Stagnation Line in Thermochemical Non-Equilibrium.* 2024. doi: 10.2514/6.2024-0648. URL `https://arc.aiaa.org/doi/abs/10.2514/6.2024-0648`.

Tuncer Cebeci. *Analysis of turbulent boundary layers.* Elsevier, 2012.

Divya Chalise, K. Shah, R. Prasher, and A. Jain. Conjugate heat transfer analysis of thermal management of a li-ion battery pack. 15:011008, 2018. doi: 10.1115/1.4038258.

Justin Clarke, Peter L. Collen, Matthew McGilvray, and Luca di Mare. *Numerical Simulation of a Shock Tube in Thermochemical Non-Equilibrium.* 2022. doi: 10.2514/6.2023-1797. URL `https://arc.aiaa.org/doi/abs/10.2514/6.2023-1797`.

E. W. Comings, J. T. Clapp, and J. F. Taylor. Air turbulence and transfer processes. *Industrial & Engineering Chemistry*, 40(6):1076–1082, 1948. doi: 10.1021/ie50462a019. URL `https://doi.org/10.1021/ie50462a019`.

Paul I Crumpton and Michael B Giles. Multigrid aircraft computations using the oplus parallel library. In *Parallel Computational Fluid Dynamics 1995*, pages 339–346. Elsevier, 1996.

M Cui and Sanjeeb Bose. Investigation of the effect of conjugate heat transfer on the adiabatic effectiveness of an annular gas turbine engine combustor. In *Proceedings of the Summer Program, Center for Turbulence Research, Stanford University*, 2022.

Pramote Dechaumphai, Earl A. Thornton, and Allan R. Wieting. Flow-thermal-structural study of aerodynamically heated leading edges. *Journal of Spacecraft and Rockets*, 26 (4):201–209, 1989. doi: 10.2514/3.26055. URL `https://doi.org/10.2514/3.26055`.

Nitin S Dhamankar, Gregory A Blaisdell, and Anastasios S Lyrintzis. Overview of turbulent inflow boundary conditions for large-eddy simulations. *Aiaa Journal*, 56(4): 1317–1334, 2018.

L Di Mare, M Klein, WP Jones, and J Janicka. Synthetic turbulence inflow conditions for large-eddy simulation. *Physics of Fluids*, 18(2), 2006.

A. Sh. (Abram Shlemovich) Dorfman. *Conjugate problems in convective heat transfer.* Heat transfer. CRC Press, Boca Raton, 2010. ISBN 9781420082388.

Earl H Dowell and Kenneth C Hall. Modeling of fluid-structure interaction. *Annual review of fluid mechanics*, 33(1):445–490, 2001.

Yann Dreze and Luca di Mare. Unsteady conjugate heat transfer effects on flow characteristics in transonic flow. *International Journal of Heat and Mass Transfer*, 246: 127036, 2025. ISSN 0017-9310. doi: https://doi.org/10.1016/j.ijheatmasstransfer.2025.127036. URL `https://www.sciencedirect.com/science/article/pii/S0017931025003771`.

Yann Dreze, Muting Hao, and Luca di Mare. Divergence-free turbulent inflow data from realistic covariance tensor. *Physics of Fluids*, 35(2):025120, 02 2023. ISSN 1070-6631. doi: 10.1063/5.0136568. URL `https://doi.org/10.1063/5.0136568`.

Yann Dreze, Muting Hao, and Luca di Mare. Multiscale unsteady conjugate transfer via modal projection. *Journal of Computational Physics*, 2025.

F. Duchaine, A. Corpron, L. Pons, V. Moureau, F. Nicoud, and T. Poinsot. Development and assessment of a coupled strategy for conjugate heat transfer with large eddy simulation: Application to a cooled turbine blade. *International Journal of Heat and Fluid Flow*, 30(6):1129–1141, 2009. ISSN 0142-727X. doi: https://doi.org/10.1016/j.ijheatfluidflow.2009.07.004. URL `https://www.sciencedirect.com/science/article/pii/S0142727X09001180`.

Florent Duchaine, S Mendez, F Nicoud, A Corpron, V Moureau, and Thierry Poinsot. Coupling heat transfer solvers and large eddy simulations for combustion applications. In *Proceedings of the summer program*, volume 6, pages 113–126, 2008.

Florent Duchaine, Nicolas Maheu, Vincent Moureau, Guillaume Balarac, and Stéphane Moreau. Large-Eddy Simulation and Conjugate Heat Transfer Around a Low-Mach Turbine Blade. *Journal of Turbomachinery*, 136(5), 10 2013. ISSN 0889-504X. doi: 10.1115/1.4025165. 051015.

C.D. Ellis and H. Xia. Impact of inflow turbulence on large-eddy simulation of film cooling flows. *International Journal of Heat and Mass Transfer*, 195:123172, 2022. ISSN 0017-9310. doi: https://doi.org/10.1016/j.ijheatmasstransfer.2022.123172. URL `https://www.sciencedirect.com/science/article/pii/S0017931022006421`.

Marc-Paul Errera. Advanced numerical methods for conjugate heat transfer problems. *Computers & Fluids*, 292:106594, 2025. ISSN 0045-7930. doi: https://doi.org/10.1016/j.compfluid.2025.106594.

Marc-Paul Errera and Sébastien Chemin. Optimal solutions of numerical interface conditions in fluid–structure thermal analysis. *Journal of Computational Physics*, 245: 431–455, 2013.

Joseph C. Ferguson, Sadaf Sobhani, and Matthias Ihme. Pore-resolved simulations of porous media combustion with conjugate heat transfer. *Proceedings of the Combustion Institute*, 38(2):2127–2134, 2021. ISSN 1540-7489. doi: https://doi.org/10.1016/j.proci.2020.06.064.

Joel H Ferziger, Milovan Peric, and Robert L Street. *Computational methods for fluid dynamics*. springer, 2019.

Remy Fransen, Nicolas Gourdain, and L.Y.M. Gicquel. Steady and unsteady modeling for heat transfer predictions of high pressure turbine blade internal cooling. volume 4, 06 2012. doi: 10.1115/GT2012-69482.

Kai Fukami, Yusuke Nabae, Ken Kawai, and Koji Fukagata. Synthetic turbulent inflow generator using machine learning. *Physical Review Fluids*, 4(6):064603, 2019.

Zhihong Gao, Diganta P Narzary, and Je-Chin Han. Film cooling on a gas turbine blade pressure side or suction side with axial shaped holes. *International Journal of Heat and Mass Transfer*, 51(9-10):2139–2152, 2008.

W. H. Giedt. Effect of turbulence level of incident air stream on local heat transfer and skin friction on a cylinder. *Journal of the Aeronautical Sciences*, 18(11):725–730, 1951. doi: 10.2514/8.2092. URL `https://doi.org/10.2514/8.2092`.

M. B. Giles. Stability analysis of numerical interface conditions in fluid-structure thermal analysis. *International Journal for Numerical Methods in Fluids*, 25(4):421–436, 1997. doi: https://doi.org/10.1002/(SICI)1097-0363(19970830)25:4<421::AID-FLD557>3.0.CO;2-J. URL `https://onlinelibrary.wiley.com/doi/abs/10.1002/%28SICI%291097-0363%2819970830%2925%3A4%3C421%3A%3AAID-FLD557%3E3.0.CO%3B2-J`.

Xavier Gloerfelt and Thomas Le Garrec. Generation of inflow turbulence for aeroacoustic applications. In *14th AIAA/CEAS Aeroacoustics Conference (29th AIAA Aeroacoustics Conference)*, page 2926, 2008.

R. Gonçalves dos Santos, M. Lecanu, S. Ducruix, O. Gicquel, E. Iacona, and D. Veynante. Coupled large eddy simulations of turbulent combustion and radiative heat transfer. *Combustion and Flame*, 152(3):387–400, 2008. ISSN 0010-2180. doi: https://doi.org/10.1016/j.combustflame.2007.10.004. URL `https://www.sciencedirect.com/science/article/pii/S001021800700288X`.

Sigal Gottlieb. On high order strong stability preserving runge-kutta and multi step time discretizations. *Journal of scientific computing*, 25:105–128, 2005.

Miles Greiner, Paul F Fischer, and Henry Tufo. Numerical simulations of resonant heat transfer augmentation at low reynolds numbers. *J. Heat Transfer*, 124(6):1169–1175, 2002.

Ezer Griffiths and JH Awbery. Heat transfer between metal pipes and a stream of air. *Proceedings of the Institution of Mechanical Engineers*, 125(1):319–382, 1933.

Nicolas Guézennec and Thierry Poinsot. Acoustically nonreflecting and reflecting boundary conditions for vortcity injection in compressible solvers. *AIAA journal*, 47(7): 1709–1722, 2009.

P. E. Hancock and P. Bradshaw. The effect of free-stream turbulence on turbulent boundary layers. *Journal of Fluids Engineering*, 105(3):284–289, 09 1983. ISSN 0098-2202. doi: 10.1115/1.3240989. URL `https://doi.org/10.1115/1.3240989`.

Muting Hao, Joshua Hope-Collins, and Luca di Mare. Generation of turbulent inflow data from realistic approximations of the covariance tensor. *Physics of Fluids*, 34(11):115140, 11 2022. ISSN 1070-6631. doi: 10.1063/5.0106664. URL `https://doi.org/10.1063/5.0106664`.

L. He and M. L. G. Oldfield. Unsteady conjugate heat transfer modeling. *Journal of Turbomachinery*, 133(3):031022, 11 2010. ISSN 0889-504X. doi: 10.1115/1.4001245.

L He and MLG Oldfield. Unsteady conjugate heat transfer modeling. *Journal of turbomachinery*, 133(3), 2011.

Li He. Chapter two - conjugate heat transfer: Some fundamentals and recent progress. volume 55 of *Advances in Heat Transfer*, pages 41–87. Elsevier, 2023. doi: https://doi.org/10.1016/bs.aiht.2023.02.002. URL `https://www.sciencedirect.com/science/article/pii/S0065271723000035`.

James D. Heidmann, Alain J. Kassab, Eduardo A. Divo, Franklin Rodriguez, and Erlendur Steinthorsson. Conjugate heat transfer effects on a realistic film-cooled turbine vane. Volume 5: Turbo Expo 2003, Parts A and B:361–371, 06 2003.

William D. Henshaw and Kyle K. Chand. A composite grid solver for conjugate heat transfer in fluid–structure systems. *Journal of Computational Physics*, 228(10): 3708–3741, 2009. ISSN 0021-9991. doi: https://doi.org/10.1016/j.jcp.2009.02.007. URL `https://www.sciencedirect.com/science/article/pii/S0021999109000667`.

Gregor Herkewitz. Novel high-performance cfd methods for advanced simulations in turbines. 2024.

Tobias Hermann. Correlation for wall-temperature oscillations in unsteady stagnation point convective heating. *International Journal of Heat and Mass Transfer*, 244:126907, 2025. ISSN 0017-9310. doi: https://doi.org/10.1016/j.ijheatmasstransfer.2025.126907. URL `https://www.sciencedirect.com/science/article/pii/S0017931025002480`.

Mark Ho, Edward Obbard, Patrick A Burr, and Guan Yeoh. A review on the development of nuclear power reactors. *Energy Procedia*, 160:459–466, 2019.

Justin Hodges. Gas turbine blade heat transfer via unsteady flow mechanisms using harmonic balance conjugate heat transfer simulation. 2018.

MJ Holland and TF Thake. Rotor blade cooling in high pressure turbines. *Journal of aircraft*, 17(6):412–418, 1980.

C.J. Hoogendoorn. The effect of turbulence on heat transfer at a stagnation point. *International Journal of Heat and Mass Transfer*, 20(12):1333–1338, 1977. ISSN 0017-9310. doi: https://doi.org/10.1016/0017-9310(77)90029-1. URL `https://www.sciencedirect.com/science/article/pii/0017931077900291`.

Joshua Hope-Collins. Low mach number numerical methods, and dns of turbulent heat transfer. 2022.

Joshua Hope-Collins and Luca di Mare. Artificial diffusion for convective and acoustic low mach number flows i: Analysis of the modified equations, and application to roe-type schemes. *Journal of Computational Physics*, 475:111858, 2023. ISSN 0021-9991. doi: https://doi.org/10.1016/j.jcp.2022.111858. URL `https://www.sciencedirect.com/science/article/pii/S0021999122009214`.

T Horbach, A Schulz, and H-J Bauer. Trailing edge film cooling of gas turbine airfoils—external cooling performance of various internal pin fin configurations. 2011.

Sunwoo Hwang, Changmin Son, Doyoung Seo, Dong-Ho Rhee, and Bongjun Cha. Comparative study on steady and unsteady conjugate heat transfer analysis of a high pressure turbine blade. *Applied Thermal Engineering*, 99, 01 2016. doi: 10.1016/j.applthermaleng.2015.12.139.

LD Hylton, MS Mihelc, ER Turner, DA Nealy, and RE York. Analytical and experimental evaluation of the heat transfer distribution over the surfaces of turbine vanes. Technical report, 1983.

Justin B Illingworth, Nicholas J Hills, and Christopher J Barnes. 3d fluid–solid heat transfer coupling of an aero engine pre-swirl system. In *Turbo Expo: Power for Land, Sea, and Air*, volume 47268, pages 801–811, 2005.

Antony Jameson and Sriram Shankaran. An assessment of dual-time stepping, time spectral and artificial compressibility based numerical algorithms for unsteady flow with applications to flapping wings. In *19th AIAA computational fluid dynamics*, page 4273. 2009.

Johannes Janicka, Amsini Sadiki, Michael Schäfer, and Christof Heeger. *Flow and combustion in advanced gas turbine combustors*, volume 102. Springer Science & Business Media, 2012.

James W. Jewkes, Yongmann M. Chung, and Peter W. Carpenter. Modifications to a turbulent inflow generation method for boundary-layer flows. *AIAA Journal*, 49(1): 247–250, 2011. doi: 10.2514/1.J050318.

Bibin John, P Senthilkumar, and Sreeja Sadasivan. Applied and theoretical aspects of conjugate heat transfer analysis: A review. *Archives of Computational Methods in Engineering*, 2(26):475–489, 2018.

Harold A Johnson and MW Rubesin. Aerodynamic heating and convective heat transfer—summary of literature survey. *Transactions of the American Society of Mechanical Engineers*, 71(5):447–456, 1949.

Ojas Joshi and Penelope Leyland. Stability analysis of a partitioned fluid–structure thermal coupling algorithm. *Journal of Thermophysics and Heat Transfer*, 28(1):59–67, 2014. doi: 10.2514/1.T4032. URL `https://doi.org/10.2514/1.T4032`.

Yousef Kanani, Sumanta Acharya, and Forrest Ames. Numerical predictions of turbine cascade secondary flows and heat transfer with inflow turbulence. *Journal of Turbomachinery*, 143(12):121008, 2021.

H. Kanchi, K. Sengupta, and F. Mashayek. Effect of turbulent inflow boundary condition in les of flow over a backward-facing step using spectral element method. *International Journal of Heat and Mass Transfer*, 62:782–793, 2013. ISSN 0017-9310. doi: https://doi.org/10.1016/j.ijheatmasstransfer.2013.03.038. URL `https://www.sciencedirect.com/science/article/pii/S0017931013002457`.

Massoud Kaviany. *Essentials of heat transfer: principles, materials, and applications.* Cambridge University Press, 2011.

V. Kazemi-Kamyab, A.H., and H. Bijl. Analysis and application of high order implicit runge-kutta schemes for unsteady conjugate heat transfer: A strongly-coupled approach. *Journal of Computational Physics*, 272:471–486, 2014a. ISSN 0021-9991. doi: https://doi.org/10.1016/j.jcp.2014.04.016. URL `https://www.sciencedirect.com/science/article/pii/S0021999114002794`.

V. Kazemi-Kamyab, A. H. van Zuijlen, and H. Bijl. Accuracy and stability analysis of a second-order time-accurate loosely coupled partitioned algorithm for transient conjugate heat transfer problems. *International Journal for Numerical Methods in Fluids*, 74(2): 113–133, 2014b. doi: https://doi.org/10.1002/fld.3842. URL `https://onlinelibrary.wiley.com/doi/abs/10.1002/fld.3842`.

Andreas Kempf, Markus Klein, and Johannes Janicka. Efficient generation of initial-and inflow-conditions for transient turbulent flows in arbitrary geometries. *Flow, Turbulence and combustion*, 74(1):67–84, 2005.

J. Kestin. The effect of free-stream turbulence on heat transfer rates. volume 3 of *Advances in Heat Transfer*, pages 1–32. Elsevier, 1966. doi: https://doi.org/10.1016/S0065-2717(08)70049-2. URL `https://www.sciencedirect.com/science/article/pii/S0065271708700492`.

David E Keyes and et. al. Multiphysics simulations: Challenges and opportunities. *The International Journal of High Performance Computing Applications*, 27(1):4–83, 2013. doi: 10.1177/1094342012468181.

David E Keyes, Lois C McInnes, Carol Woodward, William Gropp, Eric Myra, Michael Pernice, John Bell, Jed Brown, Alain Clo, Jeffrey Connors, et al. Multiphysics simulations: Challenges and opportunities. *The International Journal of High Performance Computing Applications*, 27(1):4–83, 2013.

Kyung Min Kim, Namgeon Yun, Yun Heung Jeon, Dong Hyun Lee, Hyung Hee Cho, and Sin-Ho Kang. Conjugated heat transfer and temperature distributions in a gas turbine combustion liner under base-load operation. *Journal of mechanical science and technology*, 24:1939–1946, 2010.

Robert David Knapke and Robert David. High-Order Unsteady Heat Transfer with the Harmonic Balance Method. *PhDT*, 2015.

Chai Koren, Ronan Vicquelin, and Olivier Gicquel. An acceleration method for numerical studies of conjugate heat transfer with a self-adaptive coupling time step method: Application to a wall-impinging flame. In *Turbo Expo: Power for Land, Sea, and Air*, volume 50893, page V05CT17A006. American Society of Mechanical Engineers, 2017a.

Chai Koren, Ronan Vicquelin, and Olivier Gicquel. Self-adaptive coupling frequency for unsteady coupled conjugate heat transfer simulations. *International Journal of Thermal Sciences*, 118:340–354, 2017b.

Niklas Kotarsky and Philipp Birken. A time adaptive multirate quasi-newton waveform iteration for coupled problems. *arXiv preprint arXiv:2502.03265*, 2025.

Y. Kuwata, K. Tsuda, and K. Suga. Direct numerical simulation of turbulent conjugate heat transfer in a porous-walled duct flow. *Journal of Fluid Mechanics*, 904:A9, 2020. doi: 10.1017/jfm.2020.669.

Lee S. Langston. Turbines, gas. pages 221–230, 2004. doi: https://doi.org/10.1016/B0-12-176480-X/00098-X.

Leigh Lapworth. Hydra-cfd: a framework for collaborative cfd development. In *International conference on scientific and engineering computation (IC-SEC)*, volume 30, 2004.

HUNG Le, PARVIZ Moin, and JOHN Kim. Direct numerical simulation of turbulent flow over a backward-facing step. *Journal of Fluid Mechanics*, 330:349–374, 1997. doi: 10.1017/S0022112096003941.

Vinh Tung Le, Ngoc San Ha, and Nam Seo Goo. Advanced sandwich structures for thermal protection systems in hypersonic vehicles: A review. *Composites Part B: Engineering*, 226:109301, 2021. ISSN 1359-8368. doi: https://doi.org/10.1016/j.compositesb.2021.109301. URL `https://www.sciencedirect.com/science/article/pii/S1359836821006752`.

Hongjun Li and Alain Kassab. Numerical prediction of fluid flow and heat transfer in turbine blades with internal cooling. In *30th Joint Propulsion Conference and Exhibit*, page 2933, 1994.

Ce Liang, Yu Rao, Jiahao Luo, and Xiling Luo. Experimental and numerical study of turbulent flow and heat transfer in a wedge-shaped channel with guiding pin fins for turbine blade trailing edge cooling. *International Journal of Heat and Mass Transfer*, 178:121590, 2021.

John H. Lienhard. Learning and teaching heat transfer. *Heat Transfer Engineering*, 6(3): 26–34, 1985.

Kunlun Liu and Richard H Pletcher. Inflow conditions for the large eddy simulation of turbulent boundary layers: a dynamic recycling procedure. *Journal of Computational Physics*, 219(1):1–6, 2006.

Martina Lomele, Amanda S Smyth, Xiaosheng Chen, and Richard H Willden. Aerodynamic damping assessment on wind turbine blades using 2d and 3d computational fluid dynamics. In *AIAA SCITECH 2025 Forum*, page 1236, 2025.

G.W. Lowery and R.I. Vachon. The effect of turbulence on heat transfer from heated cylinders. *International Journal of Heat and Mass Transfer*, 18(11):1229–1242, 1975. ISSN 0017-9310. doi: https://doi.org/10.1016/0017-9310(75)90231-8. URL `https://www.sciencedirect.com/science/article/pii/0017931075902318`.

Qi Lu, Yu Liu, Jian Deng, Xiaowei Luo, Zhiyong Deng, and Zhengpeng Mi. Review of interdisciplinary heat transfer enhancement technology for nuclear reactor. *Annals of Nuclear Energy*, 159:108302, 2021.

JK Luff and JJ McGuirk. Conjugate heat transfer predictions of a combustor heatshield containing pedestals. In *Proc. of NATO AVT Meeting on Heat Transfer and Cooling in Propulsion and Power Systems*, 2001.

John L Lumley. Coherent structures in turbulence. In *Transition and turbulence*, pages 215–242. Elsevier, 1981.

Thomas S Lund, Xiaohua Wu, and Kyle D Squires. Generation of turbulent inflow data for spatially-developing boundary layer simulations. *Journal of computational physics*, 140(2):233–258, 1998.

H. Ma, Z. Wang, L. Wang, Q. Zhang, Z. Yang, and Y. Bao. Ramp heating in high-speed transient thermal measurement with reduced uncertainty. *Journal of Propulsion and Power*, 32(5):1190–1198, 2016. doi: 10.2514/1.B35803. URL `https://doi.org/10.2514/1.B35803`.

Zahra Mansouri, Rathinam Panneer Selvam, and Arindam Gan Chowdhury. Performance of different inflow turbulence methods for wind engineering applications. *Journal of Wind Engineering and Industrial Aerodynamics*, 229:105141, 2022.

Richard Mathie, Hajime Nakamura, and Christos N Markides. Heat transfer augmentation in unsteady conjugate thermal systems–part ii: Applications. *International Journal of Heat and Mass Transfer*, 56(1-2):819–833, 2013.

Omid Mehdizadeh, Stephane Vilmin, Benoit Tartinville, and Charles Hirsch. Nonlinear harmonic method applied to turbine conjugate heat transfer analysis for efficient simulation of hot streak clocking and unsteady heat transfer. 06 2017. doi: 10.1115/GT2017-63622.

Peter Meisrimel and Philipp Birken. Waveform relaxation with asynchronous time-integration. *ACM Trans. Math. Softw.*, 48(4), December 2022. ISSN 0098-3500. doi: 10.1145/3569578. URL `https://doi.org/10.1145/3569578`.

Maxence Miguel-Brebion, Daniel Mejia, Pradip Xavier, Florent Duchaine, Benoît Bédat, Laurent Selle, and Thierry Poinsot. Joint experimental and numerical study of the influence of flame holder temperature on the stabilization of a laminar methane flame on a cylinder. *Combustion and Flame*, 172:153–161, 2016.

Brent Miller, Andrew Crowell, and Jack McNamara. Computational modeling for conjugate heat transfer of shock-surface interactions on compliant skin panels. In *52nd AIAA/ASME/ASCE/AHS/ASC Structures, Structural Dynamics and Materials Conference 19th AIAA/ASME/AHS Adaptive Structures Conference 13t*, page 2017, 2017.

Yann Moguen, Pascal Bruel, Vincent Perrier, and Erik Dick. Non-reflective inlet conditions for the calculation of unsteady turbulent compressible flows at low mach number. *Mechanics & Industry*, 15(3):179–189, 2014.

A. Montenay, L. Paté, and J. M. Duboué. Conjugate heat transfer analysis of an engine internal cavity. Volume 3: Heat Transfer; Electric Power; Industrial and Cogeneration: V003T01A086, 05 2000. doi: 10.1115/2000-GT-0282. URL `https://doi.org/10.1115/2000-GT-0282`.

Brandon Morgan, Johan Larsson, Soshi Kawai, and Sanjiva K Lele. Improving low-frequency characteristics of recycling/rescaling inflow turbulence generation. *AIAA journal*, 49(3):582–597, 2011.

T. Mukha and M. Liefvendahl. The generation of turbulent inflow boundary conditions using precursor channel flow simulations. *Computers & Fluids*, 156:21–33, 2017. ISSN 0045-7930. doi: https://doi.org/10.1016/j.compfluid.2017.06.020. URL `https://www.sciencedirect.com/science/article/pii/S0045793017302311`. Ninth International Conference on Computational Fluid Dynamics (ICCFD9).

Wim Munters, Charles Meneveau, and Johan Meyers. Turbulent inflow precursor method with time-varying direction for large-eddy simulations and applications to wind farms. *Boundary-layer meteorology*, 159(2):305–328, 2016.

MSR Chandra Murty, P Manna, and Debasis Chakraborty. Conjugate heat transfer analysis in high speed flows. *Proceedings of the Institution of Mechanical Engineers, Part G*, 227(10):1672–1681, 2013. doi: 10.1177/0954410012464920. URL `https://doi.org/10.1177/0954410012464920`.

Farah Nazifa Nourin and Ryoichi S Amano. Review of gas turbine internal cooling improvement technology. *Journal of Energy Resources Technology*, 143(8):080801, 2021.

Tae Kyung Oh, Danesh K. Tafti, and Krishnamurthy Nagendra. Fully Coupled Large Eddy Simulation-Conjugate Heat Transfer Analysis of a Ribbed Cooling Passage Using the Immersed Boundary Method. *Journal of Turbomachinery*, 143(4):041012, 03 2021. ISSN 0889-504X. doi: 10.1115/1.4050111. URL `https://doi.org/10.1115/1.4050111`.

E. Ortega, E. Castillo, R.C. Cabrales, and N.O. Moraga. Effect of time integration scheme in the numerical approximation of thermally coupled problems: From first to third order. *Computers and Mathematics with Applications*, 99:345–360, 2021. ISSN 0898-1221. doi: https://doi.org/10.1016/j.camwa.2021.08.018. URL `https://www.sciencedirect.com/science/article/pii/S0898122121003096`.

T.L. Perelman. On conjugated problems of heat transfer. *International Journal of Heat and Mass Transfer*, 3(4):293–303, 1961. ISSN 0017-9310. doi: https://doi.org/10.1016/0017-9310(61)90044-8.

M. Piro and B. W. Leitch. Conjugate heat transfer simulations of advanced research reactor fuel. *Nuclear Engineering and Design*, 274:30–43, 2014. doi: 10.1016/J.NUCENGDES.2014.03.054.

T J&amp Poinsot and SK Lelef. Boundary conditions for direct simulations of compressible viscous flows. *Journal of computational physics*, 101(1):104–129, 1992.

Alfio Quarteroni and Alberto Valli. *Domain decomposition methods for partial differential equations*. Oxford University Press, 1999.

Farid K. Rafla. *Aerodynamic Heating Coupled with Structural Temperature Response Analysis for Hypersonic Flight Vehicles*. 2019. doi: 10.2514/6.2019-3132. URL `https://arc.aiaa.org/doi/abs/10.2514/6.2019-3132`.

Faisal Rahman, Jan A Visser, and Reuben M Morris. Capturing sudden increase in heat transfer on the suction side of a turbine blade using a navier–stokes solver. 2005.

Man Mohan Rai and Parviz Moin. Direct numerical simulation of transition and turbulence in a spatially evolving boundary layer. *Journal of Computational Physics*, 109(2):169–192, 1993.

Hans Reiss, Uwe Drost, and Albin Bölcs. The transient liquid crystal technique employed for sub- and transonic heat transfer and film cooling measurements in a linear cascade. 1998.

Andrew Richards. *University of Oxford Advanced Research Computing*, August 2015. URL `https://doi.org/10.5281/zenodo.22558`.

Markus Schmidt and Christoph Starke. Comparison of steady and unsteady coupled heat-transfer simulations of a high-pressure turbine blade. In *Turbo Expo: Power for Land, Sea, and Air*, volume 56710, page V05AT10A016. American Society of Mechanical Engineers, 2015.

Sebastian Scholl, Tom Verstraete, Florent Duchaine, and Laurent Gicquel. Conjugate heat transfer of a rib-roughened internal turbine blade cooling channel using large eddy simulation. *International Journal of Heat and Fluid Flow*, 61:650–664, 2016.

J.W. Scholten and D.B. Murray. Unsteady heat transfer and velocity of a cylinder in cross flow—i. low freestream turbulence. *International Journal of Heat and Mass Transfer*, 41 (10):1139–1148, 1998. ISSN 0017-9310. doi: https://doi.org/10.1016/S0017-9310(97)00250-0. URL `https://www.sciencedirect.com/science/article/pii/S0017931097002500`.

Matthew J. Schwartz and Daniel J. Garmann. *Investigation of Turbulent Inflow Techniques for High-Fidelity Simulations*. doi: 10.2514/6.2023-2628. URL `https://arc.aiaa.org/doi/abs/10.2514/6.2023-2628`.

Siddhesh Shinde and Eric Johnsen. Synthetic inflow methods for turbulent boundary layer simulations: a physics-based approach versus a data-driven approach. In *2018 Fluid Dynamics Conference*, page 3403, 2018.

Francis Shum-Kivan, Florent Duchaine, and Laurent Gicquel. Large-Eddy Simulation and Conjugate Heat Transfer in a Round Impinging Jet. Volume 5A: Heat Transfer, 06 2014. doi: 10.1115/GT2014-25152. V05AT11A001.

Christoph Starke, Erik Janke, Toma´ sˇ Hofer, and Davide Lengani. Comparison of a conventional thermal analysis of a turbine cascade to a full conjugate heat transfer computation. In *Turbo Expo: Power for Land, Sea, and Air*, volume 43147, pages 1013–1024, 2008.

Richard J.A.M. Stevens, Jason Graham, and Charles Meneveau. A concurrent precursor inflow method for large eddy simulations and applications to finite length wind farms. *Renewable Energy*, 68:46–50, 2014. ISSN 0960-1481. doi: https://doi.org/10.1016/j.renene.2014.01.024. URL `https://www.sciencedirect.com/science/article/pii/S0960148114000536`.

S. P. Sutera. Vorticity amplification in stagnation-point flow and its effect on heat transfer. *Journal of Fluid Mechanics*, 21(3):513–534, 1965. doi: 10.1017/S0022112065000307.

Kenjiro Suzuki and Hiroshi Suzuki. Unsteady heat transfer in a channel obstructed by an immersed body. *Annual Review of Heat Transfer*, 5, 1994.

Siddharth Thakur, Jeffrey Wright, and Wei Shyy. Convective film cooling over a representative turbine blade leading-edge. *International journal of heat and mass transfer*, 42(12):2269–2285, 1999.

Marco Tosetti, P. Maggiore, A. Cavagnino, and S. Vaschetto. Conjugate heat transfer analysis of integrated brushless generators for more electric engines. *IEEE Transactions on Industry Applications*, 50:2467–2475, 2014. doi: 10.1109/TIA.2013.2296657.

ER Turner, MD Wilson, LD Hylton, and RM Kaufman. Turbine vane external heat transfer. volume 1: analytical and experimental evaluation of surface heat transfer distributions with leading edge showerhead film cooling. Technical report, 1985.

Gerald Urbin and Doyle Knight. Large-eddy simulation of a supersonic boundary layer using an unstructured grid. *AIAA Journal*, 39(7):1288–1295, 2001. doi: 10.2514/2.1471. URL `https://doi.org/10.2514/2.1471`.

J. Uribe, C. Moulinec, M. Rabbitt, R. Howard, and D. Emerson. Les of the flow inside the lower plenum of an advanced gas-cooled reactor with conjugate heat transfer. *Procedia Engineering*, 61:192–197, 2013. doi: 10.1016/J.PROENG.2013.08.002.

G. J. Van Fossen, R. J. Simoneau, and C. Y. Ching. Influence of turbulence parameters, reynolds number, and body shape on stagnation-region heat transfer. *Journal of Heat Transfer*, 117(3):597–603, 08 1995. ISSN 0022-1481. doi: 10.1115/1.2822619. URL `https://doi.org/10.1115/1.2822619`.

John A Verdicchio, John W Chew, and Nick J Hills. Coupled fluid/solid heat transfer computation for turbine discs. In *Proceedings of the ASME Turbo Expo*, volume 3, 2001.

Tom Verstraete and R. Braembussche. A novel method for the computation of conjugate heat transfer with coupled solvers. pages 1–17, 01 2009. ISBN 978-1-56700-263-8. doi: 10.1615/ICHMT.2009.HeatTransfGasTurbSyst.570.

Tom Verstraete and Sebastian Scholl. Stability analysis of partitioned methods for predicting conjugate heat transfer. *International Journal of Heat and Mass Transfer*, 101:852–869, 2016. ISSN 0017-9310. doi: https://doi.org/10.1016/j.ijheatmasstransfer.2016.05.041. URL `https://www.sciencedirect.com/science/article/pii/S001793101531245X`.

Feng Wang and Luca di Mare. Favre-averaged nonlinear harmonic method for compressible periodic flows. *AIAA Journal*, 57(3):1133–1142, 2019.

JH Wang, J Messner, and H Stetter. An experimental investigation on transpiration cooling part ii: comparison of cooling methods and media. *International Journal of Rotating Machinery*, 10(5):355–363, 2004.

Xiaohua Wu. Inflow turbulence generation methods. *Annual Review of Fluid Mechanics*, 49(1):23–49, 2017.

Yu-Ting Wu, Chuan-Yao Lin, and Tsang-Jung Chang. Effects of inflow turbulence intensity and turbine arrangements on the power generation efficiency of large wind farms. *Wind Energy*, 23(7):1640–1655, 2020.

Sheng Xu and M. Pino Martin. Assessment of inflow boundary conditions for compressible turbulent boundary layers. *Physics of Fluids*, 16(7):2623–2639, 07 2004. ISSN 1070-6631. doi: 10.1063/1.1758218. URL `https://doi.org/10.1063/1.1758218`.

Ru-Dai Xue, Xiao-Hui Xiong, and Guang Chen. Flow dynamics of train under turbulent inflow at different crosswind yaw angles. *Physics of Fluids*, 36(3):035176, 03 2024. ISSN 1070-6631. doi: 10.1063/5.0195426. URL `https://doi.org/10.1063/5.0195426`.

Zifeng Yang and Hui Hu. An experimental investigation on the trailing edge cooling of turbine blades. *Propulsion and Power Research*, 1(1):36–47, 2012.

Mustafa Z Yousif, Linqi Yu, and HeeChang Lim. Physics-guided deep learning for generating turbulent inflow conditions. *Journal of Fluid Mechanics*, 936:A21, 2022.

Mustafa Z Yousif, Meng Zhang, Linqi Yu, Ricardo Vinuesa, and HeeChang Lim. A transformer-based synthetic-inflow generator for spatially developing turbulent boundary layers. *Journal of Fluid Mechanics*, 957:A6, 2023.

Linqi Yu, Mustafa Z. Yousif, Meng Zhang, Sergio Hoyas, Ricardo Vinuesa, and Hee-Chang Lim. Three-dimensional esrgan for super-resolution reconstruction of turbulent flows with tricubic interpolation-based transfer learning. *Physics of Fluids*, 34(12):125126, 12 2022. ISSN 1070-6631. doi: 10.1063/5.0129203. URL `https://doi.org/10.1063/5.0129203`.

Yuxin Zhang, Shuyang Cao, and Jinxin Cao. An improved consistent inflow turbulence generator for les evaluation of wind effects on buildings. *Building and Environment*, 223: 109459, 2022. ISSN 0360-1323. doi: https://doi.org/10.1016/j.buildenv.2022.109459. URL `https://www.sciencedirect.com/science/article/pii/S0360132322006904`.

Chao Zong, Chenzhen Ji, Jiaying Cheng, and Tong Zhu. Comparison of adiabatic and conjugate heat transfer models on near-wall region flows and thermal characteristics of angled effusion cooling holes. *Thermal Science and Engineering Progress*, 30:101269, 2022. ISSN 2451-9049. doi: https://doi.org/10.1016/j.tsep.2022.101269. URL `https://www.sciencedirect.com/science/article/pii/S2451904922000762`.

Yuri B Zudin. *Theory of periodic conjugate heat transfer*. Springer, 2012.